Spin-Orbit Coupled Quantum Magnetism in the 3D-Honeycomb Iridates

by

Itamar Kimchi

A dissertation submitted in partial satisfaction of the

requirements for the degree of

Doctor of Philosophy

in

Physics

in the

Graduate Division

of the

University of California, Berkeley

Committee in charge:

Professor Ashvin Vishwanath, Chair

Professor Joel E. Moore

Professor K. Birgitta Whaley

Spring 2015

Spin-Orbit Coupled Quantum Magnetism in the 3D-Honeycomb Iridates

Abstract

Spin-Orbit Coupled Quantum Magnetism in the 3D-Honeycomb Iridates

by

Itamar Kimchi

Doctor of Philosophy in Physics

University of California, Berkeley

Professor Ashvin Vishwanath, Chair

In this doctoral dissertation, we consider the significance of spin-orbit coupling for the phases of matter which arise for strongly correlated electrons. We explore emergent behavior in quantum many-body systems, including symmetry-breaking orders, quantum spin liquids, and unconventional superconductivity. Our study is cemented by a particular class of Mott-insulating materials, centered around a family of two- and three-dimensional iridium oxides, whose honeycomb-like lattice structure admits peculiar magnetic interactions, the so-called Kitaev exchange. By analyzing recent experiments on these compounds, we show that this unconventional exchange is the key ingredient in describing their magnetism, and then use a combination of numerical and analytical techniques to investigate the implications for the phase diagram as well as the physics of the proximate three-dimensional quantum spin liquid phases. These long-ranged-entangled fractionalized phases should exhibit special features, including finite-temperature stability as well as unconventional high-T_c superconductivity upon charge-doping, which should aid future experimental searches for spin liquid physics. Our study explores the nature of frustration and fractionalization which can arise in quantum systems in the presence of strong spin-orbit coupling.

Contents

Acknowledgments

Scientific research is a collaborative enterprise. Fellow scientists will appreciate that the acknowledgments section is not an acknowledgment of specific contributions, but rather a recognition that research is the product of many minds and hands. Whether the communication is through informal verbal discussion or through reading of notes and manuscripts, the net outcome is a product of the communication network itself, as much as of any of its nodes.

I would like to first acknowledge the people in my life who have had the most impact, indirect yet momentous, on my work. This thesis is dedicated to my spouse and partner, Mollie Schwartz, whose thoughtful encouragement inspires my strengths; and to my brother Ofer and my sister Anat, and our parents, Chava and Avi, whose love for science and for uncovering the mysteries of nature will always remain my inspiration.

It has been a great privilege to be advised by Ashvin Vishwanath through the course of my PhD research. Whether closely involved in technical computations or guiding with a broader sense of a research philosophy, Ashvin has been a true mentor. I am grateful to have been so closely exposed to his thoughts and advice over these years.

I have also had the honor of working closely with remarkable physicists who make measurements on real materials. Both James Analytis and Radu Coldea have guided me, in technical understanding and through larger questions concerning the nature of good science. The opportunity to learn from them and from their brilliant group members has shaped my vision of physics research.

I am grateful to Joel Moore and to Birgitta Whaley, who served as my committee members, for their time as well as for guiding my early research explorations and serving as research role models during my graduate studies.

My undergraduate teachers and mentors at MIT paved the path of my physics education. I would like to acknowledge my research advisor Bob Jaffe and my academic advisor Barton Zwiebach. My friends and colleagues, back in my undergraduate as well of course as here during my graduate studies at Berkeley, were a great positive influence for me. I am grateful for their encouragement, and for the many hikes, picnics and barbecues we've had in sunny Berkeley.

I had the great pleasure of learning a great deal by working with many great physicists during these years, and most especially from working closely with Yi-Zhuang You, Sid Parameswaran, Ari Turner, Fa Wang, and Andrew Potter; as well as George Jackeli, Giniyat Khaliullin, Ehud Altman, Dan Stamper-Kurn and his group, Ali Yazdani and his group, Bela Bauer, Brayden Ware, Ru Chen, and recently Norman Yao. I am grateful for their patience in teaching as well as their inspiration in research.

I learned much from others who walked the halls of Birge, especially Tarun Grover, Jens Bardarson, Yuan-Ming Lu, and the many other postdoctoral fellows who lent me their time, as well as fellow students including Michael P. Zaletel, Pavan Hosur, Frank

Yi Zhang, Haruki Watanabe, Philipp Dumitrescu, Yasaman Bahri, Adrian Po, Tess Smidt, and Alejandro Ruiz. During conferences and visits elsewhere, I am grateful for many inspiring discussions with Christopher Henley, Roderich Moessner, Hong Yao, Frank Pollmann, Olexei Motrunich, Kirill Shtengel, Duncan Haldane, Matthew Fisher, Leon Balents, and Masaki Oshikawa. The research presented here is a product of all of these collaborations and discussions.

No acknowledgments section would be complete without funding agencies. Though a complete list is here impossible, I am grateful for the support of the National Science Foundation, which impacted my research through many grants but in particular also through the Graduate Research Fellowship Program (DGE 1106400) and a semester with the Kavli Institute for Theoretical Physics Graduate Fellowship Program (NSF PHY11-25915). I have also benefitted from funding under ARO MURI grant W911NF-12-0461 and from Contract No. DE-AC02-05CH11231 of the Office of Basic Energy Sciences in the Materials Sciences and Engineering Division of the U.S. Department of Energy.

Despite the best efforts, there may be many significant people who, due to the rush to the filing deadline, did not get appropriately thanked or acknowledged; I offer my sincere apologies in advance for any omissions or mistakes.

Chapter 1

Introduction

1.1 Overview: many-electron physics

When the valence electrons in a piece of solid are primarily captured by atomic orbitals with small spatial extent, large angular momentum quantum number ℓ and intermediate principal quantum number n, the strong Coulomb repulsion between the electrons can restrict the amplitude for two electrons to occupy the same tight space around a nucleus. At appropriate (commensurate) electron densities, these valence electrons become stuck, as in a traffic jam in a fully packed parking lot, and cannot efficiently transport heat or electric current. The resulting insulator may be called a Mott insulator, in contrast to the band insulator which can arise in a Fermi gas interacting with the periodic crystal potential. Though the distinction between Mott and Band insulating behavior is not rigorously defined when the translation symmetries require a unit cell with an even number of electrons, a qualitative difference remains – the requirement of a theoretical treatment incorporating strong inter-electron interactions.

Many-body quantum systems in three dimensions are currently believed to be generically "impossible" to solve; that is, the computational cost (on a classical computer) scale exponentially with the number of interacting particles. Finding the ground state exactly, in some basis, would require diagonalizing a matrix which is exponentially large in the system size. Of course even if the wavefunction was magically obtained, it is not clear how to make sense of a set of exponentially-many amplitudes. The free particle picture, of fermions filling a band structure or of bosons condensing, is not only a computational tool but also a qualitative framework which no longer applies in strongly interacting phases.

Classical physics can often come to the rescue. When symmetries are spontaneously broken[1], the resulting order parameter is a classical variable which gives a

[1]Spontaneous symmetry breaking occurs when, as the system size is taken to infinity (the thermodynamic limit), the ground state manifold becomes a set of degenerate wavefunctions whose overlap

usable handle for describing (and measuring) the system. Interesting questions remain regarding microscopic (but possibly quite general) mechanisms for the formation of a given order. Classical pictures are also appropriate for describing the frozen Mott insulator, where real space localization allow us to forget the wave nature of particles. Even complicated ordering patterns, of magnetic moments on a lattice, can be described classically within some zero-fluctuation limit.

Yet other phases of matter are possible still — phases for which the entanglement among constituent particles is not a perturbative afterthought but rather a necessary required ingredient. These are not classical. For example, one can write[2] a wave function for particles on the graphene lattice at a density of one-half per site ("half filling") forming a Mott insulator (no Dirac cones) without breaking symmetries, but with unavoidable fluctuations in local particle number. No obvious experimental realization exists. Related phases with similar unavoidable short-ranged entanglement, but which are captured by non-interacting treatments, are topological insulators and topological semi-metals (Weyl or Dirac), and offer experimental realizations or promising candidates. Strongly-interacting variants are still elusive.

The bulk of this thesis will be motivated by a different subject, framed by a particular lithium-iridium-oxide series of compounds. We shall deal with concrete experiments on real materials, while simultaneously seeking to build a bridge to a class of quantum phases of matter, even more exotic than those described above. This class, going by names such as "spin liquids" or "topological order" in certain cases, involves necessary long-range entanglement among the constituent strongly-interacting particles. (One picture for its emergence involves condensation of extended string-like objects.) The resulting effective excitations, i.e. those that emerge at low energies, can be wildly different – emergent fermions in a system of interacting bosons, or fractional quantum numbers as in the charge $e/3$ excitations of a fractional quantum hall liquid. But because these phases are not described by a (local) classical order parameter, they are inherently difficult to identify. These phases may be fragile, but they are mysterious and interesting beyond any potential technological applications. In setting some foundation stones for a bridge connecting theory and experiment in this particular Li_2IrO_3 context, this thesis aims to inspire further work on this or on other bridges.

---

remains vanishing even after any finitely-many local transformations (superselection rules). Superpositions of these states then cannot be physically constructed. Examples include a liquid freezing into a crystalline solid with its cornerstone atom sitting at the origin instead of epsilon away, or in a broader sense, a certain cat in a box spontaneously choosing to appear alive instead of in a winter hibernation.

[2] I give this particular example here just because it is the subject of one of my other research projects, on "featureless insulators" (see Proc. Nat. Acad. Sci. 110 (41) 16378-16383 (2013) and Phys. Rev. Lett. 110, 125301 (2013) for reference[1, 2]). However, the discussion of these subjects is beyond the scope of this thesis.

1.2 Entanglement – the quantum information perspective

Beyond the traditional interplay between physics, chemistry and material science, common in condensed matter physics, an additional set of ingredients has been increasingly present in the field. These new ingredients originate in quantum information science. As well as being technical necessary for much of the research techniques presented in this thesis, quantum information provides a useful perspective on the the physics in quantum magnets.

Consider a classical configuration of spins on a discrete lattice, also known as a (classical) mean field ansatz. This configuration corresponds to a quantum wave function which is a direct product over single-site wave functions. This ansatz forms a subspace of variational states within the full quantum Hilbert space. The single-site wave functions may be taken to be, for instance, $S = 1/2$ spinor functions, or $S = 1$ orbital wave functions, or classical $S = \infty$ vectors. Regardless of that choice, the resulting many-body wave function is in a deeper sense fully classical.

Quantum fluctuations require states beyond such a mean field ansatz. The strength of such fluctuations can be considered in a controlled manner, on the level of wave functions, by introducing a measure of entanglement. Consider two isolated $S = 1/2$ objects, which in a different context may be called quantum bits (or qubits). The quantum wave function of this pair of states includes configurations where these qubits cannot be written as a site-product state regardless of the choice of local $S = 1/2$ basis, such as the rotationally-symmetric singlet (or valence bond) state. Such entangled configurations can be recorded by writing the wave function as a sum over products of coefficients in the single-sites basis, rather than as a single term of a pure product of such coefficients. In the case of the two qubits, this sum of products can be represented using matrix multiplication of two 2×2 matrices.

Such matrix multiplication schemes enable us to represent many entangled quantum many-body states. These ansatz states (matrix product states in 1D, tensor network states in certain higher-dimensional schemes) involve some control parameter for the maximum entanglement between nearby sites, associated with the maximum dimension of the matrix multiplication, and known as the bond dimension. Non-ordered states with necessary quantum entanglement can be captured in this scheme, such as the AKLT state in the topological Haldane phase of the $S = 1$ 1D spin chain, which can already be captured with maximal bond dimension equal to two, yet representing a major qualitative distinction from mean field states with bond dimension equal to one. This entanglement-controlled approach can also capture some states with topological order, allowing for possibilities for variational computations (such as the density-matrix renormalization-group), yielding quantitative as well as qualitative information on quantum states of entangled spins.

1.3 Frustration (it's a good thing)

An additional useful viewpoint on spin liquids is gained by considering the concept of frustration. This is related to the viewpoint of spin liquids as arising via quantum melting of magnetic (or other broken symmetry) orders.

The concept of frustration in a quantum Hamiltonian involves a classical analogue or basis choice. Given a quantum many body Hamiltonian, it can be difficult to immediately gain intuition for the "effects" of its various non-commuting terms. (A Hamiltonian is quantum if its terms do not all commute with each other, in contrast with, for example, an Ising model.) One can often gain intuition by considering a classical variant. For a Heisenberg model, one can pick a particular quantization axis, generalize the Heisenberg term to an XXZ interaction with a stronger coupling along the quantization axis, and consider the XY terms as a perturbation, adding quantum fluctuations, to the quantization-axis Ising interaction. In general one can take the large-spin (classical) limit, equivalently restricting the Hilbert space to products (over sites) of spin coherent states, and treat the Pauli matrices as classical vectors.

One can then study this analogous classical energy function. In many cases, the degenerate minima of the classical problem are labeled by a global quantity, that is related to the symmetry of the problem. A ferromagnet spontaneously chooses an ordering axis. However in some cases, the degeneracy can be extensive, so that the number of classical lowest-energy configurations grows exponentially with the system size. (By system size we refer to the measure of the bulk, rather than say the surface, of the system.) This extensive classical degeneracy is the signal of frustration in the quantum problem. Even when the Hamiltonian is slightly modified, the extensive manifold of nearly-degenerate classical configurations offers a wide playground for inexpensive coherent quantum superpositions. The quantum fluctuations, i.e. the terms which were missing in the classical energy function, then have the defining effect in constructing the ground states from within this manifold, using quantum superpositions that can easily entangle even distant objects. Thus, in quantum Hamiltonians exhibiting frustration, one can hope that truly quantum behavior may arise.

Frustration can also be manifested in computational algorithms. One may want to write the Hamiltonian in a particular convenient basis, and then to use this basis to express the time evolution operator $U = e^{-iHt}$ in small discrete time interval steps (i.e. to "Trotterize"), for example in order to write a path integral. Similarly, one may want to perform such a discretization, in a particular basis, on the imaginary time evolution operator $e^{-\beta H}$, to compute the partition function. This is an attempted rewriting of the d-dimensional quantum problem as a $(d+1)$-dimensional classical statistical mechanics problem. It is (one description of) the approach used in quantum Monte Carlo algorithms, which perform classical Monte Carlo simulations on this higher dimensional stat mech model. However, the quantum Monte Carlo approach can fail: the $(d+1)$-dimensional operator may fail to be purely real. Then the amplitudes sampled by Monte Carlo, $e^{-\beta H}$, can be negative or even complex. This is

known as the "sign problem"; it occurs, for example, when there are Berry's phases in the resulting action, or often for fermions away from half filling. The occurrence of an unavoidable sign problem in a bosonic model is generally associated with frustration.

In both of the senses described above, frustration signals the breakdown of classical treatments, and can often be roughly associated with new kinds of quantum behavior.

1.4 Mean field theories for fractionalization: a handle on spin liquids and descendant superconductors

Consider a frustrated magnetic Hamiltonian of $S = 1/2$ spins on a lattice. The frustration may enable quantum fluctuations to melt any candidate magnetic ordering. A mean field treatment which requires spins to gain a expectation value should then not be used. Indeed, the quantum ground state may be a spin liquid, whose excitations are emergent particles involving many entangled spins. How can one hope to describe such a phase? One set of approaches consists of so-called slave-particle mean fields. Here we briefly mention some of these approaches; for references and a more complete description, the reader is pointed to chapters 3 and 4 of this manuscript.

The approach involves re-writing the $S = 1/2$ operators on each site using an enlarged Hilbert space. For example, consider a particle creation operator $a^\dagger$ which has two spin species, $a = (a_\uparrow, a_\downarrow)$. We may rewrite the spin operator on each site using

$$\vec{S} = \frac{1}{2} a^\dagger \vec{\sigma} a \tag{1.1}$$

where $\vec{\sigma}$ is the vector of the three Pauli matrices, acting on the spinor indices of the particle a. This enlarged Hilbert space has two important and related properties. First, there is some local (gauge) freedom in re-writing the a operators. For instance one could multiply a by an arbitrary phase, without changing the spin operator. Second, to restore the physical spin Hilbert space, one must introduce a single-occupancy constraint,

$$a_\uparrow^\dagger a_\uparrow + a_\downarrow^\dagger a_\downarrow = 1 \tag{1.2}$$

The constraint can be implemented in the action via a Lagrange multiplier, defined on every site, which may be considered as a scalar potential. Therefore a description of the spins via the a particles necessarily has the a particles coupled to a gauge field.

The resulting theory is highly interacting, and in particular offers two drastically different types of phases: the gauge field may be confining, in which case the a operators do not represent particles free to move across the lattice with a dispersion relation, and the enlarged Hilbert space is not a useful approach; or the gauge field may be deconfining, in which case the low energy excitations are not spins but rather can be associated with the a operators and related emergent "particles". In this latter

case, emergent particles are deconfined and the microscopic variables are fractionalized, so that this enlarged Hilbert space approach can be a potentially useful starting point. The fractionalized quantum numbers may be seen for example in a Heisenberg magnet: the excitations of magnetically ordered states involve a spin flip which changes the spin quantum number by an integer $1\hbar$, while the emergent a excitations can carry half-integer spin $\hbar/2$.

The many possibilities of the resulting spin-disordered phase can be partially distinguished, in this mean field approach, by expectation values of operators constructed of a operators on different sites, such as $a_i^\dagger \sigma^\mu a_j$ or $a_i \epsilon \sigma^\mu a_j$, where μ could be zero (representing the identity matrix) and $\epsilon = i\sigma^2$ is the 2×2 antisymmetric matrix. These condensed operators define the gauge freedom which remains in the spin liquid phase, giving rise for example to U(1) or Z_2 spin liquids. This remaining gauge freedom allows the symmetries of the original problem to act in a projective manner on the fractionalized excitations: a symmetry operation can act simultaneously with some other transformation, and even a product of symmetry operations which acts as the identity on the microscopic spin variables (i.e. it is a defining relation for the group) can be taken to act as a gauge transformation, within the "invariant gauge group", on the emergent fractionalized excitations.[3]

We have so far avoided being specific about the statistics of the a particles in this mean field treatment. It is important to note that the choice of statistics in the mean field description can be misleading: a phase which may be in some way captured by the bosonic mean field, could still have low lying deconfined fermions. With this caveat in mind, let us note some rough basic statements contrasting the approaches of bosonic and fermionic mean fields.

The Schwinger boson approach, where a is taken to be bosonic, has the advantage of straightforwardly capturing some magnetic orders as well as some spin liquid phases. The single-occupancy constraint $n_i = 1$ can be generalized to $n_i = \kappa$, where κ should be taken to be twice the spin in order to faithfully represent the Hilbert space, but can be studied to arbitrary values of κ to produce a phase diagram. At large κ, fluctuations in the boson number become less costly and one often finds that the boson operators a themselves gain an expectation value and condense, which immediately gives an expectation value to the spin operators, describing a magnetic state. At small κ, the fluctuations are costly and the spins remain disordered.

The Schwinger fermion approach, where a is taken to be fermionic, has often been extended to describe doped Mott insulators. It is thus also known as a slave-boson approach. When doped charges, e.g. holes, are introduced in the magnetic Mott insulator, the construction of the spin from electron variables as $\vec{S} = \frac{1}{2} c^\dagger \vec{\sigma} c$ suggests

[3]When considering emergent projective symmetries, it may be helpful to keep in mind one familiar example of projective representations, namely half-integer spin. The spinor $S = 1/2$ is a conventional representation of SU(2), but may also be considered as a projective representation of SO(3). In this case, rotations by 2π, which act as the identity within SO(3), produce an additional minus sign on the $S = 1/2$ spinor.

a description of the electron as a product of a fermion a which carries spin half, and a holon which carries the electron's electric charge. The holon may naively be taken to be bosonic. If the undoped Mott insulator forms a spin liquid where the fermions a are deconfined, then introducing charges will produce deconfined holons. Indeed doped charges may be more mobile in a spin liquid than in an antiferromagnet, where their roughly-spin-conserving motion leaves behind a trail of mismatched bonds – the description here may thus also apply for doped magnetic insulators, which may emulate the properties of a doped spin liquid.

Now consider the behavior of the doped spin liquid in this slave boson approach. With sufficient doping, the bosonic charged holons can then directly condense, resulting in a superconducting phase. What is special about this superconductor? Consider that the T_c of conventional BCS superconductors is set by the weak residual attractive interactions, mediated by phonons, which pair electrons into Cooper pairs. Once the BCS Cooper pairs are formed (in a clean system), the temperature is already quite low compared to the temperature of their condensation transition. In contrast, for the doped spin liquid, one merely requires the bosonic holons to condense. This condensation temperature is not exponentially small, but rather is controlled by the density of dopants and by their mass, which naively may be comparable to the very small mass of the electron, resulting in a superconducting transition T_c which theoretically can be quite large. Such a high T_c would of course give just a hint of the exotic physics lying underneath; but the fractionalization of the frustrated Mott insulator is expected to at least give rise to unconventional and possibly dramatic signatures upon charge doping.

Finally we note that though these slave-particle mean field theories are in general uncontrolled, certain limits offer theoretical control. The Schwinger boson theories become exact under certain large-N generalizations of spin SU(2) symmetry. The Schwinger fermion theory remarkably becomes exact for a particular spin model (and its generalizations), the Kitaev honeycomb model (see arxiv:0506438 for Kitaev's up-to-date original manuscript, and arxiv:0904.2771 for a summary). The mean field description of these models yields a gauge field which is static, and thus permits the exact solution described by Kitaev (Details are deferred to chapters 3, 4, and 6). Much of this manuscript will explore these Kitaev-type models. The Hamiltonian involves Ising-like interactions between $S = 1/2$ degrees of freedom, but with different quantization axes for the Ising interaction on different bonds across the lattice, varying in a particular pattern. Any hope of realizing this seemingly-exotic model in a real solid state system will thus necessarily involve a coupling between spin and the lattice.

1.5 When the electron spin is no longer internal

Special relativity sets special constraints on the otherwise-internal electron spin. In a fully relativistic (3+1)D field theory, the spin of a particle even uniquely sets

its statistics (bosonic vs fermionic). When spatial symmetries are broken, the story gains complications and richness. Relativistic motion exchanges electric into magnetic fields; clearly it significantly impacts the internal electron spin, in a manner dependent on its motion. The resulting object is no longer purely internal and need not preserve the spin rotation SU(2) symmetry. The reduced symmetry permits a much larger playing field for the behavior of this magnetic quantum degree of freedom.

As can be seen by studying the "hydrogen atom" with arbitrary nuclear charge and a single electron, a large nuclear charge (as in heavy elements) produces electron orbits for which relativistic corrections are significant, with energy scaling as the fourth power of the charge, Z^4. These corrections produce a spin-orbit coupling, $-L \cdot S$. For an element with large atomic number, such as iridium with $Z = 77$, spin-orbit coupling is frequently significant for chemistry and electronic physics. Its interplay with the electronic correlations – arising from Coulomb interactions which are often considered to be of "intermediate strength" for d-orbitals of transition metals like iridium – can be especially rich. Certainly the splitting of band degeneracies by the spin-orbit coupling, and the subsequent narrowing of the band width, should enhance the effects of Coulomb interactions to produce effectively stronger correlations. But this interplay can also exhibit more subtle effects, as discussed later in this thesis.

1.6 The Ir^{4+} ion in its octahedral cage

The physical systems we will most focus on, which exhibit this large spin-orbit coupling, will involve the $Z = 77$ iridium atom, and moreover its appearance in a particular class of crystalline lattices. Let us thus briefly review the orbital splitting for the iridium ion which will be an ingredient for much of this thesis. Though this story is standard in chemistry courses, we include it here since such discussion is sometimes absent in undergraduate physics curricula. Consider an isolated Ir^{4+} ion. It has five valence electrons, occupying the 5d orbitals. Now transport this isolated ion into a lattice, where it is locally surrounded by 6 oxygen O^{2-} ions. Roughly we imagine that these oxygens form the vertices of an octahedron, with the iridium ion at its center.

The 5d orbital of the Ir valence electrons is sufficiently spread out (unlike say the 3d orbitals) so that Hund's coupling is not sufficiently strong to overcome the Coulomb interaction with nearby ions, especially not these oxygen ions; thus iridium is in a low-spin state. We can consider its electrons to be non-interacting, and just draw the energy level diagram for the five independent electrons.

The 5d orbitals are split by the electric field of the nearby oxygens. This effect is known as the crystal field splitting (though we consider only the local environment, rather than the entire crystal). For the ideal octahedron of oxygens which we consider here, it is quite useful to denote the resulting orbitals by considering them as repre-

sentations of the cubic symmetry of the octahedron.[4] These are known here as t_{2g}, with three pairs (spin-up and spin-down) of levels; and e_g, with two pairs of levels. The cubic symmetry is represented by sets of quadratic polynomials as $xy,\ yz,\ zx$ for t_{2g}, and $x^2 - y^2,\ 2z^2 - x^2 - y^2$ for e_g. The t_{2g} orbitals face away from the negatively charged oxygen ions, and thus are lower in energy than e_g.

Five electrons fill the six single-particle energy levels of t_{2g}. In the absence of any distortions away from cubic symmetry, we can consider the splitting due to the next energy scale, which is the spin-orbit coupling. For certain other representations, including in this case the e_g levels, the orbital angular momentum operator $\vec{L}$ has zero expectation value, i.e. it is quenched, so spin-orbit coupling does not split the energy levels. However in our case of t_{2g}, angular momentum is not quenched, and we must study the spin-orbit splitting. When projected into the three t_{2g} orbitals, the angular momentum operators $L_k = -i\epsilon_{ijk} r_i \partial_j$ effectively act as in an $L = 1$ representation, though with a significant distinction. Computing the action of the angular momentum raising and lowering operators on $L_z = -1, 0, 1$ combinations of the t_{2g} levels, one finds that a raising operator acts to lower L_z and vice versa. (This behavior is sometimes described as an $L = -1$ representation.) The result is that when $-\lambda L \cdot S$ splits t_{2g} into multiplets of definite total angular momentum $j = 1/2$ and $j = 3/2$, the $j = 3/2$ level has lower energy $-\lambda/2$ while $j = 1/2$ has higher energy λ. The five electrons completely fill the $j = 3/2$ multiplet and leave a single electron within the $j = 1/2$ Kramer's doublet; the state of the system is then described as an effective spin-1/2 degree of freedom.

A few words on the magnitudes of these various energy scales: they are not reliably known. However, some values which are often accepted, in the context of these materials, are roughly as follows. The crystal field splitting between t_{2g} and e_g is about 4 eV, and the hybridization with oxygen 2p orbitals is suppressed by the charge transfer gap of about 3 eV. The splitting from spin-orbit coupling, between the $j = 3/2$ and $j = 1/2$, is about 3/4 eV, associated with a spin-orbit coupling parameter λ with magnitude about 0.5 eV. The Coulomb repulsion U is also about 0.5 eV. Note that the full interaction matrix for the d orbitals involves not only U but also a Hund's coupling J_H, which is smaller; its magnitude is more uncertain.[5] The hopping integral in the resulting multi-band Hubbard model, on these lattices, might be somewhere on the rough order of 30 meV.

The relation of the atomic picture presented above to the physics of the bulk solids is subtle, but a few points can be made. The description above applies in cases where the electrons of the isolated iridium ions remain mostly localized when

[4] You can see the cubic symmetry of the octahedron by putting a dot at the center of every face, and connecting these dots. If needed you may want to review the relationship between triangle faces and cubic symmetry by recalling the construction of the face-centered-cubic lattice as a stacking of triangular lattice layers.

[5] An additional inter-orbital interaction parameter "V" exists in general but can be expressed solely in terms of U and J_H for these d orbitals.

it is placed in the lattice, i.e. when the material is insulating. Of course some local hybridization with oxygen p orbitals does occur. One can also consider the distinction between insulating behavior arising from Mott (correlation) physics compared to band (independent-electron) physics. Since we primarily consider lattices with an even number of sites per unit cell, the distinction is not sharply defined but rather becomes one of a crossover between regimes. However, the presence of local moments, seen in thermodynamic susceptibility measurements as well as in low temperature scattering probes, suggests that a localized Mott picture can serve as an appropriate starting point, and moreover that quantitative results are likely better computed in the strongly correlated, rather than the weakly correlated, regime.

1.7 Overview of this manuscript

The material presented in this manuscript follows a particular logical progression in presenting the iridates under study, at times focusing on analysis of experiments and at times on abstract theory. This progression is roughly in correspondance with the chronological order in which the research results were uncovered.

The story begins with the next chapter, Chapter **2**, which considers some experimental evidence for the possibility of a certain model describing 2D layered iridates. The key immediate historical context for this work is the seminal 2009 Letter of George Jackeli and Giniyat Khaliullin (Phys. Rev. Lett. 102, 017205, 2009). Chapter **3** then considers certain theoretical implications of this class of models, when mobile charges are introduced. The interesting predictions serve as one of several background motivations for this line of research.

The following chapters then turn again to face experiments. A central event in the story is the synthesis and characterization of a completely new three-dimensional iridate compound, through work in the groups of James Analytis and Radu Coldea. First, Chapter **4** presents the culmination of early work (presented in early 2012) on 2D and 3D extensions of the work by Jackeli and Khaliullin. It is then followed by the experimental report of (with theoretical discussion of early measurements) of this new 3D iridate compound, in Chapter **5**.

Chapter **6** presents a comprehensive theoretical analysis of some exciting theoretical possibilities for this class of 3D materials, combining some analysis of experiments together with theoretical tools including a tensor network computation of the quantum model. The peculiar phases in the phase diagram increase the urgency of characterizing the appropriate model for the new 3D compounds (a related 3D iridate was also synthesized at about the same time by Hide Takagi). This is answered in remarkable fullness by the experimental work, together with the theoretical analysis, presented in Chapter **7**, which uncovers an unconventional spiral magnetic ordering in the material. The complete theoretical analysis of this magnetic order, for this and a related 3D compound, is presented in Chapter **8**, and gives substantial evidence

that a variant of the exotic Kitaev model should be close to the model Hamiltonian of the actual compound.

The content of much of this thesis has been previously presented in various forms. The publications which are purely or mostly theory have been modified only mildly for inclusion in this manuscript; the publications which were heavily based on experimental reports, here associated with Chapters 5 and 7, were modified significantly for this manuscript, to include the theoretical analysis together with its minimal experimental context. This Introduction serves as Chapter 1. The citations relevant to Chapters 2–8 are, respectively by chapter number, as follows:

(2) Kitaev-Heisenberg-J_2-J_3 model for the iridates A_2IrO_3. I. Kimchi and Y. Z. You. Physical Review B Rapid Communications 84, 180407(R) (2011).

(3) Doping a spin-orbit Mott insulator: topological superconductivity from the Kitaev-Heisenberg model and possible application to $(Na_2/Li_2)IrO_3$. Y. Z. You, I. Kimchi, A. Vishwanath. Physical Review B 86, 085145 (2012).

(4) Kitaev-Heisenberg models for iridates on the triangular, hyperkagome, kagome, fcc, and pyrochlore lattices. Itamar Kimchi, Ashvin Vishwanath. Phys. Rev. B 89, 014414 (2014).

(5) Realization of a three-dimensional spinanisotropic harmonic honeycomb iridate. K. A. Modic, T. E. Smidt, I. Kimchi, N. P. Breznay, A. Biffin, S. Choi, R. D. Johnson, R. Coldea, P. Watkins-Curry, G. T. McCandless, F. Gandara, Z. Islam, A. Vishwanath, J. Y. Chan, A. Shekhter, R. D. McDonald, J. G. Analytis. Nature Communications 5, 4203 (2014).

(6) Three dimensional quantum spin liquids in models of harmonic-honeycomb iridates and phase diagram in an infinite-D approximation. Itamar Kimchi, James G. Analytis, Ashvin Vishwanath. Phys. Rev. B 90, 205126 (2014).

(7) Non-coplanar and Counter-rotating Incommensurate Magnetic Order Stabilized by Kitaev Interactions in γ-Li_2IrO_3. A. Biffin, R.D. Johnson, I. Kimchi, R. Morris, A. Bombardi, J.G. Analytis, A. Vishwanath, and R. Coldea. Phys. Rev. Lett. 113, 197201 (2014).

(8) Unified theory of spiral magnetism in the harmonic-honeycomb iridates α, β, γ-Li_2IrO_3. Itamar Kimchi, Radu Coldea, Ashvin Vishwanath. Arxiv: 1408.3640, under peer review.

Finally, Chapter **9** presents a conclusion and the outlook for future work.

Chapter 2

Kitaev-Heisenberg-J_2-J_3 model for the iridates A_2IrO_3

In this chapter, a Kitaev-Heisenberg-J_2-J_3 model is proposed to describe the Mott-insulating layered iridates A_2IrO_3 (A=Na,Li), based on the experimental information available as of early 2011. The model is a combination of the Kitaev honeycomb model and the Heisenberg model with all three nearest neighbor couplings J_1, J_2 and J_3. A rich phase diagram is obtained at the classical level, including the experimentally suggested zigzag ordered phase; as well as the stripy phase, which extends from the Kitaev-Heisenberg limit to the J_1-J_2-J_3 one. Combining the experimentally observed spin order with the optimal fitting to the uniform magnetic susceptibility data gives an estimate of possible parameter values, which in turn reaffirms the necessity of including both the Kitaev and farther neighbor couplings.

Frustrated spin systems have long served as a relatively simple yet rich source of exotic phenomena such as spin liquids and unconventional order. The frustration may arise either geometrically on a lattice incompatible with the spin ordering, or dynamically from non-commuting competing terms in the Hamiltonian. The nearest neighbor $S = 1/2$ Heisenberg model on the kagome lattice is an instance of geometrical frustration that may even host a quantum spin liquid ground state[3]. Bipartite lattices such as the honeycomb can still be geometrically frustrated by including farther than nearest neighbor antiferromagnetic Heisenberg exchange, giving so called J_1-J_2-J_3 models. Such models on the honeycomb in particular have seen a recent surge of work[4, 5, 6, 7, 8], though a quantum spin liquid phase may require charge as well as spin fluctuations[9, 10, 11]. Breaking spin rotational symmetry provides avenues for dynamical frustration, as in the Kitaev honeycomb model[30], a nearest neighbor Ising coupling of spin component set by a bond label γ as in Fig. 3.1a. This seemingly artificial model is exactly solvable with a spin liquid ground state exhibiting an emergent Majorana fermion with a Z_2 gauge background.

A recent and surprising addition to the experimentally relevant J_1-J_2-J_3 models of frustrated spin systems, the Kitaev coupling has been recently proposed [34, 35]

to occur in the Mott insulating[31] iridates A_2IrO_3 (A=Na,Li), where the iridium ions are arranged in layers of 2D honeycomb lattices. Uniform susceptibility and heat capacity studies on these materials[31, 32] found Curie-Weiss temperatures of -125 K for Na_2IrO_3 and -33 K for Li_2IrO_3, and a low magnetic ordering temperature of 15 K for both, suggesting strong frustration. A resonant x-ray scattering measurement[17] on Na_2IrO_3 found the ground state has antiferromagnetic order at wavevector M, suggested by a first principles calculation[17] to be a *zigzag* rather than a *stripy* configuration (see Fig. 2.2).

Strong spin-orbit coupling splits the iridium t_{2g} states into a filled manifold and a half filled Kramer's doublet, an effective spin-1/2 degree of freedom which need no longer respect the rotational symmetry. Thus the 90° angles of the Ir-O-Ir hopping path within the oxygen octahedra, together with d-orbital Hund's rule coupling and orbital interactions, are able to give the Kramer's doublet highly anisotropic exchanges of the Kitaev form. Higher order hopping paths, direct orbital overlaps, trigonal distortions and spin-orbit energy splittings within the iridium two electron propagator all contribute spin interactions other than the Kitaev term, primarily including antiferromagnetic Heisenberg exchange.

Keeping only the nearest neighbor Heisenberg exchange yields the Heisenberg-Kitaev model[35, 18, 38, 20], Eq. (2.1) with J_2, J_3 set to zero, which has been previously used to describe the A_2IrO_3 materials[31, 32, 17, 35]. The phase diagram[35, 18] in the parameter $0 \leq \alpha \leq 1$ consists of a Neel phase for the Heisenberg model at small $0 \leq \alpha < 0.4$, the Kitaev spin liquid at large $0.8 < \alpha \leq 1$, and an intermediate antiferromagnetically ordered *stripy* phase (see Fig. 2.2). The *stripy* configuration is the exact ground state at $\alpha = 0.5$, solvable by means of a periodic site dependent spin rotation[35] which turns the Hamiltonian into a Heisenberg ferromagnet in the rotated spins.

Preserving J_2 and J_3 to produce the previously unstudied Kitaev-Heisenberg-J_2-J_3 model is important for two reasons. First, substantial J_2 and J_3 are likely to exist in the materials; density functional theory (DFT) calculations[41] for Na_2IrO_3 found $J_2/J_1 \approx 0.5$, and a later tight binding fit of the DFT data including J_3 found J_2, J_3 to be approximately equal[22]. Second, the experimentally suggested *zigzag* ordered ground state[17] can not be realized in a Kitaev-Heisenberg model alone. It is found that an antiferromagnetic J_3 term is needed to stabilize the *zigzag* order. Moderate Kitaev and J_2 couplings stabilize both *zigzag* and *stripy* orders. We will also show that in order to reproduce the experimentally measured uniform susceptibility $\chi(T)$, the farther neighbor J_2 and J_3 couplings as well as the Kitaev term are likely needed.

The Kitaev-Heisenberg-J_2-J_3 Hamiltonian is

$$H = J\left[(1-\alpha)\left(\sum_{\langle ij\rangle} + J_2\sum_{\langle\langle ij\rangle\rangle} + J_3\sum_{\langle\langle\langle ij\rangle\rangle\rangle}\right)\boldsymbol{\sigma}_i\cdot\boldsymbol{\sigma}_j - 2\alpha\sum_{\langle ij\rangle}\sigma_i^{\gamma_{ij}}\sigma_j^{\gamma_{ij}}\right] \tag{2.1}$$

where $\langle ij\rangle$, $\langle\langle ij\rangle\rangle$ and $\langle\langle\langle ij\rangle\rangle\rangle$ stand for the first, second and third nearest neighbor bonds, and γ_{ij} is a nearest neighbor bond label, as illustrated in Fig. 3.1a. The model interpolates between the J_1-J_2-J_3 model at $\alpha = 0$ and the Kitaev model at $\alpha = 1$, maintaining the second and third neighbor coupling strengths J_2 and J_3 in units of the nearest neighbor Heisenberg coupling strength.

A recently proposed alternative model for Na_2IrO_3 based on *ab initio* calculations[41] takes the limit where trigonal distortion effects are stronger than spin-orbit coupling, finding a Hamiltonian with Ising anisotropy and no Kitaev term[22, 23]. Putting this interesting scenario aside[24], we find that mild $\hat{c} \equiv (1,1,1)$ uniaxial trigonal distortion is consistent with our approach. The effective spin-1/2 Kramer's doublet remains well separated from the filled states. Its modified wavefunction creates anisotropies in the magnetic field coupling (g-factor tensor) and combines with the non-90° Ir-O-Ir hopping path to perturb Eq. (1), possibly enhancing both Kitaev and Heisenberg terms in addition to creating small Ising $S^{\hat{c}}S^{\hat{c}}$ and Ising-Kitaev $S^{\gamma_{ij}}S^{\hat{c}}$ terms. Both modifications are expected from the observed anisotropy in single crystal Na_2IrO_3 susceptibility[31] and do not change our results.

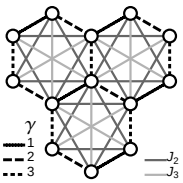

Figure 2.1: The honeycomb lattice, with Kitaev label γ for nearest neighbor bonds, and including second and third neighbor bonds with Heisenberg couplings J_2 and J_3.

Since there is ample evidence[31, 32, 17] for magnetic ordering in both Na_2IrO_3 and Li_2IrO_3 we will leave the calculation of the quantum phase diagram of Eq. (2.1) for future work, instead turning to the magnetically ordered phases which may be studied by a purely classical analysis. For each point (α, J_2, J_3) in the three dimensional phase diagram we determined the magnetic ordering configurations using a quadratic (unconstrained) classical spin model[25], which we diagonalized analytically in momentum space. Since $\Gamma = -\Gamma$ and $M = -M$ these two wavevectors automatically

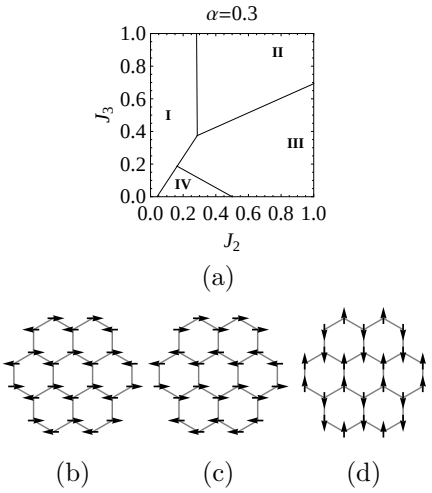

Figure 2.2: (a) Sample (J_2, J_3) slice of the classical phase diagram, with phases (I), (II) and (IV) represented in (b), (c) and (d) respectively. Region (III) contains various noncollinear spiral configurations. (b) (I) *Neel*. (c) (II) *Zigzag*. (d) (IV) *Stripy*.

give configurations of collinear unit-length normalized spins despite the absence of the unit-length constraint in the calculation, reaffirming the validity of the classical solution at these points. Solutions at wavevector K or at generic incommensurate wavevectors correspond to noncollinear spiral configurations, which we label as a single phase.

In order to discuss results on the classical phase diagram we introduce standard nomenclature from the literature. For each ordering wavevector the phases are labeled by a Roman numeral[4, 5] as follows. Γ: (I) *Neel*. M: (IV) *stripy*[35]; and (II) *zigzag*[17] (or *columnar*[8]). All other wavevectors: (III) *spiral*. Figure 2.3 displays six (J_2, J_3) slices of the classical phase diagram at various fixed α.

Quantum fluctuations modify the classical phase diagram in two ways. First, they create regions of quantum phases such as the plaquette valence bond solid or the Kitaev spin liquid; the former has been seen in the J_1-J_2-J_3 model[4], while the latter appears[18, 35] at small J_2, J_3 starting at $\alpha \geq 0.8$. Second, they shift the boundaries between the magnetically ordered phases. Quantum fluctuations disfavor the spiral configurations[4, 5] in favor of the collinear ordered phases, shrinking region (III); they also favor the *Neel* state (I) over the other orders[35, 4].

The three dimensional phase diagram offers insights otherwise unavailable in its various limits. The *stripy* (IV) region in the J_1-J_2-J_3 model at $\alpha = 0$ is in the same phase as the fluctuation-free exactly solvable point $\alpha = 0.5, J_2 = J_3 = 0$ which may be understood only within the Kitaev-Heisenberg model[35]. As α increases, both the *stripy* and the *zigzag* phases grow substantially larger. The dynamic frustration by the Kitaev term and the geometric frustration by the J_2 term have similar effects

on the ordered phases, destabilizing *Neel* in favor of *stripy* and *zigzag*.

It is worth reporting the direction of magnetic ordering in the various phases (excepting the special points $\alpha = 0$ and $\alpha = 1/2$). The direction of the collinear magnetic ordering in both *stripy* and *zigzag* phases is constrained already at the classical level. For M_z *stripy* order the spins lie along S^z, as was already determined by the spin rotation[35] solution of the $J_2 = J_3 = 0,\ \alpha = 0.5$ Hamiltonian. For *zigzag* order we found that the spins are constrained to the $S^x S^y$ plane (see Fig. 2.2). Thermal and quantum fluctuations ("order from disorder") force the spins to lie along a cubic axis within the classically allowed space, in this case the S^x and S^y axes. Trigonal distortion gives other perturbations: for example for M_z *stripy* order it cants the spin axis from S^z toward the distortion axis, and for the *Neel* phase the distortion axis may be an energy minimum or maximum within the Bloch sphere. A linear spin wave analysis found that directions closest to cubic axes are still preferred by quantum fluctuations. However, anisotropy in the real material likely overcomes all these effects to determine the ordering direction[17].

Next we discuss the comparisons between experimentally measured susceptibility[31, 32] and exact diagonalization (ED), first describing each in turn. Uniform magnetic susceptibility data for the sodium and lithium materials at temperatures up to 300 K was taken from the most recent study[32], with the constant background removed[32]. We used data from temperatures above 150K in order to avoid finite size effects when comparing to ED. ED using the "fulldiag" ALPS module[26] was performed keeping all eigenstates to enable comparison with high temperature data. The system diagonalized was an eight spin cluster, the unit cell of the $\alpha = 1/2$ site dependent spin rotation[35], with periodic boundary conditions. As expected, the eight-spin ED, corresponding to a high temperature series expansion with eight-spin clusters, is reliable to far lower temperatures than the two-spin Curie-Weiss expression which only holds at $T \gg J$. We found that ED finite size effects for eight-spin clusters were only visible in the susceptibility at low temperatures $T \lesssim J/2$, well below J. The highest J values needed for good fits were below the 150 K data cutoff, self consistently affirming the reliability of the ED fits.

For each parameter set (α, J_2, J_3) we diagonalized the system to generate a curve $\chi(T)$. The Hamiltonian Eq. (2.1) with a magnetic field coupling term has two parameters in addition to (α, J_2, J_3), namely the overall scale J and the magnetic field coupling $g\,\mu$. Since the effective spin-1/2 turns out to have the same g-factor as an electron spin, we fix $g = 2$ and expect μ/μ_B to remain close to $\mu/\mu_B = 1$. For each (α, J_2, J_3) point the curve $\chi(T)$ was fit to the experimental data by the two parameters J (corresponding to horizontal stretching) and μ/μ_B (with $(\mu/\mu_B)^2$ corresponding to vertical stretching). The resulting fit was evaluated by a "goodness function," the product of three Gaussian distributions, enforcing the following three conditions for a good fit. First, the magnetic moment μ/μ_B found by the best fit must be close to 1, with a standard deviation of 0.15. This constraint on μ effectively constrained J as well. Second, the root-mean-square relative fit residual must be near zero with a

standard deviation of 10^{-3}. Third, the third neighbor coupling must be smaller or not much larger than the second neighbor coupling, $J_3 \lesssim J_2$, relaxed by a standard deviation of 0.2. The absolute (unscaled) value of this goodness function was used to produce the shading in Fig. 2.3, with darker shading corresponding to better fits.

Given knowledge of the ground state magnetic order in Na_2IrO_3 and Li_2IrO_3, appropriate values for α, J_2 and J_3 are found by intersecting the darker shaded regions in Fig. 2.3 with the domain of the ordered phase. The estimated Na_2IrO_3 and Li_2IrO_3 parameters given either *stripy* or *zigzag* magnetic order are summarized in Table I. All material and order combinations yielded fitted values of J in the range $J \approx 60$–150 K, with the likeliest values $J \approx 100$ K. The lithium material has less structural distortion than the sodium material[32], suggesting a larger α, in agreement with the fitting results if they have the same magnetic order. For zigzag ordered Li_2IrO_3 we find $\alpha \approx 0.7$, i.e. $J_K \sim 4$–$5\ J_1$ with a numerical value of $J_K \approx 130$ K. Such a large Kitaev term relative to the other couplings suggests that the Kitaev spin liquid phase may be within experimental reach[32]. In particular, doping Li_2IrO_3 may suppress its magnetic order to reveal characteristics of a doped Kitaev spin liquid[27].

In conclusion, we propose the Kitaev-Heisenberg-J_2-J_3 model, determining its ordered phases and further using ED fits of susceptibility measurements to demonstrate its applicability to Na_2IrO_3 and Li_2IrO_3. We find that the geometrical frustration due to J_2, J_3 and the dynamical frustration due to the Kitaev term both stabilize the same unconventional *stripy* and *zigzag* ordered ground states before the onset of the Kitaev spin liquid. We extract appropriate values for the spin couplings by first restricting to the experimentally observed magnetic order in the phase diagram, and then by requiring good fitting of the susceptibility $\chi(T)$ by ED data. For *zigzag* ordered Li_2IrO_3, a significant Kitaev term $J_K \approx 130$ K, five times larger than the nearest neighbor Heisenberg coupling, as well as substantial J_2 and J_3 couplings, are required for good agreement with experimental data.

Table 2.1: Parameters for given M-wavevector order

	Na_2IrO_3:		
Stripy (IV)	$\alpha \approx 0.2$–0.3,	$J_2 \lesssim 0.5$, $J_3 \lesssim 0.2$	$J \approx 110$ K
Zigzag (II)	$\alpha \approx 0.4$–0.6,	$J_2, J_3 \gtrsim 0.4$	$J \approx 100$ K
	Li_2IrO_3:		
Stripy (IV)	$\alpha \approx 0.5$,	$J_2, J_3 \lesssim 0.3$	$J \approx 100$ K
Zigzag (II)	$\alpha \approx 0.7$,	$J_2, J_3 \gtrsim 0.4$	$J \approx 90$ K

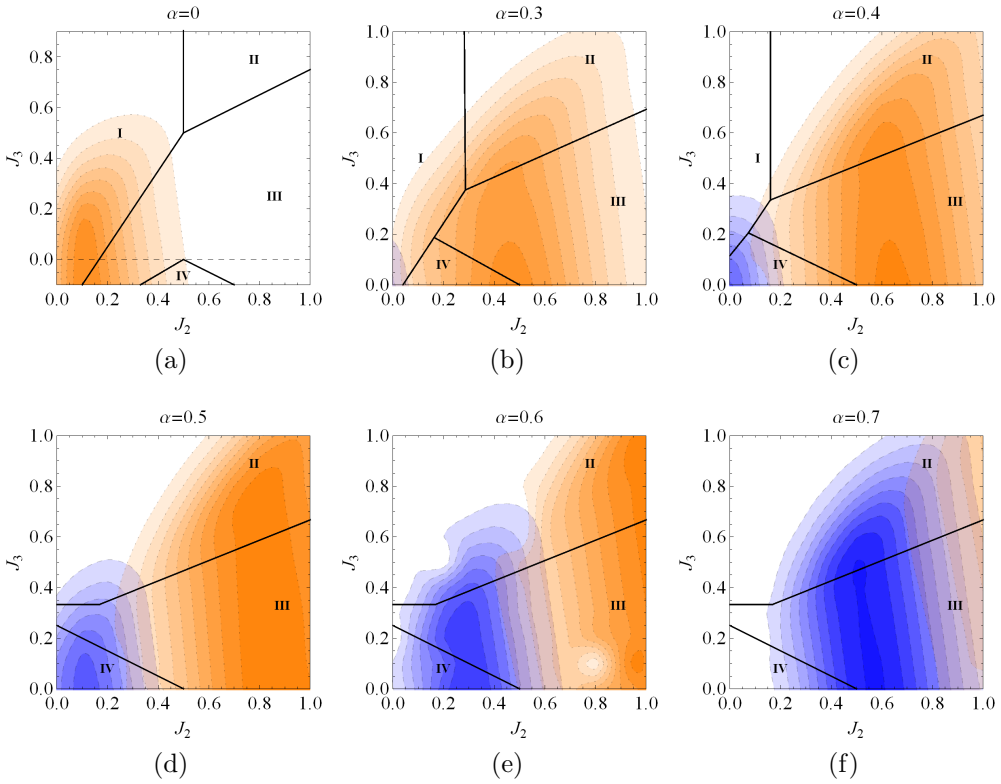

Figure 2.3: (Color online.) Fixed α slices in (J_2, J_3) showing the magnetically ordered phases (I, II, III, IV)=(*Neel*, *zigzag*, *spiral*, *stripy*) and shading corresponding to the ED $\chi(T)$ fit goodness. Increasing the Kitaev term (i.e. increasing α) enlarges the extent of the *zigzag* and *stripy* phases, which occur at both small and large α. Fits to Na_2IrO_3 are shaded in orange (with dotted contour lines) and fits to Li_2IrO_3 are in blue (with dashed contour lines); darker shading corresponds to good fitting with $\mu/\mu_B \approx 1$ and $J_2 \gtrsim J_3$, while lighter shading corresponds to poor agreement. Given a magnetically ordered ground state for each of the materials, the range of allowed parameters is found by intersecting the darker shaded region with the magnetically ordered phase.

Chapter 3

Doping a Spin-Orbit Mott Insulator: Topological Superconductivity from the Kitaev-Heisenberg Model and Possible Application to $(Na_2/Li_2)IrO_3$

Motivated by the analysis of experiments presented in the previous chapter, we now turn to a purely theoretical study of the implications of the possibility of finding a magnetic material which is described by the Kitaev model, when mobile charges are introduced. We study the effects of doping a Mott insulator on the honeycomb lattice where spins interact via direction dependent Kitaev couplings $J_{\rm K}$, and weak antiferromagnetic Heisenberg couplings J. This model is known to have a spin liquid ground state and may potentially be realized in correlated insulators with strong spin orbit coupling. The effect of hole doping is studied within a t-J-$J_{\rm K}$ model, treated using the SU(2) slave boson formalism, which correctly captures the parent spin liquid. We find superconductor ground states with spin triplet pairing that spontaneously break time reversal symmetry. Interestingly, the pairing is qualitatively different at low and high dopings, and undergoes a first order transition with doping. At high dopings, it is smoothly connected to a paired state of electrons propagating with the underlying free particle dispersion. However, at low dopings the dispersion is strongly influenced by the magnetic exchange, and is entirely different from the free particle band structure. Here the superconductivity is fully gapped and topological, analogous to spin polarized electrons with $p_x + ip_y$ pairing. These results may be relevant to honeycomb lattice iridates such as A_2IrO_3 (A = Li or Na) on doping.

3.1 Introduction

The interplay of electron correlations and strong spin-orbit coupling (SOC) is currently attracting much attention. Mott insulators with strong SOC, such as transition metal oxides (TMO) of $5d$ elements, can display entirely different properties from those with weak SOC, such as cuprates, manganites and nickelates[28]. For example, the breakdown of the spin rotation symmetry allows for magnetic Hamiltonians very different from traditionally studied SU(2) symmetric models. This can introduce a new source of frustration[29] leading to quantum spin liquid ground states. The Kitaev honeycomb lattice model, with spin dependent interactions between spin half moments, is a remarkable example that admits an exact spin liquid ground state[30]. It has recently been argued to be a natural Hamiltonian for a class of strong SOC magnets, such as the layered iridates A_2IrO_3 (A = Na, Li)[31, 32], where Iridium atoms form the sites of a honeycomb lattice. In the iridium oxides, when an octahedral cage of oxygen atoms surrounds an Iridium ion, a $j = 1/2$ doublet is proposed on the Ir site[33], for which a single band Hubbard model with strong spin orbit couplings can be invoked. In the Mott insulator, Ref. [34, 35] proposed that the spin couplings include both the isotropic Heisenberg term and the strongly anisotropic Kitaev coupling:

$$H_{\rm HK} = \sum_{\langle ij \rangle} J \boldsymbol{S}_i \cdot \boldsymbol{S}_j - J_{\rm K} S_i^a S_j^a \tag{3.1}$$

where $S_i^a S_j^a$ is Ising coupling of the spin component $a(= 1, 2, 3)$ according to the type of $\langle ij \rangle$ bond[30] (see Fig. 3.1a).

Numerical calculations[35, 36] of Eq. (3.1) indicate the Kitaev spin liquid phase appearing at $J = 0$ persists in the range $0 \leq J < J_{\rm K}/8$. Although both A_2IrO_3 (A = Na, Li) are found to be magnetically ordered[31, 32, 37], their transition temperatures are relatively low. Recent experimental papers reporting magnetic susceptibility[31, 32] have suggested that these iridates, particularly Li_2IrO_3 may be proximate to the Kitaev spin liquid phase [35, 36, 38]. Fits by exact diagonalization of the model Eq. (3.1) have reached similar conclusions[39], but indicate that farther neighbor interactions also play a role. On the other hand, Ref. [40, 41] proposed a rather different magnetic Hamiltonian, arising from large trigonal distortions, and Ref. [42] proposed a quantum spin-Hall insulator. Future experiments should pin down the magnetic Hamiltonian in these materials. A different realization of the Hamiltonian Eq. (3.1) is in perovskite iridate heterostructures of $SrIrO_3$[43], which produces a honeycomb lattice when grown along the (111) direction.

Motivated by these potential experimental realizations, here we will study the effects of doping the Heisenberg-Kitaev model, and investigate the conducting state that arises. To describe the physics of doping, we introduce the t-J-$J_{\rm K}$ model, with

the hole doping of δ per site,

$$H = -t \sum_{\sigma \langle ij \rangle} \mathcal{P} c^\dagger_{i\sigma} c_{j\sigma} \mathcal{P} - \mu \sum_{\sigma i} c^\dagger_{i\sigma} c_{i\sigma} + H_{\rm HK} \tag{3.2}$$

where the projection operator $\mathcal{P}$ removes doubly occupied sites, and the chemical potential μ is adjusted such that $\langle \sum_\sigma c^\dagger_{i\sigma} c_{i\sigma} \rangle = 1 - \delta$. The hopping term is nearest neighbor and spin independent. The symmetry of the honeycomb lattice along with reflection in the plane forbid a spin dependence in the nearest neighbor hopping, as evidenced by microscopic considerations[42]. Farther neighbor hoppings can be spin dependent, but are expected to be smaller and omitted in this minimal model. However, the spin-orbit interactions are nevertheless retained in the $J_{\rm K}$ term. Similar Hamiltonian is also studied in Ref. [48, 49].

The t-J-$J_{\rm K}$ model allows us the unique theoretical opportunity of doping a magnet which is exactly soluble in the insulating limit (at the Kitaev point), and in a spin liquid phase. The exact solution singles out the correct low energy variables — spins represented by neutral fermions (spinons), naturally motivating a slave boson formalism. Unlike in other studies of doped Mott insulators[44, 45], here such a formalism can be a priori justified.

Our key results are as follows: (i) Doping Kitaev spin liquid leads to a spin triplet superconductor which spontaneously breaks the time reversal symmetry. (ii) A first order transition occurs within the superconducting phase on increasing doping, which separates the two regimes $\rm SC_1$ and $\rm SC_2$. In contrast, in a similar treatment of the well known square lattice t-J model, d-wave superconductivity appears across the entire doping range at low temperature, and only quantitative properties are modified with doping. (iii) In the low doping regime ($\rm SC_1$ phase), quasiparticle dispersions are controlled by the magnetic exchange, and leads to a time-reversal-broken triplet superconductor with the same properties as a spin-polarized $p_x + ip_y$ superconductor, which is fully gapped in the bulk but have chiral edge states and isolated Majorana modes in the vortex core[46]. This peculiar superconducting state arises because of the unusual spinon dispersion of the Kitaev spin liquid. (iv) At higher doping ($\rm SC_2$ phase), the superconductor obtained reflects the bare dispersion of electrons, and can be smoothly connected to the weak coupling limit, where magnetic interactions lead to pairing near the Fermi surface.

This paper is structured as follows. We begin by analyzing the quantum order underlying the Kitaev spin liquid, characterized by the symmetry transformations of fractionalized excitations, a description known as the projective symmetry group[47] (PSG). We find that the Kitaev quantum order locks the spin and gauge rotations together; the two holon species transform like a spin, and spontaneously break time reversal when condensed. Next we map out the mean field phase diagram within the SU(2) slave boson formalism as constrained by the Kitaev PSG, exact at zero doping, and demonstrate that the $\rm SC_1$ and $\rm SC_2$ phases are dominated by different physics. Controlled by the quantum order, a time-reversal-broken triplet superconductor $\rm SC_1$

emerges from the doped Kitaev spin liquid. We close with comments on related recent work[48, 49] and the relevance of our result to experimental realizations.

3.2 Kitaev Spin Liquid

To explore the physics of the t-J-J_{K} model, we start from the well-controlled undoped and $J = 0$ limit, where the model reduces to the Kitaev model. Its exact solution is given by Kitaev[30] and is already well-known. Here we would like to analyze the symmetry property of the model and its spin liquid ground state.

3.2.1 Symmetries of the Kitaev Model

First, we consider the space group symmetries of the model. The symmetries are most naturally expressed by embedding the honeycomb within a 3D cubic lattice, exactly in the same manner that the Kitaev honeycomb model arises in three-dimensional layered iridates. Then the symmetry transformations, which due to spin-orbit coupling act simultaneously on spin and space, are represented in the same manner on the spin space and the 3D real space.

Specifically, the space group is generated by two translations T_1 and T_2, an operation C_6 composed of a 6-fold c-axis rotation followed by a reflection across the lattice plane (the $c = 0$ plane), and a reflection σ across the $x = y$ plane, as illustrated in Fig. 3.1.

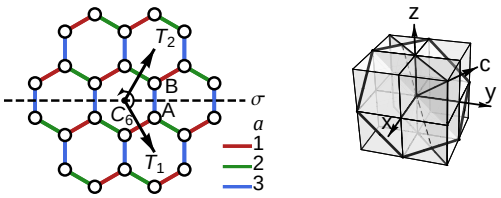

(a) (b)

Figure 3.1: (Color online.) (a) Lattice symmetries of the Kitaev model. The operations C_6 and σ act simultaneously on lattice and spin. The three bond types ($a = 1, 2, 3$) are colored red, green and blue respectively. (b) A hexagon plaquette embedded in the cubic lattice. The c-axis is the (111) axis. The 6-fold c-axis rotation is not a symmetry by itself, but becomes a symmetry when combined with the reflection across the lattice plane.

Besides the space group symmetries illustrated above, the Kitaev model is also symmetric under time reversal $\mathcal{T}$. Time reversal has no effect on the lattice but acts as $i\sigma_2$ followed by complex conjugation $\mathcal{K}$ on the spins. While $\mathcal{T}^2 = -1$ on a single spin, the global time reversal symmetry operation acting on the bipartite honeycomb

lattice squares to +1. Combining $\mathcal{T}$ with the space group yields the full symmetry group (SG), with the presentation SG $= \langle \mathcal{T}, T_1, T_2, C_6, \sigma | \mathcal{T}^2 = 1, \sigma^2 = 1, (C_6)^6 = 1 \rangle$ subject to 13 definition relations, listed in Eq. (3.39).

3.2.2 Symmetries in a Schwinger Fermion Decomposition: the Projective Symmetry Group

In order to study the Kitaev spin liquid and nearby phases, we must decompose the spin operator $S_i^\alpha = \frac{1}{2} f_i^\dagger \sigma_\alpha f_i$ into fermionic spinons $f_i^\dagger = (f_{i\uparrow}^\dagger, f_{i\downarrow}^\dagger)$, with σ_α being the Pauli matrices. Compared to the spin operators S_i^α, the spinon operators $f_{i\sigma}$ have an additional SU(2) gauge structure, best seen by arranging the operators into the following matrix[125]

$$F_i = \begin{pmatrix} f_{i\uparrow} & -f_{i\downarrow}^\dagger \\ f_{i\downarrow} & f_{i\uparrow}^\dagger \end{pmatrix}. \tag{3.3}$$

Any right SU(2) rotation $F_i \to F_i G : G \in \mathrm{SU}(2)$ leaves the physical spin S_i^α (and hence the spin Hamiltonian) unchanged, as can be seen from the following equivalent expression of S_i^α

$$S_i^\alpha = \frac{1}{4} \mathrm{Tr} F_i^\dagger \sigma_\alpha F_i. \tag{3.4}$$

Therefore the right rotation G corresponds to a gauge SU(2) rotation, whose generators (the SU(2) gauge charges of spinons) are given by

$$K_i^l = \frac{1}{4} \mathrm{Tr}\, F_i \sigma_l F_i^\dagger. \tag{3.5}$$

On the other hand, the left rotation $F_i \to U^\dagger F_i : U \in \mathrm{SU}(2)$ corresponds to the spin SU(2) rotation, whose generators are the spin operators S_i^α.

Because of the gauge SU(2) redundancy in the Schwinger fermion representation, any SU(2) gauge operation leaves the physical spin system invariant. Any operator acting on the spins, such as a symmetry transformation, may also act within this SU(2) gauge space. Thus when we fractionalize spins in a Schwinger fermion decomposition, we must also specify how the symmetry operations of the model act within the gauge freedom. This extra information, known as the projective symmetry group [47] (PSG), characterizes the fractionalized phase. Symmetry operations therefore consist of a symmetry group operation $g \in$SG with the corresponding spin operation U_g and gauge operation G_g, such that the spinons transform as

$$F_i \to U_g^\dagger(i) F_{g(i)} G_g(i). \tag{3.6}$$

The index i labels the site.

In fact, the spin operation $U_g(i) = U_g$ are always site-independent, so the site index may be omitted. U_g's are given by

$$\begin{aligned} &U_{T_1} = U_{T_2} = 1, \\ &U_{C_6}(A) = U_{C_6}(B) = \sigma_{C_6}, \\ &U_\sigma(A) = U_\sigma(B) = \sigma_\sigma, \end{aligned} \tag{3.7}$$

where $\sigma_{C_6} = (\sigma_0 + i\sigma_1 + i\sigma_2 + i\sigma_3)/2$ and $\sigma_\sigma = i(\sigma_1 - \sigma_2)/\sqrt{2}$. σ_0 is the 2×2 identity matrix. These matrix representations are literally translated from the descriptions of the symmetry operations on the cubic lattice, see Fig. 3.1b. The antiunitary time reversal operation can be represented by a unitary transformation followed by a complex conjugation $\mathcal{K}$, which transforms the spinons by

$$F_i \to \mathcal{K} U_{\mathcal{T}}^\dagger(i) F_i G_{\mathcal{T}}(i) \mathcal{K}, \tag{3.8}$$

where the unitary operation acting on the spin reads

$$U_{\mathcal{T}}(A) = U_{\mathcal{T}}(B) = i\sigma_2. \tag{3.9}$$

The complex conjugate operation $\mathcal{K}$ flips the sign of the imaginary unit, i.e. $\mathcal{K}i = -i\mathcal{K}$, while keeping everything else invariant ($\mathcal{K}^2 = 1$).

3.2.3 Projective Construction for the Kitaev Spin Liquid

The Kitaev model can be solved exactly[30] by introducing 4 Majorana fermions χ_i^α ($\alpha = 0, 1, 2, 3$) on each site, and rewriting the spin operators as $S_i^\alpha = i\chi_i^0 \chi_i^\alpha$ under the constraint $\chi_i^0 \chi_i^1 \chi_i^2 \chi_i^3 = 1/4$. The Majorana fermions are normalized as $\{\chi_i^\alpha, \chi_{i'}^{\alpha'}\} = \delta_{ii'}\delta_{\alpha\alpha'}$ in this work. It has been pointed out[51] that under certain SU(2) gauge choice, the Majorana fermions χ_i^α are related to the Schwinger fermions $f_{i\sigma}$ by the following matrix identity

$$F_i = \frac{1}{\sqrt{2}}(\chi_i^0 \sigma_0 + i\chi_i^1 \sigma_1 + i\chi_i^2 \sigma_2 + i\chi_i^3 \sigma_3), \tag{3.10}$$

or more explicitly as $f_{i\uparrow} = \frac{1}{\sqrt{2}}(\chi_i^0 + i\chi_i^3)$, $f_{i\downarrow} = \frac{1}{\sqrt{2}}(i\chi_i^1 - \chi_i^2)$. The Majorana fermions introduced by Kitaev are just another representation of the spinons. All the emergent SU(2) gauge structure for Schwinger fermions $f_{i\sigma}$ applies to the Majorana fermions χ_i^α as well.

The exact ground state can be obtained by the following projective construction[52]. First take the Majorana bilinear Hamiltonian

$$H = J_K \sum_{\langle ij \rangle} \left(i u_{ij}^a \chi_i^0 \chi_j^0 + i u_{ij}^0 \chi_i^a \chi_j^a - u_{ij}^0 u_{ij}^a \right), \tag{3.11}$$

where the bond parameters $u_{ij}^{\alpha} = \langle i\chi_i^{\alpha}\chi_j^{\alpha}\rangle$ ($\alpha = 0, 1, 2, 3$) can be regarded as the mean field ansatz, self-consistently given by

$$u_{ij}^{\alpha} = \begin{cases} -0.262433 & \text{if } \alpha = 0, \\ 1/2 & \text{if } \alpha = a, \\ 0 & \text{otherwise.} \end{cases} \tag{3.12}$$

Here a denotes the type of the bond $\langle ij\rangle$. We choose $i \in A$ sublattice and $j \in B$ sublattice to be the positive bond direction. Given the ansatz Eq. (3.12), the mean field Hamiltonian Eq. (3.11) produces a graphene-like band structure for χ^0 and degenerate flat bands for χ^1, χ^2 and χ^3, as shown in Fig. 3.2a. Take the Majorana Fermi liquid ground state and project to the physical Hilbert space by imposing the condition $\chi_i^0\chi_i^1\chi_i^2\chi_i^3 = 1/4$, the resulting state is the exact ground state given by Kitaev.

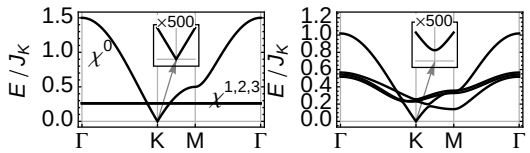

(a) (b)

Figure 3.2: Mean field band structure of Majorana spinons (a) in the undoped limit, (b) with doping $\delta t/J_{\mathrm{K}} = 0.2$. The inset shows the $\times 500$ zoom-in around the K point.

The spin correlation in this state was shown to be short-ranged[53], which identifies the ground state of the Kitaev model as a quantum spin liquid. However what really differentiates the spin liquid from a trivial spin disordered paramagnetic state is the quantum order[54] encoded in the Majorana Fermi liquid from which the spin liquid is obtained by projection. Given the particular mean-field ansatz parameterized by u_{ij}^{α}, the χ^0 fermion has a band structure different from $\chi^{1,2,3}$, so it is no longer possible to mix χ^0 with the other Majorana fermions. Thus the emergent SU(2) gauge structure of mixing spinon flavors is broken down to the $\mathbb{Z}_2$ gauge structure of changing sign of χ^{α}. The broken gauge structure can be imagined as a hidden order of spinon superconductivity[51]. Although it will not manifest as electron superconductivity in the spin liquid due to the lack of charge fluctuation, its existence as a quantum order is real, and will be revealed, once the charge fluctuation is introduced by doping.

3.2.4 Projective Symmetry Group of the Kitaev Spin Liquid

More precisely, the quantum order[54] of the $\mathbb{Z}_2$ spin liquid is characterized by the PSG of the mean field ansatz. The PSG of Kitaev spin liquid can be determined

starting from the fact that χ^0 is a special flavor which should not be mixed with other flavors, any PSG operation must at least preserve the flavor of χ^0. χ^0 appears in the F matrix as $F \sim \chi^0\sigma_0$, while F transforms under PSG operations as $F \to U_g^\dagger F G_g$, so apart from some sign factor, $\chi^0\sigma_0 \to \pm\chi^0 U_g^\dagger G_g$. Therefore, to preserve the flavor of χ^0, $G_g = \pm U_g$ is simply required to hold for all $g \in$ SG: the gauge operation G_g must always follow the spin operation U_g up to a sign factor. From the spin operations U_g given in Eq. (3.7) and Eq. (3.9) it is not difficult to figure out the gauge operations G_g, which read

$$\begin{aligned} &G_{T_1} = G_{T_2} = 1, \\ &G_{C_6}(A) = -G_{C_6}(B) = \sigma_{C_6}, \\ &G_\sigma(A) = -G_\sigma(B) = \sigma_\sigma, \\ &G_{\mathcal{T}}(A) = -G_{\mathcal{T}}(B) = i\sigma_2. \end{aligned} \tag{3.13}$$

The matrices σ_{C_6} and σ_σ were defined right below Eq. (3.7). The sublattice-dependent sign factors are determined as follows. Both C_6 and σ switch the sublattice A and B, carrying u^α_{AB} to u^α_{BA} under the lattice transformation. However, $u^\alpha_{ij} = -u^\alpha_{ji}$ is odd under the reversal of bond direction, so in order to keep it unchanged, the sign must be rectified by the gauge operation that follows, therefore both G_{C_6} and G_σ have a sign difference between the sublattices. However for the time reversal operation, under complex conjugate $i \to -i$, so $u^\alpha_{AB} = \langle i\chi^\alpha_A \chi^\alpha_B\rangle \to \langle -i\chi^\alpha_A\chi^\alpha_B\rangle = -u^\alpha_{ij}$, thus the gauge transform $G_{\mathcal{T}}$ must also carry the sublattice-dependent sign to compensate the sign generated by the complex conjugate.

A prominent property of the PSG of the Kitaev spin liquid is that U_g and G_g are always the same (up to a sign), which implies that the spin and gauge degrees of freedom are locked together by the underlying quantum order in the spin liquid state. As a result, the PSG operation $U_g^\dagger F G_g$ literally carries out the rotations and reflections by treating χ^0 as a scalar and $\boldsymbol{\chi} \equiv (\chi^1, \chi^2, \chi^3)$ as a pseudo vector. Therefore C_6 actually permutes $\chi^3 \to \chi^2 \to \chi^1 \to \chi^3$, and σ exchanges $\chi^1 \leftrightarrow \chi^2$, with some additional sign factors (see Tab. 3.1), thus giving exactly the right transforms to preserve all the mean field ansatz, which can be checked straightforwardly.

In conclusion, the PSG of the Kitaev spin liquid is defined by Eq. (3.6) in general (and by Eq. (3.8) for the time reversal operation), with the spin and gauge transforms specified by Eq. (3.7), Eq. (3.9) and Eq. (3.13). Its effect on the Majorana spinons are concluded in Tab. 3.1. This PSG belongs to the class (I)(B) according to the PSG classification of $\mathbb{Z}_2$ spin liquid on the honeycomb lattice (see Appedix 3.5 for details of the classification).

All the PSG's in this class have the common property that the gauge charge is reversed under time reversal just the same as the spin. To see this, substitute Eq. (3.10) into Eq. (3.4) and Eq. (3.5), and write the spin and gauge charge operators

Table 3.1: The PSG transforms of Majorana fermions.

$g:$	$T_{1,2}$	C_6	σ	$\mathcal{T}$
$\chi_A^0 \to$	χ_A^0	χ_B^0	χ_B^0	χ_A^0
$\chi_A^1 \to$	χ_A^1	χ_B^3	$-\chi_B^2$	χ_A^1
$\chi_A^2 \to$	χ_A^2	χ_B^1	$-\chi_B^1$	χ_A^2
$\chi_A^3 \to$	χ_A^3	χ_B^2	$-\chi_B^3$	χ_A^3
$\chi_B^0 \to$	χ_B^0	$-\chi_A^0$	$-\chi_A^0$	$-\chi_B^0$
$\chi_B^1 \to$	χ_B^1	$-\chi_A^3$	χ_A^2	$-\chi_B^1$
$\chi_B^2 \to$	χ_B^2	$-\chi_A^1$	χ_A^1	$-\chi_B^2$
$\chi_B^3 \to$	χ_B^3	$-\chi_A^2$	χ_A^3	$-\chi_B^3$

in terms of Majorana fermions as

$$\begin{aligned} \boldsymbol{S}_i &= \frac{i}{2}\big(\chi_i^0 \boldsymbol{\chi}_i - \frac{1}{2}\boldsymbol{\chi}_i \times \boldsymbol{\chi}_i\big), \\ \boldsymbol{K}_i &= \frac{i}{2}\big(\chi_i^0 \boldsymbol{\chi}_i + \frac{1}{2}\boldsymbol{\chi}_i \times \boldsymbol{\chi}_i\big), \end{aligned} \tag{3.14}$$

Applying the PSG transformation rules of the time reversal: $\chi_A^\alpha \to \chi_A^\alpha$, $\chi_B^\alpha \to -\chi_B^\alpha$ (see Tab. 3.1) and $i \to -i$, it is easy to show that both the spin and gauge charge operators are odd under time reversal

$$\boldsymbol{S}_i \xrightarrow{\mathcal{T}} -\boldsymbol{S}_i, \boldsymbol{K}_i \xrightarrow{\mathcal{T}} -\boldsymbol{K}_i. \tag{3.15}$$

Therefore, there are in principle two ways to to break the time reversal symmetry in the Kitaev spin liquid: one is to polarize the spin and the other is to condense the gauge charge. The spin polarization can be achieved by applying an external magnetic field in the (111) direction (perpendicular to the lattice plane), which drives the gapless Kitaev spin liquid into the gapped non-Abelian phase[30, 36]. In the following, we will explore the second possibility, namely the gauge charge condensation. This can be achieved by introducing the gauge charge through doping the spin liquid. According to the SU(2) slave boson theory, the condensed holon will pick out an SU(2) gauge direction and break the time reversal symmetry spontaneously.

3.3 Doping the Kitaev model within SU(2) Slave Boson Theory

3.3.1 SU(2) Slave Boson / Schwinger Fermion Representation

We now consider doping (say) holes into the insulating magnet, while preserving the strong onsite correlations that penalize double occupancy. As discussed above,

the exact solution of the Kitaev spin liquid is naturally expressed within a particular kind of Schwinger fermion / slave boson representation. The most naive way is to directly assign the spinons to the electrons $c_{i\sigma} = b_i f_{i\sigma}$ with additional U(1) slave boson b_i to carry the electric charge. However this approach completely neglects the SU(2) gauge redundancy in the spin liquid: annihilation of a spin up electron by $c_\uparrow$ can be accomplished (in the spin sector) either by the annihilation of up spinon $f_\uparrow$ or by the creation of down spinon $f_\downarrow^\dagger$ (to neutralize the up spin into spin singlet), so the electron operator must be a linear combination of both[45, 57], formulated as $c_{i\uparrow} = \frac{1}{\sqrt{2}}(b_{i1}^\dagger f_{i\uparrow} - b_{i2}^\dagger f_{i\downarrow}^\dagger)$, $c_{i\downarrow} = \frac{1}{\sqrt{2}}(b_{i1}^\dagger f_{i\downarrow} + b_{i2}^\dagger f_{i\uparrow}^\dagger)$, or equivalently as[125]

$$C_i = \frac{1}{\sqrt{2}} F_i B_i, \tag{3.16}$$

where C_i, F_i and B_i are 2×2 matrices of operators

$$C_i = \begin{pmatrix} c_{i\uparrow} & -c_{i\downarrow}^\dagger \\ c_{i\downarrow} & c_{i\uparrow}^\dagger \end{pmatrix}, B_i = \begin{pmatrix} b_{i1}^\dagger & -b_{i2} \\ b_{i2}^\dagger & b_{i1} \end{pmatrix}, \tag{3.17}$$

and F_i is given by Eq. (3.3) in terms of Schwinger fermions or equivalently by Eq. (3.10) in terms of Majorana fermions. The holon creation operators $b_{i1}^\dagger$ and $b_{i2}^\dagger$ carry different SU(2) gauge charges, but the same electric charge as a hole c_i.

Let $|0\rangle_{\text{slave}}$ be the vacuum state of both spinons and holons, s.t. $f_{i\sigma}|0\rangle_{\text{slave}} = b_{i\nu}|0\rangle_{\text{slave}} = 0$. Then on each site, there are only three physical states in the Hilbert space:

$$\begin{aligned} |0\rangle &= \frac{1}{\sqrt{2}} \left(b_{i1}^\dagger + b_{i2}^\dagger f_{i\uparrow}^\dagger f_{i\downarrow}^\dagger \right) |0\rangle_{\text{slave}}, \\ c_{i\uparrow}^\dagger |0\rangle &= f_{i\uparrow}^\dagger |0\rangle_{\text{slave}}, \\ c_{i\downarrow}^\dagger |0\rangle &= f_{i\downarrow}^\dagger |0\rangle_{\text{slave}}. \end{aligned} \tag{3.18}$$

Here $|0\rangle$ denotes the electron empty state. The double occupied state is automatically ruled out from the physical Hilbert space in the SU(2) slave boson formalism.

Each empty site has one holon, therefore the doping δ is: $\delta = \frac{1}{N}\sum_i (b_{i1}^\dagger b_{i1} + b_{i2}^\dagger b_{i2})$, where N denotes the total number of sites. Adopting Gutzwiller approximation, the spin operator will be written as $S_i^a = i\chi_i^0 \chi_i^a (1-\delta)$.

3.3.2 SU(2) Gauge Charge

As both spinons and holons carry the SU(2) gauge charges, the gauge SU(2) generators K_i^l $(l = 1, 2, 3)$ are generalized from Eq. (3.5) to

$$K_i^l = \frac{1}{4} \text{Tr}\, F_i \sigma_l F_i^\dagger - \frac{1}{4} \text{Tr}\, \sigma_3 B_i^\dagger \sigma_l B_i, \tag{3.19}$$

or explicitly written as (with implicit sum over dummy indices)

$$K_i^l = -\frac{1}{2}(i\chi_i^0\chi_i^l + \frac{i}{2}\epsilon_{lmn}\chi_i^m\chi_i^n + b_{i\nu}\sigma_{\nu\nu'}^l b_{i\nu'}^\dagger), \tag{3.20}$$

where ϵ_{lmn} is the Levi-Civita symbol. It can be verified that $[K_i^l, F_i] = \frac{1}{2}F_i\sigma_l$, $[K_i^l, B_i] = -\frac{1}{2}\sigma_l B_i$, therefore $[K_i^l, C_i] = 0$, showing that K_i^l are indeed the generators of gauge SU(2) transforms that leave the electron operators unchanged.

The physical state, as enumerated in Eq. (3.18), are SU(2) gauge invariant. Therefore the SU(2) singlet condition $K_i^l = 0$ should be imposed. This condition is equivalent to the single occupancy condition for both spinons and holons, as is evidenced from $K_i^3 = (1 - f_{i\uparrow}^\dagger f_{i\uparrow} - f_{i\downarrow}^\dagger f_{i\downarrow} - b_{i1}^\dagger b_{i1} + b_{i2}^\dagger b_{i2})/2 = 0$.

The PSG operations are naturally extended to the holons, such that they transform as

$$\begin{aligned} &B_i \to G_g^\dagger(i) B_{g(i)}, \quad (\text{for } g \neq \mathcal{T}) \\ &B_i \to \mathcal{K} G_{\mathcal{T}}^\dagger B_i \mathcal{K}. \end{aligned} \tag{3.21}$$

In particular, under the time reversal operation,

$$\begin{pmatrix} b_{A1} \\ b_{A2} \end{pmatrix} \xrightarrow{\mathcal{T}} \begin{pmatrix} -b_{A2} \\ b_{A1} \end{pmatrix}. \tag{3.22}$$

One can see the holon SU(2) gauge charges transform under time reversal in a way similar to the physical spins. Therefore one could expect that the condensation of holons will spontaneously breaks the time reversal symmetry.

3.3.3 Mean Field Phase Diagram

The exact solution of the Kitaev spin liquid at zero doping involves an enlarged hilbert space with spinons and holons which implements a particular PSG. We expect these deconfined excitations, which transform under symmetry operations as defined by the Kitaev-limit PSG, to survive into finite doping. At small finite doping the SU(2) slave boson mean field with this particular PSG becomes inexact, but should still provide the most accurate treatment possible.

Using Eq. (3.16), the t-J-J_{K} model can be written in terms of spinons and holons (for simplicity we set $J = 0$, finite J is discussed in Appendix 3.7). Then use the mean field treatment by introducing the following mean field parameters:

$$u_{ij}^\alpha = \langle i\chi_i^\alpha\chi_j^\alpha\rangle, \quad w_{ij}^\nu = \langle ib_{i\nu}^\dagger b_{j\nu}\rangle, \tag{3.23}$$

we arrive at the mean field Hamiltonian (see Appendix 3.6 for detailed deductions)

$$\begin{aligned} H_{\mathrm{MF}} = &\sum_{\langle ij\rangle} U_{ij}^\alpha i\chi_i^\alpha\chi_j^\alpha + W_{ij}^\nu(ib_{i\nu}^\dagger b_{j\nu} + h.c.) \\ &+ \sum_i a_i^l K_i^l - \mu b_{i\nu}^\dagger b_{i\nu}, \end{aligned} \tag{3.24}$$

where summation is implied over repeated indices $\alpha = 0 \ldots 3$, $\nu = 1, 2$ and $l = 1 \ldots 3$. The hopping amplitudes for fermions U_{ij}^{α} and for bosons W_{ij}^{ν} should be determined self-consistently from

$$\begin{aligned} U_{ij}^{\alpha} = & -\frac{t}{4}\sum_{\nu=1}^{2}(w_{ij}^{\nu} + c.c.) \\ & + J_K(1-\delta)^2(u_{ij}^{a}\delta_{0\alpha} + u_{ij}^{0}\delta_{a\alpha}), \\ W_{ij}^{\mu} = & -\frac{t}{4}\sum_{\alpha=0}^{3}u_{ij}^{\alpha}. \end{aligned} \tag{3.25}$$

The index a denotes the direction of $\langle ij \rangle$. The boson chemical potential μ is chosen such that $\sum_{i,\nu}\langle b_{i\nu}^{\dagger} b_{i\nu}\rangle = \delta N$. The SU(2) gauge charge operators are given in Eq. (3.20). The gauge potentials a_i^l are chosen to enforce the SU(2) gauge singlet constraint on average $\langle K_i^l \rangle = 0$. In the undoped limit, Eq. (3.24) reduces to the mean field description of the spin liquid exact solution. With finite doping, the hidden superconductivity of spinons will be rendered into the true superconductivity of electrons once the holons condense.

We would like to stress that the quantum order of the Kitaev spin liquid puts a strong constraint on the possible form of the mean field ansatz. This quantum order is described by the Kitaev spin liquid PSG as discussed previously. We assume that this PSG is respected by the mean field solution throughout, and that symmetry breaking occurs only through holon condensation. At small dopings this is required by continuity to the Kitaev solution. The most general parameterization of the mean field ansatz under the PSG restriction is as follows. First assign on the type-3 bond

$$\begin{aligned} & u_{ij}^{0} = u_0, u_{ij}^{1} = u_{ij}^{2} = u_b, u_{ij}^{3} = u_a, \\ & w_{ij}^{1} = w_{ij}^{2} = w. \end{aligned} \tag{3.26}$$

Then the mean field parameters on the other bonds are obtained by using the PSG operation to carry the above assignment throughout the lattice. u_0, u_a, u_b and w are real numbers that parameterize the mean field ansatz.

Based on the parameterization, a self-consistent mean field solution of Eq. (3.24) gives the phase diagram shown in Fig. 3.3. We show results for $J = 0$. Introducing $J < J_{\mathrm{K}}/8$, to remain within the boundary of the spin liquid phase[35, 36], has little effect on the phase diagram (discussed in Appendix 3.7).

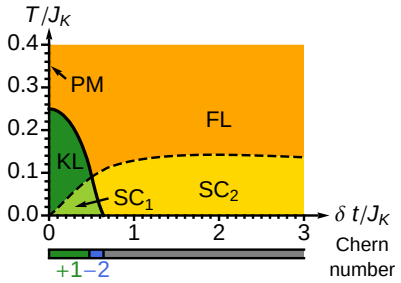

Figure 3.3: (Color online) Mean field phase diagram for $t = 10J_{\rm K}$ and $J = 0$. The low doping Kitaev spin liquid (KL) phase and the high doping Fermi liquid (FL) phase are separated by first order transition. Once holons condense, two classes of superconducting (SC_1 and SC_2) phases appear. The bar below shows the Chern number of the superconducting state.

3.3.4 Spin Liquid and Adjacent Phases

In the undoped limit, one recovers the Kitaev spin liquid mean field parameters: $u_b = w = 0$, and u_0 and u_a are determined by the following self-consistent equations

$$\begin{aligned} u_a &= -\frac{1}{2}\tanh\frac{\beta J_K u_0}{2}, \\ u_0 &= -\frac{1}{3N}\sum_{\boldsymbol{k}\in \mathrm{BZ}} |\Gamma(\boldsymbol{k})| \tanh\frac{\beta J_K u_a |\Gamma(\boldsymbol{k})|}{2}, \end{aligned} \tag{3.27}$$

where $\Gamma(\boldsymbol{k}) = e^{ik_y} + 2e^{-ik_y/2}\cos(\sqrt{3}k_x/2)$, and N is the number of sites. At zero temperature, the solution is $u_0 = -0.262433$ and $u_a = 1/2$, corresponding to the exact ground state of the Kitaev model. So the SU(2) slave boson mean field theory is asymptotically exact in the small doping limit. At the mean field level, a finite temperature transition is found at $T_c = J_K/4$, above which ($T > T_c$) all the mean field parameters vanish, $u_0 = u_a = u_b = w = 0$. The confining gauge fluctuation will recombine spinons and holons into electrons, resulting in a paramagnetic (PM) phase.

With increasing doping, mean field parameters u_b and w grow in proportional to δ, and eventually trigger a first order phase transition at $\delta_c \simeq 2u_a J_{\rm K}/t$, see Fig. 3.4. The transition is driven by the competition between the kinetic energy of holes (t term) and the magnetic energy of spins ($J_{\rm K}$ term). The magnetic energy favors the Kitaev spin liquid state, in which the mobility of $\chi^{1,2,3}$ fermions is sacrificed (as they form degenerate flat bands). For larger doping, more kinetic energy can be gained by allowing $\chi^{1,2,3}$ fermions to move in the same way as χ^0, as $u_0 \simeq u_a \simeq u_b$, so that the flat band gets dispersed as shown in Fig. 3.2b. In the large doping limit, all flavors of Majorana fermions move with the same amplitude, providing identical

graphene-like band structures, which can be recombined into band electrons, labeled by Fermi liquid (FL) in Fig. 3.3. As discussed below, the nature of superconductivity is very different depending on the normal state, Kitaev spin liquid or FL, from which it emerges.

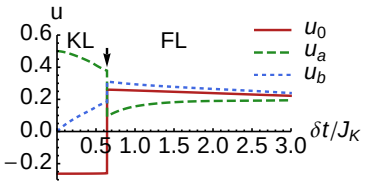

Figure 3.4: (Color online.) Mean field parameters u_0, u_a, u_b v.s. doping δ at zero temperature. The arrow indicates the 1st order transition between KL/SC_1 phase and FL/SC_2 phase. The calculation is done at $t = 10J_K$ and $J = 0$.

3.3.5 Holon Condensation and Superconductivity

At low temperature, the holons condense to their band minimum at zero-momentum, leading to the following condensate amplitude ($\nu = 1, 2$)

$$\langle b_{A\nu} \rangle = z_\nu, \langle b_{B\nu} \rangle = iz_\nu, \tag{3.28}$$

with the density $|z_1|^2 + |z_2|^2 = \delta$ following the doping level. The electron pairing is found between opposite sublattices (because the intra-sublattice coupling of χ^α is forbidden by PSG): $\Delta_{AB,b}(\boldsymbol{k}) = c^\intercal_{\boldsymbol{k}A} \epsilon \sigma_b c_{-\boldsymbol{k}B}$, ($b = 0, 1, 2, 3$) where $c_{\boldsymbol{k}A(B)} = (c_{\boldsymbol{k}A(B)\uparrow}, c_{\boldsymbol{k}A(B)\downarrow})^\intercal$ denote the electron operators in the momentum space and $\epsilon = i\sigma_2$ is the anti-symmetric matrix[58]. Using Eq. (3.16), the pairing is expressed in terms of the mean field parameters:

$$\Delta_{AB,b}(\boldsymbol{k}) = \frac{\alpha_b}{2} \sum_{a=1}^{3} d_{ab} e^{i\boldsymbol{k}\cdot\boldsymbol{r}_a}, \tag{3.29}$$

where $\boldsymbol{r}_1 = (-\sqrt{3}/2, -1/2)$, $\boldsymbol{r}_2 = (\sqrt{3}/2, -1/2)$, $\boldsymbol{r}_3 = (0, -1)$ denote the three displacement vectors from site A to site B, and b labels the singlet ($b = 0$) or triplet ($b = 1, 2, 3$) channels. $\alpha_b = z^\intercal \epsilon \sigma_b z$ with $z = (z_1, z_2)^\intercal$ refer to the holon condensate amplitude, and $d_{ab} = u_0 - u_a + 2(u_a - u_b)\delta_{ab}$ parameterize the the spinon pairing amplitude. The electron superconductivity is a joint effect of holon condensation and spinon pairing.

Obviously $\alpha_0 = 0$ for whatever z, so $\Delta_{AB,0} = 0$, thus the electron paring is purely triplet. This demonstrates the spin-gauge locking effect of the Kitaev spin liquid, that a singlet in the spin space will be rendered by the PSG to a singlet in the SU(2) gauge

space (seen from the expression of α_b). However gauge charges can not condensed to a singlet state due to their bosonic nature, thus the single pairing is ruled out, as long as the quantum order persists.

The superconductivity transition temperature in the phase diagram shown with the dashed line is estimated as follows. At small doping, the phase stiffness $\rho_b = t_b\delta$ is proportional to doping, where $t_b = 3t(u_0 + u_a + 2u_b)/8$, and T_c is estimated from the Kosterlitz-Thouless transition[59] temperature $T_c = \pi\rho_b/2$. At large doping, the mean field gap is small which controls $T_c \sim \Delta_f$, where $\Delta_f \simeq J_{\rm K}(u_0^2+u_a^2)^{1/2}(1-\delta^2)/4$. In between, we interpolate via the formula[60] $T_c^{-1} = (\pi\rho_b/2)^{-1} + \Delta_f^{-1}$. Note, due to the absence of a finite temperature transition of the two dimensional free bosons, a naive mean field transition temperature is not specified.

3.3.6 Symmetry and Topological Properties

The mean field Hamiltonian of the Kitaev spin liquid appears surprising at first, since the only Majorana fermion with extended hopping is χ^0, the real part of $f_\uparrow$, which seems to single out one spin species and break the time reversal symmetry. Actually, this is a gauge artifact. The SU(2) rotations between $f_{i\sigma}$ and $c_{i\sigma}$ will restore the time reversal symmetry on the electron level for the spin liquid. However, the SU(2) gauge redundancy is parameterized by holon fields $b_{i\nu}$ and must be resolved as the holon condenses. So, as has been discussed from the PSG prospective, the holon condensation must break the time reversal symmetry spontaneously, leading to a class D superconductor[46], denoted as SC_1, with uniform magnetization $\langle \boldsymbol{S}\rangle \sim z^\dagger \boldsymbol{\sigma} z$.

Let us elaborate on the microscopic mechanism which gaps the χ^0 Majoranas in SC_1. If we view the charge and spin as separate excitations, one may expect the same spectrum as the Kitaev spin liquid, i.e. gapless χ^0 Majorana modes, to persist into the superconductor. However, the time reversal symmetry, which protects this gaplessness in the spin liquid, is lost in the superconductor. This can lead to an energy gap for χ^0 (as shown in Fig. 3.2b), tied to the strength of the condensate. Because the uniform SU(2) gauge charge provided by the holon condensate offsets the SU(2) gauge potential a^l $(l = 1, 2, 3)$ from zero, in order to preserve the overall gauge singlet condition. It is found that $a^l \simeq \delta J_{\rm K}$ increases with doping. For small doping δ, we treat $a^l/J_{\rm K}$ as a perturbation. Integrating out the gapped Majorana modes $\chi^{1,2,3}$ generates next nearest neighboring (nnn) (Fig. 3.5b) hopping of χ^0 fermions through a 3rd order perturbation correction, as illustrated in Fig. 3.5a. The effective Hamiltonian for χ^0 reads

$$H_{\rm eff} = J_K\eta \sum_{\langle ij\rangle} i\chi_i^0\chi_j^0 + v\sum_{\langle\langle ij\rangle\rangle} i\chi_i^0\chi_j^0, \tag{3.30}$$

where $v = a^1a^2a^3/(8J_{\rm K}^2u_0^2)$ and $\langle\langle ij\rangle\rangle$ denotes the oriented nnn bond, with the bond direction specified in Fig. 3.5b. According to the Kitaev spin liquid PSG (see Tab. 3.1),

the nnn coupling term is time reversal odd (since $i \to -i$), and is allowed only because time reversal symmetry is broken by the gauge charge condensation here.

The resulting χ^0 Hamiltonian Eq. (3.30) is a Majorana version of the Haldane model[61]. It is known that the nnn coupling gaps the Dirac cones and leaves one unit of Chern number in the ground state. This requires all a^l to be nonvanishing. It is actually energetically favorable for the holon condensate (i.e. magnetization) to be in the (111) (or equivalent $(\pm 1 \pm 1 \pm 1)$) direction, corresponding to $a^1 = a^2 = a^3$ which maximizes the spinon gap $m = 3\sqrt{3}|v| \sim |a^1 a^2 a^3|$. Therefore in the small doping limit, the ground state is a fully-gapped topological superconductor with $+1$ Chern number, which implies a gapless chiral Majorana edge mode and a Majorana zero mode in the vortex core. This is the same topology as a $p_x + ip_y$ superconductor of spin polarized fermions[46]; here the "spin-polarization" arises from the peculiar dispersion of fermions in the Kitaev spin liquid. At larger doping the Chern number changes, as shown in Fig. 3.3. The transition $+1 \to -2$ in the SC_1 phase corresponds to a band gap closing at M point due to the softening of $\chi^{1,2,3}$ modes.

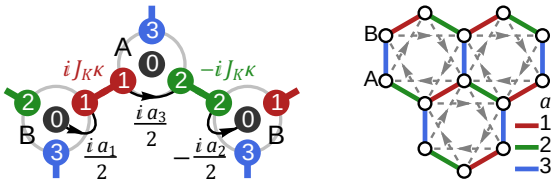

(a) (b)

Figure 3.5: (Color online.) (a) The path of 3rd order perturbation. The 4 Majorana fermions on each site are denoted by their flavor indices. The effective second nearest neighbor hopping of χ^0 fermion is bridged by two nearest-bond hopping of $\chi^{1,2,3}$. The on-site flavor changing process is assisted by the time-reversal-broken gauge potential. (b) Gray dashed arrows indicate the directions of the second nearest neighboring bond.

3.4 Discussion and Conclusion

3.4.1 Overdoped Regime and Weak Coupling BCS

In the overdoped FL phase where correlations are weak, the superconductivity (SC_2) can be studied under the BCS paradigm by treating H_{HK} as an interaction and decomposing it into the Cooper channel. In the small J limit, The instability is found in the spin-triplet pairing channel, because the spin model is ferromagnetic. To first order in weak coupling both the time reversal invariant superconductor (the two dimensional analog of He_3 B phase) and the time reversal symmetry broken triplet superconductor (the analog of the He_3 A phase) are degenerate. To next order, the

calculation in Ref. [48] showed that the time-reversal-invariant p-wave superconductor is preferred. Beyond weak coupling it is hard to decide which of these two possibilities is realized, a problem that is well known from He_3 physics[67]. Here, our choice of PSG selects the time reversal (T) broken state, while a different choice would yield the T symmetric state. Therefore we mention both these possibilities as potentially relevant to the material at hand at high doping. In either case, the SC_2 phase is dominated by the Fermi liquid physics and is separated by a first order transition from the spin-liquid-controlled time-reversal-broken SC_1 phase elaborated in this work. Because of the distinct underlying mechanism, its is not surprising that SC_1 and SC_2 can be quite different in many aspects.

3.4.2 Conclusion

A time-reversal-broken spin-triplet topological superconductor was found in the doped Kitaev spin liquid within the SU(2) slave boson formalism. A first order quantum transition around $\delta_c \sim J_K/t$ separates the spin triplet superconductor into two distinct classes: SC_1 (controlled by J_K) is governed by the spin liquid physics and reflects the underlying quantum order, while SC_2 (controlled by t) is a more conventional BCS-type superconductor. Although both ultimately trace their origins to the magnetic couplings, the detailed mechanisms are rather different. This is in sharp contrast to the t-J model in the context of cuprates, where, at least qualitatively, d-wave superconductivity is realized throughout.

A promising candidate material is A_2IrO_3 (A = Na, Li) [31, 32, 37], although experiments suggest magnetic ground state, rather than spin liquid. However, it has been argued that doped charges are more mobile in spin liquids, as compared to antiferromagnetic states where they interfere with the ordered pattern[44]. Therefore one may hope that the results derived here also hold for magnetic ground states that are proximate to the Kitaev phase. Our main prediction is that doping these systems should lead to spin triplet topological superconductors with superconducting T_c a fraction of the magnetic exchange. Assuming $J_K \sim 100$ - 150K [31, 32, 39] a crude estimate of maximum superconducting transition temperature is 15 - 20K. Although we are not aware of doping studies on this class of materials, the related iridium perovskite Sr_2IrO_4, a 5d cuprate analog [34, 65] has been doped in the bulk[66], and recent years have witnessed significant progress in doping techniques. We hope our results will spur future experiments in this direction.

3.5 Appendix: $\mathbb{Z}_2$ Projective Symmetry Group on Honeycomb Lattice

Here we present the classification of $\mathbb{Z}_2$ projective symmetry group (PSG) on Honeycomb lattice without spin rotational symmetry (but preserving time several

symmetry). 144 solutions of algebraic PSG were found.

On the Honeycomb lattice, each unit cell is labeled by its integer coordinates x_1 and x_2 along the translation axes of T_1 and T_2. A spin site is further specified by its sublattice label A or B within the unit cell, see Fig. 3.1a. The symmetry group operators act on the lattice by

$$\begin{aligned} T_1(x_1, x_2) &= (x_1 + 1, x_2), \\ T_2(x_1, x_2) &= (x_1, x_2 + 1), \\ C_6(x_1, x_2, A) &= (x_1 - x_2, x_1, B), \\ C_6(x_1, x_2, B) &= (x_1 - x_2 - 1, x_1, A), \\ \sigma(x_1, x_2, A) &= (x_2, x_1, B), \\ \sigma(x_1, x_2, B) &= (x_2, x_1, A). \end{aligned} \tag{3.31}$$

The sublattice label is omitted if a formula holds in both sublattices. Later we will refer to the principal unit cell by omitting the unit cell index, i.e. $(0, 0, A) \equiv (A)$, $(0, 0, B) \equiv (B)$. The representation of symmetry operators in the spin space will be given after further discussion in Eq. (3.7).

The symmetry group of a general spin model on the Honeycomb lattice is generated by 5 generators $\mathcal{T}$, T_1, T_2, C_6 and σ with the following 13 definition relations

$$T_1 T_2 T_1^{-1} T_2^{-1} = 1, \tag{3.32}$$
$$\mathcal{T} T_1 \mathcal{T} T_1^{-1} = \mathcal{T} T_2 \mathcal{T} T_2^{-1} = 1, \tag{3.33}$$
$$C_6 T_1 C_6^{-1} T_1^{-1} T_2^{-1} = C_6 T_2 C_6^{-1} T_1 = 1, \tag{3.34}$$
$$\sigma T_1 \sigma^{-1} T_2^{-1} = \sigma T_2 \sigma^{-1} T_1^{-1} = 1, \tag{3.35}$$
$$\mathcal{T}^2 = C_6^6 = \sigma^2 = 1, \tag{3.36}$$
$$\mathcal{T} C_6 \mathcal{T} C_6^{-1} = 1, \tag{3.37}$$
$$\mathcal{T} \sigma \mathcal{T} \sigma^{-1} = 1, \tag{3.38}$$
$$C_6 \sigma C_6 \sigma = 1. \tag{3.39}$$

In general each definition relation takes the form of $\cdots g_2 g_1 = 1$, where $\cdots g_2 g_1$ denotes a sequence of symmetry group operations. Then according to Eq. (3.6), under the PSG operation, the spinon matrix F_i transforms as

$$F_i \to U_{g_1}^\dagger U_{g_2}^\dagger \cdots F_{\cdots g_2 g_1(i)} \cdots G_{g_2}\left(g_1(i)\right) G_{g_1}(i). \tag{3.40}$$

Because the bunch of operations $\cdots g_2 g_1$ actually result in the identity operation, so they must not affect the spin degree of freedom: $U_{g_1}^\dagger U_{g_2}^\dagger \cdots = \sigma_0$ and must also restore the original lattice site: $\cdots g_2 g_1(i) = i$, hence the PSG operation becomes a pure gauge operation

$$F_i \overset{\cdots g_2 g_1}{\longrightarrow} F_i \cdots G_{g_2}\left(g_1(i)\right) G_{g_1}(i). \tag{3.41}$$

All the pure gauge operations that leaves the mean field ansatz invariant constitute a subgroup of the PSG, known as the invariant gauge group (IGG). So we must have $\cdots G_{g_2}\left(g_1(i)\right) G_{g_1}(i) \in \mathrm{IGG}$. Here we are interested in the classification of $\mathbb{Z}_2$ spin liquid, so we will focus on the case that $\mathrm{IGG} = \mathbb{Z}_2$. Thus for each definition relation $\cdots g_2 g_1 = 1$, there is a corresponding PSG representation

$$\cdots G_{g_2}\left(g_1(i)\right) G_{g_1}(i) = \eta_m, \tag{3.42}$$

where $\eta_m = \pm\sigma_0$ will be used to denote the sign factors hereon. For the 13 definition relations, we introduce 13 sign factors $\eta_1, \eta_2, \cdots, \eta_{13}$ to denote the corresponding IGG elements. In the following, we may write the PSG representation Eq. (3.42) in short as $\cdots G_{g_2} G_{g_1} = \eta_m$ by omitting the site labels so as to save the space.

However special attention should be paid to the time reversal operation, because it involves the complex conjugate operator $\mathcal{K}$ which does not commute with G_g in general. As can be seen from Eq. (3.8), $\mathcal{K}$ must be placed right after each $G_{\mathcal{T}}$. For example, $\mathcal{T} C_6 \mathcal{T} C_6^{-1} = 1$ should be represented as

$$G_{\mathcal{T}}(i)\mathcal{K} G_{C_6}(i') G_{\mathcal{T}}(i')\mathcal{K} G_{C_6}^{-1}(i') = \eta_{11}, \tag{3.43}$$

where $i' = C_6^{-1}(i)$. Here we have used the rule that $G_{g^{-1}}(g(i)) = G_g^{-1}(i)$ to simplify the inverse operations.

To classify the PSG's one should take care of the gauge redundancy in the solution of G_g. Two PSG's are gauge equivalent if their solutions of G_g are related by a set of local SU(2) gauge transform $G_g(i) \to W_{g(i)}^{\dagger} G_g(i) W_i : W_i \in \mathrm{SU}(2)$. To reduce the gauge redundancy, gauge fixing will be used while solving the equations of G_g. First of all, the relative gauge between the unit cells can be fixed by setting $G_{T_2}(x_1, x_2) = \sigma_0$, and $G_{T_1}(x_1, 0) = \sigma_0$, then Eq. (3.32) can be represented as $G_{T_1}(x_1, x_2 + 1) = \eta_1 G_{T_1}(x_1, x_2)$, which gives the solution for translations

$$G_{T_1}(x_1, x_2) = \eta_1^{x_2}, G_{T_2}(x_1, x_2) = \sigma_0. \tag{3.44}$$

Substitute Eq. (3.44) into the PSG representation of Eq. (3.33): $G_{\mathcal{T}}\mathcal{K} G_{T_1}\mathcal{K} = \eta_2 G_{T_1}$ and $G_{\mathcal{T}}\mathcal{K} G_{T_2} G_{\mathcal{T}}\mathcal{K} = \eta_3 G_{T_2}$, we obtain

$$\begin{aligned} G_{\mathcal{T}}(x_1 + 1, x_2)\mathcal{K} G_{\mathcal{T}}(x_1, x_2)\mathcal{K} &= \eta_2, \\ G_{\mathcal{T}}(x_1, x_2 + 1)\mathcal{K} G_{\mathcal{T}}(x_1, x_2)\mathcal{K} &= \eta_3, \end{aligned} \tag{3.45}$$

while on the other hand, from $G_{\mathcal{T}}\mathcal{K} G_{\mathcal{T}}\mathcal{K} = \eta_8$, we know $\mathcal{K} G_{\mathcal{T}}(x_1, x_2)\mathcal{K} = \eta_8 G_{\mathcal{T}}^{-1}(x_1, x_2)$, so Eq. (3.45) becomes

$$\begin{aligned} G_{\mathcal{T}}(x_1 + 1, x_2) &= \eta_2 \eta_8 G_{\mathcal{T}}(x_1, x_2), \\ G_{\mathcal{T}}(x_1, x_2 + 1) &= \eta_3 \eta_8 G_{\mathcal{T}}(x_1, x_2). \end{aligned} \tag{3.46}$$

The solution is

$$G_{\mathcal{T}}(x_1, x_2) = \eta_2^{x_1} \eta_3^{x_2} \eta_8^{x_1 + x_2} G_{\mathcal{T}}(0, 0). \tag{3.47}$$

Similarly by inserting Eq. (3.44) into the PSG representation of Eq. (3.34): $G_{C_6}G_{T_1} = \eta_4 G_{T_2}G_{T_1}G_{C_6}$, $G_{C_6}G_{T_2} = \eta_5 G_{T_1}^{-1}G_{C_6}$, and Eq. (3.35): $G_\sigma G_{T_1} = \eta_6 G_{T_2}G_\sigma$, $G_\sigma G_{T_2} = \eta_7 G_{T_1}G_\sigma$, we find

$$\begin{aligned} G_{C_6}(x_1+1,x_2) &= \eta_1^{x_1-x_2}\eta_4 G_{C_6}(x_1,x_2), \\ G_{C_6}(x_1,x_2+1) &= \eta_1^{-x_1}\eta_5 G_{C_6}(x_1,x_2), \\ G_\sigma(x_1+1,x_2) &= \eta_1^{x_2}\eta_6 G_\sigma(x_1,x_2), \\ G_\sigma(x_1,x_2+1) &= \eta_1^{x_1}\eta_7 G_\sigma(x_1,x_2), \end{aligned} \tag{3.48}$$

whose solutions are

$$\begin{aligned} G_{C_6}(x_1,x_2) &= \eta_1^{x_1(x_1-1)/2-x_1x_2}\eta_4^{x_1}\eta_5^{x_2}G_{C_6}(0,0), \\ G_\sigma(x_1,x_2) &= \eta_1^{x_1x_2}\eta_6^{x_1}\eta_7^{x_2}G_\sigma(0,0). \end{aligned} \tag{3.49}$$

However, it worth mention that η_4, η_5, η_6 and η_7 are not independent[55]. Because in their equations, either G_{T_1} or G_{T_2} only appears once, which means if we fix the inter-unit-cell gauge in a different way such that $G_{T_1} \to -G_{T_1}$ or $G_{T_2} \to -G_{T_2}$, the above four η's will be affected. But this does not affect the mean field ansatz, as all the ansatz are given in the bilinear form which are invariant under this $\mathbb{Z}_2$ gauge transform. Therefore, make use of this $\mathbb{Z}_2$ gauge freedom, one can set two out of the four η's to identity, say $\eta_4 = \eta_5 = \sigma_0$.

Substitute Eq. (3.44), Eq. (3.47), and Eq. (3.49) into the PSG representation of the rest of the definition relations, we find some constrains between the η's. For example, from Eq. (3.36) one can obtain

$$G_\sigma(A)G_\sigma(B) = G_\sigma(B)G_\sigma(A) = (\eta_6\eta_7)^{x_1+x_2}\,\eta_{10}. \tag{3.50}$$

The left-hand-side is independent of (x, y), so must the right-hand-side be, therefore we must have $\eta_6\eta_7 = \sigma_0$, which means $\eta_6 = \eta_7$. Similarly from Eq. (3.37) and Eq. (3.38) we find $\eta_2 = \eta_3 = \eta_8$ and from Eq. (3.39) we find $\eta_5 = \eta_6$, so eventually $\eta_4 = \eta_5 = \eta_6 = \eta_7 = \sigma_0$.

Now all the $G_g(x_1, x_2)$ has been reduced to $G_g(0, 0)$ with in a single unit cell, concluded as follows

$$\begin{aligned} G_{T_1}(x_1,x_2) &= \eta_1^{x_2}, \\ G_{T_2}(x_1,x_2) &= \sigma_0, \\ G_{\mathcal{T}}(x_1,x_2) &= G_{\mathcal{T}}(0,0), \\ G_{C_6}(x_1,x_2) &= \eta_1^{x_1(x_1-1)/2-x_1x_2}G_{C_6}(0,0), \\ G_\sigma(x_1,x_2) &= \eta_1^{x_1x_2}G_\sigma(0,0). \end{aligned} \tag{3.51}$$

The remaining task is to determine $G_{\mathcal{T}}(0, 0)$, $G_{C_6}(0, 0)$ and $G_\sigma(0, 0)$ from the following

equations

$$G_{\mathcal{T}}(A)\mathcal{K}G_{\mathcal{T}}(A)\mathcal{K} = G_{\mathcal{T}}(B)\mathcal{K}G_{\mathcal{T}}(B)\mathcal{K} = \eta_8, \tag{3.52}$$
$$G_{\mathcal{T}}(B)\mathcal{K}G_{C_6}(A)G_{\mathcal{T}}(A)\mathcal{K} = \eta_{11}G_{C_6}(A), \tag{3.53}$$
$$G_{\mathcal{T}}(A)\mathcal{K}G_{C_6}(B)G_{\mathcal{T}}(B)\mathcal{K} = \eta_{11}G_{C_6}(B), \tag{3.54}$$
$$G_{\mathcal{T}}(B)\mathcal{K}G_{\sigma}(A)G_{\mathcal{T}}(A)\mathcal{K} = \eta_{12}G_{\sigma}(A), \tag{3.55}$$
$$G_{\mathcal{T}}(A)\mathcal{K}G_{\sigma}(B)G_{\mathcal{T}}(B)\mathcal{K} = \eta_{12}G_{\sigma}(B), \tag{3.56}$$
$$G_{\sigma}(A)G_{\sigma}(B) = G_{\sigma}(B)G_{\sigma}(A) = \eta_{10}, \tag{3.57}$$
$$\left(G_{C_6}(B)G_{\sigma}(A)\right)^2 = \left(G_{C_6}(A)G_{\sigma}(B)\right)^2 = \eta_1\eta_{13}, \tag{3.58}$$
$$\left(G_{C_6}(B)G_{C_6}(A)\right)^3 = \left(G_{C_6}(A)G_{C_6}(B)\right)^3 = \eta_1\eta_9. \tag{3.59}$$

The solution of the above equations leads to 144 algebraic PSG's which will be classified below. There are only two remaining SU(2) gauge freedom: the local gauge transform on site A or site B in the unit cell.

We start from the solution of $G_{\mathcal{T}}$. Let $G_{\mathcal{T}} = a_0\sigma_0 + ia_1\sigma_1 + ia_2\sigma_2 + ia_3\sigma_3$ be the most general form of a SU(2) matrix (with $a_\mu \in \mathbb{R}$). Plug into the left-hand-side of Eq. (3.52), one finds

$$\begin{aligned} G_{\mathcal{T}}\mathcal{K}G_{\mathcal{T}}\mathcal{K} =& (a_0^2 + a_1^2 - a_2^2 + a_3^2)\sigma_0 \\ &+ 2ia_2(a_3\sigma_1 + a_0\sigma_2 - a_1\sigma_3). \end{aligned} \tag{3.60}$$

So if $\eta_8 = -\sigma_0$, the solution is $a_2 = \pm 1$, $a_0 = a_1 = a_3 = 0$, i.e. $G_{\mathcal{T}} = \pm i\sigma_2$. Note that $i\sigma_2\mathcal{K}$ as a whole is SU(2) gauge invariant, thus the remaining gauge freedoms are preserved (even though σ_2 seems to be a special direction). While if $\eta_8 = \sigma_0$, the solution is $a_2 = 0$, $a_0^2 + a_1^2 + a_3^2 = 1$. One can choose $G_{\mathcal{T}}(A) = G_{\mathcal{T}}(B) = \sigma_0$. In this case, the SU(2) gauge freedoms on both sites are fixed.

Class (I): $\eta_8 = -\sigma_0$. Then $G_{\mathcal{T}}(A) = i\sigma_2$, $G_{\mathcal{T}}(B) = i\eta_{14}\sigma_2$, where $\eta_{14} = \pm\sigma_0$ is a new sign factor. Substitute into Eq. (3.53,3.54,3.55,3.56), one finds $\eta_{11} = \eta_{12} = -\eta_{14}$, with no restriction on G_{C_6} and G_σ. Fix the relative gauge between sites A and B by $G_\sigma(A) = \sigma_0$, then from Eq. (3.57), $G_\sigma(B) = \eta_{10}$. Plug into Eq. (3.58),

$$G_{C_6}(B)^2 = G_{C_6}(A)^2 = \eta_1\eta_{13}. \tag{3.61}$$

According to the sign of $\eta_1\eta_{13}$, the class (I) is further divided into two subclasses.

Class (I)(A): $\eta_1\eta_{13} = \sigma_0$. Then the solution of Eq. (3.61) reads $G_{C_6}(A) = \sigma_0$, $G_{C_6}(B) = \eta_{15}$. Substitute into Eq. (3.59), one finds $\eta_{15} = \eta_1\eta_9$.

The solutions in the class (I)(A) are summarized as

$$\begin{aligned} G_{\mathcal{T}}(A) &= i\sigma_2, \\ G_{\mathcal{T}}(B) &= i\eta_{14}\sigma_2, \\ G_{C_6}(A) &= \sigma_0, \\ G_{C_6}(B) &= \eta_1\eta_9, \\ G_\sigma(A) &= \sigma_0, \\ G_\sigma(B) &= \eta_{10}, \end{aligned} \tag{3.62}$$

which are controlled by $\eta_1, \eta_9, \eta_{10}, \eta_{14}$, providing $2^4 = 16$ PSG's.

Class (I)(B): $\eta_1\eta_{13} = -\sigma_0$. Then from Eq. (3.61), the general solution of G_{C_6} is a linear combination of $i\sigma_1, i\sigma_2, i\sigma_3$. Because the global gauge freedom has not been fixed, so using this freedom, one can set $G_{C_6}(A) = i\sigma_1$. Further assume $G_{C_6}(B) = \eta_1\eta_9(i\sigma_1\cos\theta_1 + (i\sigma_2\cos\theta_2 + i\sigma_3\sin\theta_2)\sin\theta_1)$, and plug into Eq. (3.59), one finds $\cos 3\theta_1 = 1, \sin 3\theta_1 = 0$, whose solution is $\theta_1 = 0, \pm 2\pi/3$, and there is no restriction on θ_2.

The solutions in the class (I)(B) are summarized as

$$\begin{aligned} G_{\mathcal{T}}(A) &= i\sigma_2, \\ G_{\mathcal{T}}(B) &= i\eta_{14}\sigma_2, \\ G_{\sigma}(A) &= \sigma_0, \\ G_{\sigma}(B) &= \eta_{10}, \\ G_{C_6}(A) &= i\sigma_1, \\ G_{C_6}(B) &= \eta_1\eta_9 i\sigma_1 \exp(i\sigma_2\theta_1 e^{i\sigma_1\theta_2}), \end{aligned} \tag{3.63}$$

which are controlled by $\eta_1, \eta_9, \eta_{10}, \eta_{14}, \theta_1$, providing $2^4 \times 3 = 48$ PSG's. Here $\theta_2 \in [0, 2\pi)$ is a free angle.

Class (II): $\eta_8 = \sigma_0$. Then $G_{\mathcal{T}}(A) = G_{\mathcal{T}}(B) = \sigma_0$. Therefore Eq. (3.53,3.54,3.55,3.56) become

$$\begin{aligned} \mathcal{K}G_{C_6}(A)\mathcal{K} &= \eta_{11}G_{C_6}(A), \\ \mathcal{K}G_{C_6}(B)\mathcal{K} &= \eta_{11}G_{C_6}(B), \\ \mathcal{K}G_{\sigma}(A)\mathcal{K} &= \eta_{12}G_{\sigma}(A), \\ \mathcal{K}G_{\sigma}(B)\mathcal{K} &= \eta_{12}G_{\sigma}(B). \end{aligned} \tag{3.64}$$

The general solution of $\mathcal{K}G_g\mathcal{K} = G_g$ is $G_g = e^{i\sigma_2\theta}$, while the general solution of $\mathcal{K}G_g\mathcal{K} = -G_g$ is $G_g = i\sigma_3 e^{i\sigma_2\theta}$. According to the sign of η_{11} and η_{12}, the class (II) is further divided into four subclasses.

Class (II)(A1): $\eta_{11} = \eta_{12} = \sigma_0$. Then the general solution of Eq. (3.64) reads $G_{C_6}(A) = e^{i\sigma_2\theta_1}$, $G_{C_6}(B) = \eta_1\eta_9 e^{i\sigma_2\theta_2}$, $G_{\sigma}(A) = e^{i\sigma_2\theta_3}$, $G_{\sigma}(B) = \eta_{10}e^{i\sigma_2\theta_4}$. Then according to Eq. (3.57), $\theta_4 = -\theta_3$. Substitute into Eq. (3.58), we obtain $e^{2i\sigma_2(\theta_2+\theta_3)} = e^{2i\sigma_2(\theta_1-\theta_3)} = \eta_1\eta_{13}$, which implies $e^{2i\sigma_2(\theta_1+\theta_2)} = \sigma_0$, then Eq. (3.59) can be reduced to $e^{i\sigma_2(\theta_1+\theta_2)} = \sigma_0$, thus $\theta_2 = -\theta_1$. While θ_1 and θ_3 are related by

$$\theta_1 = \theta_3 + \begin{cases} 0 & \eta_1\eta_{13} = \sigma_0, \\ \pi/2 & \eta_1\eta_{13} = -\sigma_0. \end{cases} \tag{3.65}$$

The solutions in the class (II)(A1) are summarized as

$$\begin{aligned} G_{\mathcal{T}}(A) &= \sigma_0, \\ G_{\mathcal{T}}(B) &= \sigma_0, \\ G_{C_6}(A) &= e^{i\sigma_2\theta_1}, \\ G_{C_6}(B) &= \eta_1\eta_9 e^{-i\sigma_2\theta_1}, \\ G_{\sigma}(A) &= e^{i\sigma_2\theta_3}, \\ G_{\sigma}(B) &= \eta_{10} e^{-i\sigma_2\theta_3}, \end{aligned} \tag{3.66}$$

which are controlled by $\eta_1, \eta_9, \eta_{10}, \eta_{13}$, providing $2^4 = 16$ PSG's. Here θ_3 can be any angle, and θ_1 follows from Eq. (3.65).

Class (II)(B1): $-\eta_{11} = \eta_{12} = \sigma_0$. The solution of G_σ is the same as the class (II)(A1), however the general solution of G_{C_6} becomes: $G_{C_6}(A) = i\sigma_3 e^{i\sigma_2\theta_1}$, $G_{C_6}(B) = -\eta_1\eta_9 i\sigma_3 e^{i\sigma_2\theta_2}$. From Eq. (3.58) one finds $\eta_1\eta_{13} = -\sigma_0$. While from Eq. (3.59), $e^{3i\sigma_2(\theta_1-\theta_2)} = 1$, thus $(\theta_1 - \theta_2) = 0, \pm 2\pi/3$.

The solutions in the class (II)(B1) are summarized as

$$\begin{aligned} G_{\mathcal{T}}(A) &= \sigma_0, \\ G_{\mathcal{T}}(B) &= \sigma_0, \\ G_{C_6}(A) &= i\sigma_3 e^{i\sigma_2\theta_1}, \\ G_{C_6}(B) &= -\eta_1\eta_9 i\sigma_3 e^{i\sigma_2\theta_2}, \\ G_{\sigma}(A) &= e^{i\sigma_2\theta_3}, \\ G_{\sigma}(B) &= \eta_{10} e^{-i\sigma_2\theta_3}, \end{aligned} \tag{3.67}$$

which are controlled by $\eta_1, \eta_9, \eta_{10}, (\theta_1 - \theta_2)$, providing $2^3 \times 3 = 24$ PSG's. Here θ_2 and θ_3 can be any angles, and $(\theta_1 - \theta_2) = 0, \pm 2\pi/3$.

Class (II)(A2): $-\eta_{11} = -\eta_{12} = \sigma_0$. Then the general solution of Eq. (3.64) reads $G_{C_6}(A) = i\sigma_3 e^{i\sigma_2\theta_1}$, $G_{C_6}(B) = -\eta_1\eta_9 i\sigma_3 e^{i\sigma_2\theta_2}$, $G_\sigma(A) = i\sigma_3 e^{i\sigma_2\theta_3}$, $G_\sigma(B) = -\eta_{10} i\sigma_3 e^{i\sigma_2\theta_4}$. Then according to Eq. (3.57), $\theta_3 = \theta_4$. Substitute into Eq. (3.58), then combining with Eq. (3.59), one finds $\theta_2 = -\theta_1$, and θ_1 and θ_3 are related by Eq. (3.65).

The solutions in the class (II)(A2) are summarized as

$$\begin{aligned} G_{\mathcal{T}}(A) &= \sigma_0, \\ G_{\mathcal{T}}(B) &= \sigma_0, \\ G_{C_6}(A) &= i\sigma_3 e^{i\sigma_2\theta_1}, \\ G_{C_6}(B) &= -\eta_1\eta_9 i\sigma_3 e^{i\sigma_2\theta_1}, \\ G_{\sigma}(A) &= i\sigma_3 e^{i\sigma_2\theta_3}, \\ G_{\sigma}(B) &= -\eta_{10} i\sigma_3 e^{i\sigma_2\theta_3}, \end{aligned} \tag{3.68}$$

which are controlled by $\eta_1, \eta_9, \eta_{10}, \eta_{13}$, providing $2^4 = 16$ PSG's. Here θ_3 can be any angle, and θ_1 follows from Eq. (3.65).

Class (II)(B2): $\eta_{11} = -\eta_{12} = \sigma_0$. The solution of G_σ is the same as the class (II)(A2), however the general solution of G_{C_6} becomes $G_{C_6}(A) = e^{i\sigma_2\theta_1}$, $G_{C_6}(B) = \eta_1\eta_9 e^{i\sigma_2\theta_2}$. From Eq. (3.58), it is found that $\eta_1\eta_{13} = -\sigma_0$. And Eq. (3.59) gives $e^{3i\sigma_2(\theta_1+\theta_2)} = 1$, so $(\theta_1 + \theta_2) = 0, \pm 2\pi/3$.

The solutions in the class (II)(B2) are summarized as

$$\begin{aligned} G_{\mathcal{T}}(A) &= \sigma_0, \\ G_{\mathcal{T}}(B) &= \sigma_0, \\ G_{C_6}(A) &= e^{i\sigma_2\theta_1}, \\ G_{C_6}(B) &= \eta_1\eta_9 e^{i\sigma_2\theta_2}, \\ G_\sigma(A) &= i\sigma_3 e^{i\sigma_2\theta_3}, \\ G_\sigma(B) &= -\eta_{10} i\sigma_3 e^{i\sigma_2\theta_3}, \end{aligned} \tag{3.69}$$

which are controlled by $\eta_1, \eta_9, \eta_{10}, (\theta_1 + \theta_2)$, providing $2^3 \times 3 = 24$ PSG's. Here θ_2 and θ_3 can be any angles, and $(\theta_1 + \theta_2) = 0, \pm 2\pi/3$.

Now all the 144 algebraic PSG's has been classified. Given Eq. (3.13), one can check $\eta_8 = G_{\mathcal{T}}\mathcal{K}G_{\mathcal{T}}\mathcal{K} = -\sigma_0$ and $\eta_1\eta_3 = (G_{C_6}(A)G_\sigma(B))^2 = (-\sigma_{C_6}\sigma_\sigma)^2 = -\sigma_0$, which match the criterion of the class (I)(B). So the PSG of Kitaev spin liquid belongs to the class (I)(B) with $\eta_1 = -\eta_9 = -\eta_{10} = -\eta_{14} = \sigma_0$ and $\theta_1 = 2\pi/3$.

Finally our classification is related to the previous work[55] in the following table. The number of PSG's in the class (II)(ii)(B)(β) was miscounted in Ref. [55] as 24, which should be 8 instead.

Table 3.2: Relation between the new classification and the previous one.

This work	Ref. [55]
(I)(A)	(I)(A)
(I)(B)	(I)(B)
(II)(A1)	(II)(i)(A) + (II)(i)(B)(α)
(II)(B1)	(II)(ii)(B)(α)
(II)(A2)	(II)(ii)(A) + (II)(ii)(B)(β)
(II)(B2)	(II)(i)(B)(β)

3.6 Appendix: Mean Field Decomposition

Rewrite the hopping term on a single bond in terms of F_i and B_i matrices as

$$\begin{aligned}\sum_{\sigma}\left(c_{i\sigma}^{\dagger}c_{j\sigma}+h.c.\right) &= \mathrm{Tr}\,\sigma_3 C_i^{\dagger}C_j \\ &= \frac{1}{2}\mathrm{Tr}\,\sigma_3 B_i^{\dagger}F_i^{\dagger}F_j B_j.\end{aligned} \tag{3.70}$$

According to Eq. (3.10),

$$\begin{aligned}F_i^{\dagger}F_j = &\frac{1}{2}\sum_{\alpha=0}^{3}\chi_i^{\alpha}\chi_j^{\alpha}\sigma_0 + \\ &\frac{1}{2}\sum_{\alpha=1}^{3}\left(i\chi_i^0\chi_j^{\alpha}-i\chi_i^{\alpha}\chi_j^0+\sum_{\beta,\gamma=1}^{3}i\epsilon^{\alpha\beta\gamma}\chi_i^{\beta}\chi_j^{\gamma}\right)\sigma_{\alpha}.\end{aligned} \tag{3.71}$$

Here we may simplify the expression by dropping the second term, and use $F_i^{\dagger}F_j \simeq \sum_{\alpha=0}^{3}\chi_i^{\alpha}\chi_j^{\alpha}\sigma_0$. There are two reasons. First, consider the dihedral group $D_2 = \{1, e^{i\pi S_i^1}, e^{i\pi S_i^2}, e^{i\pi S_i^3}\}$, which is a symmetry of the model Hamiltonian, and should not be broken in the spin liquid or Fermi liquid phase. Under these D_2 operations, Majorana fermions undergo sign changes, say for example $e^{i\pi S_i^3}$: $\chi_i^0 \to \chi_i^0$, $\chi_i^1 \to -\chi_i^1$, $\chi_i^2 \to -\chi_i^2$, $\chi_i^3 \to \chi_i^3$, which can be seen from the behavior of spin operators $S_i^1 \to -S_i^1$, $S_i^2 \to -S_i^2$, $S_i^3 \to S_i^3$. Then any term that change the flavor of Majorana fermions acquires a minus sign under at least one of the D_2 operations. So the D_2 symmetry preserves the flavor of Majorana fermions, and terms like $\chi_i^0\chi_j^{\alpha}$ and $i\epsilon^{\alpha\beta\gamma}\chi_i^{\beta}\chi_j^{\gamma}$ are not allowed. Secondly, in the time reversal broken phase like the superconducting phase, the D_2 symmetry is broken. But in this case the bosons condense to a state described by Eq. (3.28), which does not support any boson gauge current, i.e. $\mathrm{Tr}\,\langle\sigma_3 B_i^{\dagger}\sigma_{\alpha}B_j\rangle = 0$ $(\alpha = 1,2,3)$. So the second term in Eq. (3.71) can not make a contribution to the mean field Hamiltonian in any case, and thus can be neglected for the sake of simplicity. Therefore the electron hopping term can be written as

$$\begin{aligned}H_t &= -\frac{t}{4}\sum_{\langle ij\rangle}\sum_{\alpha=0}^{3}i\chi_i^{\alpha}\chi_j^{\alpha}\mathrm{Tr}\,\sigma_3 B_i^{\dagger}\left(-i\sigma_0\right)B_j \\ &= -\frac{t}{4}\sum_{\langle ij\rangle}\sum_{\alpha=0}^{3}i\chi_i^{\alpha}\chi_j^{\alpha}\sum_{\nu=1}^{2}\left(ib_{i\nu}^{\dagger}b_{j\nu}+h.c.\right)\end{aligned} \tag{3.72}$$

For the Kitaev spin coupling term H_J, we first rewrite the spin operator to match Kitaev's convention by combining it with the neutral gauge charge $\boldsymbol{K} = 0$,

$$S_i^a \to S_i^a + K_i^a \simeq (i\chi_i^0\chi_i^a)(1-\delta). \tag{3.73}$$

The single-occupancy projector $(1-\delta)$ is appended to project out the holon gauge charge terms in K_i^a. Physically $(1-\delta)$ represents the probability that one electron actually appears on site so that the spin operator can make a effect. Substitute Eq. (3.73) into H_{J_K},

$$H_{J_K} = J_K(1-\delta)^2 \sum_{\langle ij \rangle} i\chi_i^0 \chi_j^0 i\chi_i^a \chi_j^a, \tag{3.74}$$

where a denotes the type of the bond $\langle ij \rangle$.

Then by introducing the mean field parameters in Eq. (3.23) and following the standard slave boson mean field approach, Eq. (3.72) and Eq. (3.74) can be decomposed to the mean field Hamiltonian Eq. (3.24) through Hubbard-Stratonovich transform, with additional Lagrangian multipliers to enforce the doping and SU(2) gauge constraints.

3.7 Appendix: Case of Finite J

Starting from the t-J-$J_{\rm K}$ model, $H = H_t + H_{\rm HK}$ with

$$\begin{aligned} H_t &= -t \sum_{\langle ij \rangle \sigma} \mathcal{P} c_{i\sigma}^\dagger c_{j\sigma} \mathcal{P} + h.c. - \mu \sum_{i\sigma} c_{i\sigma}^\dagger c_{i\sigma}, \\ H_{\rm HK} &= J \sum_{\langle ij \rangle} \boldsymbol{S}_i \cdot \boldsymbol{S}_j - J_{\rm K} \sum_{\langle ij \rangle} S_i^a S_j^a. \end{aligned} \tag{3.75}$$

Following the SU(2) slave boson theory, introducing the mean field parameters: $u_{ij}^\alpha = \langle i\chi_i^\alpha \chi_j^\alpha \rangle$, $w_{ij}^\nu = \langle i b_{i\nu}^\dagger b_{j\nu} \rangle$, one obtains the mean field Hamiltonian

$$\begin{aligned} H_{\rm MF} = &\sum_{\langle ij \rangle} \left(\sum_{\alpha=0}^{3} U_{ij}^\alpha i\chi_i^\alpha \chi_j^\alpha + \sum_{\nu=1}^{2} W_{ij}^\nu (i b_{i\nu}^\dagger b_{j\nu} + h.c.) \right) \\ &+ \sum_i \left(\sum_{l=1}^{3} a_i^l K_i^l - \mu \sum_{\nu=1}^{2} b_{i\nu}^\dagger b_{i\nu} \right), \end{aligned} \tag{3.76}$$

where the fermion bond strength reads

$$\begin{aligned} U_{ij}^\alpha = &-\frac{t}{4} \sum_{\nu=1}^{2} (w_{ij}^\nu + c.c.) \\ &+ (1-\delta)^2 \Bigg(u_{ij}^0 (J_{\rm K}\delta_{\alpha a} - J_{\rm H}(1-\delta_{\alpha 0})) \\ &+ \sum_{\beta=1}^{3} u_{ij}^\beta (J_{\rm K}\delta_{\beta a} - J_{\rm H})\delta_{\alpha 0} \Bigg), \end{aligned} \tag{3.77}$$

and the boson bond strength reads

$$W_{ij}^{\nu} = -\frac{t}{4}\sum_{\alpha=0}^{3} u_{ij}^{\alpha}. \tag{3.78}$$

The index a denotes the type of bond $\langle ij\rangle$. The boson chemical potential μ is chosen such that $\sum_{i,\nu}\langle b_{i\nu}^{\dagger} b_{i\nu}\rangle = \delta N$. The gauge potential a_i^l is adjusted to ensure the gauge singlet condition $\langle K_i^l\rangle = 0$.

The mean field phase diagram can be obtained by solving the mean field Hamiltonian H_{MF} self-consistently. All phase diagrams contains SC_1 phase with Chern number $+1$ at small doping limit and SC_2 phase at large doping, separated by the first order transition at δ_c. Tab. 3.3 list the values of δ_c for different settings of t and J. $J/J_{\mathrm{K}} = 1/8$ corresponds to $\alpha = 0.8$ according to the convention $J = 1-\alpha$, $J_{\mathrm{K}} = 2\alpha$. We conclude that small Heisenberg coupling will not affect the phase diagram much on the mean field level.

Table 3.3: Kitaev spin liquid-FL transition point.

t/J_{K}	$J_{\mathrm{H}}/J_{\mathrm{K}}$	δ_c
10	0	0.064
	1/8	0.056
5	0	0.12
	1/8	0.11
2	0	0.22
	1/8	0.20

On the type-3 bond, parameterize the mean field ansatz by $u_{ij}^0 = u_0$, $u_{ij}^1 = u_{ij}^2 = u_b$, $u_{ij}^3 = u_a$, $w_{ij}^1 + w_{ij}^2 = w$. Then

$$U_{ij}^0 = -\frac{tw}{2} + (1-\delta)^2((J_{\mathrm{K}} - J)u_a - 2Ju_b). \tag{3.79}$$

The evolution of fermion mean field parameters with doping at zero temperature is shown in Fig. 3.4. The first order transition between the Kitaev spin liquid and the Fermi liquid phases happens when $U_{ij}^0 = 0$ (at this point, the χ^0 band becomes completely flat and can not gain more energy from the magnetic interaction). It is found that the mean field solution follows $w = \delta$ and $u_b \simeq t\delta/(3J_{\mathrm{K}})$ at zero temperature, then the first order transition point δ_c can be roughly estimated from the equation

$$\frac{t\delta_c}{2} = (1-\delta_c)^2\left((J_{\mathrm{K}} - J)u_a - \frac{2Jt\delta_c}{3J_{\mathrm{K}}}\right). \tag{3.80}$$

Considering the case of $J = 0$ and large t, the transition point will be simply given by $\delta_c = 2u_a J_{\mathrm{K}}/t$, where the value of $u_a \sim 0.3$ can be determined by the mean field solution.

Chapter 4

Kitaev-Heisenberg models for iridates on the triangular, hyperkagome, kagome, fcc, and pyrochlore lattices

The context for this work was the experimental relevance for this line of projects at the time this project began, when only the 2D layered honeycomb materials were known to exist. Specifically, the Kitaev-Heisenberg (KH) model has been proposed to capture magnetic interactions in iridate Mott insulators on the honeycomb lattice, by Chaloupka, Jackeli and Khaliullin [PRL 105, 027204 (2010)].

In this work, we look to possible future extensions. We show that analogous interactions arise in many other geometries built from edge-sharing IrO_6 octahedra, including the pyrochlore and hyperkagome lattices relevant to Ir_2O_4 and $Na_4Ir_3O_8$ respectively. The Kitaev spin liquid exact solution does not generalize to these lattices. However, a different exactly soluble point of the honeycomb lattice KH model, obtained by a four-sublattice transformation to a ferromagnet, generalizes to all of these lattices and even to certain additional further neighbor Heisenberg couplings. A Klein four-group $\cong \mathbb{Z}_2 \times \mathbb{Z}_2$ structure is associated with this mapping (hence *Klein duality*). A finite lattice admits the duality if a simple geometrical condition is met. This duality predicts fluctuation free ordered states on these different 2D and 3D lattices, which are analogs of the honeycomb lattice KH *stripy* order. This result is used in conjunction with a semiclassical Luttinger-Tisza approximation to obtain phase diagrams for KH models on the different lattices. We also discuss a Majorana fermion based mean field theory at the Kitaev point, which is exact on the honeycomb lattice, for the KH models on the different lattices. We attribute the rich behavior of these models to the interplay of geometric frustration and frustration induced by spin-orbit coupling.

4.1 Introduction

Long viewed as a perturbative correction, relativistic spin-orbit coupling has in recent years been increasingly asserting its role within condensed matter physics. It took center stage with topological insulators, time reversal invariant states of electrons with no strong interactions that use spin-orbit coupling to generate nontrivial topology in the band structure[185, 121, 120]. Electron correlations may amplify[184, 206] the effects of spin-orbit coupling (SOC), enriching the taxonomy of possible phases. Thus Mott insulating states of heavy magnetic ions could realize novel Hamiltonians, which may be hitherto unexplored or not thought to describe real materials.

One such S=1/2 Hamiltonian has been proposed by Jackelli and Khaliullin[129, 106] to occur in the honeycomb iridates Na_2IrO_3 and Li_2IrO_3. It includes the Kitaev exchange, a nearest neighbor ising coupling of spin component $\gamma \in \{x, y, z\}$ set by the spatial orientation of the bond[134, 146]. The pure Kitaev honeycomb Hamiltonian is exactly solvable with a quantum spin liquid (QSL) ground state of a gapless Majorana coupled to $\mathbb{Z}_2$ fluxes[146]. The proposed magnetic model for these iridates includes the Kitaev as well as SU(2) symmetric Heisenberg coupling, yielding the Kitaev-Heisenberg $S = 1/2$ Hamiltonian[106]. It may be written as

$$H_{\mathrm{KH}} = \sum_{\langle ij \rangle} \eta \left[(1 - |\alpha|)\, \vec{S}_i \cdot \vec{S}_j - 2\alpha S_i^{\gamma_{ij}} S_j^{\gamma_{ij}} \right] \tag{4.1}$$

with $\eta = \pm 1$ and $-1 \leq \alpha \leq 1$. Here η sets the sign of Heisenberg exchange, and negative α gives the same sign for both exchanges. Pairs of endpoints of the two α-segments for $\eta = +1, -1$ are identified as a single point by the product $\eta\alpha = +1$ (FM Kitaev) and similarly $\eta\alpha = -1$ (AF Kitaev), forming an (η, α) parameter ring[107]. We will primarily focus on this idealized Hamiltonian but also consider some extensions such as farther neighbor couplings.

The phase diagram of H_{KH} on the honeycomb lattice is known from a combination of exact diagonalization[106, 107], other numerical methods[190, 131] and the presence of exactly soluble points. In addition to the exact solution using majorana fermions of the Kitaev Hamiltonians $\alpha = \pm 1$, and the obvious SU(2)-symmetric ferromagnet ($\eta = -1, \alpha = 0$), a four sublattice site-dependent spin rotation[106] transforms H_{KH} at $\eta = +1, \alpha = 1/2$ into a ferromagnet in the rotated basis. The original spins are then "stripy" ordered. Neel order from the Heisenberg antiferromagnet is unfrustrated on the bipartite honeycomb, and was recently shown[107] to map under this transformation to a physical parameter regime hosting the spin pattern known as "zigzag".

This zigzag phase was determined in recent experiments[110, 161, 217] to be the low temperature ordering pattern of Na_2IrO_3. The zigzag order was earlier theoretically found to be most stabilized by combining Kitaev interactions and the further neighbor[91, 187] exchanges J_2, J_3 which naturally arise across a honeycomb hexagon[169, 116], and which together fit the available experimental data in

comparisons to exact diagonalization[143]. Indeed, within a classical approximation to the phase diagram (Luttinger-Tisza described below), the zigzag phase within the pure Kitaev-Heisenberg model lies nearly at the boundary of the large zigzag-ordered region stabilized by J_2, J_3 exchanges[128]. Interestingly, the zigzag phase in its $J_1 - J_2 - J_3$ limit and in its Eq. 5.1 limit may offer experimentally relevant distinguishing characteristics[107, 202].

So far only the honeycomb iridates Na_2IrO_3 and Li_2IrO_3 have been studied in the context of the Kitaev-Heisenberg model. Despite initial worries that trigonal distortion would invalidate the derivation of the Kitaev exchange discussed below, recent resonant inelastic x-ray scattering results[95] support the validity of the strong spin-orbit coupling approach. For the sodium iridate Na_2IrO_3, attempts to extract the magnetic Hamiltonian from fits to experiments including susceptibility and spin wave spectra[197, 198, 110, 143, 161, 217, 107] and to electronic properties[112, 202] have so far proved unable to distinguish between substantial Kitaev exchange and a complete lack of it. Few experimental results on magnetic behavior in the lithium iridate Li_2IrO_3 are currently available, though the relatively small magnitude of the Curie Weiss scale extracted from susceptibility suggests the Kitaev exchange may be strong[198, 143].

Beyond the possible Kitaev-Heisenberg physics in the layered honeycomb iridates, other iridates have also attracted much attention. Layered compounds include the Mott insulator Sr_2IrO_4[139, 138] and its bilayer variant $Sr_3Ir_2O_7$[105, 174], both with ordered SOC magnetic moments. Notable examples with a fully three dimensional structure include the 2-2-7 pyrochlore iridates, where changing the A site rare earth metal yields radically varying properties[214, 206, 165, 184]; the sodium iridate $Na_4Ir_3O_8$ spin liquid candidate, with Ir on the pyrochlore-descendent hyperkagome lattice[181]; and a recently epitaxially-stabilized iridium spinel Ir_2O_4 with empty cation sites[149] leaving Ir on a pyrochlore lattice. Despite the variety of elemental composition and geometrical structure in this list, there is a simple but fundamental distinction separating the latter two compounds from the others listed.

In this manuscript we show that the iridates $Na_4Ir_3O_8$ and Ir_2O_4, as well as possible compounds in certain other geometries, may be described by generalizations of the Hamiltonian Eq. 5.1 to the relevant lattices (hyperkagome for $Na_4Ir_3O_8$ and pyrochlore for Ir_2O_4). The key quantum chemistry ingredients which can generate the interactions $H_{\rm KH}$ have been already pointed out by Jackeli and Khaliullin[129] but the extension to three dimensional lattices, as well as to these compounds, has not been previously exposed. We begin by recalling the derivation of $H_{\rm KH}$ and systematically extending it to other geometries in two and three dimensions; it applies when oxygen octahedra are edge-sharing, yielding lattices that are in a certain sense subsets of the fcc. We then proceed to investigate the phase diagram of $H_{\rm KH}$ on these lattices, using primarily analytical approaches. We generalize the honeycomb four-sublattice transformation into a duality on graphs and lattices with Kitaev labeled bonds in any dimension, and even with certain further neighbor pure Heisenberg couplings;

we shall refer to it as the *Klein duality* since, as we shall show, it is structured by the Klein four-group $\cong \mathbb{Z}_2 \times \mathbb{Z}_2$. We give a simple algorithm determining which graphs admit the duality, based on this Klein group structure. The Klein duality gives stripy phases as FM-duals. Diagonalizing the classical version of H_{KH} with spins of unconstrained length (i.e. the Luttinger-Tisza approximation), we identify unconventional ordering patterns and also find hints of quantum magnetically disordered phases, most interestingly on the hyperkagome. The Luttinger-Tisza phase diagrams are shown in Fig. 4.1. To directly capture Majorana fermion quantum spin liquids analogous to the Kitaev honeycomb QSL, we decompose spins into Majorana combinations of Schwinger fermions, a mean field treatment which is exact for the Kitaev honeycomb model, finding on all other lattices fermionic QSLs which break time reversal and carry gapless excitations, but which are not exact solutions. For the honeycomb and hyperkagome pure Kitaev Hamiltonians, the lattice fragments under a bond type γ into disjointed localized clusters, giving flat bands in the Majorana mean field as well as in the Luttinger-Tisza approximation, which hints at a possible analogy between the honeycomb Kitaev QSL and the Kitaev Hamiltonian ground state on the hyperkagome.

We focus on two candidate materials, while also considering other related compounds. The recently epitaxially fabricated Ir_2O_4 is a spinel without the A cation, leaving the iridium ions on a pyrochlore lattice with oxygens positioned appropriately, as described below; Ir_2O_4 was found to be a narrow gap insulator[149]. The spin liquid candidate $Na_4Ir_3O_8$ is an iridate with $S = 1/2$ moments on the three dimensional hyperkagome lattice, which exhibits no magnetic order down to at least 2K[181]. In addition to these two iridates, this study may also capture compounds in which iridium is replaced by a transition metal ion with strong spin orbit coupling, intermediate correlations and valency appropriate for a magnetic effective spin one half model (see below). Recently, the osmium oxides $CaOs_2O_4$ and $SrOs_2O_4$ were computationally predicted[207] to be stabilized in the spinel structure relevant to Kitaev-Heisenberg physics; if they indeed exist in this geometry, H_{KH} should form at least part of their magnetic Hamiltonian. Kagome and triangular lattice iridates may be seen as appropriate layers within epitaxially stabilized Ir_2O_4, coupled together in a nontrivial manner. Triangular lattice iridates could potentially also be stabilized as analogues of the cobaltates[150] Na_xCoO_2, where Co is on a triangular lattice; the preferred valency would exist uniformly only in the limit $x \to 0$, but small x should offer interesting perturbations as well as likely separate layers of triangular lattices. However, no triangular lattice iridate with the relevant edge sharing octahedra structure is currently available; a compound of the type Na_xIrO_2 may or may not turn out to be stabilized.

In addition to the honeycomb Kitaev-Heisenberg model, other previous work has investigated Hamiltonians related to H_{KH} on other lattices. Chen and Balents[108] studied spin Hamiltonians on the hyperkagome lattice for $Na_4Ir_3O_8$, in the strong and weak SOC limits (relative to octahedral distortions). Within the strong SOC

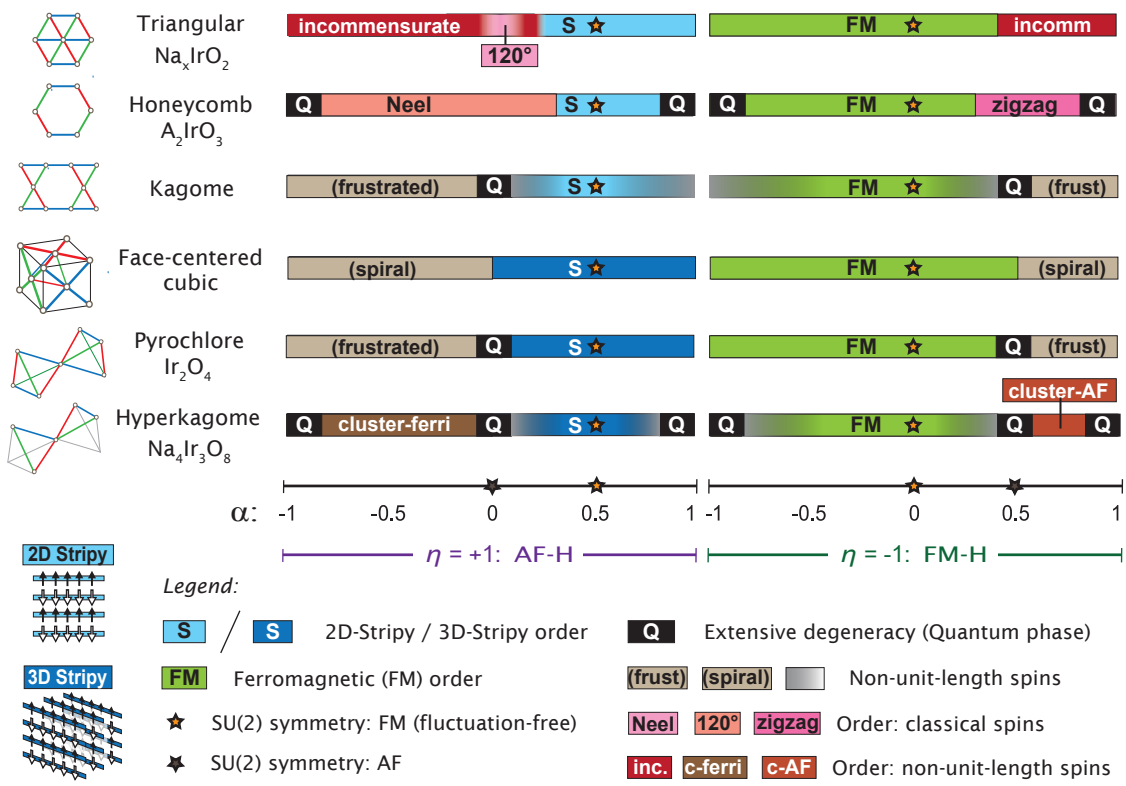

Figure 4.1: **P**hase diagrams using the Klein duality as well as the Luttinger-Tisza approximation (LTA). Phase diagrams are shown for the Kitaev-Heisenberg Hamiltonian, $H_{KH} = \eta\,(1-|\alpha|)\,\vec{S}_i \cdot \vec{S}_j - 2\eta\alpha S_i^{\gamma_{ij}} S_j^{\gamma_{ij}}$ with $\eta = \pm 1$, on the various lattices. Note that the parameter space is a ring: for the α parameter segments shown here the endpoints should be identified, i.e. writing the parameter as (η, α), identify the points (-1,-1)≅(+1,+1) and also identify the points (-1,+1)≅(+1,-1). Rich phase diagrams are found. 2D and 3D stripy magnetic phases (blue), found on all lattices, are exact and fluctuation free by the Klein duality at the FM SU(2) point (yellow star) η=+1, α=1/2. On the kagome and hyperkagome lattices, outside the FM SU(2) points, the FM and stripy orders are given non-unit-length spins by the LTA (gray shading), suggesting frustration. Extensive degeneracy of LTA ordering wavevectors hints at a non-spin-ordered "quantum" phase, labelled "Q": where the Hamiltonians hosting Q phases have been solved, exactly[146] for the honeycomb at α=±1 and numerically[213, 130] for the kagome at η=+1, α=0, they have turned out to host non-magnetic phases. The hyperkagome hosts Q points at the Heisenberg antiferromagnet and its Klein dual, as well as at the pure Kitaev Hamiltonians, because any single Kitaev bond type fragments the hyperkagome into disjoint clusters (Fig. 4.4). The 120° triangular lattice and Neel and zigzag honeycomb orders are found with normalized spins. Apparent ordering with LTA non-normalized spins is found at incommensurate wavevectors on the triangular lattice and in the cluster-ferrimagnet and cluster-antiferromagnet (AF) regimes on the hyperkagome. Kagome, fcc and pyrochlore lattices also host frustrated regimes with no definitive ordering within the LTA, as described in the text (gray).

case they considered the single superexchange pathway via oxygen ions generating the single point $H_{\rm KH}$ at $\alpha = 1/2$, for which they found that classical configurations of stripy patterns were completely unfrustrated [1]. Superexchange via oxygen ions generating anisotropic spin interactions for the SOC Kramers doublet in $Na_4Ir_3O_8$ was also considered by Micklitz and Norman[179, 172] in electronic structure computations and associated microscopic tight binding parametrization. Recently Reuther, Thomale and Rachel[188] studied a family of related Hamiltonians including on triangular lattices formed by second neighbors of the honeycomb, with an associated hidden ferromagnet. Very recently the classical $H_{\rm KH}$ Hamiltonian was studied on the triangular lattice by Rousochatzakis, Rossler, Brink and Daghofer[191]. Their study included a classical Monte Carlo computation suggesting the intriguing possibility that Kitaev exchange can stabilize an incommensurate vortex lattice of the $\mathbb{Z}_2$ topological defects of the Heisenberg antiferromagnet 120° order.

4.2 Kitaev couplings in lattices beyond the honeycomb

Generating the Kitaev coupling requires a subtle recipe with ingredients from chemistry, geometry, and a hierarchy of energy scales, as we now recall[129, 106, 107]. Spin orbit coupling is key, together with (intermediate) correlations; let us focus on iridium. The iridium ions should retain their 5d electrons in localized orbitals, and exist in the 4+ valence. Each iridium should be surrounded by six oxygen ions (or other electronegative ions with valence p-orbitals), which form the vertices of an octahedron cage, shown in Fig. 8.5. The octahedral crystal field splits the 5d orbitals into an empty e_g pair and a triplet of t_{2g} orbitals with five electrons and one hole. Strong spin-orbit coupling further splits t_{2g} down to a half-filled Kramer's doublet, the spin-1/2 degree of freedom defining the low energy manifold. The final key ingredient is the geometrical structure: edge sharing octahedra with 90° Ir-O-Ir bond angles.

In perturbation theory from the Mott insulator limit, virtual hopping of holes from iridium t_{2g} orbitals through intermediate oxygen p orbitals generate the low energy spin Hamiltonian. There are multiple relevant exchange paths[106, 107]. When holes hop through intermediate oxygens and meet on an iridium d-orbital, the resulting coupling is a pure Kitaev term, and is proportional to $J_H/\left((U_d - 3J_H)(U_d - J_H)\right) \approx J_H/U_d^2$. The iridium Coulomb exchange U_d and Hund's rule coupling J_H together specify all of the multi-band interaction parameters, due to the symmetries of d-orbitals. A second exchange path, with two holes meeting on an oxygen or cycling around the Ir-O square, contributes a combination of Kitaev and Heisenberg couplings equal to $H_{\rm KH}$ at $\alpha = 1/2$, with a coefficient and sign η depending on the oxy-

[1] We now know that even the *quantum* Hamiltonian is exactly soluble with its ground state free of fluctuations, via the Klein duality.

gen p-orbitals charge-transfer gap and Coulomb repulsion. Direct iridium wavefunction overlap gives a pure Heisenberg coupling. Recently[107], an additional pathway through the higher e_g orbitals has been proposed to be relevant as well, contributing $H_{\rm KH}$ at $\eta = -1$, $\alpha = 1/2$. The interplay of these exchanges suggests α may not be computable microscopically.

Generalizing this derivation to geometries beyond the honeycomb requires preserving the edge sharing octahedra with 90° Ir-O-Ir bonds. Many commonly studied iridates such as the layered perovskites and the "2-2-7" pyrochlores have corner sharing octahedra and thus are not captured by this derivation. Fig. 8.5 shows two adjacent octahedra, with edges color coded by the spin component coupling they generate when the octahedra of neighboring Ir ions share that edge. It is evident that all twelve octahedra edges may be shared while still maintaining 90° bonds and three-fold symmetries (coupled space and spin rotations). Tiling octahedra which touch along edges builds a face-centered cubic (fcc) lattice of the octahedra centers.

We thus find that in two and three dimensions, all lattices whose graph of nearest neighbor bonds is a subset of the nearest neighbor bonds of the fcc, including the fcc itself, may host analogues of the Kitaev exchange. Possible geometries include the kagome and triangular lattices in two dimensions, and the face-centered cubic, pyrochlore (as realized in spinel-based compounds) and hyperkagome geometries in three dimensions. These are shown in Fig. 4.3. These six are commonly studied lattices which are such subsets of the fcc, but an infinite number of lattices may be added to this list. The materials discussed above all have these edge-sharing octahedral structures and their magnetic Ir ions form one of these lattices. As for the honeycomb iridates, reduced crystal symmetry distorting Ir-O angles away from 90° will generate other magnetic exchanges. Despite apparently strong $> 10\%$ distortions of the bond angle in the sodium honeycomb iridate and a slew of experiments on this material, a Kitaev exchange comparable to or even stronger than the Heisenberg exchange is still consistent with current experimental results, suggesting a hopeful outlook for the other materials.

Note that the quantum chemistry considerations pictured in Fig. 8.5 tightly constrain the possible lattice realizations of Eq. 5.1. Specifically, these constraints are *tighter* than those imposed by naive symmetry considerations of SOC. For example, it is natural to define an implementation of SOC that couples spin component S^z to bonds along $\hat{z}$, i.e. locks the Bloch sphere to real space. This would generate Eq. 5.1 on the simple cubic lattice with S^zS^z coupling along $\hat{z}$ bonds, as well as on the square lattice with $\gamma = x, y$. But the exchange pathways of Ir t_{2g} orbitals forbid this scenario. Instead, the analysis above shows that for t_{2g} orbitals as in iridium, SOC couples spin component S^z to the fcc lattice bonds lying normal to $\hat{z}$. The simple cubic lattice version of $H_{\rm KH}$ cannot be generated, and a compound structured as layers of a square lattice would collapse its Kitaev exchange to uniform ising couplings along all square lattice bonds.

The honeycomb and hyperkagome lattices share a common feature distinguishing

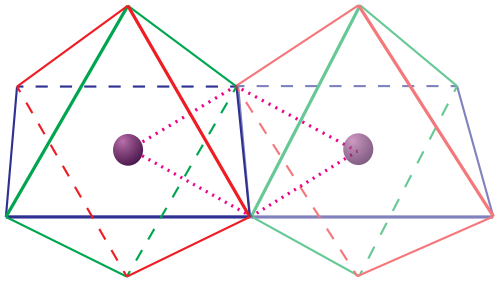

Figure 4.2: **E**dge-sharing IrO_6 Octahedra generating Kitaev exchange. Iridium ions (spheres) are each coordinated by six oxygen ions forming vertices of octahedra. Octahedra of neighboring Ir ions share edges. Dotted (purple) lines show the iridium-oxygen-iridium hopping paths, which form a square with 90° angles. As described in the text, these superexchange paths generate an ising interaction between the iridium effective spins, which couple a spin component x, y or z depending on the orientation of the shared octahedra edge (shown in red, green and blue). Ir lattices hosting this Kitaev exchange must arise from a regular tiling of these edge-sharing octahedra.

them from the other lattices: if we only keep bonds of a single Kitaev type γ, the lattice fragments into localized disconnected *clusters*. On the honeycomb, each cluster contains two sites, and forms the unit cell. On the hyperkagome, each cluster contains three sites, arranged into a line segment. For a given bond label γ, the twelve site unit cell fragments into four disjointed clusters, whose line segments are oriented parallel within each of two pairs and perpendicular between the pairs. The structure on the hyperkagome unit cell is shown in Fig. 4.4. As discussed below, this fact has dramatic repercussions for the Kitaev Hamiltonians in both the Luttinger-Tisza approximation and in the Schwinger fermion Majorana mean field (which on the honeycomb describes the Kitaev QSL). In both cases, certain excitations only propagate within a single Kitaev bond type γ, and the localized disconnected clusters imply these excitations must have completely flat bands.

4.3 Klein duality and hidden ferromagnets

4.3.1 Connections to previous work

Exactly solvable quantum Hamiltonians are rare in dimension higher than one. It is quite remarkable that the stripy phase at $\eta = +1$, $\alpha = 1/2$ found for the honeycomb Kitaev-Heisenberg model[106] is exact, a hidden ferromagnet exposed by

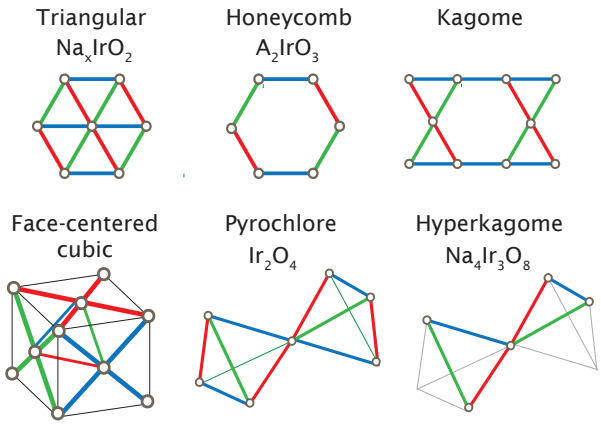

Figure 4.3: **K**itaev-Heisenberg lattices. Iridium ions arranged in these lattices may generate the Kitaev spin exchange, coupling component x, y, z on bonds colored red, green, blue respectively. A blue colored bond connecting two Ir sites implies that the respective IrO^6 octahedra share a blue edge as in Fig. 8.5. We also list examples of possible relevant iridium compounds which form these lattices.

the site dependent spin rotation which quadruples the unit cell[2]. Unlike Neel order on even bipartite lattices, this stripy antiferromagnetic order is exact and fluctuation-free at $\alpha = 1/2$.

This "four sublattice rotation trick" has been known by Khaliullin and Okamoto for t_{2g} orbitals in a cubic environment since as early as 2002[136]. It was used for Kitaev-Heisenberg-like Hamiltonians in ferromagnetic titanates[136, 137] as well as in other systems, including an explicit transformation on the triangular lattice[135] [3] to find the dual of 120° order for CoO_2. It was then applied to the honeycomb lattice by Chaloupka, Jackeli and Khaliullin in their derivation of the Kitaev-Heisenberg model for the honeycomb iridates[106]. However, its general structure has not been previously elucidated. We will now show that this duality transformation may be defined on general graphs with Kitaev γ bond labels and that it has the structure of the Klein four-group, isomorphic to $\mathbb{Z}_2 \times \mathbb{Z}_2$. This will then lead to a geometrical condition specifying which lattices and finite graphs admit the Klein duality, a result especially useful for designing finite graphs for numerical studies.

[2]Spin exchanges with lower symmetry may even be mapped to antisymmetric Dzyaloshinskii-Moriya exchanges.

[3]In this work[135], see especially the discussions related to Fig. 1 (p.170) and Fig. 5 (p.194).

4.3.2 Deriving the Klein transformation on graphs with Kitaev bond labels

We begin by defining a general unitary transformation, and then we will show that under certain special conditions it acts as a duality transformation on Eq. 5.1. Throughout this paper, by a "duality transformation" we refer to a mapping between Hamiltonians that maps a set of Hamiltonians (and the associated phase diagram) to itself (of course without mapping each particular Hamiltonian to itself). Consider a lattice or finite graph in any dimension which connects $S = 1/2$ spins, and assume each bond (i, j) carries a Kitaev *type* label

$$\gamma_{i,j} \in \{1, x, y, z\}. \tag{4.2}$$

The set $\gamma \in \{x, y, z\}$ corresponds to Kitaev coupling $S_i^\gamma S_j^\gamma$ on that bond, where $\{x, y, z\}$ identifies a set of orthogonal axes in the spin Bloch sphere. The Hamiltonian on the bond may have other terms such as Heisenberg coupling and various anisotropies; but the transformation will turn out to be most useful if the coupling includes only Kitaev and Heisenberg terms, as in Eq. 5.1. The label $\gamma_{i,j} = 1$ can be assigned to a bond that does not have a Kitaev exchange (only Heisenberg and possible anisotropies), such as a second or third neighbor interaction. In general such farther neighbor interactions supplementing H_{KH} will frustrate the transformation, so when making use of the Klein duality the lattice should usually be considered to be just the pure nearest neighbor Kitaev-Heisenberg model H_{KH} , where all bonds carry $\gamma \in \{x, y, z\}$. But we will show below that certain farther neighbor Heisenberg interactions do preserve the duality structure, and may be fruitfully included as $\gamma = 1$.

Let us proceed by describing the relevant transformations on individual sites. Assign each site a label

$$a_i \in \{1, X, Y, Z\} \tag{4.3}$$

which will specify a unitary transformation on that site, specifically rotation by π around the Bloch sphere axis S^a for $a \in \{X, Y, Z\}$, and no rotation for the identity element $a = 1$. Note that π rotation around S^a flips the sign of the spin components perpendicular to a, so that the rotation $a_i = Z$ multiplies the (x, y, z) components of S_i by the sign structure $g[Z] = (-1, -1, 1)$, and also that $g[1] = (1, 1, 1)$.

Now, observe that both bond labels $\gamma_{i,j}$ and site labels a_i may be interpreted as elements of the single set $\{1, X, Y, Z\}$. We may turn this set into a group by defining a multiplication rule. A possible definition is suggested by the multiplication of the associated sign structures g, which entails for example $g[X]g[Y] = g[Z]$, suggesting we should define $X\,Y = Z$. The resulting multiplication table is defined by

$$X^2 = Y^2 = Z^2 = XYZ = 1 \tag{4.4}$$

with 1 acting as the identity. This is the presentation of the group with generators (X, Y, Z) and relations (X^2, Y^2, Z^2, XYZ), known as the *Klein four-group*. The

Klein group is abelian and with four elements is the smallest non-cyclic group; it is isomorphic to $\mathbb{Z}_2 \times \mathbb{Z}_2$.

There is an alternative, *geometrical,* way to define multiplication on the elements a_i and $\gamma_{i,j}$. We define the geometric multiplication $(*)$ of a site i and one of its bonds (i,j) to be the site reached by traversing the bond, $i*(i,j) = j$. The associated Klein group elements a_i and $\gamma_{i,j}$ inherit this geometric multiplication as

$$a_i * \gamma_{i,j} = a_j. \tag{4.5}$$

The Klein group product $(\times)$ and the geometric multiplication $(*)$ are consistent on a bond if they give the same answer, $a_i * \gamma_{i,j} = a_i \times \gamma_{i,j}$. We say the transformation given by site labels $\{a_i\}$ is the *Klein* transformation if the geometrical multiplication is consistent with Klein group multiplication on *every* bond in the lattice.

If the transformation site labels a_i, a_j across a bond are consistent with the Klein group product, i.e.

$$a_i \times \gamma_{i,j} = a_j \tag{4.6}$$

or equivalently (since elements in the Klein group square to the identity)

$$a_i \times a_j = \gamma_{i,j} \ , \tag{4.7}$$

then the transformation changes the form of a Kitaev-Heisenberg coupling in an especially simple way. This is simply because the sign flips $g[a]$ multiply by the Klein group rules, so the diagonal spin exchange $\sum_\alpha J^\alpha_{i,j} S^\alpha_i S^\alpha_j$ transforms by

$$J^\alpha_{i,j} \to g[a_i]_\alpha g[a_j]_\alpha J^\alpha_{i,j} = g[\gamma_{i,j}]_\alpha J^\alpha_{i,j} \tag{4.8}$$

where $g[a]_\alpha \in \pm 1$ is component number α of the vector $g[a]$ of ± 1 signs. The transformation flips the sign of the components of J perpendicular to the bond type label. For Kitaev Heisenberg exchange, this means that the Heisenberg coefficient flips sign and the Kitaev coefficient gains twice the (old) Heisenberg coefficient.

Even if the transformation labels on two sites are consistent with the Klein group product on that bond, it might seem improbable that the a_i rotation labels can be chosen across the entire lattice in a pattern that is Klein group consistent on all bonds. Such consistency for all bonds is necessary for the transformation to change the Hamiltonian uniformly. Now the Klein group structure shows its worth. The condition on the transformation $\{a_i\}$ — consistency between geometric and Klein group multiplication on each bond — can be expressed as a condition which refers only to the lattice: that the $\gamma_{i,j}$ encountered in any closed path multiply to the identity 1. In other words, all closed loops on the lattice must be composed of the identity operators $1, X^2, Y^2, Z^2, XYZ$. Then the transformation may be consistently defined by Klein group multiplication of bond labels on a any path,

$$a_j = \left(\prod_{\ell \in \mathrm{path}_{i \to j}} \gamma_\ell \right) a_i. \tag{4.9}$$

4.3.3 Geometrical condition for the Klein duality

We have shown that the existence of the Klein duality can be expressed as a condition on the lattice. Using the Klein group structure, we can write this condition as follows. *Any closed loop, containing N_x x-bonds, N_y y-bonds and N_z z-bonds, must satisfy*

$$N_x,\ N_y,\ N_z \quad \text{all even or all odd.} \tag{4.10}$$

The three N_is can be all even because Klein group elements square to the identity, or all odd because $XYZ = 1$. If this condition Eq. 4.10 is satisfied on all closed loops then the Klein duality can be constructed consistently as follows: choosing a reference site i which for simplicity will be unchanged in the duality, $a_i = 1$, assign any site j a rotation label a_j as simply the Klein group product of the Kitaev bond labels γ on any path from i to j. The constraint Eq. 4.10 ensures this duality construction is consistent regardless of the choice of paths i to j. The Klein duality then maps Eq. 5.1 to itself, transforming the parameters α and η according to Fig. 4.5.

It is easy to see that the Klein duality indeed exists on all of the infinite lattices shown in Fig. 4.3; because the Klein group is abelian, it is sufficient to check that the condition is satisfied on small local loops. For example, triangle faces have $N_x = N_y = N_z = 1$. The condition also holds on other lattices such as the simple cubic that can host symmetric Kitaev exchange but cannot generate it via t_{2g}-p orbital superexchange. Adding pure Heisenberg ($\gamma = 1$) further neighbor interactions generally spoils the Klein duality, though if all the resulting loops satisfy Eq. 4.10, the Klein duality survives unscathed and moreover does not modify the pure Heisenberg $\gamma = 1$ interactions, even while it flips the sign of Heisenberg interactions on Kitaev-labeled bonds. This occurs, for example, with J_3 Heisenberg exchanges on the honeycomb and kagome lattice, connecting sites on opposite corners of a hexagon. The family of Hamiltonians preserved by the duality is then enlarged to $J_K - J_1 - J_3$, ie nearest neighbor Kitaev-Heisenberg plus third neighbor Heisenberg. This $J_K - J_1 - J_3$ family of Hamiltonians maps to itself (non-trivially) under the Klein transformation, with J_3 unchanged.

For graphs and finite lattices with periodic boundary conditions (PBC), considering small local loops is insufficient; loops traversing the PBC may break Eq. 4.10 and spoil the Kitaev duality. Such winding loops must be checked explicitly. Here the condition Eq. 4.10 should serve much practical use, as finite sized versions of the Fig. 4.3 lattices with PBC are useful for numerical studies, and it may otherwise be difficult to construct or identify the choice of PBC which admit the Klein duality. In many cases the appropriate PBC involve nontrivial twists that, in a continuum limit, appear as cutting and gluing operations on the boundaries.

4.3.4 The Klein duality on $H_{\mathbf{KH}}$, Klein self-dual points and Klein $\mathbb{Z}_2$ symmetry

In order to describe the action of the Klein duality on the parameter space of Eq. 5.1 , let us first discuss the η, α snd other parametrizations. In Eq. 5.1 , the sign $\eta = \pm 1$ is the sign of the Heisenberg exchange and the sign of α is minus the relative sign between the Kitaev and Heisenberg exchanges. This is a compatible extension of the α parametrization introduced in Ref [106]; restricting to $\eta = +1$, $0 \leq \alpha \leq 1$ gives the original parameter space[106] with antiferromagnetic (AF) Heisenberg and ferromagnetic (FM) Kitaev interactions. It is clear that both the FM and AF pure Kitaev Hamiltonians are each described by two parameter points, which must be identified,

$$\begin{aligned} (\eta = +1, \alpha = +1) &\cong (\eta = -1, \alpha = -1) \\ (\eta = +1, \alpha = -1) &\cong (\eta = -1, \alpha = +1). \end{aligned} \tag{4.11}$$

Identifying (i.e. gluing) these pairs makes the (η, α) parameter space into a circle. In the axis shown at the top of Fig. 4.5, the two α segments (for $\eta = +1, -1$) are connected both in the middle where they are drawn to almost touch and also at their distant endpoints (where arrows are drawn). Comparing to the angular parametrization presented in Ref. [107], $\eta = +1 (\eta = -1)$ is the right(left) side of the circle, and $\alpha = -1, ..., +1, -1, ..., +1$ increases going clockwise. (We will also sometimes refer to both FM and AF pure Kitaev Hamiltonians simultaneously, in which case the notation $\alpha = \pm 1$ is unambiguous.) Note that the η, α parametrization, though (piecewise) linear, is non-analytic at $\alpha = 0, \pm 1$, which may be an issue for certain numerical computations.

Now we may discuss how the Klein duality acts on Eq. 5.1 . In other words, the Hamiltonian Eq. 5.1 with certain parameters η, α is equivalent to the Hamiltonian Eq. 5.1 on the rotated spins but with different parameters η', α'. The duality is shown by the blue lines in Fig. 4.5. Note that where the blue lines are roughly vertical, the duality approximately just flips the sign of both η and α, i.e. just flips the sign of the Heisenberg term. In general it flips the sign of the Heisenberg term but also adds twice the (old) Heisenberg term to the Kitaev term,

$$J_H \vec{S}_i \cdot \vec{S}_j + J_K S_i^{\gamma_{ij}} S_j^{\gamma_{ij}} \longrightarrow (-J_H) \vec{S}_i \cdot \vec{S}_j + (J_K + 2J_H) S_i^{\gamma_{ij}} S_j^{\gamma_{ij}}. \tag{4.12}$$

Note that with Eq. 5.1 as written, changing α also changes the overall energy scale; this can be avoided by dividing Eq. 5.1 by $(1 - |\alpha|)$, so that the magnitude of the Heisenberg term remains fixed at 1.

On Eq. 5.1 the duality always takes $\eta \to -\eta$, but acts on α in a nonlinear way, approximately shown by the changing slope of the blue lines in Fig. 4.5. The relation between α and α' is given implicitly by

$$\alpha' \alpha = (1 - c_{\alpha'})(1 - c_\alpha) \quad , \quad c_\alpha \equiv \begin{cases} 0 & \alpha \leq 0 \\ 2\alpha & \alpha \geq 0 \end{cases} . \tag{4.13}$$

As is clear from Fig. 4.5, the relation may be written explicitly as a simple piecewise function,

$$\alpha' = \begin{cases} \frac{1}{\alpha+2} & -1 \leq \alpha \leq 0 \\ \frac{1-2\alpha}{2-3\alpha} & 0 \leq \alpha \leq \frac{1}{2} \\ \frac{1}{\alpha} - 2 & \frac{1}{2} \leq \alpha \leq 1 \end{cases} . \tag{4.14}$$

The family of Hamiltonians Eq. 5.1 can be generalized by modulating the strength of couplings on different bonds in arbitrary ways; the Klein rotation generalizes as well to arbitrary configurations of coupling strengths. Generically it will no longer map one simple family of Hamiltonians to itself, but it may still offer hidden exactly solvable points, such as by mapping Eq. 5.1 with toric code anisotropies of the Kitaev coupling strength into a mixed ising-Heisenberg ferromagnet with an exact ground state. Specifically, given Kitaev bond strengths of $(1 - a/2, 1 - a/2, 1 + a)$ on the three bond types, the location of the hidden ising ferromagnet shifts to $\eta = +1$, $\alpha = 1/(2 - a/2)$.

Duality relations in condensed matter physics typically map order to disorder or strong coupling to weak coupling, such as the duality relating the paramagnetic and ferromagnetic phases in the transverse field (quantum) ising model. The Klein rotation is a duality in the sense of mapping a family of Hamiltonians to itself, but it is not amenable to this typical interpretation. First, there is no sense of weak and strong coupling regimes within the parameter space of Eq. 5.1 . Second, this parameter space forms a ring, and rather than a single self-dual point, it offers *two* distinct Hamiltonians which are self-dual under the Klein duality. Third, as is rigorously known for the honeycomb lattice and suggested by the LTA for the other lattices below, the self-dual pure Kitaev Hamiltonians lie in the interior of a phase rather than signifying a phase boundary.

The Hamiltonians at the two Klein self dual points may alternatively be interpreted as possessing an enlarged symmetry group. The additional symmetry is generated by the Klein duality and has $\mathbb{Z}_2$ characteristic. It thus acts in a highly nontrivial manner on spins on different sites. Phases that preserve this Klein $\mathbb{Z}_2$ symmetry must contain this highly nontrivial structure; there is currently one known example of such a phase, the Kitaev honeycomb spin liquid. If any lattice turns out to host a magnetically ordered phase which does not spontaneously break the Klein $\mathbb{Z}_2$ symmetry, such a phase would have a complex pattern of noncoplanar spin order. This is unlikely, but there may also be phases which break the Klein $\mathbb{Z}_2$ symmetry but do not break too many other symmetries, yielding a ground state manifold that naturally splits into the two Klein $\mathbb{Z}_2$ broken portions. Determining which or whether any of these scenarios holds on any particular lattice is left for future work.

4.4 Exactly soluble stripy phases as Klein duals of the ferromagnet

The most obvious consequence of the existence of the Klein duality is seen by applying the duality on the Heisenberg ferromagnet. At the resulting parameter point $\eta = +1$, $\alpha = 1/2$, the ground state manifold of the quantum Hamiltonian is known exactly and consists of simple product states, parametrized by the full SU(2) symmetry. The ground states may be found by taking a ground state of the Heisenberg ferromagnet, and applying the rotations defined by the Klein duality on this magnetic order. The result is the *stripy* collinear magnetic order. We will use the name *stripy* to refer to the FM-dual phase on lattices in any dimension, both to preserve the analogy to the honeycomb and also because, as shown below, the 3D-stripy orders can have some "stripy" features in their own right.

Away from the SU(2) symmetric point the symmetries reduce to the lattice SOC operations. The stripy ordering breaks the three-fold rotation symmetry, present in all Kitaev lattices as in Fig. 4.3, that simultaneously permutes the suitably chosen Euclidean directions $\hat{x} \to \hat{y} \to \hat{z} \to \hat{x}$, the same axes on the Bloch sphere and also the Kitaev bond labels $x \to y \to z \to x$. The appropriate coordinate system is set by an IrO_6 octahedron, in which the ordering is along one of the three directions $(1,0,0), (0,1,0), (0,0,1)$ i.e. $\hat{x}, \hat{y}, \hat{z}$. $\hat{z}$-type stripy order has z-bonded spins aligned parallel and x or y bonded spins aligned antiparallel. The collinear spin axis is then fixed to S^z, though the direction of the ordered moment will likely be determined by other effects in any material realization.

The stripy orders on the various lattices share common features but also host distinguishing characteristics. On the two dimensional lattices, which always appear as layers perpendicular to the $(1,1,1)$ axis in the IrO_6 coordinate system, the ordering breaks the (SOC version of) 120° lattice rotation symmetry. On the triangular lattice it is literally alternating stripes (i.e. lines of sites) of up spins and down spins. On the honeycomb lattice, each stripe is composed of the two-site clusters that lie on a given line; this order is also known as "IV" in the J_1-J_2-J_3 literature. On the kagome lattice, stripy order gives the same configuration on each unit cell (is wavevector Γ) of two spins up and one spin down, meaning it is *ferrimagnetic* with a nonzero net magnetization. At the exact $\alpha = 1/2$ point the spins are saturated and the net magnetization is 1/3 that of the ferromagnet.

In three dimensions, the 3D-stripy orders involves alternating planes of up spins and down spins. For say $\hat{z}$ stripy order the planes are normal to $\hat{z}$. On the face centered cubic (fcc) lattice, the planes are faces of the fcc cube. On the pyrochlore lattice, the stripy order acquires an additional feature: spin-up planes are broken up into *chains* aligned in one particular direction, and spin-down planes are composed of chains aligned in the perpendicular direction. On the hyperkagome lattice this feature persists, and moreover the chains are broken into oriented linear clusters: for z-stripy

order the z-type three-spin-chain clusters of Fig. 4.4 are oriented uniformly within the spin-up planes, and also uniformly but in a perpendicular orientation within the spin-down planes. The 3D-stripy orders are shown in Fig. 4.6.

4.5 Luttinger-Tisza approximation phase diagrams

Except for the Heisenberg ferromagnet and its Klein dual point as described above, the Kitaev-Heisenberg Hamiltonians are *frustrated* [4]. The resulting sign problem for quantum Monte Carlo renders their quantum phase diagrams, especially for the three dimensional lattices, exceedingly difficult to compute. The Hamiltonians Eq. 5.1 on the various lattices are quite unique in that they all offer an exact solution at a nontrivial point in the phase diagram, the Klein dual to the ferromagnet. To explore the remainder of the phase diagrams we must use approximation methods, as we shall now describe.

For an initial survey of the phase diagrams we employ the Luttinger-Tisza Approximation (LTA), also known as the spherical model[164, 163, 92, 132]. It is a semiclassical approximation in that it improves upon the classical Hamiltonian, incorporating some notion of quantum fluctuations and a reduced ordered moment. While the classical version of a Hamiltonian has the hard constraint that the ordered moment (i.e. the spin vector) on each site must have magnitude S, quantum fluctuations are expected to relax this constraint. Implementing this constraint only on average with a single global Lagrange multiplier, the Hamiltonian Eq. 5.1 becomes free quadratic and the lowest energy configuration of the classical spins may simply be found by a Fourier Transform and a diagonalization of the spin and sublattice indices.

The LTA always computes a lower bound to the energy of the *classical* model; this inequality becomes a strict equality when the LTA minimum energy configuration happens to obey the unit length constraint. In turn, classical configurations of spins with length S give upper bounds to the true ground state energy of a spin-S quantum Hamiltonian[93], simply by defining site-product wave functions which by the variational principle have at least the ground state energy. When a non-normalized configuration is chosen by the LTA, its energy is lower than the classical minimum energy which in turn is generally higher than the quantum ground state energy, so the energy of the LTA configuration can match the true ground state energy. Relaxing the unit length constraint indeed allows the classical ordered moments to fluctuate, and in some ways improves upon the constrained classical Hamiltonian as an approximation to the quantum Hamiltonian.

On a Bravais lattice and for the case with SU(2) spin rotation symmetry, solutions with normalized spins can always be constructed from the LTA minimum

[4] the antiferromagnet and its Klein dual on the bipartite honeycomb are of course exceptions as well.

eigenvalues[132]. For momenta q satisfying $q = -q$ there is a family of degenerate orders but even for arbitrary incommensurate momenta there are coplanar spiral solutions with normalized spins, with the first(second) spin component modulated by the real(imaginary) part of $\exp[iqr]$. However, when SU(2) spin rotation symmetry is broken such as by SOC, there may only be one low energy spin component and this approach can fail, requiring $q = -q$ to construct states with unit length normalized spins. On lattices with multiple sites per unit cell, the LTA may assign different lengths to sites in the unit cell, which again points to frustration, though if the spins have nearly the same length then we expect that ordering pattern to be robust[**?**]. Note that even when classical solution do exist, when the LTA identifies extensive ground state degeneracy or includes degenerate ground state configurations with vanishing ordered moment, it suggests quantum fluctuations will melt any magnetic order. In such cases determining the ground state requires a full quantum analysis. Thus while the Luttinger-Tisza approximation cannot characterize non-classical phases, it is a useful first approach for identifying features in the phase diagram.

The LTA phase diagrams are shown in Fig. 4.1. Here we discuss general features; see the Appendix for details. Stripy phases are found surrounding the FM-dual point in all of the lattices; they are exact ground states at $\eta{=}+1, \alpha{=}1/2$ even within the LTA. However, the kagome and hyperkagome lattices exhibit an interesting frustration: while spins are uniformly normalized at the SU(2) FM-dual point, away from $\alpha = 1/2$ the energy is minimized when spins within the unit cell are of different lengths. As it must by the Klein duality, this frustration is observed in the ferromagnet phase as well. Evidently for the kagome and hyperkagome, but not for the pyrochlore or the other lattices, even small SU(2) breaking within the ferromagnetic phase creates substantial frustration visible in the LTA.

At certain points in the phase diagram, all wavevectors in the BZ offer spin configurations with the same minimum energy, so that the lowest band is flat. While subextensive degeneracies occur generically at certain parameter points and are expected to be completely lifted by boundary conditions, such extensive degeneracies, marked by "Q" in Fig. 4.1, likely signify a new phase. What could the new phase be? There are only two Hamiltonians hosting LTA extensive degeneracies for which the quantum ground state is known: the honeycomb Kitaev model ($\alpha = \pm 1$) which is exactly soluble, hosting the Kitaev QSL with Majorana fermionic spinons; and the kagome Heisenberg antiferromagnet, which was recently found by DMRG simulations[213, 130] to host a QSL phase, consistent with a bosonic $\mathbb{Z}_2$ QSL[193]. The ground states of pyrochlore and hyperkagome Heisenberg antiferromagnets, which also have LTA flat bands, are not conclusively known but have been proposed to be plaquette or dimer valence bond solids (VBS) as well as various fractionalized QSLs[94, 152, 220, 147].

There are thus two conclusions to draw about the other Q points in Fig. 4.1. First, by the Klein duality, any lattice hosting a phase with no magnetic order in its AF Heisenberg model also has the same type of phase surrounding the $\eta{=}-1, \alpha{=}1/2$ point, with FM Heisenberg and AF Kitaev exchanges. For example, the recent dis-

covery of the kagome AF Heisenberg QSL then immediately yields the Klein dual of this QSL at the dual point; this Klein dual QSL will likely have distinct physical properties in its response to external fields. Second, by analogy with the known Q points mentioned above, we may guess that the pure Kitaev models on the hyperkagome also host a quantum phase with no magnetic order, either a VBS or a QSL.

It is especially encouraging that the LTA flat bands within the honeycomb and the hyperkagome pure Kitaev models arise via the same mechanism. Consider that LTA flat bands in the AF Heisenberg models occur due to the lattice specific band structure from a hopping model with π flux. For the pure Kitaev models $\alpha = \pm 1$, a given spin component such as S^z hops only on z-type bonds. As mentioned above, for the honeycomb and hyperkagome lattices, turning off y and x bonds splits the lattice into an extensive number of localized disconnected segments, as shown for the hyperkagome in Fig. 4.4. Localization in the disjointed clusters yields the flat bands. Moreover, unlike for the Heisenberg case where (in the relevant lattices we study) there are gapless excitations where the flat lowest band touches higher ones, for the Kitaev cases the disjointed clusters yield a band structure where all bands are completely flat and fully gapped, in the hyperkagome case also fourfold degenerate at each wavevector due to four clusters in the unit cell.

Returning to the survey of the LTA phase diagrams, we find other regions with strong frustrations. On the kagome and pyrochlore lattices, over wide regions of parameter space the LTA fails spectacularly: in the regimes labeled "frustrated", the unit cell in both lattices has two spins aligned antiparallel but with the remaining one (kagome) or two (pyrochlore) spins chosen to have exactly zero ordered moment by the LTA. Viewing the LTA as an enhancement of classical solutions which incorporates quantum fluctuations, we see that here the expected quantum fluctuations are sufficiently strong to eliminate some of the ordered moments, pointing to especially strong quantum frustration. A related regime on the fcc, a Bravais lattice, finds subextensive degeneracy involving incommensurate momenta, that would form spiral orders but with only one low energy spin component cannot achieve correctly normalized spins across the spiral.

Finally, on the hyperkagome the LTA finds two regimes with apparent magnetic order with unconventional spin configurations. Though in both cases the spins cross the unit cell are not chosen to have the same ordered moment, this is expected with such a large unit cell, and the LTA configurations should serve as good starting points for quantum Hamiltonian ground states, likely with quantum fluctuations greatly reducing the ordered moment. For η=+1 and $\alpha < 0$ we find that for z-type order, z-clusters all have the identical spin ordering "(up, down, up)", resulting in an AF state with a nonzero net magnetization which we thus term the "cluster-ferrimagnet". The Klein dual of this order, for large α at η=−1, has the same "(up, down, up)" pattern in each z-cluster except clusters are flipped on alternating planes, so there is zero net magnetization; we term it the "cluster-AF" state. These two Klein dual orders are shown in Fig. 4.7 and Fig. 4.8.

4.6 Searching for analogues of the Kitaev Majorana spin liquid beyond the honeycomb

All the lattices in Figure 4.3 except the honeycomb have coordination number larger than three, spoiling the Kitaev honeycomb spin liquid exact solution. However, similar Majorana QSL phases could still occur for the Kitaev Hamiltonians on the other lattices, only without an exact solution and with nonzero correlation length. Since it is generally highly difficult to determine whether the true ground state of a spin Hamiltonian forms a QSL, we will not attempt to answer this question. Instead, we will study possibilities for similar Majorana QSLs on the other lattices using an appropriate choice of mean field.

The exact solution of the Kitaev honeycomb model in terms of Majorana fermion operators is a specific case of a Schwinger fermion decomposition mean field, which becomes *exact* for this model[218, 102, 180]. To search for similar Majorana QSLs on the other lattices, we thus employ this mean field. Spins are decomposed into bilinears in four Majorana species $\chi^{0,1,2,3}$ as

$$S^a \to i\chi^0\chi^a \quad \text{with} \quad \{\chi^a, \chi^b\} = \delta^{a,b}. \tag{4.15}$$

This mapping is exact under the single fermion occupancy constraint $\chi_i^0\chi_i^1\chi_i^2\chi_i^3 = 1/4$. On the honeycomb lattice this constraint commutes with the pure Kitaev Hamiltonian, but that does not occur on the other lattices. The $\mathbb{Z}_2$ gauge freedom in defining the Majorana operators enables a choice of attaching gauge transformations to the physical symmetry operations, called a projective symmetry group (PSG)[210]; see the Appendix for details. The PSG of the Kitaev honeycomb model was previously studied[218] and determined to be flux-free, with (χ_1, χ_2, χ_3) transforming as a pseudovector and each bond permitting Majorana bilinear expectation values only for two Majoranas of the same species a, yielding a total of three mean field parameters:

$$u_\gamma^0 \equiv u_0, \;\; u_a^a \equiv u_a, \;\; u_a^{b\neq a} \equiv u_b \tag{4.16}$$

with

$$u_{\gamma[v]}^\alpha \equiv \langle i\chi_j^\alpha \chi_{j+v}^\alpha \rangle \tag{4.17}$$

where b is a bond. u_b is set to zero for the pure Kitaev model. The resulting mean field Hamiltonian is

$$\begin{aligned} H_{\text{MF}} &= -\tfrac{1}{2}\textstyle\sum_{i,v[i],\alpha} \text{sign}[v]\nu_{\gamma[v]}^\alpha i\chi_i^\alpha\chi_j^\alpha \\ \nu_\gamma^a &= \eta\left((1-|\alpha|) - 2\alpha\delta_\gamma^a\right)u_0 \\ \nu_\gamma^0 &= \textstyle\sum_a J_\gamma^a u_\gamma^a = \eta\left((2-2\alpha-2|\alpha|)u_b - 2\alpha u_a\right) \end{aligned} \tag{4.18}$$

where J_γ^a is the coupling of spin component a on a γ-bond, i is a site, $v[i]$ are the bonds of site i and sign$[v]$ is the orientation of the bond v within the PSG. This

orientation determines how operators on the bond transform under symmetries. On the honeycomb, bonds are oriented from sublattice A to B. The bond orientations used in the PSGs for the triangular and the kagome lattice are depicted in Ref. [193] (though that work dealt with bosonic QSLs, the bond orientation diagrams we take are the same). For the triangle, it is known as the zero flux PSG. For the kagome, this zero flux PSG is known as $\sqrt{3}\times\sqrt{3}$ or $Q_1 = -Q_2$. The PSG analysis for this type of mean field has not been successfully carried out on the 3D lattices; the pyrochlore does not appear to give a unique decomposition[201]. On the hyperkagome however one of the four spins in each tetrahedra is removed, so we can consistently choose the orientation $A \to B \to C \to A$ within a triangular face in Fig. 4.4, giving a unique PSG (given a choice of hyperkagome chirality[181]).

The mean field Hamiltonian H_{MF} is a free Majorana bilinear Hamiltonian, so its ground state is immediately known by computing its band structure. The qualitative properties of this band structure carry the primary information, though the band structure energy scales contain the unknown mean field parameters u. The parameters u can be determined self-consistently from the band structure by computing the Majorana propagator, as a Matsubara frequency integral of the inverse of the frequency-dependent Hamiltonian kernel. We have carried out the self consistency computation on the triangular and honeycomb lattice, using the Kitaev-type majorana flux-free PSG which is defined on these two lattices, and find that the mean fields evolve with α smoothly away from the Kitaev limit, with no first order transitions.

Regardless of the exact values of the mean field parameters, choosing the mean field to be analogous to the Kitaev honeycomb QSL already determines key properties of the resulting states on the various lattices. First, all the lattices except for the honeycomb possess cycles with an odd number of bonds, such as triangles; this immediately requires the Kitaev Majorana mean field to spontaneously break time reversal symmetry[215]. These time reversal broken spin liquids might not display typical characteristics of time-reversal broken states. For example, on the triangular lattice, even though time reversal as well as $2\pi/6$ rotation each independently flip the flux pattern in triangular faces, the combined operation of time reversal with $2\pi/6$ rotation is still preserved as a single symmetry operation, so the Hall conductance vanishes. Second, lattices with an odd number of sites per unit cell necessarily have a spinon Fermi surface; the even-unit-cell lattices of pyrochlore and hyperkagome may or may not host gapped spinons.

Third, certain qualitative features of the band structure are determined by the choice of mean fields, such as the consideration of only nearest neighbor bonds and the PSG. There are four Majorana fermion species per site; for a pure Kitaev Hamiltonian, $\chi^{1,2,3}$ have bands related to each other by the 120° SOC combined spin-spatial rotation, while χ^0 has a generally different dispersion. For the honeycomb model, χ^0 has a Majorana analogue of the Dirac cone, i.e. relativistic with zero mass, while $\chi^{1,2,3}$ all have completely flat bands separated from zero energy by a complete gap. The kagome lattice $\chi^{1,2,3}$ also has a flat band but it lies at zero energy i.e. at the

Fermi energy, yielding the Fermi surface which necessarily arises here. The flatness results from a localized unpaired Majorana mode on one of the three sites in each unit cell; but since the remaining two sites form a line spanning the lattice, they disperse and the other bands are not flat, touching zero energy along lines in a quasi-1D spectrum. For the pyrochlore even qualitative statements cannot be currently made, since as mentioned above, there is no special choice of minimal flux PSG. On the hyperkagome with bond orientations as described above, χ^0 has some gapless subextensively degenerate modes (such as from Γ to M); but $\chi^{1,2,3}$, like for the honeycomb, have completely flat bands. These arise, as previously mentioned, because both the honeycomb and the hyperkagome fragment into extensively many disconnected clusters when only bonds of a single Kitaev label are kept. However, while the honeycomb clusters have an even number of sites and hence can form two fully gapped bands, separated from zero energy, the hyperkagome clusters have an odd (three) number of sites; each cluster always has one energy band at zero energy and hence $\chi^{1,2,3}$ are gapless.

4.7 Outlook

On the honeycomb lattice, the roles of the SU(2)-symmetric Heisenberg coupling and the SOC Kitaev coupling are distinct and clear: Heisenberg exchange yields magnetic order, Kitaev exchange yields the exactly solvable QSL phase. The natural interpolation between the two limits, that would occur if the couplings arise in iridium oxide compounds, is consistent with this framework: the intermediate region simply holds more magnetic order. However, as we have discussed above, generalizations of the Kitaev coupling naturally arise in iridium structures and other geometries of edge-sharing octahedra on many other lattices, motivating the study of the phase diagrams of Eq. 5.1 on these various 2D and 3D lattices. Beyond the honeycomb, the roles of the two exchanges begin to break down.

The effect of lattice geometry on the "frustration" of a lattice is quite different for the two terms; the Hamiltonian and the lattice determine the frustration together, not independently. More surprisingly, even in cases when the Heisenberg Hamiltonian appears highly frustrating, interpolating between the AF Heisenberg and the Kitaev limits, we find a phase which occurs on *all* the lattices and which is exact and fluctuation free at a certain parameter point. Subtle interplays of different magnetic couplings, rather than a monotonic "frustration" measure, seem to be at play. The intermediate stripy phase is exact by virtue of being related to the ferromagnet, through a duality that emerges through the SOC on the t_{2g} orbitals microscopically generating the Hamiltonian.

The Klein group structure of the mapping between Hamiltonians (a duality) is in some sense highly specific to these quantum chemistry considerations but in another sense, as a mathematical object $\mathbb{Z}_2 \times \mathbb{Z}_2$, quite universal. The duality transformation

it generates is interesting here for another reason: while most dualities fix a single self-dual Hamiltonian and map the two regimes on either side of that point, with qualitatively different features, to each other, the Klein duality is different. It admits two self-dual Hamiltonians, which seem to generally lie in the interior of a phase. And it acts in a complicated way on spin and spatial indices, making its action as a $\mathbb{Z}_2$ symmetry operation highly nontrivial.

Regarding possible experimental significance of Hamiltonians arising from strong SOC, it is important to observe that the Kitaev couplings naturally occur in a manner more subtle and constraining than naive symmetry considerations would suggest: for example, Kitaev interactions can arise for iridium ions on the fcc but not on the simple cubic. Computations of the quantum phase diagrams on the various lattices, especially the pyrochlore and hyperkagome, will pave the way towards predictions and comparisons with experimental results.

4.8 Technical details on the Luttinger-Tisza Approximation phase diagrams for the various lattices

Here we give the results of the Luttinger-Tisza Approximation (LTA) analyses in more detail. The classical Kitaev-Heisenberg model on the triangular lattice has been recently studied[191], and the phase diagram for the honeycomb is already known[106]; we begin by reviewing the results for the triangular and honeycomb lattices for the sake of direct comparison with the other lattices. Note that on all the lattices, the pure Kitaev points $\alpha = \pm 1$ always host degeneracies in the BZ; except where noted below, these are just subextensive degeneracies, which we expect will be lifted by small perturbations or by boundary conditions for a finite system.

Triangular lattice: *AFM Heisenberg,* $\eta = +1$. The pure Heisenberg antiferromagnet $\alpha = 0$ hosts ordering at wavevector K (BZ corner), corresponding to 120° order with a tripled unit cell. This ordering can also be seen by explicitly working with the enlarged unit cell. For $0 < \alpha < 1/5$ the ordering wavevector is incommensurate as it migrates from K to M (BZ edge midpoint). For $-1 < \alpha < 0$ the ordering wavevector is also incommensurate, moving from K in the direction of Γ. Only one spin component has minimum energy for a given momentum here, preventing the construction of any order with unit length spins such as the usual coplanar spiral. The antiferromagnetic Heisenberg limit 120° order actually has point topological defects (vortices), with Z_2 character; the recent triangular lattice classical model study included classical Monte Carlo computations[191] which found they may be stabilized into a vortex lattice in this incommensurate ordering phase. Finally, for $1/5 < \alpha < 1$, we find stripy order at wavevector M. *FM Heisenberg,* $\eta = -1$. For $-1 < \alpha < 3/7$ there is ferromagnetic order. For $3/7 < \alpha < 1$ continues the phase of incommensurate

ordering wavevector between Γ and K from $\eta = +1$.

Honeycomb lattice: For pure Kitaev exchange $\alpha = \pm 1$ there are extensive degeneracies. *AFM Heisenberg,* $\eta = +1$. For $-1 < \alpha < 1/3$, simple Neel order (wavevector Γ) is stabilized, as the honeycomb is bipartite. For $1/3 < \alpha < 1$ there is stripy order at M. *FM Heisenberg,* $\eta = -1$. Because we have a quadratic spin Hamiltonian and a bipartite lattice, this regime can be mapped to $\eta = +1$ by flipping all spin components on one of the two sublattices. For $-1 < \alpha < 1/3$ there is a ferromagnet, for $1/3 < \alpha < 1$ there is zigzag order at M.

Kagome lattice. *AFM Heisenberg,* $\eta = +1$. The $\alpha = 0$ Heisenberg antiferromagnet hosts extensive degeneracy. For $0 < \alpha < 1$ there is stripy order (wavevector Γ), here ferrimagnetic. But while spins are uniformly normalized at the SU(2) point $\alpha = 1/2$, away from $\alpha = 1/2$ the energy is minimized when spins within the unit cell are of different lengths, suggesting the ordering becomes increasingly frustrated. For example near $\alpha = 1/2$, if two of the spins within the unit cell are chosen to be normalized with magnitude $+1$, the third has magnitude $\frac{1-3\alpha+\sqrt{9+\alpha(-22+17\alpha)}}{2(-1+\alpha)}$, or roughly $-2+2\alpha$. For $-1 < \alpha < 0$ the LT method fails: two spins within a triangle plaquette align antiparallel along the axis of their bond label γ, but the third is so frustrated that its magnitude is set to exactly zero, also giving spurious subextensive line degeneracies from Γ to M. *FM Heisenberg,* $\eta = -1$. $\alpha = 0.5$, the Klein rotation of the Heisenberg antiferromagnet, again hosts extensive degeneracy. The ferromagnet exists over a wide range $-1 < \alpha < 1/2$ but with the same strong frustration as for the stripy phase: away from the Heisenberg limit $\alpha = 0$, the energy is minimized by having spins of different lengths within the unit cell. For example, at $\alpha = -2/5$, the unit cell has all spins aligned but with one spin at $2/3$ the magnitude of the others. The regime $0.5 < \alpha < 1$ continues the antiferromagnetic-Kitaev regime of $\eta = +1$, with two oppositely aligned spins and the third spuriously set to zero.

Face centered cubic (fcc) lattice. *AFM Heisenberg,* $\eta = +1$. $0 < \alpha < 1$ hosts the 3D-stripy order, antiferromagnetic along a cubic axis, which for the fcc BZ is at wavevector X (center of one of three square faces of the BZ). For X_z order, stripy-ordered spins align along S^z.s For $-1 < \alpha < 0$, there is a line degeneracy from X to W (i.e. along diagonals of a square face of the BZ). The square face lies at some Euclidean direction, say $\hat{z}$. The two perpendicular spin components (here S^x and S^y) participate at X, with one of the two stabilized as the wavevector moves towards a corner W. The set of minimal energy spin configurations, with normalized spins, therefore contains the wavevector X stripy order though with spins uniformly rotated to the S^x, S^y plane. The orders at generic degenerate $q = (1-r)X + rW$ would usually form a spiral but here only have minimized energy for one of the three spin components, so they cannot stabilize any order with unit length spins. For the constrained classical Hamiltonian and the quantum Hamiltonian, the higher energy spin component(s) are likely to be mixed into the ground state, so it appears the LT method hints at spiral order in this regime. *FM Heisenberg,* $\eta = -1$. The ferromagnet

is stable for $-1 < \alpha < 1/2$. The region $1/2 < \alpha < 1$ is part of the spiral-like phase of $\eta = +1$, forming a single phase stabilized by antiferromagnetic Kitaev interactions regardless of the sign or presence of Heisenberg exchange.

Pyrochlore lattice. *AFM Heisenberg,* $\eta = +1$. The $\alpha = 0$ Heisenberg antiferromagnet hosts extensive degeneracy. Stripy order (wavevector Γ) is stable for $0 < \alpha < 1$. For $-1 < \alpha < 0$ the LT method fails: the preferred states have two of the four spins in the unit cell pointing antiparallel to each other, with the other two spuriously set to zero. The (subextensive) degeneracy extends across planes in the BZ, specifically the high symmetry planes containing the gamma point and the centers of (both hexagonal and square) faces. *FM Heisenberg,* $\eta = -1$. $\alpha = 1/2$, the Klein rotation of the Heisenberg antiferromagnet, again hosts extensive degeneracy. The ferromagnet is stable for $-1 < \alpha < 1/2$. Strong antiferromagnetic Kitaev exchange at $1/2 < \alpha < 1$ continues the $\eta = +1, \alpha < 0$ regime of plane degeneracies and two missing spins. There are subextensive degeneracies at $\alpha = \pm 1$. Note that unlike the kagome case, here even away from SU(2) points, the ferromagnet and stripy regimes have all spins of unit length.

Hyperkagome lattice: *AFM Heisenberg,* $\eta = +1$. The $\alpha = 0$ Heisenberg antiferromagnet hosts extensive degeneracy, as do the two pure Kitaev limits $\alpha = \pm 1$. Stripy order (wavevector Γ) nominally exists for $0 < \alpha < 1$, but with the same strong frustrations (except for the SU(2) point $\alpha = 1/2$) as for the kagome. For say $\hat{z}$ ordering, the four spins in the middle of their respective z-type clusters are chosen smaller(larger) than unity for $\alpha < 1/2 (\alpha > 1/2)$. The region with antiferromagnetic Kitaev exchange $-1 < \alpha < 0$ hosts a magnetically ordered phase which we term the *cluster-ferrimagnet*. In the z-type cluster-ferrimagnet, z-clusters all have the identical spin ordering "(up, down, up)", resulting in a state with a nonzero net magnetization. The LTA gives the spins in the middle of each cluster a somewhat larger, unphysical, normalization, but this magnetic pattern is likely to be robust. *FM Heisenberg,* $\eta = -1$. $\alpha = 1/2$, the Klein rotation of the Heisenberg antiferromagnet, hosts extensive degeneracy like in the pyrochlore. (As already mentioned, the $\alpha = \pm 1$ points do as well.) The ferromagnet over $-1 < \alpha < 1/2$ again has different length spins within the unit cell, except for the SU(2) Heisenberg point $\alpha = 0$. For $0.5 < \alpha < 1$ there is the *cluster-antiferromagnet*, which is the Klein dual of the cluster-ferrimagnet. The two orders appear to be separated by the likely quantum phase, associated with extensive degeneracy, at $\eta\alpha = +1$. In this order, like for the cluster-ferrimagnet, the middle spin in each cluster points opposite to the other two and prefers to have a larger magnitude. Unlike the cluster-ferrimagnet, the cluster-antiferromagnet has no net magnetization since a pair of clusters is flipped relative to the other pair, as can be seen by the Klein duality.

4.9 Technical details on mean fields and the projective symmetry group (PSG)

The choice of partons (here Majorana fermions) with which to decompose the spin is not unique; there is actually full gauge SU(2) freedom in defining the parton operators. When parton mean field hopping and pairing terms gain nonzero expectation values, the freedom is partially lost so that the mean field Hamiltonian is only invariant under a global $\mathbb{Z}_2$ transformation. This is known as the invariant gauge group (IGG). Beyond the mean field level, the partons couple to a dynamical gauge field, with the gauge group of the IGG. Hence when IGG$= \mathbb{Z}_2$, the spin liquid is known as a $\mathbb{Z}_2$ spin liquid.

The mean field ansatz may be chosen to preserve as many of the symmetries of the original Hamiltonian as possible, say a set of symmetries S. While the mean field ansatz (the collection of mean field amplitudes on the lattice) may not be immediately invariant under a symmetry in S, we may choose to always attach an SU(2) gauge transformation to the symmetry, such that the mean field ansatz is invariant under their combination. Relations of S (operators that multiply to the identity) must have associated gauge transformations that multiply to an element of the IGG, ie a global 1 or -1 sign in the case where IGG$= \mathbb{Z}_2$. This collection of attached real and gauge symmetry operations that leave the mean field Hamiltonian invariant is known as the projective symmetry group (PSG). It is a necessary part of the description of any mean field ansatz, and distinguishes different spin liquid phases even when they have the same gauge group.

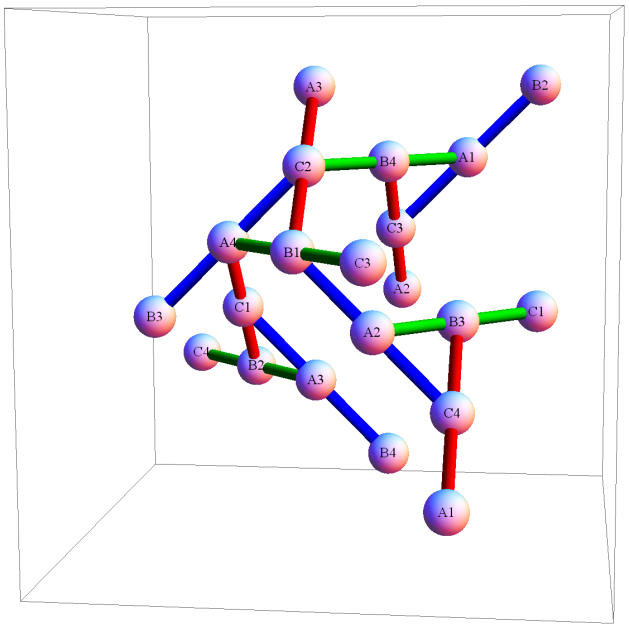

Figure 4.4: **H**yperkagome unit cell and decomposition into Kitaev clusters. A symmetric depiction of the hyperkagome structure, highlighting the four disjointed three-site clusters which split up the unit cell for a given Kitaev bond label (red,green,blue). The fact that the lattice fragments into these disjointed clusters for a given Kitaev bond type has substantial repercussions, as described in the text. The four clusters of a given type appear in two parallel-orientation pairs which are perpendicular to each other (with different shading). The unit cell is composed of the 12 sites participating in the four drawn triangular faces, as well as all 24 drawn bonds. We label the 12 sites by a letter A,B,C as in Ref. [151] so that A spins lie on midpoints of type-A (here blue) clusters, etc; and by a number 1–4 (chosen to not repeat within a triangle face or cluster). The camera angle, i.e. the vector pointing into the page, is just slightly off (up-right) of a Cartesian (here also Bravais) axis; for $Na_4Ir_3O_8$ it is the vector from an iridium ion to a neighboring coordinating oxygen.

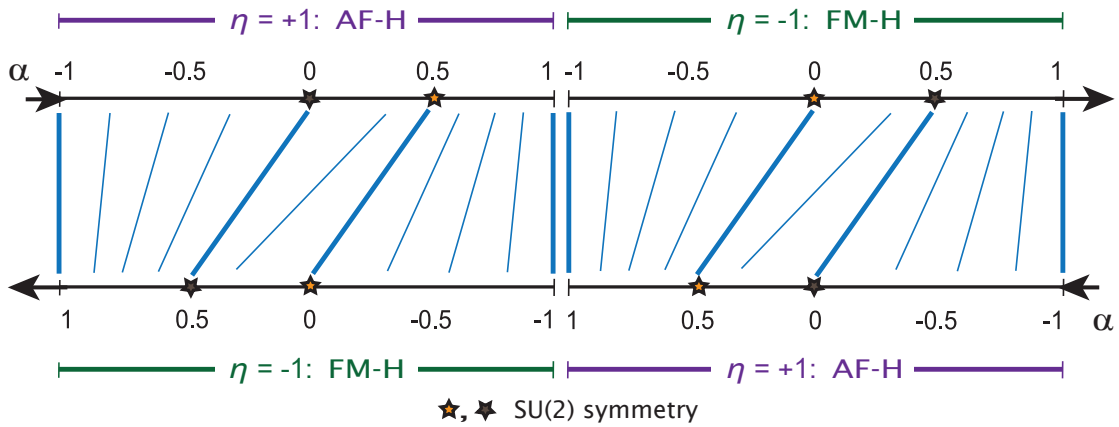

Figure 4.5: **A**ction of the Klein duality on the Kitaev-Heisenberg Hamiltonian. The η, α parameters on the top line (oriented left to right) of the Hamiltonian Eq. 5.1 map according to the blue lines to η, α parameters on the bottom line (oriented right to left) in the Klein-dual Hamiltonian. Thick blue lines map the points shown exactly, thin blue lines are a qualitative sketch. Note that the right and left edges of the figure are identified, forming a ring. Both pure Kitaev Hamiltonians ($\alpha = \pm 1$) are *self-dual*, mapping to themselves. The points at $\alpha = 1/2$ and $\eta = +1$, $\eta = -1$ are dual to the SU(2) symmetric FM-Heisenberg and AF-Heisenberg points (yellow and brown stars) respectively, with the FM dual point hosting the exactly soluble *stripy* phases on all lattices in Fig. 4.3.

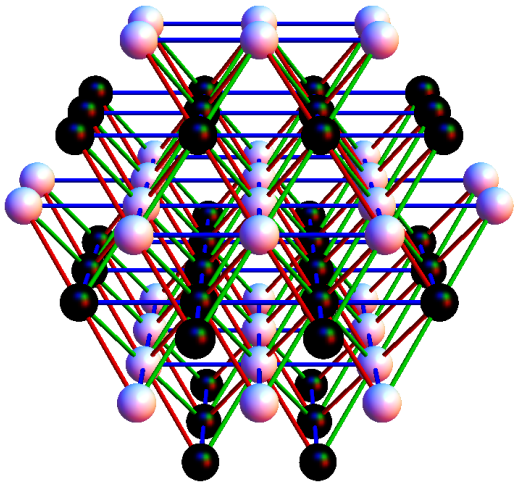

(a) 3D-stripy order on the face centered cubic (fcc) lattice.

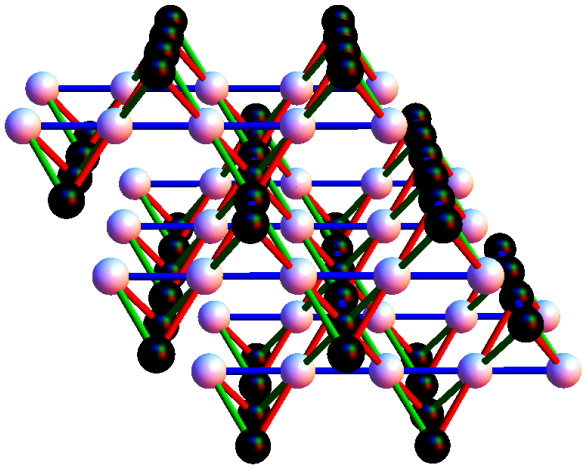

(b) 3D-stripy order on the pyrochlore lattice.

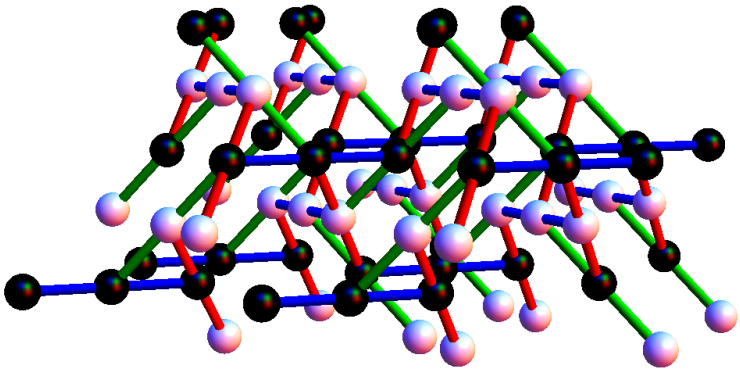

(c) 3D-stripy order on the hyperkagome lattice.

Figure 4.6: **3**D-Stripy orders on the fcc, pyrochlore and hyperkagome lattices. Black(white) spheres represent up(down) spins. Bonds are colored red, green, and blue according to the Kitaev label. The ordering pattern is of alternating planes, here normal to $\hat{z}$; z-type bonds (blue), i.e. those within the planes, connect spins of the same orientation. On the pyrochlore and hyperkagome, planes are broken up into uniformly oriented chains, with chains in spin-up planes oriented perpendicularly to chains on spin-down planes. On the hyperkagome, the chains are further broken into the linear three site clusters shown in Fig. 4.4. These stripy orders are exact at $\eta{=}{+}1, \alpha{=}1/2$, being Klein-duals of the ferromagnet.

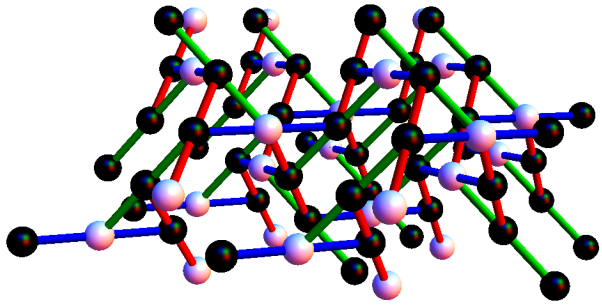

Figure 4.7: **M**agentic order of the cluster-ferrimagnet state on the hyperkagome. Black(white) spheres are up(down) spins; bonds are colored according to Kitaev label. Here shown for $\hat{z}$ ordering, notice that the z-type clusters (blue), lying in planes normal to $\hat{z}$, all have "(up, down, up)" spin configurations. This configuration has *nonzero* net magnetization. Note that the cluster-ferrimagnet order is Klein-dual to the cluster-AF order.

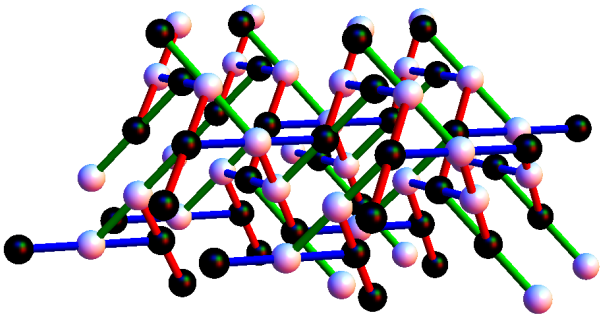

Figure 4.8: **M**agentic order of the cluster-AF state on the hyperkagome. Black(white) spheres are up(down) spins; bonds are colored according to Kitaev label. Here shown for $\hat{z}$ ordering, notice that the z-type clusters (blue), lying in planes normal to $\hat{z}$, have "(up, down, up)" spin configurations on even-numbered planes, and the opposite "(down, up, down)" spin configurations on odd-numbered planes. This configuration has *zero* net magnetization. Note that the cluster-AF order is Klein-dual to the cluster-ferrimagnet order.

Chapter 5

Realization of a three-dimensional spin-anisotropic harmonic honeycomb iridate

5.1 Synthesis and characterization of an iridate with a new 3D lattice

This chapter turns to experiment, presenting the characterization and early measurements of a remarkable new 3D material, related to the theoretical discussion of the previous chapter.

This chapter is composed of excerpts from the related publication, Nature Communications 5, 4203 (2014). The full author list of the publication is as follows: K. A. Modic, Tess E. Smidt, Itamar Kimchi, Nicholas P. Breznay, Alun Biffin, Sungkyun Choi, Roger D. Johnson, Radu Coldea, Pilanda Watkins-Curry, Gregory T. McCandless, Julia Y. Chan, Felipe Gandara, Z. Islam, Ashvin Vishwanath, Arkady Shekhter, Ross D. McDonald and James G. Analytis.

Here we present some of the relevant experimental discussion from the publication, together with some of the theoretical synthesis. The reader is invited to turn to the published version of the manuscript for the full information on the experimental methods, results and analysis.

Spin and orbital quantum numbers play a key role in the physics of Mott insulators, but in most systems they are connected only indirectly — via the Pauli exclusion principle and the Coulomb interaction. Iridium-based oxides (iridates) introduce strong spin-orbit coupling directly, such that the Mott physics has a strong orbital character. In the layered honeycomb iridates this is thought to generate highly spin-anisotropic magnetic interactions, coupling the spin orientation to a given spatial direction of exchange and leading to strongly frustrated magnetism. Here we report a new iridate structure that has the same local connectivity as the layered honeycomb

and exhibits striking evidence for highly spin-anisotropic exchange. The basic structural units of this material suggest that a new family of three-dimensional structures could exist, the 'harmonic honeycomb' iridates, of which the present compound is the first example.

5.2 Introduction

Quantum spin systems are characterized by small moments where the spin orientation is decoupled from the crystal lattice, in contrast to Ising-like spin systems that often apply to higher spin states. In the Heisenberg model describing spin-isotropic exchange between neigboring spins, spatial anisotropies of the exchange suppress long-range order [**?**], but do not lead to anisotropy of the magnetic susceptibility. Striking examples of this are quasi-1D and -2D systems where the exchange differs by orders of magnitude for neighbors along distinct crystallographic directions [**?**, **?**]. The spin-orbit interaction introduces magnetic anisotropy by coupling the spin to the symmetry of the local orbital environment. Although in spin-$^1/_2$ systems the crystal field does not introduce single-ion anisotropy (due to Kramer's protection of the spin-$^1/_2$ doublet), it can — via spin-orbit — introduce spin-anisotropies in the g-factor and in the exchange interactions. The strength of the spin-orbit coupling varies by orders of magnitude between the $3d$ and $5d$ transition metals. In the former, quenching of the orbital moment decouples the orbital wavefunction from the spin, giving a g-factor anisotropy that is typically small and an even smaller spin-anisotropy. For example, spin-$^1/_2$ copper in a tetragonal crystal field has a g-factor anisotropy of order 10%, whereas the spin-anisotropy of exchange is of the order of 1% [**?**].

The stronger spin-orbit coupling of the $5d$ transition metals is known to give rise to larger magnetic anisotropies. In materials with edge-shared IrO_6 octahedra, spin-anisotropy of the exchange between neighboring effective spin-$^1/_2$ states is enhanced by the interference of the two exchange paths across the planar Ir-O_2-Ir bond. Jackeli and Khaliullin (JK) suggested that in the honeycomb iridates this may lead to extreme spin-anisotropy of the exchange coupling, where in the limiting case, the only non-vanishing interaction is for the spin component normal to the Ir-O_2-Ir plane [129, 106, **?**]. In the honeycomb lattice, such an interaction couples different orthogonal spin components for the three nearest neighbors; no single exchange direction can be simultaneously satisfied, leading to strong frustration. It is the possibility of engineering spin-anisotropy coupled to spatial exchange pathways that has spurred intense scientific research, particularly in connection to the search for quantum spin-liquids [**?**, 129, 106, **?**]. However, whether the spin-anisotropic exchange interaction that is coupled to the Ir-O_2-Ir bonding plane is realized in such materials remains an intense subject of scientific debate [198, **?**, **?**, **?**], highlighting the need for the discovery of new materials with related structures and strongly anisotropic exchange interactions.

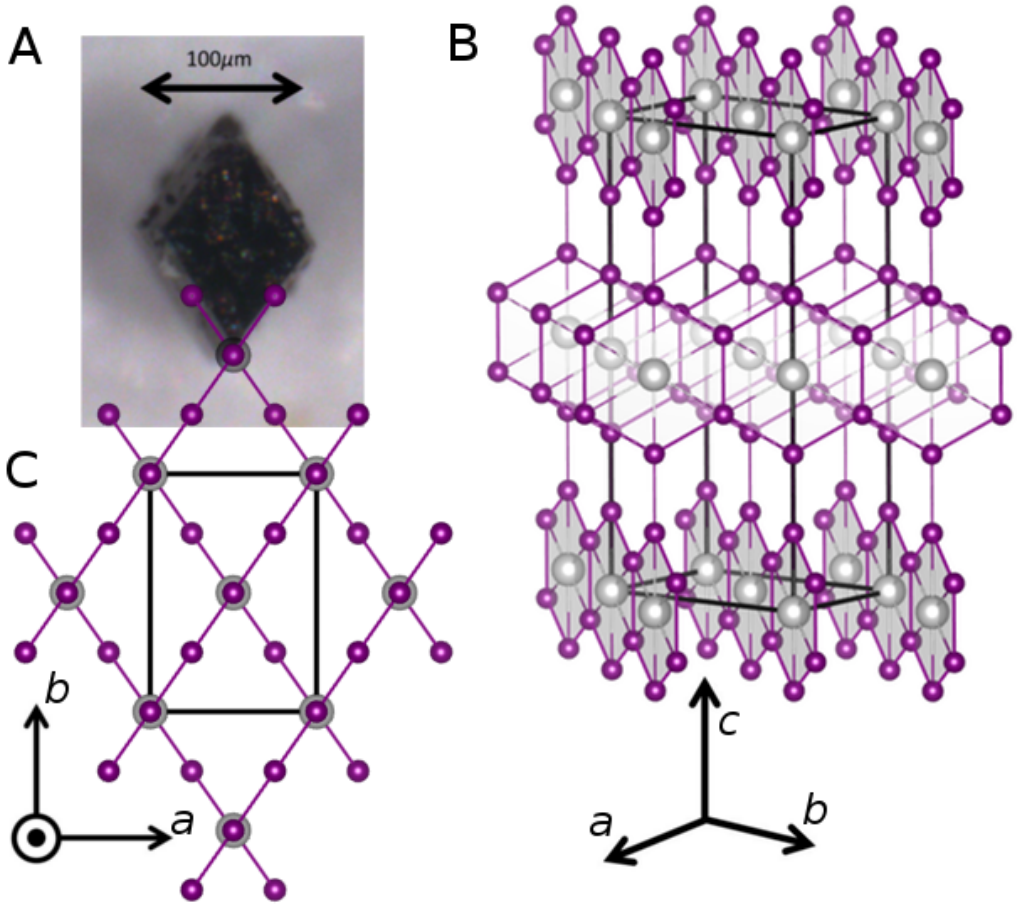

Figure 5.1: **S**ingle crystal of $^{\mathcal{H}}\langle 1\rangle$-$Li_2IrO_3$ and the Ir lattice structure. Figure reproduced from published version, Nat. Comm. 5, 4203 (2014). (A) Single crystal oriented to be parallel to the crystallographic axes shown in (C), (B) 3D view and (C) projection in the *ab* plane. In (B) gray shading emphasizes the Ir (purple balls) honeycomb rows that run parallel to the $\boldsymbol{a} \pm \boldsymbol{b}$ diagonals, alternating upon moving along the *c*-axis. For simplicity only Li ions (grey balls) located in the center of Ir honeycombs are shown. In (B) and (C) the rectangular box indicates the unit cell. Comparing (A) and (C) we note that the $\sim 70^\circ$ angle between honeycomb rows is evident in the crystalline morphology.

We have synthesized single crystals of a new polytype of Li_2IrO_3 in which we reveal the effect of the spin-anisotropy of exchange from the temperature dependence of the anisotropic magnetic susceptibility.

5.3 Results

5.3.1 Crystal structure

Single crystals of Li_2IrO_3 were synthesized as described in Methods. As shown in Figure 5.1A, the crystals are clearly faceted and typically around $100\times100\times200\mu m^3$ in size. In contrast to the monoclinic structure of the layered iridate, we find that these materials are orthorhombic and belong to the non-symmorphic space group $Cccm$, with lattice parameters $a = 5.9119(3)$ Å, $b = 8.4461(5)$ Å, $c = 17.8363(10)$ Å (see Supplementary Discussion for details of the crystallography). The structure (shown in Figure 5.1B and C) contains two interlaced honeycomb planes, the orientation of which alternate along the c axis. The x-ray refinement (see original published manuscript) is consistent with fully stoichiometric Li_2IrO_3. In this case the Ir oxidation state is Ir^{4+} ($5d^5$), fixing the effective Ir local moment $J_{\text{eff}} = 1/2$, which is consistent with the magnetic properties of our crystals (see Figure 5.2). In addition, highly-sensitive single-crystal susceptibility and torque measurements (see below) observe sharp anomalies at the transition to magnetic order, with no measurable variability in this transition temperature between many crystals measured, indicating that the observed magnetic order is well-formed and intrinsic to the crystals. This suggests that if present, Li vacancy disorder is small, because such vacancies will to lead non-magnetic Ir^{5+} $5d^4$[**?**], whose presence is expected to give rise to spin-glass behavior [**?**] which we do not observe. Taken together, our experiments indicate that our crystals are representative of the high-purity, stoichiometric limit. We denote the crystal structure ${}^{\mathcal{H}}\langle1\rangle$-$Li_2IrO_3$, where ${}^{\mathcal{H}}\langle1\rangle$ refers to the single, complete $\mathcal{H}$oneycomb row.

5.3.2 Anisotropy of Magnetic Suseptibility

As can be seen in Figure 5.2, the raw magnetic susceptibility shows a magnetic anomaly at 38 K, which is consistent with long range magnetic ordering.

The striking reordering of the principal components of susceptibility revealed in torque and SQUID magnetometry, is associated with a strong deviation from Curie-Weiss behavior as the temperature is lowered. This is in stark contrast to spin-isotropic Heisenberg exchange systems where the low temperature susceptibility reflects the g-factor anisotropy observed at high temperatures, even in the presence of spatially-anisotropic exchange [**?**]. The change of sign of the b-c anisotropy arises because χ_b softens, becoming an order of magnitude greater than χ_a and $\sim 5\times\chi_c$ (Figure

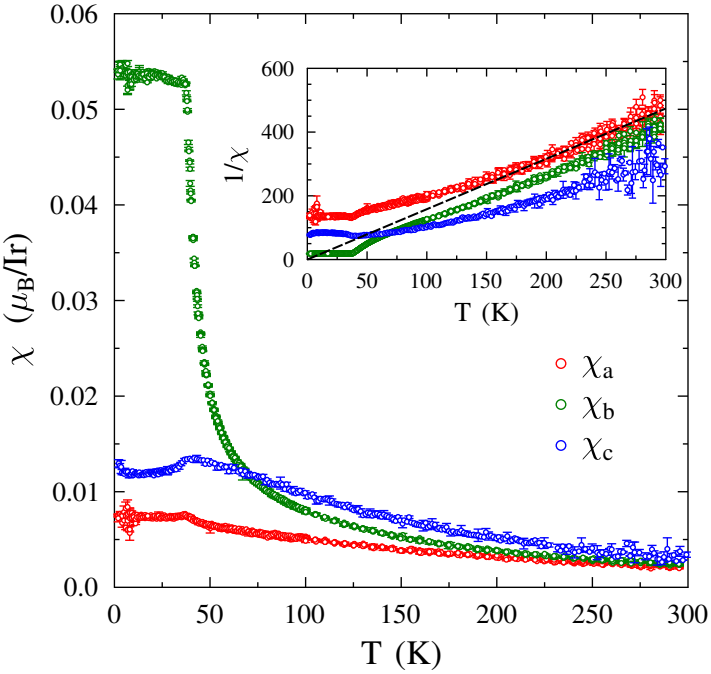

Figure 5.2: **T**he temperature dependence of the single-crystal magnetic susceptibility along the three principal crystalline directions. Figure reproduced from published version, Nat. Comm. 5, 4203 (2014). The inset shows $1/\chi$ for all three axes χ_a, χ_b, and χ_c. The dashed line indicates the slope of the inverse Curie-Weiss susceptibility for a paramagnet with effective moment of $\mu_{eff} = 1.6\mu_B$, close to that expected of an Ir $J_{eff} = 1/2$ state if g-factor anisotropy is ignored. All three components of susceptibility show strong deviation from Curie-Weiss behavior as a function of temperature.

5.2 and **??**B). As a result, the susceptibility cannot be parameterized by a Curie-Weiss temperature: the linear extrapolation of all three components of inverse susceptibility to the temperature axis depends strongly upon the temperature range considered. Between 50–150 K the extrapolation of all three components of inverse susceptibility is negative, consistent with the absence of net moment in the ordered state. However, at higher temperatures (200–300 K) the inverse susceptibilities $1/\chi_b, 1/\chi_c$ extrapolate to positive temperature intercepts (see Figure 5.2) indicating a ferromagnetic component to the interactions. Above 200 K, $1/\chi$ the Curie-Weiss slope gives $\mu_{eff} \approx 1.6\mu_B$, consistent with a $J_{eff} = 1/2$ magnetism.

The observed ten fold increase in χ_b cannot be driven by the g-factor of the local iridium environment, whose geometric constraints are temperature independent (see Supplementary Discussion). The temperature dependence of χ_b must therefore

arise from spin-anisotropic exchange. We note that all the c-axis bonds have the Ir-O_2-Ir plane normal to the b-axis, whether they preserve or rotate between the two honeycomb orientations. This is the only Ir-O_2-Ir plane that is normal to a crystallographic axis. This coupling of the spin-anisotropy to the structure, provides evidence for spin-anisotropic exchange across the c-axis links, and by extension should be present in all Ir-O_2-Ir exchange paths. This may arise from the interfering exchange mechanism suggested by Jackelli-Khaliullin in the context of the Kitaev model (see discussion below).

To see how lattice anisotropy can influence magnetic anisotropy, consider the Kitaev term, a coupling on an Ir-Ir bond between the spin components γ set by the normal vector $\hat{\gamma}$ to the Ir-O_2-Ir plane of the bond (see the appendix 5.5 for details). Not all Ir-Ir bonds are symmetry-equivalent; the c-type bonds (along $\hat{c}$) are distinguished by the crystal symmetries from the remaining "h-type" Ir-Ir bonds. Putting aside further distinctions within the c-type bonds, this suggests a possible model Hamiltonian consisting of nearest neighbor Kitaev (K) and Heisenberg (J) couplings whose strengths on the symmetry-distinguished c-type bonds (K_c, J_c) is allowed to differ from those on the remaining Ir-Ir bonds (K_h, J_h),

$$H_{\mathrm{KH}} = \sum_{c-\mathrm{bond}\langle ij\rangle} \left(K_c S_i^{\gamma_{ij}} S_j^{\gamma_{ij}} + J_c \vec{S}_i \cdot \vec{S}_j \right) + \sum_{h-\mathrm{bond}\langle ij\rangle} \left(K_h S_i^{\gamma_{ij}} S_j^{\gamma_{ij}} + J_h \vec{S}_i \cdot \vec{S}_j \right). \quad (5.1)$$

The key fact as mentioned above is that the spin component γ_{ij} on c-type bonds is $\gamma = b$, coupling $S_i^b S_j^b$ on this special bond. We can thus attempt to fit the b-axis anisotropy observed in magnetic susceptibility using this model Hamiltonian, supplamented only by weakly-anisotropic g-factors. The resulting fit, treating the model Hamiltonian by classical mean field theory, is shown in Figure 5.3 and suggests that strong Kitaev exchange can capture the observed anisotropy.

5.4 Discussion

There is a very interesting connection between the layered honeycomb Li_2IrO_3 and the polytype studied here. The ${}^{\mathcal{H}}\langle 1\rangle$-$Li_2IrO_3$ is distinguished by its c-axis bond, which either preserves or rotates away from a given honeycomb plane (see Figure 5.4A and Supplementary Figure 7); in the case that all the bonds preserve the same plane, the resulting structure is the layered honeycomb system. Further polytypes can be envisioned by tuning the c-axis extent of the honeycomb plane before switching to the other orientation (see Figure 5.4B). We denote each polytype ${}^{\mathcal{H}}\langle N\rangle$-$Li_2IrO_3$, where ${}^{\mathcal{H}}\langle N\rangle$ refers to the number of complete honeycomb rows (see Figure 5.4B and Supplementary Figure 8), and the family as the "harmonic"-honeycombs, so named to invoke the periodic connection between members. The layered compound, ${}^{\mathcal{H}}\langle\infty\rangle$-$Li_2IrO_3$ [**?**] and the hypothetical hyper-honeycomb structure, ${}^{\mathcal{H}}\langle 0\rangle$-$Li_2IrO_3$ [**?**] are the end members of this family (see also SI IV). The edge-sharing geometry of the

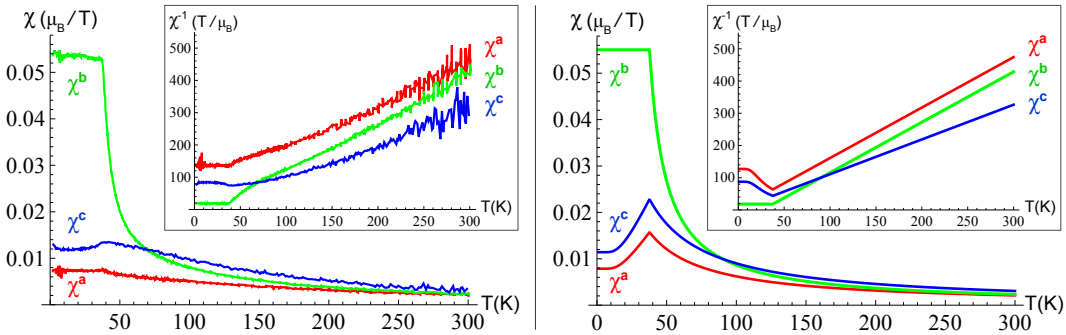

Figure 5.3: Fitting magnetic susceptibility with a model Kitaev-Heisenberg Hamiltonian incorporating lattice symmetries. The susceptibility along the crystallographic a, b, c axes measured on a single crystal (left figure) can be compared to a mean field treatment of the minimal model Hamiltonian Eq. 5.1 with particular parameters (right figure); here $K_c = -17, K_h = -7, J_c = 6, J_h = 1$ meV, with g-factors $g^a = g^b = 1.95, g^c = 2.35$. Insets show inverse susceptibility, enabling comparison at low as well as high temperatures. Large Kitaev couplings are required for a good fit.

octahedra preserves the essential ingredients of the Kitaev model and this is universal for this family of polytypes. Each structure is a material candidate for the realization of a 3D spin liquid in the pure Kitaev limit (see Supplementary Discussion and for ${}^{\mathcal{H}}\langle 0\rangle$-$Li_2IrO_3$ see Refs. [?, ?, ?]).

Finally, we speculate on the consequences and feasibility of making other members of the ${}^{\mathcal{H}}\langle N\rangle$-$Li_2IrO_3$ family. Both the layered ${}^{\mathcal{H}}\langle\infty\rangle$-$Li_2IrO_3$ and the ${}^{\mathcal{H}}\langle 1\rangle$-$Li_2IrO_3$ are stable structures, implying that intermediate members may be possible under appropriate synthesis conditions. The building blocks shown in Figure 5.4A connect each member of the harmonic honeycomb series in a manner that is analogous to how corner sharing octahedra connect the Ruddlesden-Popper (RP) series. Indeed, despite the fact that members of the RP family are locally identical in structure, they exhibit a rich variety of exotic electronic states; including superconductivity and ferromagnetism in the ruthenates [?, ?], multiferroic behavior in the titanates [?], collosal magnetoresistance in the manganites [?] and high temperature superconductivity in the cuprates [?]. The harmonic honeycomb family is a honeycomb analogue of the RP series, and its successful synthesis could similarly create a new frontier in the exploration of strongly spin-orbit coupled Mott insulators.

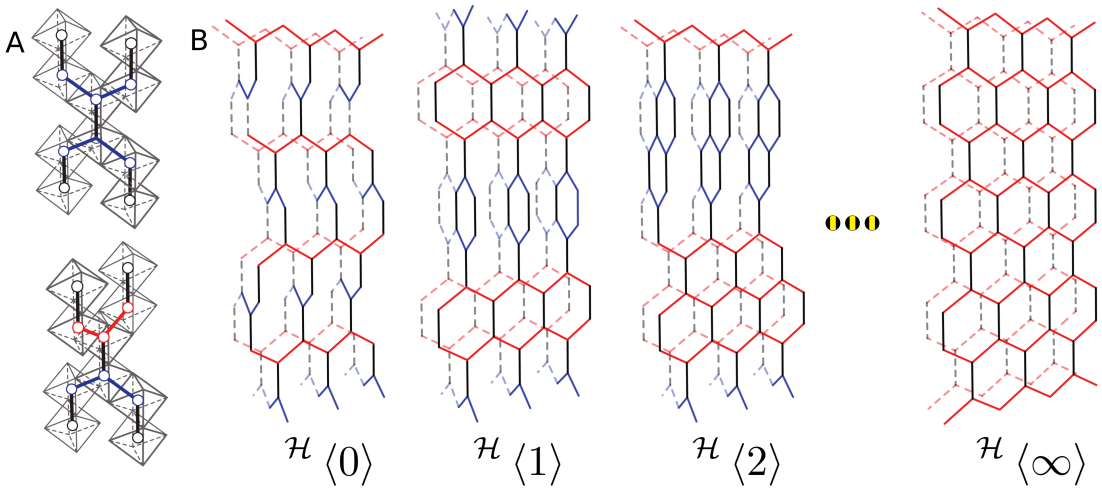

Figure 5.4: **I**ntroducing the harmonic honeycomb series. Figure reproduced from published version, Nat. Comm. 5, 4203 (2014). (A) Two kinds of c-axis bonds (black links) in the harmonic honeycomb family ${}^{\mathcal{H}}\langle N\rangle$-$Li_2IrO_3$ are shown, one linking within a honeycomb plane (for example blue to blue, top) and one that rotates between honeycomb planes (for example red to blue, bottom). For undistorted octahedra, these links are locally indistinguishable, as can be observed by the local coordination of any Ir atom (also see Figure **??**A). (B) These building blocks can be used to construct a series of structures. The end members include the theoretical $N = 0$ 'hyper-honeycomb' [**?**, **?**, **?**] and the $N = \infty$ layered honeycomb [**?**]. Here N counts the number of complete honeycomb rows in a section along the c-axis before the orientation of the honeycomb plane switches.

5.5 Supplementary Information: Kitaev quantum spin liquid

Every member of the harmonic honeycomb series is bonded by edge sharing IrO_6 octahedra. The edge-sharing geometry of the octahedra preserves the essential ingredients of the Kitaev model and this is universal for this family of structures. All three dimensional arrangements of edge-sharing octahedra maintain the interfering Ir-O_2-Ir exchange paths, where each of the three nearest neighbor Ir-Ir interactions predominantly couples a particular orthogonal component of spin. In the idealized limit of symmetric octahedra, such changes may compete primarily with the usual rotationally symmetric Heisenberg interactions. In the Kitaev limit where Heisenberg interactions may be set aside, the Hamiltonian becomes a sum of spin-anisotropic exchange terms

$$H_{\mathrm{K}} = -K^c \sum_{\langle ij\rangle\in\hat{\boldsymbol{b}}_\perp} S_i^{\hat{\boldsymbol{b}}} S_j^{\hat{\boldsymbol{b}}} - K^h \sum_{\langle ij\rangle\in(\hat{\boldsymbol{a}}+\hat{\boldsymbol{c}})_\perp} S_i^{\hat{\boldsymbol{a}}+\hat{\boldsymbol{c}}} S_j^{\hat{\boldsymbol{a}}+\hat{\boldsymbol{c}}} - K^h \sum_{\langle ij\rangle\in(\hat{\boldsymbol{a}}-\hat{\boldsymbol{c}})_\perp} S_i^{\hat{\boldsymbol{a}}-\hat{\boldsymbol{c}}} S_j^{\hat{\boldsymbol{a}}-\hat{\boldsymbol{c}}}, \quad (5.2)$$

where $S^{\hat{\boldsymbol{b}}}$ and $S^{\hat{\boldsymbol{a}}\pm\hat{\boldsymbol{c}}} = (S^{\hat{\boldsymbol{a}}} \pm S^{\hat{\boldsymbol{c}}})/\sqrt{2}$ are the spin operators in a set of three orthogonal directions, with $\hat{\boldsymbol{a}}$, $\hat{\boldsymbol{b}}$, $\hat{\boldsymbol{c}}$ being unit vectors along the orthorhombic crystallographic axes. Here we label each bond $\langle ij\rangle$ by the axis perpendicular to its Ir-O_2-Ir plane; for each bond, this normal vector lies along one of the directions $\{(\hat{\boldsymbol{a}}+\hat{\boldsymbol{c}}), (\hat{\boldsymbol{a}}-\hat{\boldsymbol{c}}), \hat{\boldsymbol{b}}\}$. The $\hat{\boldsymbol{b}}_\perp$ bonds are all oriented along the crystallographic c direction. Thus all the nearest neighbor Ir-Ir bonds can be divided into three classes, one for each component of spin: the $\hat{\boldsymbol{b}}$ component from the c-axis bonds, and the $\hat{\boldsymbol{a}} \pm \hat{\boldsymbol{c}}$ components from the h bonds defining each honeycomb plane (depicted in figures in the published version of the paper). The exchange couplings K^h are constrained by the symmetry of the space group to be the same on the $(\hat{\boldsymbol{a}} \pm \hat{\boldsymbol{c}})_\perp$ bonds, but K^c, the coefficient of $S^{\hat{\boldsymbol{b}}}$ coupling, is symmetry-distinct from K^h.

The Hamiltonian in Equation 5.2 was studied by Kitaev on the honeycomb lattice and shown to give an exactly solvable quantum spin liquid. The solution relies on the fact that spin algebra can be represented in an enlarged Hilbert space of Majorana fermions χ^α ($\alpha = 0, 1, 2, 3$) by mapping $S^\mu \to (i/2)\chi^0\chi^\mu$ (where $\mu = 1, 2, 3$) and implementing constraints to project back to the physical Hilbert space. As a result, each spin is represented in terms of two degrees of freedom — one a $\mathcal{Z}_2$ gauge field, the other a Majorana fermion moving in this field. The three-fold local connectivity of the honeycomb lattice together with the orthogonal Ising coupling of the Kitaev Hamiltonian (Equation 5.2) freezes the gauge field fluctuations associated with the Hilbert space constraint, resulting in static $\mathcal{Z}_2$ fluxes. The problem then reduces to the motion of non-interacting particles in a fixed field. The ground state of these non-interacting fermions, expressed in terms of the underlying spins, is a complicated many-body superposition, and in particular is a quantum spin liquid.

In 2D the solution is possible because the honeycomb lattice contains the right number of hexagon plaquettes (minimal closed paths linking sites) to host the $\mathcal{Z}_2$ fluxes. This can be seen via Euler's theorem — which states that the number of minimal plaquettes plus the number of sites equals the number of links, on any 2D lattice. Threefold coordination means there are three bonds per two sites, and hence there is one flux degree of freedom for every two spins, as required by the solution. In 3D, there are too many minimal plaquettes to host the required number of independent $\mathcal{Z}_2$ fluxes. However, a similar counting formula shows that the required number of independent gauge field degrees of freedom is matched by subtracting the number of enclosed volumes from the number of faces. Each enclosed volume gives a constraint; the independent flux constraints in 3D are not individual fluxes but rather unending flux lines, which form closed flux loops.

An additional difference in the 3D lattices is that, unlike the 2D honeycomb where every plaquette has six sites, in the harmonic honeycomb lattice the plaquettes vary in length, including 6, 10, 14 and so on. In particular, for the ${}^{\mathcal{H}}\langle 1\rangle$-$Li_2IrO_3$ member there are two minimal plaquettes, 6 sites long and 14 sites long. The product of spin operators around each such plaquette forms an operator which commutes with the Hamiltonian. However products of such plaquette operators around an enclosed volume are reduced to the identity operation, constraining the flux lines to form closed loops. These gauge field fluxes remain static, enabling the spin-liquid solution to be extended to 3D for all members of this family [**?**, **?**].

The ground state of the Hamiltonian described by Eq. 5.2 contains no gauge-field fluxes. In this zero flux sector, the Hamiltonian is quadratic, diagonal in momentum space. Assuming $K^c = K^h = K$, the dispersion of Majorana Fermions is given by the eight eigenvalues of the tight-binding matrix

$$K \begin{pmatrix} 0 & 1 & 0 & 0 & 0 & 0 & 0 & V_2^* U_3^* \\ 1 & 0 & V_1^* & 0 & 0 & 0 & 0 & 0 \\ 0 & V_1 & 0 & 1 & 0 & 0 & 0 & 0 \\ 0 & 0 & 1 & 0 & V_1 & 0 & 0 & 0 \\ 0 & 0 & 0 & V_1^* & 0 & 1 & 0 & 0 \\ 0 & 0 & 0 & 0 & 1 & 0 & V_2^* & 0 \\ 0 & 0 & 0 & 0 & 0 & V_2 & 0 & 1 \\ V_2 U_3 & 0 & 0 & 0 & 0 & 0 & 1 & 0 \end{pmatrix} \tag{5.3}$$

where $U_3 = \exp[i\boldsymbol{k}\cdot\boldsymbol{c}]$, $V_{1,2} = 1 + U_{1,2}$ and $U_{1,2} = \exp[i\boldsymbol{k}\cdot(\boldsymbol{a} \pm \boldsymbol{b})/2]$ with the $+/-$ sign corresponding to U_1, U_2 respectively. In the symmetric octahedra idealization where the Kitaev Hamiltonian is most likely to be relevant, the crystallographic vectors take the simple form $\boldsymbol{a} = (2, 2, 0)$, $\boldsymbol{b} = (0, 0, 4)$ and $\boldsymbol{c} = (-6, 6, 0)$ in the Ir-O Euclidean coordinate system, in unis where the Ir-O distance is 1. The tight binding dispersion above is easily generalized to the other 3D lattices with the same $\boldsymbol{a}, \boldsymbol{b}$ base-centered orthorhombic Bravais lattice vectors and arbitrarily long unit cells along $\boldsymbol{c}$,

by appropriately cycling between V_1 and V_2 in the alternating off-diagonal elements of the matrix.

The resulting spectrum of the Majorana Fermions is gapless, and remains gapless for the entire region of parameter space with $K^c \leq 2K^h$ [**?**, **?**]. The gapless fermion excitations form a 1D nodal contour within the 3D Brillouin zone, satisfied by the two equations $\boldsymbol{k} \cdot \boldsymbol{c} = 0$ and $\cos(\boldsymbol{k} \cdot \boldsymbol{a}/2) + \cos(\boldsymbol{k} \cdot \boldsymbol{b}/2) = 1/2$. For reference, note the BZ boundary satisfies the equations $\cos(\boldsymbol{k} \cdot \boldsymbol{c}) = -1$ or $\cos(\boldsymbol{k} \cdot \boldsymbol{a}/2) + \cos(\boldsymbol{k} \cdot \boldsymbol{b}/2) = 0$.

In the vicinity of the nodal contour the dispersion is linear ($\omega \sim |\boldsymbol{k}_\perp|$) in the two directions perpendicular to the nodal contour. Increasing K^c/K^h shrinks the nodal contour to a point, at $K^c = 2K^h$; for $K^c > 2K^h$ the fermion spectrum is gapped.

If flux excitations proliferate, they will confine the fermions excitations in the spin liquid. In 2D, flux excitations are point objects and proliferate at any finite temperature. But in 3D, the fluxes form closed loop, with an energy cost proportional to the length of the flux loop; large flux loop cost arbitrarily high energy. Thus, in the 3D quantum spin liquid the fermions will survive in the deconfined phase until an entropy driven phase transition at finite temperature, separating the 3D quantum spin liquid and the classical paramagnet.

Chapter 6

Three dimensional quantum spin liquids in models of harmonic-honeycomb iridates and phase diagram in an infinite-D approximation

6.1 Context

This chapter builds upon the remarkable experimental results and their theoretical analysis as presented in the previous chapter. In addition to the 3D iridate whose synthesis was presented in the previous chapter, which is here referred to as γ-Li_2IrO_3, another 3D iridate with the same chemical formula was synthesized at roughly the same time, with a different, distinct, 3D structure, here referred to as β-Li_2IrO_3. This chapter studies both lattices.

Motivated by the recent synthesis of two insulating Li_2IrO_3 polymorphs, where Ir^{4+} S_{eff}=1/2 moments form 3D ("harmonic") honeycomb structures with threefold coordination, we here study magnetic Hamiltonians on the resulting β-Li_2IrO_3 hyperhoneycomb lattice and γ-Li_2IrO_3 stripyhoneycomb lattice. Experimentally measured magnetic susceptibilities suggest that Kitaev interactions, predicted for the ideal 90° Ir-O-Ir bonds, are sizable in these materials. We first consider pure Kitaev interactions, which lead to an exactly soluble 3D quantum spin liquid (QSL) with emergent Majorana fermions and Z_2 flux loops. Unlike 2D QSLs, the 3D QSL is stable to finite temperature, with $T_c \approx |K|/100$. On including Heisenberg couplings, exact solubility is lost. However, by noting that the shortest closed loop ℓ is relatively large in these structures, we construct an $\ell \to \infty$ approximation by defining the model on the Bethe lattice. The phase diagram of the Kitaev-Heisenberg model on this lattice

is obtained directly in the thermodynamic limit, using tensor network states and the infinite-system time-evolving-block-decimation (iTEBD) algorithm. Both magnetically ordered and gapped QSL phases are found, the latter being identified by an entanglement fingerprint.

6.2 Introduction

Recently there has been growing interest in studying quantum phases of matter that are characterized by long range entanglement[211], in contrast to conventional symmetry broken states. In particular, gapped quantum phases that feature long range entanglement exhibit remarkable emergent properties such as excitations with unusual statistics and fractional quantum numbers. These properties are known to occur in two dimensional phases such as the fractional quantum Hall states, which are realized in 2D electron gases in strong magnetic fields. In solids, frustrated insulating magnets are believed to be prime candidates for avoiding conventional ordering in favor of a long range entangled phase of matter — the quantum spin liquid phase. Recent numerical studies have found mounting evidence for gapped spin liquids, phases which are long range entangled[193, 209, 162, 200, 130, 114], on two dimensional geometrically frustrated lattices such as the Kagome lattice[155, 196, 213].

However, frustration need not arise from geometry alone. In quantum magnets of heavy elements, spin-orbit coupling leads to anisotropic interactions that may engender quantum disordered ground states even in the absence of the usual geometrical frustration. A prime example is the honeycomb lattice – a bipartite lattice on which both ferromagnetic and antiferromagnetic Heisenberg couplings host ordered ground states. However, a peculiar set of anisotropic interactions proposed by Kitaev[146], where neighboring spins are coupled by Ising interactions along an axis that is set by the spatial orientation of the bond, has been shown to be in a quantum spin liquid phase. Furthermore, this is demonstrated via an exact solution – in contrast to the numerical tour de force required for identifying the spin liquid phase in the Kagome antiferromagnet[213, 130].

Interestingly, the requirement for obtaining an exactly soluble spin liquid is not specific to the honeycomb lattice. Instead, the key ingredients are the three fold coordination of the sites and the peculiar Ising interaction with rotating axes. If such a network would be created in three dimensions, it would lead to an example of a 3D quantum spin liquid. Such long range entangled quantum phases in 3D are less well explored than their 2D counterparts. While basic constraints on long range entangled quantum phases in 3D have been discussed[156, 119], few suggestions for materials candidates exist. An exception is the 3D hyperkagome material[181] $Na_4Ir_3O_8$, for which a spin liquid ground state with bosonic[151] or fermionic[**?**, 153] spinon excitations has been proposed. Related U(1) spin liquids[125, 126] have been proposed for quantum spin ice materials[194] on the pyrochlore lattice. Here we

discuss a 3D example of quantum spin liquid behavior induced by spin-orbit coupling in a 3D model with Kitaev exchanges, and explore a possible physical realization.

At first sight, the Kitaev interactions seem rather unphysical. However, as pointed out by Jackeli and Khaliullin[129], they may actually be realized under certain circumstances in iridium oxides. An Ir^{4+} ion at the center of an oxygen octahedron is expected to be in a Kramers doublet state J=1/2, with the doublet wave function set by the spin-orbit coupling. This leads to unusual magnetic exchange interactions. For example, when a pair of Ir^{4+} moments are coupled via an intermediate oxygen with a 90° bond, the usual Goodenough-Kanamori-Anderson rules would have predicted a ferromagnetic Heisenberg exchange. Here however, due to the special nature of the Kramers doublets, the coupling was shown[129] to be ferromagnetic, but of the Ising type, with the spin component involved being perpendicular to the bond's iridium-oxygen plane. Other exchange paths around the Ir-O-Ir-O square and involving higher energy states including the Ir^{4+} e_g orbitals[106, 107] also generate this type of coupling, with either sign. For the compound Na_2IrO_3 in which Ir forms independent honeycomb lattices, these mechanisms were argued[129] to lead to couplings identical to Kitaev's honeycomb model, although additional spin interaction, minimally a Heisenberg term, is also expected. An appropriate minimal model for the low energy magnetic Hamiltonian is then the nearest neighbor Kitaev-Heisenberg model[106].

In the *C2/m* layered structure[110] of Na_2IrO_3, and even more dramatically in the *Cccm* and *Fddd* 3D-Li_2IrO_3 structures we discuss below[173], space group symmetries single out the subset of Ir-Ir bonds which are oriented along a particular axis. Recent ab initio work[212] has found that already for Na_2IrO_3, the magnitude of both Kitaev and Heisenberg couplings can be quite different between these symmetry-distinguished subsets of bonds. Allowing the couplings to take a different value on the symmetry-distinguished "c-bonds" compared to the remaining "d-bonds" produces the bond-anisotropic Kitaev-Heisenberg Hamiltonian,

$$H = \sum_{c-\text{bond}\langle ij\rangle} \left(K_c S_i^{\gamma_{ij}} S_j^{\gamma_{ij}} + J_c \vec{S}_i \cdot \vec{S}_j \right) + \sum_{d-\text{bond}\langle ij\rangle} \left(K_d S_i^{\gamma_{ij}} S_j^{\gamma_{ij}} + J_d \vec{S}_i \cdot \vec{S}_j \right). \tag{6.1}$$

The geometry of IrO_6 octahedra implies that the spin component γ_{ij} coupled in a Kitaev term $K S_i^{\gamma_{ij}} S_j^{\gamma_{ij}}$ is, on any bond, one of the Ir-O Cartesian axes x, y or z.

The additional Heisenberg interactions are important; indeed, the ground state of Na_2IrO_3 is magnetically ordered and not a quantum spin liquid. The "zigzag" (wavevector M) magnetic ordering seen[161, 110, 217] in Na_2IrO_3, as well as other measured magnetic and electronic properties, remain consistent with Kitaev-Heisenberg as well as with more conventional Hamiltonians with SU(2) rotation symmetry.[197, 143, 91, 198, 110, 107, 112, 116, 140, 117, 118] Other anisotropic exchanges related

to the Jackeli-Khaliullin mechanism[129] have been described[135, 108, 179, 172] for Na_2IrO_3 and related iridates[104, 168, 167]. Alternative starting scenarios for Na_2IrO_3 have also been proposed[195, 169, 96, 170] which paint a picture of it different from a Mott insulator. Since the Chaloupka et al original formulation and solution of the Kitaev-Heisenberg model[106], much research has elucidated its various properties[198, 190, 131, 188, 191, 142]; as a model containing a QSL, it has been especially interesting to investigate its behavior under charge doping[218, 127, 180, 202, 203]. While the Kitaev-Heisenberg model may or may not apply to the particular compound Na_2IrO_3, the key point is that the Jackeli-Khaliullin mechanism can arise in any lattice of edge-sharing IrO_6 octahedra with roughly cubic local symmetry, as long as any distortion from cubic symmetry is weaker than the spin orbit coupling[129, 107, 142].

Recently, Li_2IrO_3 has been successfully synthesized in two insulating polymorph crystal structures consisting of edge-sharing IrO_6 octahedra. In the β-Li_2IrO_3 polymorph, synthesized in powder form[199], iridium ions form the 3D *hyperhoneycomb lattice* as shown in Fig. 6.4, with space group $Fddd$ (#70). In the γ-Li_2IrO_3 polymorph, synthesized as single crystals[173], iridium ions form the *stripyhoneycomb lattice* as shown in Fig. 6.1, with space group $Cccm$ (#66). Each of these three dimensional lattices is locally honeycomb-like, preserving threefold connectivity for every site. Their unified geometry suggests an extension to a structural series, the "harmonic honeycomb" series[173]; each structure in the series is labeled by an integer n, denoting the number of adjacent hexagon strips found in the lattice. In this notation, the stripyhoneycomb lattice γ-Li_2IrO_3 polymorph is the n=1 harmonic honeycomb iridate; the hyperhoneycomb lattice β-Li_2IrO_3 is the n=0 member; and the layered honeycomb α-Li_2IrO_3 is described by n=∞ (Tab. 6.1).

The γ-Li_2IrO_3 single crystals undergo a magnetic transition at about 38K, as evidenced by large anisotropic peaks in magnetic susceptibility[173]. As also pointed out in the experimental analysis[173], the bond-aisotropic Kitaev-Heisenberg model Eq. 6.1 is sufficient for capturing the large susceptibility anisotropy observed in experiment; within this scenario, large ferromagnetic Kitaev exchanges are necessary to fit the experimental data. The susceptibility fit is shown in Fig. 6.3; we elaborate on the magnetic couplings required for this fit in section 6.4.3 below. We study the Hamiltonian Eq. 6.1 with the parameters of the fit, classically as well as using the fully quantum large-ℓ approximation discussed below, and find in both cases a ground state with Stripy-X/Y magnetic order, shown in Fig. 6.6. In this pair of symmetry-related degenerate ground states, spins exhibit ferromagnetic correlations of spin component S^x across Kitaev x-type bonds or S^y across y-type bonds. Based on the susceptibility anisotropy we predict that these stripy magnetic correlations occur in the low temperature phase of γ-Li_2IrO_3. Indeed, since this work was presented, recently the magnetic order of γ-Li_2IrO_3 has been determined[98] to be a counter-rotating noncoplanar spiral order in which the dominant spin correlations are exactly these Stripy-X and Stripy-Y correlations, again requiring a magnetic Hamiltonian

Material	Harmonic-honeycomb #	Lattice name	Dim.
α-Li_2IrO_3	$n = \infty$	Honeycomb	2D
β-Li_2IrO_3	$n = 0$	Hyperhoneycomb	3D
γ-Li_2IrO_3	$n = 1$	Stripyhoneycomb	3D

Table 6.1: Iridates of the harmonic-honeycomb series: Ir lattice conventional name and dimensionality. We focus on γ-Li_2IrO_3 single crystal measurements to extract magnetic Hamiltonians, which we study on the β- and γ- Li_2IrO_3 structures as well as on their tree tensor network approximation.

with strong FM Kitaev exchange.

In parallel with this work, a few other studies of 3D Kitaev-Heisenberg models have appeared. Various properties of the hyperhoneycomb lattice model's magnetic phases and exact spin liquids were studied[145] while the magnetic phases at finite fields and temperature were explored using classical and semi-classical techniques [154]. The spin liquid was also studied at finite temperature using an Ising mapping of its Toric Code limit[177]. Another lattice related to the hyperkagome but with higher symmetry, dubbed the "hyperoctagon lattice", was introduced and the Kitaev spin liquid it supports was characterized [124].

Results here are complimentary to these studies, and are distinguished in three ways. First, we pull together the existing experimental results to make the case, based on single-crystal measurements, for strong Kitaev exchange in the 3D-Li_2IrO_3 materials. Second, we focus our attention on the hitherto-unstudied stripyhoneycomb lattice recently obtained as the structure of γ-Li_2IrO_3. Our magnetic Hamiltonians are informed by the experimental measurements and incorporate bond anisotropies dictated by the symmetries of the crystals. Most others[166, 145, 154, 177] exclusively studied the hyperhoneycomb lattice, which we also study below. Third, in addition to studying the exactly solvable 3D spin liquids, we employ tensor product states – higher dimensional generalizations of 1D matrix product states – to obtain the fully quantum phase diagram in a large-ℓ limit. The phase diagram we compute, for the frustrated quantum Hamiltonians motivated by the experiments, contains both magnetic and quantum spin liquid phases. To our knowledge this is the first identification of a quantum spin liquid phase in a tree tensor network.

6.3 Summary of results

We begin (Sec. 6.4) by analyzing the relevance of the Kitaev interactions to Li_2IrO_3 using γ-Li_2IrO_3 single-crystal measurements. We discuss the interplay of chemistry and geometry in the A_2IrO_3 structures, aiming to understand the newly synthesized stripyhoneycomb and hyperhoneycomb lattices within a framework encompass-

ing other 3D honeycomb lattices of edge-sharing IrO_6 octahedra. We analyze in detail the argument, based on fitting magnetic susceptibility, that the magnetic properties of 3D-Li_2IrO_3 are captured by the bond-anisotropic Kitaev-Heisenberg model Eq. 6.1. Its key is the geometrical contrast between the crystalline anisotropy, distinguishing the spatial c-axis, and the magnetic susceptibility anisotropy, distinguishing the b=z spin axis: the two are coupled by the S^zS^z Kitaev exchange on c-bonds. We demonstrate this mechanism by analytically fitting the measured susceptibility to mean field theory of Eq. 6.1, and find (Fig. 6.3) that it requires strong FM Kitaev exchange.

With this motivation for Eq. 6.1 as a minimal Hamiltonian with dominant Kitaev exchange, we proceed (Sec. 6.5) to study its spin liquid phase in the Kitaev limit through the Majorana fermion exact solution. We extend the previous analysis of the hyperhoneycomb-graph Kitaev model[166], and also analyze in detail the model on the stripyhoneycomb lattice of γ-Li_2IrO_3. We compute the spin correlators as well as the spectrum of the emergent Majorana fermions, and find that the low energy excitations occur on a ring-like nodal contour, identical for the two 3D lattices. Introducing bond-strength anisotropy shrinks the nodal contour, and we find that the phase boundary between the gapped and gapless spin liquids is identical on all the finite-D lattices and independent of whether the bond-anisotropy breaks or preserves the lattice symmetries.

We give a simple but general counting argument based on the Euler characteristic formula that explicitly illustrates the lack of monopoles in (3+1)D $\mathbb{Z}_2$ lattice gauge theories, showing that closed flux loops rather than individual fluxes are the gauge-invariant objects. The energy of the flux loop excitations is described not as a flux gap but rather by a loop tension, which we compute within the zero temperature exact solution to be $\tau = 0.011|K|$ on both lattices. This tension combines with the extended nature of the loops to control the finite temperature behavior of the models, producing the finite temperature loop proliferation transition which confines the Majorana fermions. Together with the robustness of fermionic statistics (since flux attachment is impossible), this stability to finite temperature hallmarks the features unique to three dimensional fractionalization.

Computing the quantum phase diagram of the full frustrated Hamiltonian is exponentially difficult; while such problems have been tackled in two dimensions, an unbiased phase diagram computation of the three dimensional model is currently impossible. We are able to capture it (Fig. 6.2 and Sec. 6.6) by employing a limit inspired by the hyperhoneycomb lattice, whose shortest loops are ℓ=10 decagons. Treating ℓ as a large control parameter and taking it to infinity, we reach the loopless Bethe tree lattice, which is infinite dimensional but preserves the key z=3 connectivity. This $\ell\to\infty$ approximation is not analytically tractable, but rather admits an entanglement-based numerical solution using tensor product states (TPS). Gapped states can be efficiently represented as a TPS on a tree lattice (tree tensor networks); on the tree, as in 1D systems, the full entanglement between two halves of the system is carried by the single bond connecting them. We employ a TPS time evolving block decimation

algorithm which works directly in the thermodynamic limit (iTEBD)[205], which has been previously extended to the Bethe lattice for magnetic phases[175, 176, 157] and other non-fractionalized phases[113, 160]. The iTEBD straightforwardly captures the FM and Neel magnetic orders as well as their duals[106, 142], the stripy and zigzag magnetic orders.

However, quantum spin liquids are generally difficult to identify positively since they lack an order parameter. Positive signatures can be elusive. Studies in 2D have relied on the sub-leading entanglement term known as the topological entanglement entropy[130, 219], but this quantity is not defined nor computable on the tree lattice. Instead, we complement the TPS computation by analytically studying the gapped Kitaev QSLs on the loopless tree using the Majorana solution, computing the entanglement entropy from the fermion and gauge sectors on each bond as a function of anisotropy. We find that the TPS algorithm partially quenches the $\mathbb{Z}_2$ gauge field entanglement, utilizing the finite entanglement cutoff of the TPS representation to produce a minimally entangled ground state, and thereby circumventing the usual artifacts of the Bethe lattice. The resulting entanglement serves as a fingerprint which, alongside the vanishing magnetic order parameters, we use to identify the QSL phase within the iTEBD computation. Ours is the first positive-signature identification of a fractionalized quantum phase in the large-ℓ limit.

This solution of the QSLs with their adjacent phases in the quantum large-ℓ approximation augments the ground state and finite temperature analysis within the solvable three dimensional QSLs, yielding a remarkably complete picture of a fractionalized phase in a potentially realizable solid state system.

6.4 Relevance of Kitaev interactions to the 3D-lithium-iridates

6.4.1 Chemical bonding with IrO_6 octahedra

Oxides with octahedrally coordinated transition metals can bond in a variety of ways, sharing octahedral corners, edges, faces or a combination of these. Each bonding geometry results in a set of structures with various shared properties. Bond lengths are one such property, with nearest neighbor distances in iridates measuring $\sim 3\mathring{A}$ in edge sharing compounds compared to $\sim 4\mathring{A}$ in corner sharing ones. Symmetries are also correlated with bonding geometry; in corner sharing iridates where one oxygen is shared by exactly two iridia, four-fold symmetric structures generally arise, as in perovskite and layered perovskite structures. Compounds with edge sharing octahedra also occur in a variety of related structures; the triangular lattice $NaCoO_2$, the hyperkagome $Na_4Ir_3O_8$ and the layered honeycomb Na_2IrO_3 are all examples.

In the edge sharing iridates we consider, two oxygens are shared by exactly two iridia, and every iridium is coordinated by three others, belonging to a single plane.

In a fixed coordinate system, there are multiple choices for the orientation of the triangular Ir-Ir-Ir plaquette, which are locally indistinguishable from the perspective of any given iridium atom. In general the octahedral symmetry will not be perfect and the distortion may favor the situation of the layered honeycomb compound Na_2IrO_3, where all of the Ir-Ir bonds lie within a common plane.

However, for sufficiently high local symmetry approaching the full O_h group, alternatives to the layered geometry become increasingly favorable. Consider now the compounds with chemical formula Li_2IrO_3: this substitution of Na by Li is known to lead to much smaller distortions, since the Ir and Li ions are more similar in size. With the decreased octahedral distortion, multiple spatial orientations of the bonds should be more likely to occur. This can result in complex structures, such as the stripyhoneycomb lattice of γ-Li_2IrO_3 and the hyperhoneycomb lattice of β-Li_2IrO_3.

6.4.2 Symmetry and geometry of the harmonic honeycomb lattices

Consider the harmonic honeycomb structures, which include all three currently known polymorphs of Li_2IrO_3. Except for the $n{=}\infty$ layered honeycomb with its vastly reduced crystal symmetry, these possess bonds with various orientations comprising *all but one* of the possible orientations for edge-sharing octahedra. This scenario is shown in Fig. 8.5: two opposite octahedra edges are forbidden from bonding, and distinguish the spatial direction c, parallel to these edges. The other edges on the same square create Ir-Ir bonds lying along the c axis, resulting in the bond anisotropy described above. The c axis is thus distinguished for all harmonic honeycomb lattices; this is also reflected in the symmetry properties of each particular lattice. For example in the stripyhoneycomb lattice, the space group *Cccm* has a single mirror plane, whose normal is the c direction. This unifying feature also suggests that a single global orthorhombic a, b, c parent coordinate system can describe the various lattices, as is indeed true. The vectors of these parent orthorhombic axes, as well as explicit coordinates for the stripyhoneycomb and hyperhoneycomb lattices, are given in Appendix 8.2.1.

Recall that Kitaev spin coupling along the Bloch sphere Cartesian axis $\gamma \in \{x, y, z\}$ occurs[129] for the four octahedra edges (and associated Ir-Ir bonds) whose plane is normal to the spatial Cartesian axis γ. The relation between the a, b, c crystallographic axes of Fig. 6.1 and the octahedral Ir-O Cartesian axes, as shown in Fig. 8.5, is $\{\hat{a}, \hat{b}, \hat{c}\} = \left\{(\hat{x}{+}\hat{y})/\sqrt{2}, \hat{z}, (\hat{x}{-}\hat{y})/\sqrt{2}\right\}$. The c-bonds (i.e. the bonds lying along the c axis) carry Kitaev coupling of spin component $\hat{b} = \hat{z}$, and will also be denoted interchangeably by their Kitaev label, with the notation "z-bonds". The remaining bonds on the lattice ("d-bonds"), which are all related to each other by symmetries, carry Kitaev labels x and y. For the stripyhoneycomb lattice, the c-bonds are further distinguished into two types, those within hexagons and those between

hexagons, which are themselves not related to each other by symmetry. For the sake of simplicity here we have not introduced additional parameters in the Hamiltonian to distinguish these two c bond types, as we expect such bond strength anisotropy between the different c bonds to be a secondary effect.

6.4.3 Capturing γ-Li_2IrO_3 susceptibility with bond-anisotropic Kitaev interactions

The symmetry distinction between z and x, y type bonds implies that if the Kitaev coupling is strong, the magnetic susceptibility should have a distinctive z-axis response compared to its x, y axes response, at least at temperatures above the magnetic transition. If the Kitaev coupling K_c on the z-bonds is more ferromagnetic than the Kitaev coupling K_d on the x, y-bonds, it suggests an anisotropic susceptibility with larger response along z. Exactly such an anisotropy is observed in the γ-Li_2IrO_3 experiment[173]. However, to preserve the strong z-axis susceptibility which is observed also below the ordering transition, the resulting magnetic order should not have any significant spin component aligned along the z axis. This places a condition on the magnetic coupling, to disfavor magnetic order alignment along z, which is partially at odds with the condition necessary to favor susceptibility anisotropy with large χ^z.

To achieve strong anisotropy in the susceptibility χ, the Heisenberg couplings must be small compared to the anisotropic single-spin-component exchanges, in this case the large ferromagnetic Kitaev exchanges. Since the low temperature phase is not a ferromagnet, the Heisenberg couplings should be antiferromagnetic. This region of parameter space hosts two types of magnetic order, *Stripy-Z* and *Stripy-X/Y*, with different symmetry properties. With no additional anisotropies, *Stripy-Z* nominally hosts spins aligned along the z axis and can thus be ruled out. A more general property of the *Stripy-Z* phase is that, because of the two symmetry-inequivalent z-type bonds of the stripyhoneycomb lattice, it should generically exhibit a nonzero net moment. We therefore focus on Hamiltonians within the *Stripy-X/Y* phase (Fig. 6.6), as the simplest "minimal order" which is consistent with magnetic susceptibility and captured by the minimal Hamiltonian Eq. 6.1. We expect additional small exchange terms to modify the ground state order, but preserve the Stripy-X/Y correlations of this minimal phase.

The constraints on the couplings can be seen explicitly by treating the Hamiltonian classically, and extracting susceptibility by mean field theory (details are given in Appendix 6.13). The magnetic interactions of Eq. 6.1 were supplemented by a g-factor tensor chosen to match the susceptibility at the highest temperatures measured, with principal values g^{x+y}=g^z=1.95, g^{x-y}=2.35. Within the mean field treatment of the *Stripy-X/Y* phase (in the regime $K < 0$, $J > 0$), the transition temperature is given

by $T_N = (J_c + |K_d|)/4$. The susceptibility peaks at this temperature, taking values

$$\chi^{bb}(T_N) = (g^b)^2\mu_B^2/(2(J_c + J_d) - (|K_c| - |K_d|)) \quad (6.2)$$
$$\chi^{aa}(T_N) = (g^a)^2\mu_B^2/(2(J_c + J_d))$$

and with χ^{cc} similar to χ^{aa}. The observed susceptibility anisotropy then suggests a large value for the difference $|K_c| - |K_d|$. However, the stability of the Stripy-X/Y phase against Stripy-Z order is controlled by the constraint

$$|K_c| - |K_d| < 2(J_c - J_d). \quad (6.3)$$

There is a finite window of parameters which fit the data within these analytical constraints. One possibility for the couplings, as shown in Fig. 6.3, is (in meV): $K_c = -17, K_d = -7, J_c = 6.3, J_d = 0.8$. The Hamiltonian with this set of parameters was also studied beyond the classical limit, using tensor product states within the infinite dimensional large-ℓ approximation, and determined to lie within the *Stripy-X/Y* quantum phase.

This parameter regime of the fit, large ferromagnetic Kitaev exchange and small antiferromagnetic exchange, is consistent with Jackeli and Khaliullin's original proposal [129] [106] and with the recent Na_2IrO_3 ab initio[212]. The extent of the anisotropy is qualitatively similar to the Na_2IrO_3 ab initio prediction as well; the parameters computed for Na_2IrO_3 are[212] $K_c = -30.7, K_d = -23.9, J_c = 4.4, J_d = 2.0$ meV, and larger anisotropy is expected for the stripyhoneycomb lattice because the special c bonds directly form the special axis of its *Cccm* space group.

6.4.4 Necessity of large Kitaev interactions for describing magnetic measurements on γ-Li_2IrO_3

The analysis in the previous section showed analytically that within mean field theory, fitting the observed anisotropic susceptibility required a large ferromagnetic Kitaev exchange, dominant over a smaller AF Heisenberg exchange. The bond-dependent Kitaev interactions K_c, K_d then capture the observed susceptibility at temperatures both above and below the ~ 40 K magnetic transition.

The primary conclusion of this analysis is the argument that the bond-anisotropic Kitaev-Heisenberg Hamiltonian is appropriate for describing current experimental data on 3D-Li_2IrO_3 and requires quite large Kitaev exchanges $|K| >> J$. The nominal ground state of the fitted Hamiltonian is the simple collinear phase Stripy-X/Y, but in the real crystal we do not expect the spin direction to be locked to $\hat{x}$ or $\hat{y}$, but rather expect it to sample across the (a, c) (or equivalently (x, y)) plane. A secondary conclusion is therefore a susceptibility-based prediction for the low temperature magnetic pattern of γ-Li_2IrO_3, namely presence of the *Stripy-X/Y* correlations of the fitted Hamiltonian.

As mentioned in the introduction, this 4-parameter fit to magnetic susceptibility, with parameters $(K_c, K_d, J_c, J_d) = (-17, -7, 6.3, 0.8)$ meV, is consistent with the 6-parameter Hamiltonian which captures the noncoplanar spiral magnetic order which has just been recently observed[98] in γ-Li_2IrO_3. That 6-parameter fit supplements Eq. 6.1 by c-axis Ising exchange I_c^c on c-bonds and J_2 Heisenberg exchange on second-neighbors, and gives the values I_c^c=−4.5, J_2=−0.9, $(K_c, K_d, J_c, J_d) = (-15, -12, 5, 2.5)$ meV. The associated Stripy-X and Stripy-Y correlations expected for such a quantitatively similar Hamiltonian are also observed in the complex spiral order. Most importantly, we observe that in each analysis, independently, large and FM Kitaev exchanges K_c, K_d are necessary to describe the material.

6.5 Quantum spin liquids in three dimensions

Let us now tune the Heisenberg couplings J to zero, taking the limit of a pure Kitaev Hamiltonian. Though this limit does not describe the experiments on Li_2IrO_3, it offers a wide range of interesting phenomena associated with 3D fractionalization, which may turn out to be experimentally accessible at a future date.

6.5.1 Solution via Majorana fermion mapping

Kitaev's solution[146] of the honeycomb spin model relies on a local condition — each site touches three bonds carrying the three different Kitaev labels — and hence may be generalized to lattices with $z = 3$ coordination number. In order to discuss important subtleties which will arise later (in infinite dimensions), let us briefly review the solution here. The $S = 1/2$ algebra is represented in an enlarged Hilbert space via four majorana fermions

$$S_i^a \to \frac{1}{2} i \chi_i^0 \chi_i^a, \quad \{\chi_i^a, \chi_{i'}^{a'}\} = 2\delta_{i,i'}\delta_{a,a'}. \tag{6.4}$$

The enlarged Hilbert space Kitaev Hamiltonian $\tilde{H}$ is then a free majorana fermion χ^0 minimally coupled to a $\mathbb{Z}_2$ vector potential $a_{i,j}$ with $e^{i\pi a_{i,j}} \equiv u_{i,j} = i\chi_i^{\gamma_{ij}} \chi_j^{\gamma_{ij}}$ living on links $\langle ij \rangle$. The gauge field operators $u_{i,j}$ all commute with each other and with $\tilde{H}$, so $\tilde{H}$ may be diagonalized by solving a free fermion problem for each gauge field configuration $\{u_{i,j} = \pm 1\}$. Here $u_{i,j}$ is identified as a gauge field because, while in the enlarged Hilbert space it is a simple $\mathbb{Z}_2$ bond variable set by the majorana fermion occupancy, there is a set of site operators $D_i \equiv \chi_i^0 \chi_i^1 \chi_i^2 \chi_i^3$ which are the identity within the physical spin Hilbert space but act as a lattice gauge transformation on the link variable $u_{i,j}$. Projection to the physical spin Hilbert space is implemented by symmetrizing over all local gauge transformations D_i, with the projection operator $P = \prod_i (1 + D_i)/2$.

Let us now discuss the consequences of this majorana fermion solution for the 3D trivalent lattices. Some of the phenomenology was previously explored[166] for a

3D lattice whose connectivity graph matches the hyperhoneycomb's. The projection from gauge to physical Hilbert space is aided by gauge invariant operators whose eigenvalues, commuting with the Hamiltonian, label physical sectors of states. These closed Wilson loops are the usual $\mathbb{Z}_2$ fluxes piercing the elementary plaquettes. Flipping $u_{i,j}$ on a bond inserts flux in adjoining plaquettes. As discussed earlier, the 3D lattices possess symmetries as well as graph connectivity which distinguish one bond type, z, from the other two bond types x and y. On the hyperhoneycomb lattice, flipping $u_{i,j}$ on a z type bond creates fluxes on the eight adjacent plaquettes, while flipping $u_{i,j}$ on x or y type bonds changes the flux on the only six adjacent plaquettes. On the stripyhoneycomb lattice, the elementary plaquettes come in multiple forms, consisting of $\ell = 6$ hexagons together with larger $\ell = 14$ plaquettes.

6.5.2 Extended flux loop excitations in the 3D QSL

The gauge field sector on the 3D-lattices Kitaev models is a 3+1D $\mathbb{Z}_2$ lattice gauge theory[148]. The product of $u_{i,j}$ around a minimal closed contour gives the flux through an elementary plaquette of the lattice. The product of fluxes on plaquettes surrounding an elementary volume element multiplies to the identity: this is equivalent to the fact that there are no magnetic monopoles in the $\mathbb{Z}_2$ theory. Each elementary volume carries a zero monopole charge and thus acts as a constraint, forcing the number of flux lines piercing the volume to be even. These constraints ensure that the flux lines only appear within closed flux loops.

It is important to note that while in the 2D honeycomb case the magnetic fluxes are the gauge invariant result of projecting the gauge theory, in the case of three spatial dimensions, individual fluxes are not gauge invariant. Rather, only closed flux loop configurations are the physical gauge invariant excitations of the model. The individual fluxes cannot be gauge invariant labels of sectors of the Hamiltonian since they don't even correctly count the physical degrees of freedom of the gauge theory. The constraint of closed loops fixes this counting; the closed magnetic loop configurations exactly label the gauge invariant sectors of the $\{u_{i,j}\}$ after projection.

This can be seen as follows (explicitly verifying this statement in the stripyhoneycomb and hyperhoneycomb lattices is also straightforward). Consider the lattice with periodic boundary conditions (rigorously it is a CW-complex topologically equivalent to the 3-torus), and count the number of cells of every dimension – sites, bonds, plaquettes and enclosed volumes. The Euler characteristic formula (as generalized by homology theory) then shows that

$$N_{\text{sites}} - N_{\text{bonds}} + N_{\text{plaquettes}} - N_{\text{volumes}} = 0. \tag{6.5}$$

The combination $N_{\text{plaquettes}} - N_{\text{volumes}}$ is of interest here, since every plaquette is associated with a flux, but each enclosed volume presents a condition on the adjacent fluxes (they must multiply to the identity). This constraint, due to the lack of monopoles

in the $\mathbb{Z}_2$ gauge theory, is responsible for the flux lines forming closed flux loops. The number of independent such loops is given by the number of possible flux lines minus the number of constraints, ie $N_{\text{flux loops}} = N_{\text{plaquettes}} - N_{\text{volumes}}$. Furthermore let us restrict to our case of interest where sites have coordination number $z = 3$ and so $N_{\text{bonds}} = (3/2)N_{\text{sites}}$. Then the formula becomes

$$N_{\text{flux loops}} = N_{\text{sites}}/2 \tag{6.6}$$

as required: the gauge field flux sector hosts half of the spin degrees of freedom, while the majorana fermion particle sector hosts the other half.

This observation implies the following important fact: while in the 2D Kitaev model, the flux sector is described by a gap to flux excitation, this is not the correct description for this 3D model. Rather, in 3D, the fluxes form closed loops, of arbitrary size. These loops possess a loop tension. The gap for a loop of a particular length is found by multiplying its length by the loop tension. We have computed a numerical value for this loop tension, as further discussed below.

Lieb's flux phase theorem[159], which shows that the 2D honeycomb ground state has zero flux per $\ell = 6$ hexagon, suggests that the $\ell = 6$, $\ell = 10$ and $\ell = 14$ loops of the stripyhoneycomb and hyperhoneycomb lattices, whose length is equal to 2 mod 4, should also carry zero flux in the ground state. We have checked numerically that the ground state on small finite systems lies in the sector with no flux loops.

We note that during the time since this work was published, recent subsequent work (PRL 114, 116803 (2015)) has found a particular configuration of fluxes on the stripyhoneycomb lattice, whose energy in the thermodynamic limit, $E_{flux} = 0.1293K$ per bond, is lower than that of the flux-free state, with energy $E_0 = 0.1290K$ per bond. The quantitative results in sections C,D,E below are applicable for the flux-free states, and remain quantitatively correct for the hyperhoneycomb lattice ground state, which is flux-free. Moreover the conclusions discussed below apply equally well to the ground states on both lattices, and hold even if additional lower-energy flux configurations are found.

6.5.3 Majorana fermion excitations

The Kitaev QSL possesses emergent quasiparticles which are fermionic, arising out of the interacting bosonic spin model. The emergent fermions are as real as physical electrons, but carry no usual electric charge; and moreover are Majorana (self-adjoint), related to the particle-hole-symmetric excitations of superconductors. As in the 2D honeycomb model, in which the fermion dispersion possesses graphene's Dirac nodes, the fermionic dispersion in the 3D lattices is gapless for the isotropic model. The sublattice symmetry present in all the 3D harmonic honeycomb lattices ensures that time reversal remains a symmetry in the QSL phase, and the Majorana fermion spectrum is particle-hole symmetric. Similarly to the graphene-like Dirac

cones appearing in the Majorana spectrum of the 2D Kitaev honeycomb model, where the 0D point-like nodes carry codimension of 2, the 3D Kitaev models can host gapless excitations along 1D nodal lines within the 3D Brillouin zone.

The spectrum of Majorana fermions is computed in Appendix 6.9, and turns out to be identical on both 3D lattices. It is formed by momenta k satisfying the two equations $\vec{k}\cdot\vec{c}=0$ and $\cos\left(\vec{k}\cdot\vec{a}/2\right)+\cos\left(\vec{k}\cdot\vec{b}/2\right)=1/2$. This set of momenta form a closed 1D ring-like contour of gapless excitations, lying within the BZ interior, which is plotted in Fig. 6.8. Indeed this is the dispersion of a nodal 3D superconductor: the Majorana fermions are gapless along a 1D ring of points in the 3D momentum space, forming a superconductor line node which here happens to close into a ring within the interior of the first Brillouin zone.

Within each sector with its associated flux loop configuration, we may study how the Majorana fermions propagate. The fermions are charged under the gauge field, and hence interact with the magnetic loop excitations through an Aharonov Bohm effect, analogous to that occurring between electrically charged electrons and conventional E&M magnetic flux lines. The interaction is as follows: when a fermion winds through the interior of a magnetic flux loop, it encircles one flux line and receives a minus one (-1) phase to its single particle wave function.

6.5.4 Spin-spin correlators

The spin-spin correlators at equal time may be computed straightforwardly within the fermion mapping; as in 2D, they are[146] only nonzero between spins on nearest-neighbor sites and then only between spin components matching that bond's Kitaev label. Hence the nonzero spin correlators G are also equivalently the energy E carried by the bond (divided by the coupling), specifically $G = E/K$. For notational simplicity we quote correlators G for $K < 0$, in which case the correlators are positive; for $K > 0$, correlators simply gain a minus sign. Here we report results at the isotropic point of the Hamiltonian, though of course lattice symmetry still comes into play. We find that the average bond correlator (again, proportional to the energy per bond) is $G_0^{3D;0} = -0.1284$ for the 3D hyperhoneycomb and $G_0^{3D;1} = -0.1290$ for the 3D stripyhoneycomb , only 2% higher than the 2D honeycomb result[146] $G_0^{2D} = -0.1312$.

For the hyperhoneycomb lattice, the z bonds and x, y bonds correlators are

$$G_z = 0.1314, \quad G_{x,y} = 0.1268. \tag{6.7}$$

The stripyhoneycomb lattice has two symmetry-distinct types of z bonds: those within hexagons ("$z[h]$") and those within length-14 loops ("$z[f]$") . The correlators are

$$G_{z[h]} = 0.1337, \quad G_{z[f]} = 0.1269, \quad G_{x,y} = 0.1283. \tag{6.8}$$

The large correlations on hexagon-z bonds could be explained as strong resonances within a hexagon, combined with a lattice symmetry effect that, for both the hyperhoneycomb and the stripyhoneycomb lattices, gives stronger correlations on the special-axis z bonds. Surprisingly, this global symmetry effect is almost as powerful as the hexagon resonances: it produces x,y-bond correlators which are only slightly stronger than those on the cross-hexagon-stripe $z[f]$ bonds.

6.5.5 Nodal contour under bond-strength anisotropies and broken symmetries

Increasing the coupling strength K on one bond type is an anisotropy which preserves exact solvability of the model, in 3D as well as 2D. Increasing K on bonds of one Kitaev-type shrinks down the nodal contour, until it vanishes and gaps out the fermions when the Kitaev exchange for any one bond type becomes larger than the sum of the other two. However, consider that the hyperhoneycomb and stripyhoneycomb lattice symmetries already distinguish z-bonds and their axis $\hat{c}$ as a special direction; increasing the strength of z bonds is an anisotropy which is generically expected to arise given the crystal symmetries.

Increasing the strength of Kitaev exchange on z-bonds shrinks the nodal contour towards its center at the Gamma point $\vec{k} = 0$. With sufficient anisotropy, the contour collapses at $\vec{k} = 0$ and then disappears, producing a gapped Majorana fermion spectrum (Fig. 6.7). But anisotropies for x or y type bonds do break a symmetry of the isotropic model. When increasing bond strength on x or y bonds, the nodal contour goes through a Van Hove singularity as it expands to touch the BZ surface, and then becomes centered around a BZ corner, towards which it gradually shrinks. This transition through a Van Hove singularity is an aspect associated with breaking crystalline symmetries. However, while these aspects of the nodal contour are different between symmetry-breaking (x, y) and non-symmetry-breaking (z) anisotropy, the resulting phase diagram of the spin liquid phase is the symmetric diagram shown in Fig. 6.7, identical to that of the symmetric 2D honeycomb lattice.

Each of the 3D lattices supports two different types of limits of large anisotropy, z and x/y types, which are associated with different three dimensional Toric Code models living on different $z = 4$ lattices. Each of these 3D Toric Code models is a pure $\mathbb{Z}_2$ gauge theory, with commuting plaquette terms formed by sites on a particular $z = 4$ lattice set by the type (z or x, y) of anisotropy. The Toric Code lattices are easily constructed by collapsing the strong-coupled bond into a site. The Toric Code $\mathbb{Z}_2$ flux operators act on plaquettes of reduced size: the hyperhoneycomb decagons turn into Toric Code hexagon plaquettes, while stripyhoneycomb hexagons (as in 2D) turn into Toric Code square plaquettes.

6.5.6 Gap via breaking of time reversal

Breaking time reversal symmetry with an external magnetic field induces oriented imaginary second neighbor hopping of the majorana fermions. The sign (orientation) of this imaginary hopping, necessary for majorana fermions, is set (as in 2D[146]) by the sign of the permutation of the two Kitaev bond labels traversed. We find that breaking time reversal gaps out all but a measure-zero set of points of the majorana nodal contour.

Interestingly, though, special behavior emerges at ultra-low fields. To lowest order, the external field introduces a mass gap which changes sign across the nodal contour, leaving two gapless band-touching points. At the next order of the external field, these points may be gapped out as well; but they may control the physics at low fields and low energy scales.

6.5.7 Fractionalization in 3D: extended loops and finite temperature confinement transition

Enlarging spatial dimensionality from two to three dimensions changes the nature of the spin liquid phase; the two most interesting differences involve fermions and finite temperature. In the two dimensional spin liquid away from the exactly solvable point[146], the flux excitations gain dynamics and interact with the majorana fermions; the low energy excitations could then be bound fermion-flux pairs, composite particles with simple bosonic statistics. In contrast, consider the three dimensional spin liquid; here fluxes are not pointlike particles but rather closed magnetic loops, so the emergent fermions cannot merely bind a (point-like) flux to transmute into bosons, and thus their 3D fermionic statistics are more robust. While fermions can e.g. bind into Cooper pairs to disappear from the lowest energy theory, a fundamental excitation in the model still necessarily preserves fermionic statistics. The fermions remain until a phase transition either confines them or transmutes them into bosons via a more complicated mechanism such as that recently explored in transitions between symmetry protected topological phases[208].

Three dimensional spin liquid phases generally admit a key characteristic distinguishing them from 2D spin liquids: the 3D spin liquid phases survive to finite temperatures. Such is true for the Kitaev 3D spin liquid phase, which undergoes a distinct entropy-driven phase transition to a classical paramagnet. In 2D QSLs a finite density of fluxes exists at any nonzero temperature; the fermions gain a phase of (-1) when encircling each of the fluxes and the resulting destructive interference results in a $T = 0$ confinement transition to the paramagnet phase. But in the 3D QSL, magnetic fields appear in extended loop excitations, whose energy is proportional to their length via an effective loop tension. The loop energy diverges with its length. At finite temperature there is a finite density only of short loops, whose small cross-sectional area renders them invisible to the fermions. A finite probability

for flux-encircling paths occurs only with macroscopically large loops, which cost diverging energy and hence appear at vanishing density. Entropy however favors longer loops, and so the free energy at finite temperature T for a loop of length L appears as (for long L)

$$F(L;T) = (\tau + \delta\tau(T) - \tilde{s}T)\, L \tag{6.9}$$

where $\tilde{s}$ is the entropy contribution to the loop tension, roughly the natural logarithm of the coordination number of the dual lattice (where magnetic loops live), $\tilde{s} \approx \log(z_{\text{dual}})$; τ is the zero temperature flux loop tension; and $\delta\tau(T)$ is the contribution to the effective loop tension at finite temperature due to interactions mediated by the gapless fermions.

Because the entropy is likely the dominant contribution and appears with a negative sign, the effective magnetic loop tension renormalizes to lower values at finite temperature. At a temperature T_c the tension becomes negative and proliferates arbitrarily large magnetic loops in a transition analogous to Kosterlitz-Thoughless flux unbinding, which then confine the fermions. We estimate the critical temperature T_c by computing the zero temperature value of the magnetic loop tension τ in the isotropic Hamiltonian, finding the result

$$\tau = 0.011|K| \tag{6.10}$$

for both stripyhoneycomb and hyperhoneycomb in different geometries and for different loops roughly independent of the loop shape, underlying bond/plaquette type, and for large loop lengths of up to 30 cross-sites (on the hyperhoneycomb lattice e.g. Fig. 6.4), implying the estimate $T_c \sim |K|/100$.

6.6 Quantum phase diagram in an infinite-D approximation

The Kitaev-Heisenberg model suffers from the "sign problem" of frustrated quantum Hamiltonians: unbiased algorithms for computing its phase diagram require computational costs scaling exponentially with system size, a problem greatly exacerbated in a three dimensional lattice. Unbiased reliable computations of the phase diagram on the three dimensional lattices are not possible at present time.

6.6.1 Duality results for the magnetic phases

Even on the 3D lattices, definitive conclusions for the magnetically ordered phases can still be made due to a general feature, the *Klein duality*, exhibited by Kitaev-Heisenberg models[135, 106, 142]. The following discussion applies to any bipartitie lattice, including the tree lattice in infinite dimension, as well as all 3D harmonic honeycomb lattices. Since these lattices are bipartite, simple Neel antiferromagnetic

order is the expected ground state for the Heisenberg antiferromagnet Hamiltonian. The Neel AF and FM orders map under the Klein duality to three dimensional generalizations of *stripy* and *zigzag* orders. Assuming that the unfrustrated Neel order is indeed the ground state for AF Heisenberg exchange (as may be verified by quantum Monte Carlo at the sign-problem-free SU(2) point), we conclude that all four of these magnetic phases must be present in the phase diagram.

6.6.2 Loop length as a control parameter

To capture the full quantum phase diagram including the quantum spin liquid phases, we employ a limit inspired by the geometry in the hyperhoneycomb lattice. Its shortest loops are the 10-site decagons. Treating this loop length $\ell = 10$ as a large parameter and formally taking it to infinity, we find the loopless $\ell = \infty$ Cayley tree or Bethe lattice with $z = 3$ connectivity in infinite dimensions. The tree lattice approximation $\ell \to \infty$ enables a solution using entanglement-based methods originally developed for 1D systems, which rely on efficient representations of matrix or tensor product states (also known as projected entangled pair states PEPS). The key for such efficient representations is that entanglement is carried by bonds: cutting a single bond serves as an entanglement bipartition, and a singular value decomposition fully determines the entanglement spectrum which can be associated with this bond.

This tree lattice is infinite dimensional in the sense that for finite trees with N_s sites, a finite fraction of sites $f_s \approx (z-2)/(z-1)$ is on the boundary. But note that this is an opposite limit of infinite dimensionality from the one commonly taken in mean field theories, which assume infinite connectivity $z \to \infty$: here we crucially fix $z = 3$. Entanglement based algorithms within our infinite-D approximation can work with the low coordination number $z = 3$ and low spin $S = 1/2$, capturing the associated strong quantum fluctuations. As discussed below, we employ an algorithm which studies the tree lattice directly in its thermodynamic limit, with no boundary sites, directly as an infinite system.

6.6.3 Tensor networks on the tree lattice

The large loop $\ell \to \infty$ limit of the hyperhoneycomb (or higher harmonic honeycomb) lattice, which yields the infinite-D Bethe tree lattice, admits a numerical solution of the gapped phases in the phase diagram. The key is that cutting a single bond gives an entanglement bipartition (as shown in Fig. 6.9) with an entanglement spectrum which is associated with that bond. Hence gapped states can be represented efficiently as tensor product states (TPS, in other contexts also known as projected entangled pair states i.e. PEPS), and the full machinery of entanglement based algorithms can be used. We choose to use a variant of the infinite system size time-evolving block decimation algorithm (iTEBD)[205]. The iTEBD algorithm has been previously used to study various Hamiltonians via tree tensor networks, with phase

diagrams containing magnetic phases[175, 176, 157], nonmagnetic phases[160] and even a symmetry protected topological phase related to the AKLT Hamiltonian[113]. The iTEBD algorithm is especially useful here since it works directly in the thermodynamic limit (using iPEPS), avoiding the issues which plague finite trees.

Specifically, each update step in the algorithm, such as an imaginary time evolution step in iTEBD, must be followed by an operation which restores the state into a correctly normalized tensor product state. This requires cutting the TPS into two parts and computing the entanglement spectrum across the cut, via a singular value (i.e. Schmidt) decomposition. These singular values are associated with the bond and placed between the adjacent site tensors when one contracts the TPS in order to measure observables. The tree lattice offers all these properties and hence entanglement based algorithms developed for 1D systems may be adapted to the tree[175].

The iTEBD algorithm performs imaginary time evolution (i.e. soft projection to the ground state) within a restricted set of tensor product states, allowing it to find a good approximation to gapped periodic ground states with sufficiently local entanglement. Since it works on an infinite system, it always chooses one minimally entangled ground state, i.e. it can exhibit spontaneous symmetry breaking. To enable such symmetry breaking consistent with the expected magnetic ordering, we choose a unit cell with 8 site tensors and 12 bond (Schmidt) vectors as shown in Fig. 6.9, employing 24 update cycles in each imaginary time evolution step. On a technical note, we performed 2×10^7 singular value decompositions (SVDs) for each parameter point; to preserve normalized tensors during the imaginary time evolution, we intersperse evolution steps with zero imaginary time (i.e. pure SVD steps), as well as work with short time steps which are gradually reduced to 10^{-6} in inverse energy. The algorithm enables us to capture any periodic state consistent with our 8-site unit cell whose entanglement is sufficiently local, as is the case for the magnetically ordered phases we expect to find as well as for the gapped quantum spin liquids.

The key parameter for TPS algorithms is the bond dimension χ, serving as a cutoff on the number of entangled states. The computational costs scale polynomially in χ, but for computations on the tree the exponent is fairly high, with scaling of χ^6. The Kitaev-Heisenberg model harbors additional computational complexity due to its lack of spin rotation symmetry, the large unit cell necessary to describe its magnetic phases and the emergent small energy scales in its quantum spin liquid phases. Our results are roughly independent of χ for $\chi \geq 6$; we report data for computations using $\chi = 12$, after verifying convergence through $\chi = 6, 8, 10$. As we discuss below, the finite χ entanglement cutoff successfully collapses the degenerate ground-state manifold expected on the Bethe lattice into a single minimally entangled ground state, which is independent of these various values for χ. Hence we expect that finite (and perhaps not too large) χ is necessary for this mechanism which circumvents some of the issues which usually plague the Bethe lattice, but any χ within a large finite window will work well at enforcing a minimally entangled ground state.

6.6.4 Definition of Hamiltonian parametrization

The bond-anisotropic Kitaev-Heisenberg Hamiltonian, Eq. 6.1, involves one overall scale and and three free parameters. In computing the quantum phase diagram via tensor product states, we will focus on two of these parameters. The Kitaev exchange, generated by spin-orbit coupling, may be especially sensitive to the bond anisotropy; we therefore focus on the effects of bond anisotropy on the Kitaev term, leaving the study of the large-ℓ quantum phase diagram with Heisenberg term bond anisotropy for future work. Note however that we have performed calculations on the full Hamiltonian Eq. 6.1 in the neighborhood of the experimentally extracted parameter values shown in Fig. 6.3, finding the magnetic Stripy-X/Y phase and a nearby phase boundary to the magnetic Stripy-Z phase.

We shall now record the resulting two-parameter Hamiltonian, together with a few different useful parametrizations of its couplings, which we use to present various figures. In particular, we define polar coordinates with $r = 1 - a$ and two different angle parameters, ϕ or the alternative θ, corresponding to two differing conventions. The Hamiltonian parametrization is:

$$H = \sum_{\langle ij \rangle} \left[K_{\gamma_{ij}} S_i^{\gamma_{ij}} S_j^{\gamma_{ij}} + J \vec{S}_i \cdot \vec{S}_j \right] \tag{6.11}$$

$$K_{\gamma_{ij}} = K * \begin{cases} (1-a) & \text{on } \gamma_{ij} = x, y \text{ bonds} \\ (1+2a) & \text{on } \gamma_{ij} = z \quad \text{bonds} \end{cases}$$

$$K = 2\sin(\phi), \quad J = \cos(\phi); \quad \theta \equiv \pi/2 - \phi.$$

The Kitaev-Heisenberg spin Hamiltonian, with the angular ϕ parametrization[107] relating the strengths of Kitaev and Heisenberg coupling, is extended with this symmetry-allowed anisotropy, parametrized by $-1/2 \leq a \leq 1$.

Let us here also note the extension of the Klein duality discussed in section 6.6.1 above, to the case of nonzero anisotropy. Recall[107] that the Klein duality relates parameters by $\tan \phi' = -(1+\tan \phi)$ for the isotropic case $a = 0$. The transformation exposes a hidden ferromagnet even with anisotropy, at $\phi_{\text{hidden FM}} = -\arctan[1/(1-a)]$. Observe that the anisotropy reduces the symmetry at the hidden-FM point from SU(2) to U(1): the dual Hamiltonian is no longer Heisenberg but rather is an easy-axis ferromagnet. The key observation, that its ground state is an exact product state, remains unchanged.

For the pure Kitaev Hamiltonians, $a = 1/4$ is the transition point between the gapless ($-1/2 \leq a \leq 1/4$) and gapped ($1/4 < a \leq 1$) Z_2 spin liquid phases. In addition to the isotropic case $a = 0$ we focus on a particular anisotropy value within the gapped QSL regime, $a = 1/2$. We sample other values of the anisotropy as well in order to generate the global phase diagram shown in Fig. 6.2.

6.6.5 Magnetically ordered phases

Let us begin our analysis of the tensor product state computation by discussing the magnetic phases captured by the iTEBD algorithm on the tree lattice. We use a variety of measures to identify phases and the phase diagram. Magnetically ordered phases can be captured directly by their magnetic order parameter, since the iTEBD always produces a single symmetry broken ground state. This analysis is shown in Fig. 6.10 for the isotropic model, and in the appendix in Fig. 6.15 for $a = 1/2$ anisotropy. The four magnetic phases expected from the discussion in section 6.6.1 above are observed. Phase transitions are also identifiable, as always, through the first and second derivatives of the energy. As a simple benchmark we have verified that the energy is always bounded from above by the energy of the expected classical product state and from below by the optimal energy for any given site in its surrounding cluster[93], as may be seen in Fig. 6.15. Phase transitions are also signaled by peaks in the entanglement carried by the various bonds in the tensor product state, and finally of course the phases can be identified using the spin-spin correlation functions; these two measures are shown in Fig. 6.17. We also verify that the entanglement correctly vanishes at the exact (hidden-)ferromagnet points.

The particular parameters of the direct first order phase transitions between the magnetic phases should be insensitive to dimensionality and loop length ℓ for sufficiently large ℓ, since the quantum fluctuations on top of these classical phases need to propagate a distance of ℓ sites to distinguish one lattice from another. The smallest value for ℓ we encounter is $\ell = 6$, so quantum fluctuations in these magnetic orders must traverse at least six nearest-neighbor bonds to distinguish the honeycomb from the stripyhoneycomb or hyperhoneycomb lattices. Hence we expect that the 2D honeycomb, 3D harmonic honeycomb and infinite-D tree lattices will exhibit similar magnetic transitions. Indeed the parameters we find for the tree lattice within iTEBD are essentially indistinguishable from those of the 2D honeycomb model[107]. As a function of anisotropy, the location of magnetic transitions can also be compared to a classical mean field theory. We find similar behavior, with larger differences closer to the isotropic point; see Appendix 6.14 for details.

6.6.6 The quantum spin liquid in a tree tensor network

Turning to the phase diagram of the QSL phases and their immediate surrounding, we first must restrict ourselves to the regime with sufficiently strong anisotropy so that the emergent majorana fermions are gapped, at $a > 1/4$. The gapped spin liquids can be well approximated by the tensor product states we use. In Fig. 6.11 we show the spin liquid phase for $K < 0$ and the nearby stripy and ferromagnetic orders. The identity of the spin liquid is already suggested by its lack of magnetic order parameter; phase transitions to this un-ordered phase are again seen in energy derivatives and as peaks in the entanglement entropies. The extent of the phase in

this computation is small, covering about a tenth of a percent of the phase diagram, but nonzero; more importantly, the extent of the spin liquid is the same throughout the full range of bond dimensions we study, implying that its stability is a consequence of any finite entanglement cutoff.

Though its lack of conventional spin order is suggestive, the QSL phase completely lacks any order parameter and thus avoids a direct identification of the type in Fig. 6.10. The exact solution of the Kitaev model on the infinite-D tree allows us to uncover the unique fingerprints of the exact QSL, and use them to unequivocally identify the QSL phase within iTEBD. Each such set of fingerprints can be computed as a function of anisotropy for the pure Kitaev model across the entire gapped phase $1/4 < a < 1$.

One obvious measure is the energy as a function of a within the Majorana solution, for which we find good agreement as shown in Fig. 6.18; but energies are notoriously lousy fingerprints for spin liquid phases. We also compute the spin-spin correlators within the iTEBD and find that they match the correlators we compute within the exact solution, as shown again in Fig. 6.18. Correlation functions are a more robust measure, but are still grossly insufficient for fully characterizing the long ranged entangled QSL.

Instead, the most valuable set of fingerprints is furnished by the entanglement entropy carried by each bond. The entanglement spectrum is an inherent part of the tensor product state description and is easily accessible from the iTEBD. Spurious "accidental" symmetry breaking exhibited by the iTEBD ground state, caused by the large unit cell and the merely finite imaginary time evolution duration, complicates the bond entanglement entropies but still permits comparison with the entanglements computed in the exact solution. This comparison is shown in Fig. 6.12, confirming that the iTEBD algorithm is indeed capturing the emergent Majorana fermions of the quantum spin liquid fractionalized phase in infinite dimensions.

Fig. 6.12 exhibits an important subtlety: the entanglement entropies from the exact solution match those from the iTEBD computation only if we assume that the gauge field sector contributes entanglement only on bonds set as strong by the anisotropy parameter. To understand this key subtlety, we now turn to the study of the exact Kitaev $\mathbb{Z}_2$ quantum spin liquid on the loopless tree lattice, focusing first on the fermion sector followed by the more subtle $\mathbb{Z}_2$ gauge field sector.

6.6.7 Majorana fermion entanglement

The spectrum of Majorana fermions hopping on the infinite tree can be computed exactly[109] using recursion on propagators (appendix 6.11). However, we are mainly interested in the entanglement entropies associated with a bipartition, which we choose to compute on finite open trees. The spectrum of a finite tree adjacency matrix has an extensive number of zero modes, which may be counted for any finite tree by noting that the number of bonds is $N_b = N_s - 1$, reduced from the expected

$N_s z/2$ by a fraction $f_b \approx (z-2)/z$; ie about $N_s/3$ of the eigenvalues are finite size boundary effects. For a site-centered tree they may be counted exactly using Lieb's sublattice imbalance theorem[158] by observing the unbalanced occupation in the bipartite tree's A and B sublattices, $|N_B - N_A|/N_s = (z-2)/z + 1/N_s$. On a bond-centered tree, in addition to the identically zero boundary eigenvalues there is an isolated low-lying eigenvalue whose gap vanishes with increasing system size, which is also associated with the boundary. We may thus take the bulk tree thermodynamic limit by discounting these boundary eigenvalues of finite tree adjacency matrices.

This finite tree thermodynamic limit, though convergent, may yield answers which are different from recursive computations directly on the infinite Bethe lattice for some physical quantities[109][1]. For example, the phase transition between the gapped and gapless phases computed by recursion equations for Green's functions (see appendix 6.11 for detail) find a phase boundary, as a function of hopping anisotropy, which is identical on the finite dimensional lattices but different on the Bethe lattice. However, we expect (and indeed show below) that total energy and the entanglement entropy in the thermodynamic limit of finite trees, with appropriate subtraction of the thermal entropy of the boundary described below, provide the correct thermodynamic limit for comparison with the iTEBD tensor network.

Using the bulk fermion correlation function and the reduced correlator for a bipartition associated with cutting the central bond in a bond centered-tree, we first compute the entanglement spectrum and entropy of the bipartition, which resides on this central bond. A second approach for computing the entanglement entropy entails subtracting the $T = 0$ thermal entropy of the finite open tree from the naively computed entanglement entropy of the bipartition, which again yields the entanglement entropy of the single bond cut without the $T = 0$ thermal entropy of the boundary zero modes. See details in appendix 6.10. The approaches agree, and thus are expected to yield the entanglement entropy contributed by the fermion sector of the exact quantum spin liquid.

6.6.8 $\mathbb{Z}_2$ gauge theory on the loopless tree

Entanglement is also contributed by the $\mathbb{Z}_2$ gauge sector of the tree Kitaev model; in order to describe this contribution we shall now discuss the unusual subtleties which arise in a $\mathbb{Z}_2$ gauge theory on a loopless lattice. We begin by noting that the gauge theory is necessarily well defined even on the loopless tree lattice, since it arises from a well defined spin model. For N_s sites there are $N_s/2$ gauge-invariant sectors after projecting the gauge fields, which combine with the $N_s/2$ majorana fermion degree of freedom to give the N_s doublet degrees of freedom for the lattice of $S = 1/2$. In 2D the $N_s/2$ sectors are labeled by fluxes; in 3D, by magnetic field loops; and in infinite dimensions, they may be associated with $N_s/2$ particular infinite magnetic

[1] We thank Frank Pollmann for pointing out this subtlety.

field lines extending across the (infinite) lattice. These field lines stretching across the system are intimately related to a more familiar set of infinite products of operators: in 2D topologically ordered phases, field lines can wind around the periodic boundary conditions. The resulting flux piercing the torus costs an energy which vanishes in the thermodynamic limit, and these operators generate the topological ground state degeneracy on the torus. On the tree lattice there is an extensive number of such operators, contributing an extensive ground state degeneracy $2^{N_s/2}$.

This degeneracy may also be seen by counting conserved quantities associated with infinite products of local operators within the original quantum spin Hamiltonian. Working either within the original spin model or within the gauge theory, we must count the number of such independent paths on the tree lattice. A moment's thought shows that independent paths may be counted as paths from a given boundary site to any other boundary site on a finite open tree. For the purposes of this counting the open tree may be compactified by identifying all boundary sites, in which case the strings again form conventional closed loops carrying a flux. The counting gives exactly $N_{\text{boundary sites}} - 1 = N_s/2$ operators, in agreement with the gauge field mechanism for $2^{N_s/2}$ degeneracy. Thus on the tree lattice within a full thermodynamic limit, the gauge theory collapses to an extensive degeneracy of $2^{N_s/2}$ states.

6.6.9 Minimally entangled states of the $\mathbb{Z}_2$ gauge theory on the loopless tree

A $\mathbb{Z}_2$ gauge theory contributes $\log 2$ of entanglement for every two bonds in the entanglement cut, or $\log(2)/2$ entanglement per bond[**?**]. Intuitively, the gauge field carries half of the information content of a physical gauge-invariant $\mathbb{Z}_2$ link variable. An additional global term of the topological entanglement entropy is generally expected to arise in the gauge theory, but does not appear on the tree lattice single-bond entanglement bipartitions: the only entanglement is that associated with the bond. Thus on the tree lattice we expect the single bond entanglement cut to carry $\log(2)/2$ entanglement from the gauge sector, in addition to any fermionic entanglement.

However, when comparing to the iTEBD result, we find that the iTEBD choice of ground state within the gauge theory's degenerate manifold effectively quenches the $\mathbb{Z}_2$ gauge sector entanglement on weak bonds, giving gauge sector entanglement only on strong bonds, which retain the gauge field entanglement $\log(2)/2$. This is reasonable since there are two $S = \log(2)/2$-carrying weak bonds per two sites, giving exactly the $\log 2$ value of entanglement associated with the twofold degeneracy also found per two sites. Thus for the iTEBD ground state on the tree, unlike for the unique ground state on the planar honeycomb, the entanglement entropy on various bonds is continuous in the Toric Code limit $a \to 1$, with weak bonds carrying vanishing entanglement like for the disjointed singlets Hamiltonian $a = 1$. The strong bonds carry entanglement of $\log(2)/2$ from the fermion sector plus $\log(2)/2$ from the gauge

field sector, but for the weak bonds the fermionic entanglement vanishes and the gauge field entanglement is quenched by the minimally entangled superposition across flux sectors.

The finite bond dimension χ entanglement cutoff of the iTEBD algorithm is likely playing the key role here, collapsing the extensive degeneracy of the gauge theory on the tree into a particular minimally entangled state which is then chosen by iTEBD as the ground state. It will be interesting to explore whether this mechanism, of a ground state selected from an extensive degenerate manifold through a minimal-entanglement constraint, changes its role if the bond dimension is vastly increased.

Armed with the understanding of these subtleties, we thus find that aside from some spurious spontaneous symmetry breaking due to the infinite system size explored by the iTEBD algorithm, the entanglement entropy of the resulting iTEBD QSL ground state, as well as its energy and correlators, exhibit close agreement with these predictions of the exact QSL solution on a finite tree, as shown in Figs. 6.12 and 6.18. The TPS computation with the finite entanglement cutoff produces a minimally entangled state within the QSL manifold, elegantly bypassing artifacts due to the Bethe lattice lack of loops to successfully capture emergent Majorana fermions within the spin model at infinite dimensions.

6.7 Conclusion

In this work we have analyzed experimental data to motivate a magnetic Hamiltonian with large Kitaev exchanges, on the hyperhoneycomb and stripyhoneycomb lattices formed by Ir in β- and γ-Li_2IrO_3. Anisotropy in the strength of couplings between z bonds and the x, y bonds is expected from the crystal symmetries, and enables a fit to the experimental susceptibility measurements, requiring strong Kitaev exchange.

We first focus on the pure-Kitaev models and discuss the exactly solvable 3D spin liquid, some of whose most interesting features are unique to three dimensionality. These features include the extended magnetic flux loop excitations as well as the existence of a finite temperature deconfined phase, neither of which can occur in the 2D honeycomb model.

Describing the Li_2IrO_3 materials also requires some Heisenberg exchange, so we compute the quantum phase diagram as a function both of the additional Heisenberg exchange and of the coupling-strength bond anisotropy parameter. Our approximation of choice is to study this system on the Bethe lattice, the tree with no closed loops. This is expected to capture the basic physics on the 3D harmonic honeycomb lattices, due to the long length of their shortest closed loop ($\ell = 10$ for the hyperhoneycomb lattice or $\ell = 6, 14$ for the stripyhoneycomb lattice). This large-ℓ approximation admits no analytical solution, but rather is numerically tractable via a class of entanglement-based algorithms. We use a TPS representation of the ground

state, which is then determined using the iTEBD algorithm directly in the thermodynamic limit. Both the magnetically ordered phases as well as the gapped quantum spin liquid phases are obtained and positively identified using this technique.

The exact 3D quantum spin liquid together with this large-ℓ approximation provide a controlled study of 3D fractionalization. Although experimentally both of the 3D harmonic honeycomb Li_2IrO_3 polymorphs appear to be magnetically ordered[199, 173], the significant Kitaev couplings indicated by experiments are promising, and suggest future directions to realize 3D QSLs in these bulk solid state systems by tuning magnetic interactions via pressure or chemical composition.

Appendices:

The sections which follow should be considered as appendices, and are more technical.

6.8 Coordinates for the lattices

In this section, we define the 3D honeycomb-like lattices discussed in the paper. For simplicity, throughout this paper we work with idealized symmetric versions of the true Ir lattices in the crystals.

We use the same parent orthorhombic coordinate system to describe both lattices. This is the coordinate system defined by the following conventional orthorhombic crystallographic vectors:

$$\boldsymbol{a} = (2, 2, 0), \quad \boldsymbol{b} = (0, 0, 4), \quad \boldsymbol{c} = (6, -6, 0). \tag{6.12}$$

In the equation above we have written the a, b, c vectors in terms of a Cartesian (cubic orthonormal) x, y, z coordinate system. The $\hat{x}, \hat{y}, \hat{z}$ lattice vectors in this coordinate system are defined as the vectors from an iridium atom to its neighboring oxygen atoms in the idealized cubic limit, with distance measured in units of the Ir-O distance. Nearest neighbors in the resulting Ir lattice are at distance $\sqrt{2}$.

For each lattice, we express its Bravais lattice vectors, as well as each of its sites of its unit cell, in terms of the a, b, c axes. A given vector or site, written as (n_a, n_b, n_c), can be converted to the Cartesian coordinate system by the usual matrix transformation $(n_x, n_y, n_z) = n_a\vec{\boldsymbol{a}} + n_b\vec{\boldsymbol{b}} + n_c\vec{\boldsymbol{c}}$. For both of the lattices, the conventional crystallographic unit cell, containing 16 sites, is found by combining the primitive unit cell with the Bravais lattice vectors.

6.8.1 Hyperhoneycomb lattice ($n = 0$ harmonic honeycomb), space group $Fddd$ (#70):

Primitive unit cell (4 sites):

$$\left(0,0,0\right);\ \left(0,0,\frac{1}{6}\right);\ \left(\frac{1}{4},\frac{-1}{4},\frac{1}{4}\right);\ \left(\frac{1}{4},\frac{-1}{4},\frac{5}{12}\right) \tag{6.13}$$

This unit cell is formed by a single 16g Wyckoff orbit of $Fddd$, position $(1/8, 1/8, z)$ with possible equivalent values of z including $z = 5/24$ (which shifts the unit cell above by $(1/8, 1/8, 1/24)$) and $z = 17/24$ (with the same shift plus an additional $(1/2, 0, 0)$).

Bravais lattice vectors (face centered orthorhombic):

$$\left(\frac{1}{2},\frac{1}{2},0\right);\ \left(\frac{1}{2},-\frac{1}{2},0\right);\ \left(\frac{1}{2},0,\frac{1}{2}\right). \tag{6.14}$$

6.8.2 Stripyhoneycomb lattice ($n = 1$ harmonic honeycomb), space group $Cccm$ (#66):

Primitive unit cell (8 sites):

$$\begin{aligned}&\left(0,0,0\right);\ \left(0,0,\frac{1}{6}\right);\ \left(\frac{1}{4},\frac{-1}{4},\frac{1}{4}\right);\ \left(\frac{1}{4},\frac{-1}{4},\frac{5}{12}\right);\\ &\left(0,0,\frac{1}{2}\right);\ \left(0,0,\frac{2}{3}\right);\ \left(\frac{1}{4},\frac{1}{4},\frac{3}{4}\right);\ \left(\frac{1}{4},\frac{1}{4},\frac{11}{12}\right)\end{aligned} \tag{6.15}$$

The sites $(0, 0, 1/6)$ and $(1/4, 1/4, 1/12)$ together represent the unit cell (shifted by $(0, 0, 1/6)$ from $(0, 0, 0)$) as the union of two distinct Wyckoff orbits, 8i with $z = 1/6$ and 8k with $z = 1/12$ ($Cccm$ origin choice 1).

Bravais lattice vectors (base centered orthorhombic):

$$\left(\frac{1}{2},\frac{1}{2},0\right);\ \left(\frac{1}{2},-\frac{1}{2},0\right);\ \left(0,0,1\right). \tag{6.16}$$

6.9 Lattice tight-binding model and Majorana spectrum

In the Kitaev spin liquid at its exactly solvable parameter point, the emergent Majorana Fermion hops within the nearest-neighbor tight binding model on the lattice. Its band structure (fixed to half filling) is given by the eigenvalues of the nearest-neighbor tight-binding matrix of the lattice.

We now give these matrices for both lattices. For the hyperhoneycomb lattice, this matrix is

$$\begin{pmatrix} 0 & u^2 & 0 & \bar{u}c_+ \\ \bar{u}^2 & 0 & uc_- & 0 \\ 0 & \bar{u}c_- & 0 & u^2 \\ uc_+ & 0 & \bar{u}^2 & 0 \end{pmatrix} \tag{6.17}$$

We have used the following symbols to represent functions of wavevector q,

$$u = \frac{1}{\bar{u}} = \exp\left(i\vec{q}\cdot\frac{\vec{c}}{12}\right),\ c_\pm = 2\cos\left(\vec{q}\cdot\frac{(\vec{a}\pm\vec{b})}{4}\right)$$

To convert them to the Ir-O Cartesian axes, recall that $\frac{\vec{c}}{12} = \frac{\hat{x}-\hat{y}}{2}$ and $\frac{(\vec{a}\pm\vec{b})}{4} = \frac{\hat{x}+\hat{y}}{2} \pm \hat{z}$. For the stripyhoneycomb lattice, the unit cell has 8 sites and so we shall write an 8×8 matrix. By choosing an enlarged 8-site unit cell for the hyperhoneycomb lattice, we can represent the tight-binding matrices for both lattices in similar notation. In the following matrix, the upper sign choice for the functions $c_\pm, c_\mp$ corresponds to the stripyhoneycomb lattice, while the lower sign choice corresponds to the hyperhoneycomb lattice with the enlarged unit cell. These tight-binding matrices are

$$\begin{pmatrix} 0 & u^2 & 0 & 0 & 0 & 0 & 0 & \bar{u}c_+ \\ \bar{u}^2 & 0 & uc_- & 0 & 0 & 0 & 0 & 0 \\ 0 & \bar{u}c_- & 0 & u^2 & 0 & 0 & 0 & 0 \\ 0 & 0 & \bar{u}^2 & 0 & uc_\mp & 0 & 0 & 0 \\ 0 & 0 & 0 & \bar{u}c_\mp & 0 & u^2 & 0 & 0 \\ 0 & 0 & 0 & 0 & \bar{u}^2 & 0 & uc_\pm & 0 \\ 0 & 0 & 0 & 0 & 0 & \bar{u}c_\pm & 0 & u^2 \\ uc_+ & 0 & 0 & 0 & 0 & 0 & \bar{u}^2 & 0 \end{pmatrix} \tag{6.18}$$

The determinant of these matrices is the same for both lattices, simplifying to $\det = (1 - 2\cos(q\cdot c)S_{ab} + S_{ab}^2)$ with S_{ab}=$4(\cos(q\cdot a/2)+\cos(q\cdot b/2))^2$. In this notation, it is evident that the zeros of the spectrum, found by setting the determinant to zero, are identical for both lattices and appear at the contour of momenta characterised by the two equations $\vec{q}\cdot\vec{c} = 0$ and $\cos(\vec{q}\cdot\vec{a}/2) + \cos\left(\vec{q}\cdot\vec{b}/2\right) = 1/2$. Note that the BZ for the 8-site unit cells is bounded by $\vec{q}\cdot\vec{c} = \pi$, $\vec{q}\cdot\vec{a} \pm \vec{q}\cdot\vec{b} = 2\pi$.

6.10 Entanglement entropy from the Majorana-fermions of the quantum spin liquid

At the exact QSL point we wish compute the entanglement entropy (and the energy) for the ground state on the tree, in order to compare this exact result to

the iTEBD computation. Within the gapped phase of the pure Kitaev (anisotropic) Hamiltonian, the system can be exactly mapped to a free majorana fermion problem with a gapped spectrum. We can thus compute quantities on finite trees independently of the iTEBD algorithm, within the majorana fermion mapping. Computing energies is straightforward and we find convergence to the thermodynamic limit using the boundary-eliminating procedure described above on trees with up to 9 layers. To describe the entanglement entropy results, let us first recall the computation of entanglement spectrum and entropy for free fermion systems[183, 115, 216, 204]. Operating on a bond-centered finite tree, we compute the correlation function by occupying half of the majorana spectrum. The reduced correlation function associated with a cut through the central bond is found by restricting the site indices of the correlator to lie within one of the two partitions. Each eigenvalue c_i of the reduced particle correlator also has an associated hole eigenvalue $1 - c_i$. The entanglement entropy of the bipartition can be computed from the particle and hole correlators, with a factor of $1/2$ for majoranas, by $S_E = -(1/2)\sum_i [c_i \log c_i + (1 - c_i)\log(1 - c_i)]$.

To eliminate tree finite size effects for computing the entanglement entropy in the fermion sector of the spin liquid, we use two approaches. In the first approach, we carefully determine which of eigenvalues of the open tree adjacency matrix are associated with the bulk, using the counting procedure described above, and keep only the eigenstates associated with these eigenvalues when computing the correlation function for the entanglement bipartition. In the second approach, we subtract the $T = 0$ thermal entropy of finite L-layered trees (with open boundary conditions) from the reduced density matrix entanglement entropy of each such tree under a bipartition through the center bond. This difference gives purely the entanglement entropy associated with the single bond cut, without the thermal entropy of the numerous zero modes of the boundary. We find agreement between the two approaches as the system size is increased (and the isolated boundary eigenvalue of the bond-centered tree vanishes).

6.11 Anisotropic hopping on the infinite Bethe lattice

We compute the density of states on a Bethe lattice directly in the thermodynamic limit[100], where all sites are identical but each site has different hopping strengths t_i $(i = 1, ..., z)$ on the z bonds connecting it to other sites. Expressing the diagonal (onsite) Green's function in terms of a self energy,

$$G(\omega) = \frac{1}{\omega(1 - S(\omega))} , \quad S = \sum_{i=1}^{z} \sigma_i$$

where we suppress notational dependence on ω; and where σ_i is the self energy contributed from forward hopping starting from a t_i hop. It obeys the following recursive

system of questions:

$$\sigma_i = \frac{t_i^2}{\omega^2} \frac{1}{1 - \sum_{j \neq i} \sigma_j}$$

These may be rewritten as a set of quadratic equations, with implicit dependence only on S,

$$\sigma_i^2 + (1 - S)\sigma_i - t_i^2 \omega^2 = 0$$

Solving this quadratic equation (the positive root is taken) and summing over i, we find a single equation for the self energy S. We may then rewrite it directly as an implicit equation for the inverse Green's function G^{-1},

$$(z-2)G^{-1} + 2\omega = \sum_{i=1}^{z} \sqrt{(G^{-1})^2 + 4t_i^2}$$

The density of states ρ is proportional to the imaginary part of G (in this notation $\rho = -\text{Im } G/\pi$). The system is gapless here if there is a solution with nonzero DoS at zero energy. Writing $r = 2\pi\rho(0)$, the equation to be solved is

$$(z-2) = \sum_{i=1}^{z} \sqrt{1 - t_i^2 r^2}$$

Let us analyze where a solution to this equation first appears. At $r = 0$, the RHS is equal to z and is greater than the LHS. The RHS decreases monotonically with r. However, r takes values between 0 and $r_{max} = 1/\max_i[t_i]$. The RHS takes its minimum value at r_{max}. The phase boundary between the gapped and gapless phases occurs when this minimum value of the RHS is just barely equal to the LHS, i.e.

$$(z-2) = \sum_{i=1}^{z} \sqrt{1 - \left(\frac{t_i}{t_{max}}\right)^2}, \quad t_{max} = \max_i[t_i]$$

Let us consider this solution for the case when all hoppings $t_i = t$ are equal except one, t_m, which is larger than the rest. The phase boundary then occurs at

$$t = \sqrt{2z-3}\frac{t_m}{(z-1)}\ ; \qquad z = 3 \ \rightarrow \ a = \frac{2-\sqrt{3}}{2+2\sqrt{3}} \approx 0.05$$

In the loopless infinite $D = \infty$ Bethe lattice, the extent of the gapless phase is shrunk compared to its extent on the $D = 2, 3$ finite-dimensional lattices. Indeed, the iTEBD computations, which are expected to break down for a gapless phase, are able to capture the gapped spin liquid characteristics down to $a \approx 0.15$, until they break down in a first order transition to full symmetry breaking.

6.12 Harmonic honeycomb series

In the notation for the n-harmonic honeycomb lattice, the integer n counts the number of hexagons forming the width of each fixed-orientation planar strip. Or equivalently, going along the direction of the special c axis, the integer $n+1$ specifies the number of z-bonds between switches of the x,y bonds orientation. Odd-n lattices posses a mirror plane perpendicular to the special axis, slicing through the midpoint of the (odd number of) hexagons; even-n lattices possess no mirror reflections, only glide planes. In this manuscript we focus on two lattices: the $n = 1$ stripyhoneycomb lattice, space group *Cccm*, recently synthesized[173] as a polytype of Li_2IrO_3, with $\ell = 6$ hexagon as well as $\ell = 14$ sized minimal loops; and the $n = 0$ hyperhoneycomb or hyperhoneycomb lattice, space group *Fddd*, with $\ell = 10$ decagon minimal loops. The two lattices are shown in Figures 6.1 and 6.4 respectively.

The "hyperhoneycomb" terminology for the hyperhoneycomb lattice may be understood through the following connection to the hyperkagome lattice (also related to the hyperoctagon lattice[124]). Consider the 2D kagome and honeycomb lattices[2]. The kagome is the *medial lattice* — formed by connecting bond midpoints – of the honeycomb lattice. This relation naturally suggests the existence of 3D honeycomb-like lattices which can be similarly associated with the 3D hyperkagome[181] lattice, the three dimensional lattice of corner-sharing triangles formed by iridium ions in $Na_4Ir_3O_8$. Indeed, the medial lattice of the hyperhoneycomb lattice has a graph (or, an adjacency matrix) which is, locally, identical to that of the hyperkagome: both feature corner-sharing triangles which combine to form $\ell = 10$ decagon loops. These decagons arise from the $\ell = 10$ minimal loops of the hyperhoneycomb lattice.

6.13 Mean field for Stripy-X/Y order

We briefly recall the self consistency equation for the mean field $S = 1/2$ moment, $2|\vec{m}_i| = \tanh[|\vec{\widetilde{B}_i}|/(2T)]$ and $\hat{m}_i = \hat{\widetilde{B}}_i$, where $\widetilde{B}_i$ is the mean field coupling to spin S_i. The spins develop a moment at a transition temperature $T_N = 2E_{site}$, where E_{site} is the classical energy per site in the ordered state (e.g. $-(1/4)(z/2)J$). Above the transition temperature the mean field produces the Curie-Weiss law, $\chi^{rr} = (g^r)^2\mu_B^2/\left(4T + \sum_j J^{rr}_{i_0 j}\right)$, where $\sum_j J^{rr}_{i_0 j} = zJ$ for nearest neighbor J. Experimentally relevant units may be restored by noting that $\mu_B = 0.672$ kelvin/tesla. In the Stripy-X/Y order, the classical mean field $\vec{\widetilde{B}_i}$ takes the form

$$\begin{aligned}\vec{\widetilde{B}_i} = g\mu_B\vec{B} - (K_d m_i^x\hat{x} + K_d m^y_{n[i]}\hat{y} + K_c m^z_{n[i]}\hat{z} \\ + J_c\vec{m}_{n[i]} + J_d\vec{m}_{n[i]} + J_d\vec{m}_i)\end{aligned} \tag{6.19}$$

[2]this construction was suggested by Christopher Henley[122, 123].

and every site carries one of two magnetizations, $\vec{m}_i$ or $\vec{m}_{n[i]}$.

Note that for the model Hamiltonians we consider, the principal axes of the susceptibility tensor are be x, y, z rather than the crystallographic axes a, b, c. Terms arising from the global symmetries of the crystal will likely change the principal axes to match the crystallographic ones. To compare with experiment without adding any such additional terms, we measure the susceptibility tensor along the crystallographic axes as shown in Fig. 6.3. The weakly anisotropic g-factors, experimentally determined at high temperature for each of the crystallographic axes, are then incorporated into each axis of χ. We use the g-factors $g^{x+y} = g^z = 1.95$, $g^{x-y} = 2.35$. Note that the overall scale of the g-factors needed to fit the susceptibility, which was measured experimentally on a single crystal, carries an additional uncertainty associated with the uncertainty of estimating the number of Li_2IrO_3 formula units in the crystal.

6.14 Comparison of magnetic transitions in iTEBD and mean field theory

Magnetic phases can be approximately described within a classical mean field theory. Such classical product states over sites, with no quantum fluctuation or entanglement, correspond to tensor product states with bond dimension $\chi = 1$. On the Bethe lattice, we have captured the magnetically ordered phases using tensor product states with various χ. We find that increasing χ to a value as low as $\chi = 4$ is sufficient for capturing most of the quantum fluctuations near a first order transition between adjacent magnetic phases. The location in parameter space of these transitions can be compared to the classical transition point. Classically, the transition occurs at $\phi = n\pi - \text{arccot}[2 + a]$, for anisotropy a, with $n = 1$ for the zigzag-FM transition and $n = 2$ fo the Stripy-Neel transition. This comparison is shown in Fig. 6.13. For concreteness, we also draw sample magnetic configurations on the hyperhoneycomb lattice, shown in Fig. 6.14.

6.15 Additional iTEBD results

Here we present additional figures with results from the iTEBD computation, as described in the main text and in the figure captions. The results are shown in Figures 6.15, 6.17, 6.16, and 6.18.

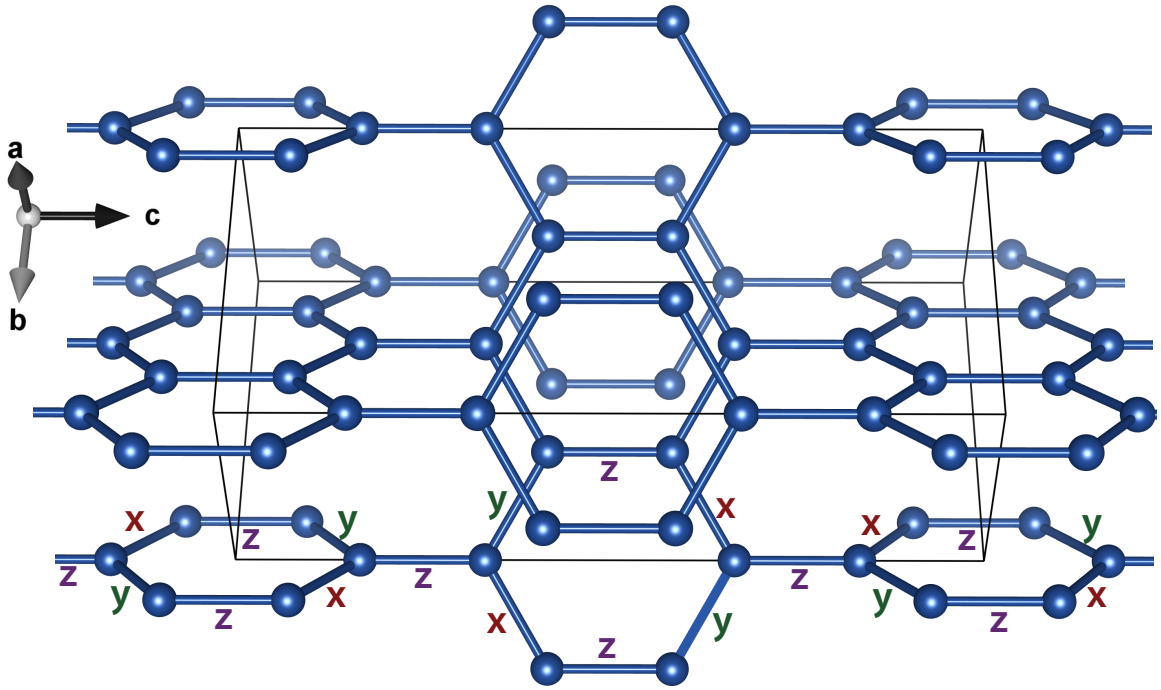

Figure 6.1: **T**he stripyhoneycomb lattice of iridium in γ-Li_2IrO_3. The recently synthesized stripyhoneycomb lattice (space group #66 *Cccm*) has threefold coordinated sites, which form hexagons arranged in stripes of alternating orientation. It is the n=1 member of the harmonic honeycomb[173] series of structures; the distinct hyperhoneycomb lattice of β-Li_2IrO_3 (Fig. 6.4) has n=0. Parent orthorhombic coordinate system and unit cell (boxed) are shown. In the limit of superexchange via ideal oxygen octahedra, the magnetic Hamiltonian is dominated by Kitaev-type couplings (x,y,z labels at bottom), leading to an exactly solvable model of a 3D quantum spin liquid.

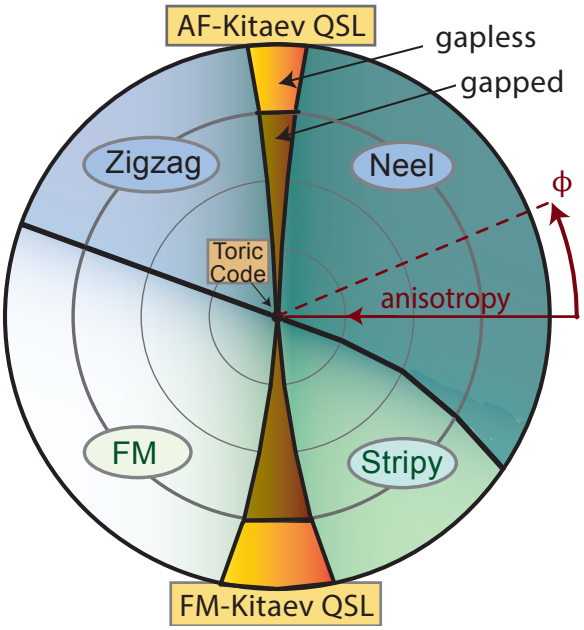

Figure 6.2: **Q**uantum phase diagram in the large-ℓ limit. Phase diagram of the frustrated quantum Hamiltonian Eq. 6.1, computed via tensor network states within an infinite-D or large-$\ell \to \infty$ approximation to the hyperhoneycomb's $\ell = 10$. Except for quantitative extent of QSLs (not to scale), we expect it to describe the stripyhoneycomb and hyperhoneycomb lattices of γ- and β-Li_2IrO_3, for which we argue this is a physical model. The 2-parameter space shown here (Eqs. 6.1,6.11) has polar axes r tuning symmetry-allowed Kitaev bond anisotropy and ϕ setting relative strength of Kitaev and Heisenberg interactions. The QSL phases, successfully stabilized on the Bethe lattice by the algorithm's finite entanglement cutoff χ, were identified by an entanglement fingerprint.

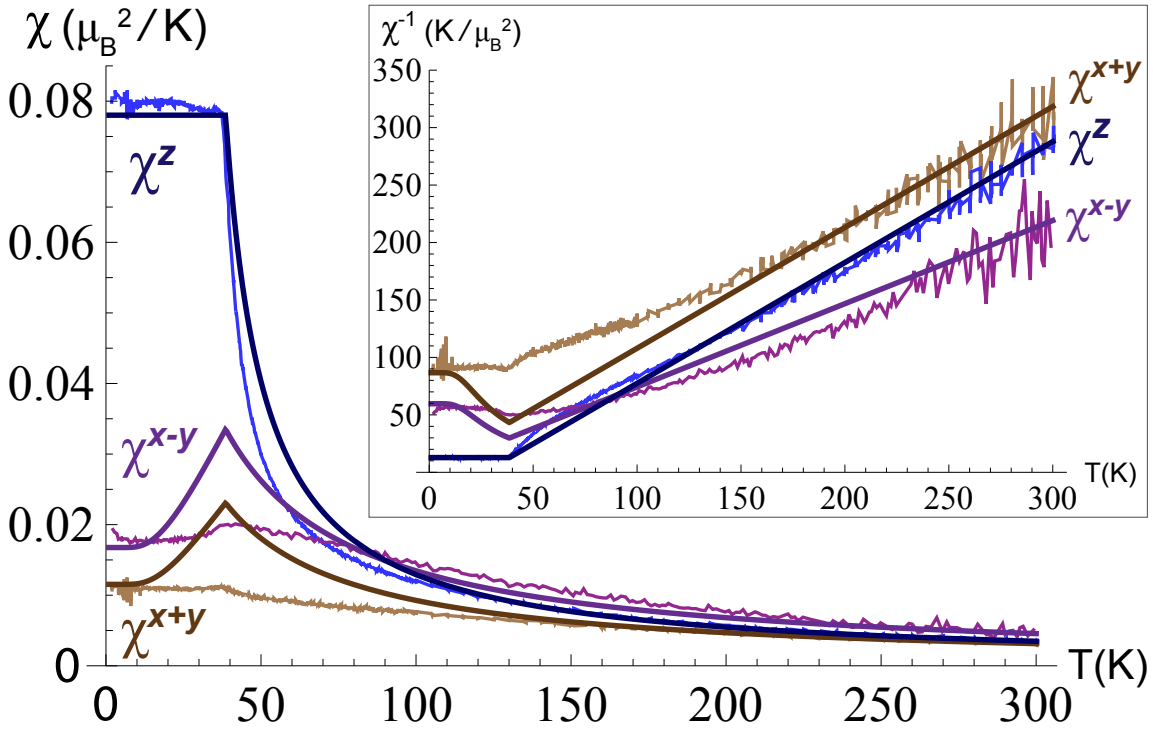

Figure 6.3: **S**trong Kitaev exchanges capturing γ-Li_2IrO_3 anisotropic susceptibility. Magnetic susceptibility (inset: inverse susceptibility) along principal axes (z=b; $x\pm y$=a, c), measured[173] for a γ-Li_2IrO_3 crystal (bright lines) and theoretical mean field fit (dark lines). Susceptibility is fitted by the minimal Hamiltonian Eq. 6.1 with parameters (K_c, K_d, J_c, J_d) at $(-17, -7, 6.3, 0.8)$ meV; magnetic order (recently found[98] to be a noncoplanar spiral) is captured[98] by Eq. 6.1 at $(-15, -12, 5, 2.5)$ meV, supplemented by c-axis Ising exchange on c-bonds and J_2 Heisenberg exchange on second-neighbors. In both cases, large Kitaev exchanges K_c, K_d are necessary to describe the material.

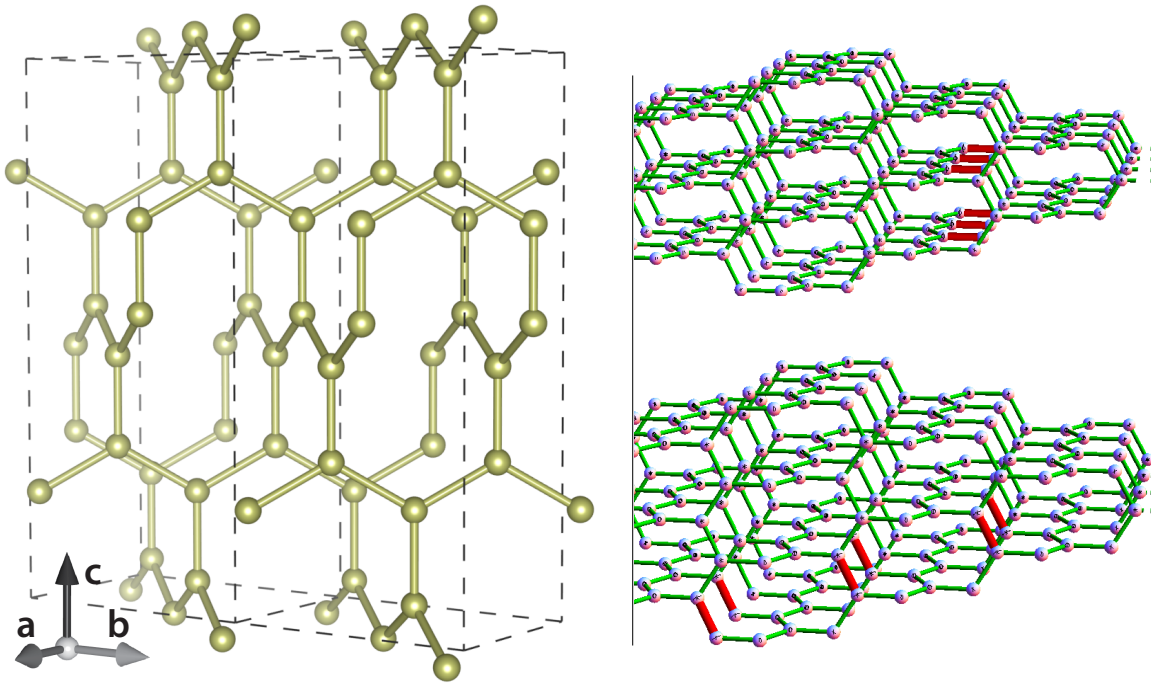

Figure 6.4: **T**he hyperhoneycomb lattice of Ir in β-Li_2IrO_3. The hyperhoneycomb lattice (space group is #70 *Fddd*) has threefold coordinated sites and is the n=0 member of the harmonic honeycomb structural series. Its shortest loops are 10-site decagons, motivating the large-ℓ loop length approximation for solving the frustrated quantum Hamiltonian on the 3D lattice. Right: $\mathbb{Z}_2$ flux loops in the QSL phase. Selected bonds (dark orange) of type z (top right) or x, y (bottom right) are chosen to host nonzero vector potential $u_{i,j} = -1$ within the QSL $\mathbb{Z}_2$ gauge sector, producing a $\mathbb{Z}_2$ closed flux loop excitation, which encircles these bonds.

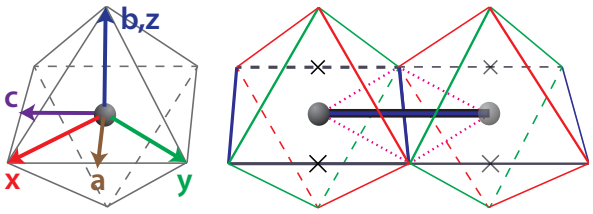

Figure 6.5: **E**dge sharing IrO_6 octahedra in the 3D lattices. Iridium (purple sphere) is coordinated by six oxygens forming vertices of an octahedra. When octahedra share edges as shown, the exchange pathways (dotted purple lines) give rise to Kitaev interactions, coupling a spin component $\gamma \in \{x, y, z\}$ normal to that Ir-Ir bond and to the shared edge (shown in corresponding color {red, green, blue}). Octahedron at left shows the relation between the Ir-O x, y, z axes and the crystallographic parent orthorhombic a, b, c axes of the 3D lattices. The symmetry-distinguished c-axis is also a preferred axis for Ir-Ir bonds (thick blue bond shown); the perpendicular edge (X'ed out gray lines) is not shared by any two IrO_6 octahedra. The c-bonds host z=b Kitaev exchange.

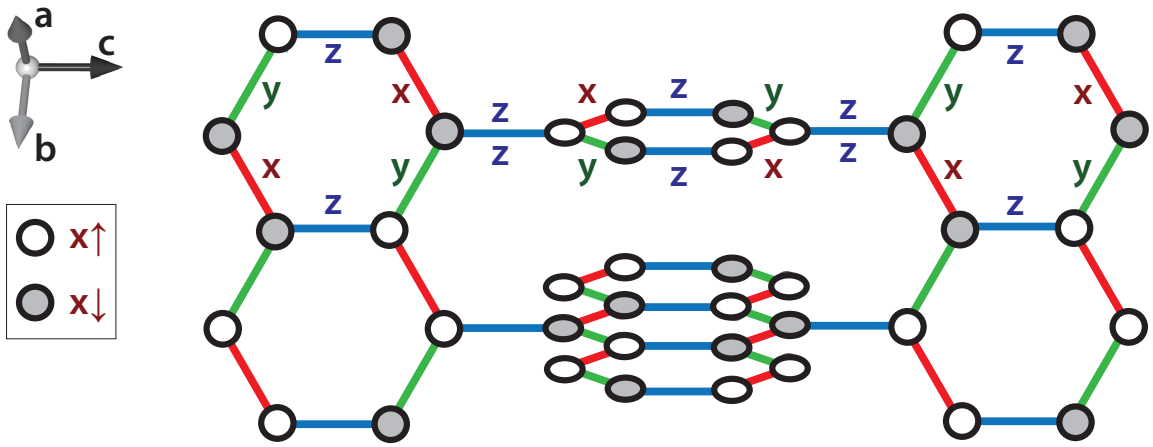

Figure 6.6: **S**tripy-X magnetic pattern on the stripyhoneycomb lattice. The classical magnetic pattern associated with the *Stripy-X/Y* AF ordered phase, here shown for Stripy-X correlations. Spins, collinear along S^x (white/gray sites correspond to S^x up/down spins), are aligned along x-type (red) bonds and anti-aligned along y-type (green) and z-type (blue) bonds. The unit cell is doubled (ordering wavevector $(\pi, \pi, 0)$) to form the full unit cell of the parent orthorhombic a, b, c axes. These Stripy-X/Y correlations are predicted by the strong FM Kitaev exchanges necessary for the mean field fit to the γ-Li_2IrO_3 magnetic susceptibility.

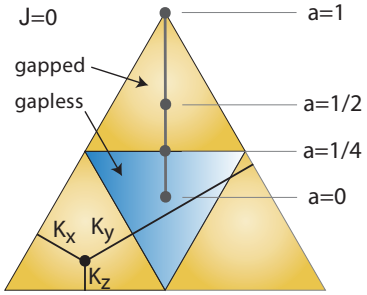

Figure 6.7: **K**itaev spin liquid with bond anisotropy. The phase diagram of the 3D Kitaev spin liquids as a function of bond anisotropy, designating whether the emergent Majorana fermions are gapped or gapless, is identical on the 3D lattices and the 2D honeycomb model, and is independent of whether the anisotropy breaks or preserves lattice symmetry. Here the magnitude of Kitaev coupling $|K_x|, |K_y|, |K_z|$ is given by the distance to the respective edge of the triangle. The vertical line corresponds to the symmetry-allowed bond-anisotropy, modifying $|K_z|$ by the parameter a (Eq. 6.11) with particular values shown.

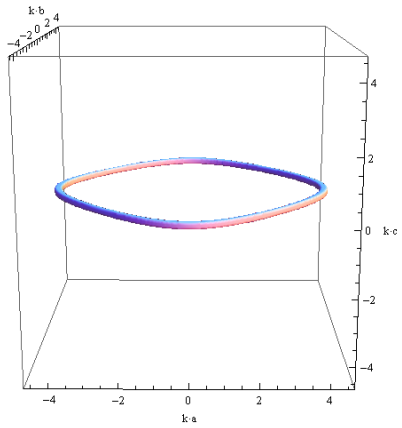

Figure 6.8: **N**odal contour of Majorana fermions in the 3D QSL. In the gapless 3D Kitaev spin liquid phase, the emergent Majorana fermions are gapless at momentum points which form this 1D contour within the 3D momentum space. The contour is identical for the QSLs on the stripyhoneycomb lattice and on the hyperhoneycomb lattice; it is set by $\vec{k} \cdot \vec{c} = 0$ and $\cos\left(\vec{k} \cdot \vec{a}/2\right) + \cos\left(\vec{k} \cdot \vec{b}/2\right) = 1/2$. with a, b, c the parent orthorhombic axes (shown). Introducing coupling-strength bond anisotropy shrinks this contour until it collapses to a point and then gaps out, yielding the gapped spin liquid phase.

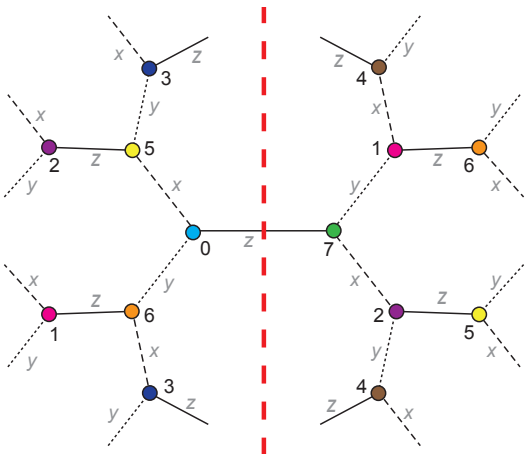

Figure 6.9: **I**nfinite-D z=3 tree with 8-site iTEBD cell. Taking the $\ell \to \infty$ limit of the hyperhoneycomb lattice ℓ=10 results in the z=3 tree, a lattice in infinite dimensions. Cutting any bond gives an entanglement bipartition (red dashed line), enabling entanglement-controlled computations with tensor network states. Bonds are labelled by Kitaev coupling; site labels show the unit cell used for the iTEBD computation. This 8-site unit cell (sites and bond Kitaev labels shown) used in the thermodynamic-limit iTEBD computation admits the Klein duality[135, 106, 142], and is thus expected to capture all the symmetry-breaking patterns in the phase diagram.

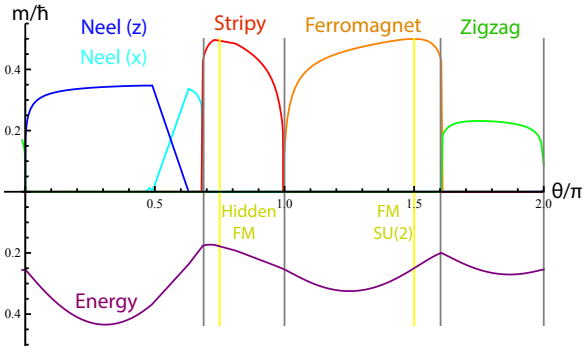

Figure 6.10: **K**itaev-Heisenberg isotropic phase diagram via iTEBD. The magnetic order parameters of the four phases are directly observed by iTEBD, working in the thermodynamic limit. The stripy and FM phases surround an exact solution with saturated magnetic order parameter $m = \hbar/2$; Neel and zigzag phases exhibit a moment reduced by quantum fluctuations. The energy per bond (purple) also provides the phase transitions, as well as benchmarking (see Fig. 6.15). The QSL phases exist around the Kitaev points at $\theta/\pi = 0, 1$ but here are gapless and cannot be numerically captured with finite entanglement.

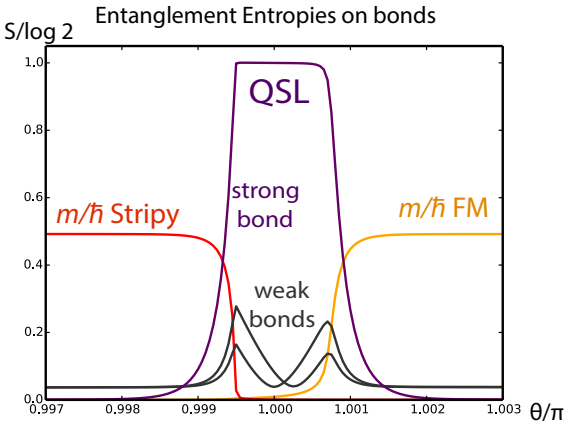

Figure 6.11: **G**apped spin liquid at $K < 0$ and surrounding magnetic phases, via $\chi = 12$ iTEBD. Sufficient bond anisotropy, here $a = 1/2$, gaps the QSL fermion spectrum and enables a tensor product state representation. The QSL phase, here for $K < 0$, is identified by the vanishing magnetic order parameters (here the stripy and ferromagnet) as well as by its entanglement entropies on the various bonds. The entanglement on the two weak bonds peaks at the transition (with slight spurious symmetry breaking), and that on the strong bond rises sharply in the QSL, matching the exact solution's entropy of Fig. 6.12.

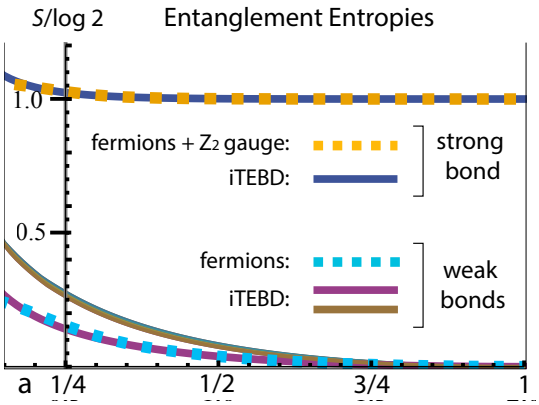

Figure 6.12: **E**ntanglement entropies as QSL fingerprints in iTEBD and exact majorana solutions. Entanglement entropies from the exact solution with Majorana fermions and $\mathbb{Z}_2$ gauge fields (dotted lines) and from iTEBD computations (solid lines). The Kitaev bond strength anisotropy parameter a is varied across the gapped phase $a > 1/4$ for which the iTEBD algorithm can capture the quantum spin liquid. The minimally entangled states of the QSL on the tree carry $\mathbb{Z}_2$ gauge sector entanglement only on strong bonds.

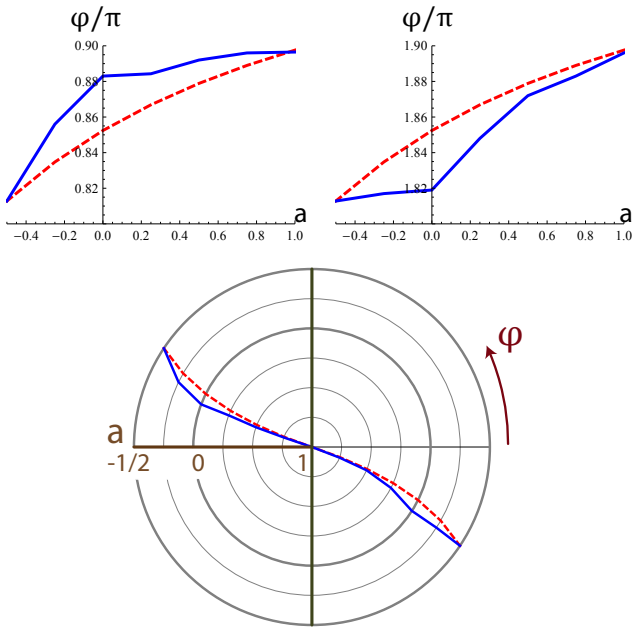

Figure 6.13: **T**ransitions between magnetic orders. Comparison between iTEBD (solid blue line) and classical mean field theory (dashed red line), of the location in ϕ as a function of anisotropy a of the first order transition between two adjacent magnetic orders. Top left: transition between zigzag and FM phases. Top right: transition between stripy and Neel phases. Bottom: transitions shown on the radial plot corresponding to Fig. 6.2.

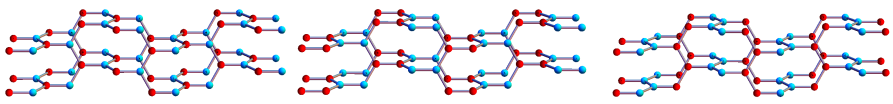

Figure 6.14: **M**agnetic orders on the hyperhoneycomb hyperhoneycomb lattice within the Kitaev-Heisenberg phase diagram. Three magnetic configurations are shown: clockwise from top-left these are Neel, Stripy-Z and Zigzag-Z. Blue spheres denote up spins and red spheres denote down spins in these collinear antiferromagneic orders. Stripy-Z is dual to a z-oriented ferromagnet, Zigzag-Z is dual to a z-oriented Neel order.

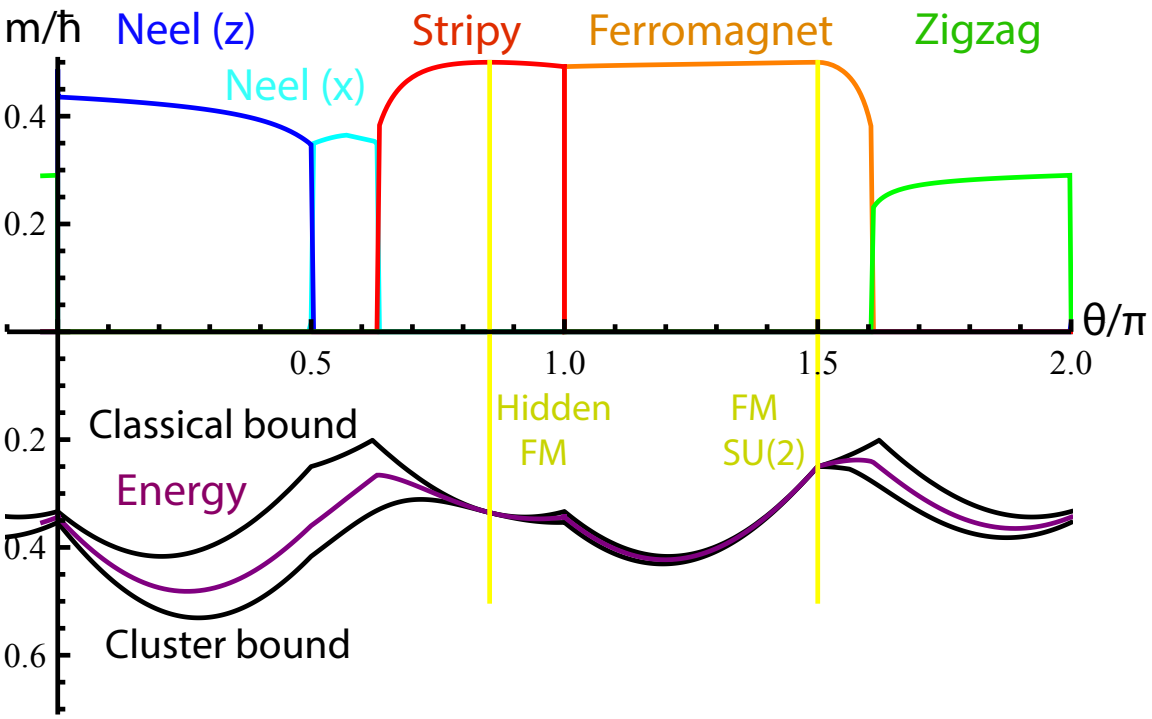

Figure 6.15: **K**itaev-Heisenberg magnetic phases with $a = 1/2$ anisotropy. See description for Fig. 6.10. The energy measured in iTEBD is always found to be bounded from above by classical product states and from below by considering a maximally-entangled cluster, providing a check on the algorithm. The QSL phases here are gapped and shown in Figs. 6.11 and 6.16, but their extent is not visible in this scale due to the strong anisotropy.

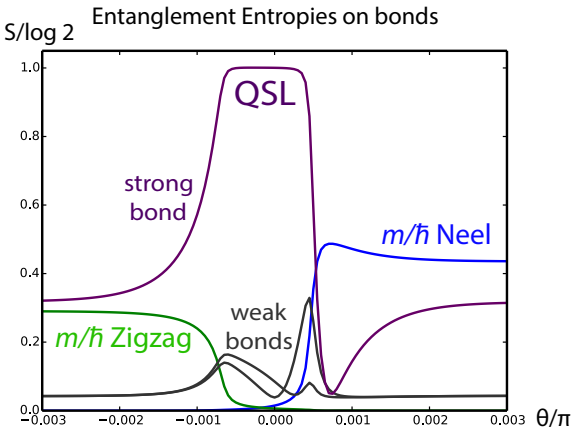

Figure 6.16: **G**apped spin liquid for $K > 0$ and surrounding magnetic phases within iTEBD. See the description in Fig. 6.11. Here we show the QSL at $a = 1/2, K > 0$, which competes with the zigzag and Neel orders. Different entropy curves occur here compared to the $K < 0$ QSL since while both the FM and stripy orders are effectively ferromagnets with nearly saturated ordered moments, the Neel and zigzag phases involve substantial quantum fluctuations.

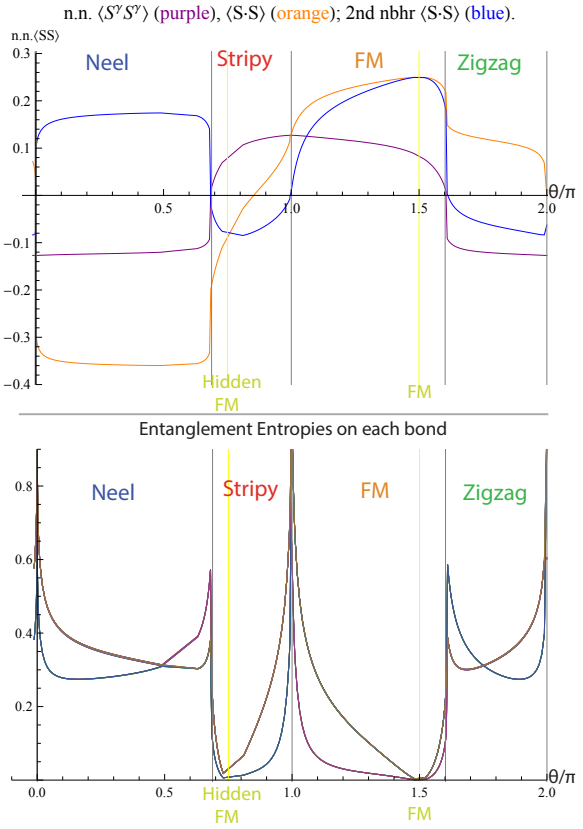

Figure 6.17: **I**sotropic $a = 0$ Kitaev-Heisenberg phase diagram via iTEBD: correlators and entanglement. The four magnetically ordered phases can be identified by various measures in addition to their direct order parameters. These include signatures of the transitions in energy derivatives (not shown here), spin-spin correlators (top) and entanglement entropies on the various bonds in the unit cell (bottom). The entanglement entropies vanish at the exactly solvable points (shown by yellow lines) where the ground state, a (hidden) ferromagnet, is a simple product state.

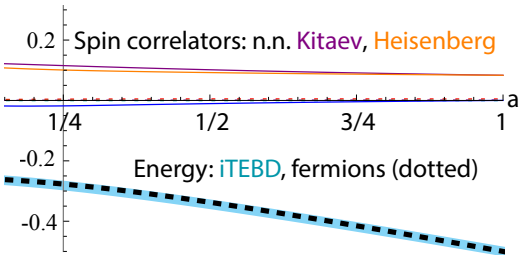

Figure 6.18: **F**urther benchmarks of iTEBD for the QSLs. The iTEBD spin correlators match the expected result for the pure Kitaev model, vanishing except for nearest neighbor Kitaev-matched spins; all magnetic order parameters vanish (shown); and the iTEBD ground state energy per bond (cyan) matches the energy computed from the majorana fermion spectrum (black), in the gapped QSL phase.

Chapter 7

Non-Coplanar and Counter-Rotating Incommensurate Magnetic Order Stabilized by Kitaev Interactions in γ-Li_2IrO_3

7.1 New experimental data on magnetic ordering

The previous chapter presents scenarios for the ground state in the iridate compounds within a particular model, but was written without knowledge of the actual ground state of the material. This chapter presents work done in collaboration with experimental groups, primarily the group of Radu Coldea. Together with Alun Biffin and Roger Johnson, as well as other collaborators, a remarkable solution of the magnetic ordering was obtained from scattering experiments. This chapter presents some of the experimental results as context, together with their theoretical analysis.

This chapter is composed of excerpts from the related publication, Phys. Rev. Lett. 113, 197201 (2014). All figures and data are reproduced from that publication (with permission). The full author list of the publication is as follows: A. Biffin, R.D. Johnson, I. Kimchi, R. Morris, A. Bombardi, J.G. Analytis, A. Vishwanath, and R. Coldea.

Here we present very brief excerpts of the relevant experimental discussion from the publication, together with some of the theoretical analysis. The reader is invited to turn to the published version of the manuscript for the full information on the experimental methods, results and analysis. The complete solution of the magnetic structure is here simply taken as a fact quoted from the experimental paper, and serves as context for the theoretical discussion that follows.

Materials that realize Kitaev spin models with bond-dependent anisotropic interactions have long been searched for, as the resulting frustration effects are predicted

to stabilize novel forms of magnetic order or quantum spin liquids. Here we explore the magnetism of γ-Li_2IrO_3, which has the topology of a 3D Kitaev lattice of interconnected Ir honeycombs. Using resonant magnetic x-ray diffraction we find a complex, yet highly-symmetric incommensurate magnetic structure with non-coplanar and counter-rotating Ir moments. We propose a minimal Kitaev-Heisenberg Hamiltonian that naturally accounts for all key features of the observed magnetic structure. Our results provide strong evidence that γ-Li_2IrO_3 realizes a spin Hamiltonian with dominant Kitaev interactions.

7.2 Introduction

Magnetic materials with bond-dependent anisotropic interactions are candidates to display novel forms of magnetic order or quantum spin liquid states, as exemplified by the Kitaev model on the honeycomb lattice [68]. Here all spins interact via nearest-neighbor Ising exchanges, but a different Ising axis $(\mathsf{x}, \mathsf{y}, \mathsf{z})$ applies for the three different bonds emerging out of each lattice site. This leads to strong frustration effects that stabilize a novel gapless quantum spin liquid state with exotic excitations (Majorana fermions), which is exactly solvable in two dimensions. It was theoretically proposed [69] that such exotic Hamiltonians might be realized in magnetic materials containing edge-sharing cubic IrO_6 octahedra. The magnetic ground state of Ir^{4+} including the cubic crystal field and spin-orbit coupling is a complex spin-orbital doublet with $J_{eff} = 1/2$ [70], and super-exchange through the two 90° Ir-O-Ir paths is expected to lead to a dominant Ising interaction for the moment components normal to the Ir-O_2-Ir plane [69]. For a three-fold coordinated IrO_6 octahedron this leads to perpendicular Ising axes for the three nearest-neighbor bonds, as required for a Kitaev model. The 2D honeycomb-lattice α-Na_2IrO_3 [71, 72, 73, 74, 75] and α-Li_2IrO_3 [76, 77] are being intensively explored as candidate Kitaev materials, but as yet no clear evidence for novel Kitaev physics has been observed.

Generalizations of the Kitaev model to 3D lattices are also expected to have quantum spin liquid states [78, 79, 80]. The recently-synthesized structural polytypes "hyper-honeycomb" $\beta-Li_2IrO_3$ [81] and "harmonic" honeycomb $\gamma-Li_2IrO_3$ [82], which maintain the local three-fold coordination of edge-sharing IrO_6 octahedra, are prime candidates to display 3D Kitaev physics. To test for signatures of such physics we have performed resonant magnetic x-ray diffraction (RMXD) measurements [83] on single crystals of γ-Li_2IrO_3, scattering at the strong Ir L_3 resonance [72]. We have determined the complete magnetic structure for all 16 iridium sites in the unit cell, and found an unexpectedly complex, yet highly symmetric magnetic structure comprised of non-coplanar, counter-rotating iridium magnetic moments located in zig-zag chains. Remarkably, the magnetic structure exhibits no net ferromagnetic or antiferromagnetic spin correlations, and as such one can rule out a model Hamiltonian whose primary ingredient is the nearest-neighbor Heisenberg interac-

tion. Instead, motivated by the work of Jackeli and Khaliullin [84], and by arguments based on susceptibility anisotropy [82, 80], we present a minimal spin Hamiltonian with dominant Kitaev interactions that naturally reproduces all key features of the observed magnetic order, in particular, we point out that counter rotating spirals on the zig-zag chains are naturally generated by Kitaev interactions. Our results therefore provide strong evidence that dominant Kitaev couplings govern the magnetic interactions in γ-Li_2IrO_3.

7.3 Experiment and extraction of ordering pattern

We refer the reader to the published manuscript at Phys. Rev. Lett. 113, 197201, 2014, for the experiment and analysis information. Here we quote a brief summary from the published paper. Systematic searches along high-symmetry directions in reciprocal space revealed that at low temperatures new magnetic Bragg peaks appeared at satellite positions of reciprocal lattice points with an incommensurate propagation vector $\boldsymbol{q} = (0.57(1), 0, 0)$ [**?**]. The satellite peaks were found to be as sharp as structural peaks in all three reciprocal space directions; indicating coherent, 3D magnetic ordering. The peaks disappeared upon heating and the temperature-dependence of the intensity had a typical order parameter behavior, which after corrections give $T_{\mathrm{N}} = 39.5$ K.

The observed behavior of the peaks, together with a detailed technical analysis, finds that the scattering describes counter-rotating moments between consecutive sites along c (curly arrows in Fig. 7.1), which form counter-rotating zig-zag chains along a. Fits to the data gave values for the moment magnitude ratios $M_x : M_y : M_z = 0.65(4) : 0.58(1) : 1$.

Imposing the constraint of near-constant magnitude moment at every site requires the phase offset between the x and y components to be π or 0, giving the basis vector combination $i(A, -A)_x, i(-1)^m(F, -F)_y, (F, F)_z$, with $m = 1$ or 2. (See the published manuscript at Phys. Rev. Lett. 113, 197201, 2014, for the details on this solution.) Both give similar structures and we plot in Fig. 7.1 the case $m = 1$. The moments are confined to rotate in one of two planes, obtained from the (ac) plane by rotation around the c-axis by an angle $\pm\phi$, with $\phi = tan^{-1}\frac{M_y}{M_x} = 42(2)^\circ$. The pattern is such that neighboring iridium zig-zag chains have alternate orientations of the spin rotation plane as indicated by the light and dark shaded envelopes in Fig. 7.1. The $m = 2$ case simply gives the opposite alternation of the rotation planes.

7.4 Analysis of the resulting magnetic structure

A key feature of the magnetic structure is the counter-rotation of neighboring moments. On two such sites, say 1 and $1'$, the spins projected to the ac-plane are $\boldsymbol{S}_{1,1'}(\boldsymbol{r}) = \hat{\boldsymbol{c}}\langle S^c\rangle \cos \boldsymbol{q}\cdot\boldsymbol{r} \pm \hat{\boldsymbol{a}}\langle S^a\rangle \sin \boldsymbol{q}\cdot\boldsymbol{r}$. We now rotate from the crystallographic

a, b, c-axes to the Kitaev $\mathsf{x}, \mathsf{y}, \mathsf{z}$-axes (see Fig. 7.1 caption) and consider the correlation between the S^{x} spin components $S_1^{\mathsf{x}} S_{1'}^{\mathsf{x}}$ across an x-type bond, or $S_1^{\mathsf{y}} S_{1'}^{\mathsf{y}}$ across a y-type bond. The net averaged correlation is finite, $\langle S_1^{\mathsf{x}} S_{1'}^{\mathsf{x}} \rangle_{\mathsf{x}} = \langle S_1^{\mathsf{y}} S_{1'}^{\mathsf{y}} \rangle_{\mathsf{y}} = \langle S^a \rangle \langle S^c \rangle \frac{1}{2} \sin \frac{\pi q}{2}$. We see that along each x-type bond the spins are aligned when they point along x, and anti-aligned when they point along y, and similarly for y-type bonds. Thus Kitaev interactions can stabilize the counter-rotating moments with a propagation vector $\boldsymbol{q}$ along $\boldsymbol{a}$. We therefore construct the following Kitaev-Heisenberg Hamiltonian as a minimal model

$$\mathcal{H} = \sum_{c-\mathrm{bonds}} \left[K_c S_i^{\eta_{ij}} S_j^{\eta_{ij}} + J_c \boldsymbol{S}_i \cdot \boldsymbol{S}_j + I_c^c S_i^c S_j^c \right] + \sum_{d-\mathrm{bonds}} \left[K_d S_i^{\eta_{ij}} S_j^{\eta_{ij}} + J_d \boldsymbol{S}_i \cdot \boldsymbol{S}_j \right] + \sum_{2^{\mathrm{nd}} \ \langle\langle ij \rangle\rangle} J_2 \boldsymbol{S}_i \cdot \boldsymbol{S}_j \tag{7.1}$$

where interactions along the vertical (along c) bonds are denoted by the subscript c and interactions along the zig-zag (diagonal) bonds are denoted by the subscript d. K_c and K_d are the Kitaev interactions along c-bonds (of type $\eta_{ij} = \mathsf{z}$) and d-bonds (of type $\eta_{ij} = \mathsf{x}$ or y), respectively. To prevent $(0, 0, q_c)$ instabilities we have introduced an Ising coupling I_c^c of the S^c spin components, and finally a Heisenberg coupling J_2 between second nearest neighbors. We take the following values for the parameters (in units of meV): $K_c = -15, K_d = -12, J_c = 5, J_d = 2.5, I_c^c = -4.5, J_2 = -0.9$ [85], where the overall scale was set such as to have the calculated ordering transition temperature agree with the experimental value.

The Hamiltonian was analyzed in Fourier space using the Luttinger-Tisza approximation [85]. This gave the lowest-energy mode identical to the (S^a, S^c) coplanar projection of the magnetic structure in Fig. 7.1 with $\langle S^c \rangle > \langle S^a \rangle$. To obtain fixed-length spins requires mixing with another mode, and the lowest energy mode available at the same wavevector has collinear order of the S^b components with a pattern such that the mixed mode exactly reproduce the observed non-coplanar structure. Furthermore, the S^b components are co-aligned along all the c-axis bonds, and hence stabilized by the large FM K_c Kitaev exchange. The mixing amplitude, related to the tilt angle ϕ, is fixed for unit length spins, but changes continuously with the Hamiltonian parameters. Decreasing the strength of the Kitaev interactions prevents the ground state from producing unit-length spins through this mixing mechanism, and importantly, we find that the non-coplanar tilt angle observed in γ-Li_2IrO_3 requires relatively large Kitaev exchanges within the minimal model.

To summarize, through RMXD measurements on γ-Li_2IrO_3 single crystals we have observed an incommensurate, non-coplanar magnetic structure with counter-rotating moments. A Kitaev-Heisenberg Hamiltonian can fully explain the observed complex magnetic structure, providing strong evidence that γ-Li_2IrO_3 is an experimental realization of 3D Kitaev physics in the solid state.

7.5 Appendix: Crystal Structure of γ-Li_2IrO_3

γ-Li_2IrO_3 has an orthorhombic crystal structure depicted in Fig. 7.2 with edge-sharing IrO_6 octahedra arranged in a three-dimensional network with a three-fold local coordination. The iridium atoms (red balls) form vertically-linked honeycomb rows (light and dark shading) that run alternatingly along the $\boldsymbol{a} \pm \boldsymbol{b}$ diagonals upon moving along the c-axis. To simplify the notation for the discussion of the magnetic structure we have labelled the two iridium sublattices as Ir and Ir$'$.

Table 7.1: Fractional atomic coordinates of the iridium sites in the primitive cell and corresponding magnetic basis vector components in the determined magnetic structure.

Site	Coordinates
1	$(0.25, 0.25, z)$
2	$(0.25, 0.75, 0.5 - z)$
3	$(0.25, 0.25, 1 - z)$
4	$(0.25, 0.75, 0.5 + z)$
$1'$	$(0.5, 0.5, z')$
$2'$	$(0.5, 0.5, 0.5 - z')$
$3'$	$(0.5, 0.5, 1 - z')$
$4'$	$(0.5, 0.5, 0.5 + z')$

Table reproduced with changes from published manuscript, Phys. Rev. Lett. 113, 197201 (2014). The magnetic ions are located on the two iridium sublattices, Ir at $8k$ $(0.25, 0.25, z)$, $z = 0.0836(2) \approx 1/12$ and Ir$'$ at $8i$ $(0.5, 0.5, z')$, $z' = 0.1670(3) \approx 1/6$, each with four sites in the primitive unit cell labelled $1-4$ and $1'-4'$ with coordinates listed explicitly in Table 7.1 and positions labelled in Fig. **??**.

7.6 Appendix: Magnetic structure with counter-rotating moments stabilized by Kitaev interactions

We now give details of the derivation of the net spin correlation between nearest-neighbor sites along the d-bonds $\langle S_n^\eta S_{n'}^\eta \rangle_\eta = \langle S^a \rangle \langle S^c \rangle \frac{1}{2} \sin \frac{\pi q}{2}$ with $\eta = \mathsf{x}$ or y. First we recall the transformation from the crystallographic axes $\hat{\boldsymbol{a}}, \hat{\boldsymbol{b}}, \hat{\boldsymbol{c}}$ to the Kitaev axes defined as $\hat{\mathbf{x}} = (\hat{\boldsymbol{a}} + \hat{\boldsymbol{c}})/\sqrt{2}$, $\hat{\mathbf{y}} = (\hat{\boldsymbol{a}} - \hat{\boldsymbol{c}})/\sqrt{2}$ and $\hat{\mathbf{z}} = \hat{\boldsymbol{b}}$, see Fig. 7.1.

The a-component of the displacement between adjacent sites of type 1 and $1'$ in a zig-zag chain is $(\boldsymbol{r}_1 - \boldsymbol{r}_{1'}) \cdot \hat{\boldsymbol{a}} = \pm a/4$, where the upper (lower) sign is to be taken if the

two sites are connected by a Kitaev bond of type x (y). More generally, for neighboring sites of type n and n' the displacement projection is $(\boldsymbol{r}_n - \boldsymbol{r}_{n'}) \cdot \hat{\boldsymbol{a}} = \pm\nu_n a/4$, where $\nu_n = +1$ for $n = 1, 4$ and $\nu_n = -1$ for $n = 2, 3$.

In this notation, we obtain from (**??**) that sites in the rotating magnetic structure carry the spin moment

$$\begin{aligned} \boldsymbol{S}_{n,n'}(\boldsymbol{r}) &= \pm\left[\nu_n \hat{\boldsymbol{a}}\langle S^a\rangle + (-1)^m \hat{\boldsymbol{b}}\langle S^b\rangle\right]\sin \boldsymbol{q}\cdot\boldsymbol{r} + \\ &\quad \hat{\boldsymbol{c}}\langle S^c\rangle \cos \boldsymbol{q}\cdot\boldsymbol{r} \end{aligned} \tag{7.2}$$

where the $\pm$ sign in front of the square bracket corresponds to unprimed/primed sites and the case $m = 1$ is depicted in Fig. **??**. The product of this $\pm$ sign in front of the square brackets and the ν_n sign factor gives a sign which alternates between + and − when sites are listed by their c-coordinate, i.e. the vertical axis in Fig. 7.1, producing the counter-rotation of the spin moments in the ac plane.

It is immediately evident that along Kitaev z-type bonds (linking sites of type $1'2'$, $3'4'$, 13 and 24, see Fig. **??**a)) the S^{z}=S^b spin components are always ferromagnetically-correlated, enabling energetic stabilization through the strong FM Kitaev interaction on these bonds, $K_c < 0$. The more subtle correlations, as discussed in the main text, are those of the $S^{\mathsf{x}}(S^{\mathsf{y}})$ spin components across x-type (y-type) Kitaev bonds. The counter-rotation of neighboring moments within the unit cell enables these subtle Kitaev correlations, as follows

$$\begin{aligned} &\langle S^\eta_n S^\eta_{n'}\rangle_{\boldsymbol{r}:\ \eta\text{-bond}} / \langle S^a\rangle / \langle S^c\rangle = \\ &\left\langle \cos\left(\boldsymbol{q}\cdot\boldsymbol{r} \pm \nu_n \frac{\boldsymbol{q}\cdot\boldsymbol{a} - \pi}{4}\right)\cos\left(\boldsymbol{q}\cdot\boldsymbol{r} \pm \nu_n \frac{\pi}{4}\right)\right\rangle_{\boldsymbol{r}} = \\ &\frac{1}{2}\cos\left(\frac{\boldsymbol{q}\cdot\boldsymbol{a} - 2\pi}{4}\right) = \frac{1}{2}\sin\left(\frac{\boldsymbol{q}\cdot\boldsymbol{a}}{4}\right) \end{aligned} \tag{7.3}$$

with $\eta =$ x or y and $\langle \ldots\rangle_{\boldsymbol{r}}$ indicates the average over all positions $\boldsymbol{r}$ of sites of type n in the crystal. Note that defining the rotating magnetic structure within the primitive unit cell (containing 8 sites) is sufficient to uniquely specify the spin moments on all sites in the crystallographic a, b, c unit cell, which contains 16 iridium sites; here $\boldsymbol{q}\cdot\boldsymbol{a}$ ranges from -2π to 2π. Within our convention of the spin components within the unit cell, positive values of q (i.e. $0 < \boldsymbol{q}\cdot\boldsymbol{a} < 2\pi$) correspond to positive Kitaev correlations, which may be stabilized by FM Kitaev interactions ($K_d < 0$).

7.7 Appendix: Luttinger-Tisza analysis of the minimal model Hamiltonian

We diagonalize the spin Hamiltonian in momentum space without the unit length constraint. The energies and modes are found as the eigenstates of the 24×24

matrix, corresponding to three spin components for each site in the primitive unit cell. Then solutions obeying the unit length constraint are constructed from the lowest eigenmode, possibly with higher energy modes mixed in.

The lowest eigenvalue of the Hamiltonian in eqn. (7.1) with parameters as given in the main text occurs at a wavevector numerically indistinguishable from $(4/7, 0, 0)$ (in r.l.u's of the orthorhombic unit cell $a \times b \times c$). This minimal energy eigenmode, with energy -13.6 meV, has the ordered spin moment $\boldsymbol{S} \propto \hat{\boldsymbol{c}} \pm i0.85\nu_n \hat{\boldsymbol{a}}$, with the upper (lower) sign for the unprimed (primed) sites, and hence does not quite obey the constraint of normalized spins. However it does exactly describe the coplanar projection of the experimental magnetic structure onto the ac plane. The next three eigenmodes again involve only S^a, S^c spin components, and cannot mix with the lowest mode. The fifth eigenmode at this wavevector, with energy -10.5 meV, has spins purely along $\hat{\boldsymbol{b}}$, with an order pattern of $\pm$ signs for unprimed/primed sites, exactly capturing the pattern of the non-coplanar tilts in the experimentally-determined structure. So mixing between this eigenmode and the lowest energy eigenmode to ensure the constraint of fixed-length spins can match all features of the experimentally-determined magnetic structure. For completeness we note that changing the sign of the mixing coefficient corresponds to changing between the cases $m = 1$ and 2 in eq. (7.2), with the two structures being degenerate in energy.

In summary, through extensive searches in parameter space for candidate spin Hamiltonians we have found that all couplings in eqn. (7.1) currently appear to be required to stabilize the observed magnetic structure as the lowest-energy structure with fixed-length spin moments. The phase obtained is stable within a range of values for the Hamiltonian parameters and the quoted values in the text are a representative solution, where the overall scale is set by the constraint that the calculated transition temperature to magnetic order matches the experimental value.

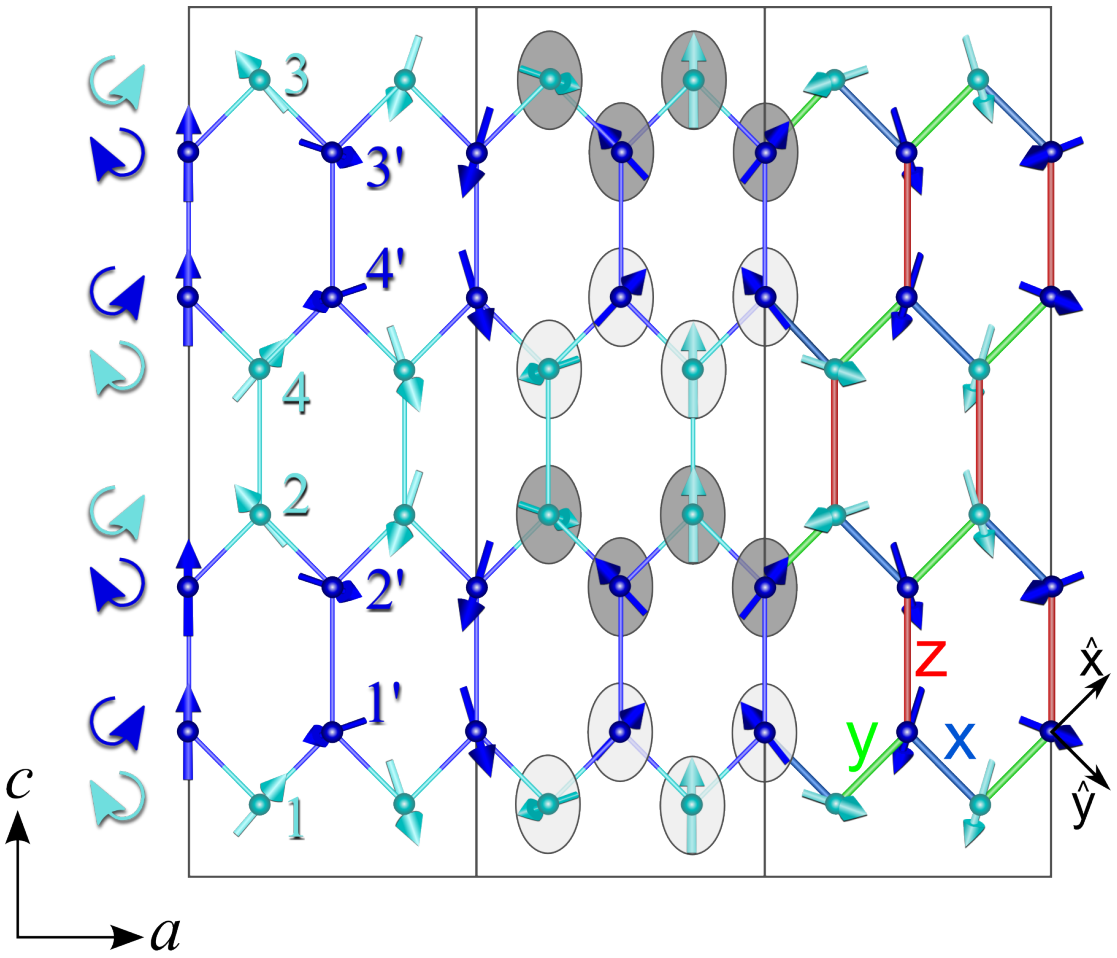

Figure 7.1: Figure reproduced from published manuscript, Phys. Rev. Lett. 113, 197201 (2014). Projection of the magnetic structure on the $(\boldsymbol{a}, \boldsymbol{c})$ plane showing 3 unit cells along the horizontal propagation direction a. Light and dark blue arrows show the moments on the Ir and Ir$'$ sublattices, with sites $1-4$ and $1'-4'$, respectively. Curly arrows on the left side illustrate counter-rotating magnetic order between consecutive sites along c. In unit cell 2 light $(-\phi)$ and dark $(+\phi)$ shaded elliptical envelopes emphasize the confinement of the moments to alternate planes obtained from the (ac) plane by a rotation by $\mp\phi$ around c. In unit cell 3 color of bonds indicates the anisotropy axis of the Kitaev exchanges in (7.1), with $\eta = \mathsf{x}, \mathsf{y}, \mathsf{z}$ for blue/green/red bonds, where $\hat{\mathbf{x}} = (\hat{\boldsymbol{a}} + \hat{\boldsymbol{c}})/\sqrt{2}$, $\hat{\mathbf{y}} = (\hat{\boldsymbol{a}} - \hat{\boldsymbol{c}})/\sqrt{2}$ and $\hat{\mathbf{z}} = \hat{\boldsymbol{b}}$).

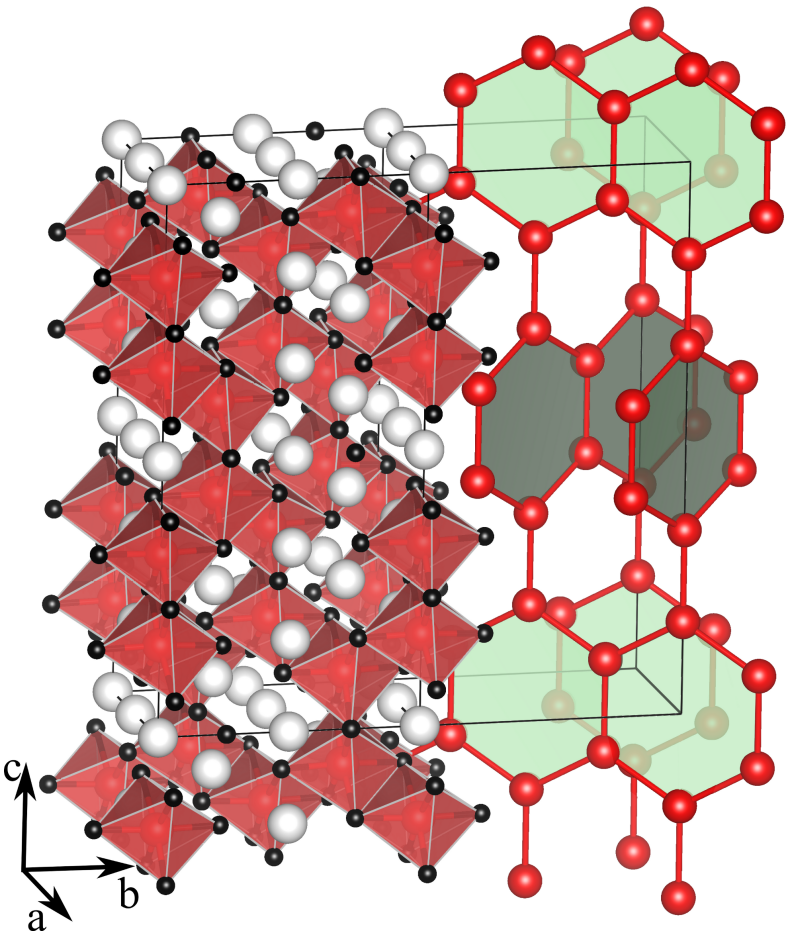

Figure 7.2: Figure reproduced from published manuscript, Phys. Rev. Lett. 113, 197201 (2014). Crystal structure of γ-Li_2IrO_3. Two neighbouring unit cells are shown: (left) full structure with Li (white balls), O (black) and Ir (red) located inside IrO_6 octahedra (shaded polyhedra), (right) 3D iridium lattice connectivity: honeycomb rows alternating in orientation (light and dark shading) are interconnected along c.

Chapter 8

Unified theory of spiral magnetism in the harmonic-honeycomb iridates α, β, γ-Li_2IrO_3

The context for this chapter is as follows. A family of insulating iridates with chemical formula Li_2IrO_3 has recently been discovered, featuring three distinct crystal structures α, β, γ (honeycomb, hyperhoneycomb, stripyhoneycomb). Measurements on the three-dimensional polytypes, β- and γ-Li_2IrO_3, found that they magnetically order into remarkably similar spiral phases, exhibiting a non-coplanar counter-rotating spiral magnetic order with equivalent $q = 0.57$ wavevectors.

In this work we examine magnetic Hamiltonians for this family and show that the same triplet of nearest-neighbor Kitaev-Heisenberg-Ising (KJI) interactions reproduces this spiral order on both β, γ-Li_2IrO_3 structures. We analyze the origin of this phenomenon by studying the model on a 1D zigzag chain, a structural unit common to the three polytypes. The zigzag-chain solution transparently shows how the Kitaev interaction stabilizes the counter-rotating spiral, which is shown to persist on restoring the inter-chain coupling. Our minimal model makes a concrete prediction for the magnetic order in α-Li_2IrO_3.

8.1 Unified theory of spiral magnetism

8.1.1 Introduction

Edge-sharing oxygen octahedra coordinating Ir^{4+} ions can exhibit unconventional magnetic interactions between the Ir S_{eff}=1/2 pseudospins. Strong spin orbit coupling in iridium, which produces these low energy Kramer's doublets, can combine with 90° Ir-O-Ir exchange pathways to generate bond-dependent couplings identical to those discussed by Kitaev[146], as has been proposed in Refs. [129] and [106] for Na_2IrO_3.

The collinear antiferromagnetic magnetism[197, 161, 217, 110] later found in Na_2IrO_3 is distinct from simple Neel order, but can be captured by various models with or without Kitaev-type spin anisotropies.[198, 110, 143, 91, 107, 112, 116, 170, 171, 140, 117, 118, 192] The isostructural compound α-Li_2IrO_3, in which Ir forms separated layers of the 2D honeycomb lattice, is available only in powder form. Thermodynamic and susceptibility measurements suggest it also orders magnetically[198], and powder neutron diffraction experiments found a magnetic Bragg peak with a small nonzero wavevector inside the first Brillouin zone[111], stimulating theoretical models[189, 178] of spiral orders.

In the past two years, compounds with chemical formula Li_2IrO_3 have been successfully synthesized in two additional crystal structures (Fig. 8.1). In γ-Li_2IrO_3 the Ir sites form the 3D stripyhoneycomb lattice[**?**, 99] (space group #66 $Cccm$), featuring hexagons which are arranged in honeycomb strips of alternating orientation. In β-Li_2IrO_3 the Ir sites form the 3D hyperhoneycomb lattice[199, 97] (space group #70 $Fddd$), featuring 10-site decagons which are reminiscent of the hyperkagome[181] lattice of $Na_4Ir_3O_8$. The relation between these structures is captured by their designation as harmonic-honeycomb iridates[**?**, 141], a structural series in which α, β, γ-Li_2IrO_3 are labelled by $n = \infty, 0, 1$ respectively. Common features include local three-fold coordination of sites, as well as identical 2D projections along the $\boldsymbol{a}$ and $\boldsymbol{b}$ parent orthorhombic axes; the $\boldsymbol{c}$ axis projections are distinct.

Recent experiments using resonant magnetic x-ray diffraction have successfully determined the magnetic ordering in β- and γ-Li_2IrO_3 single crystals[99, 97]. The results are striking. Both compounds order into a complex spiral at a temperature T_N=38 K. This order hosts counter-rotating spirals within the unit cell, exhibiting a particular pattern of non-coplanar tilts. The spiral wavevector $\boldsymbol{q}$ lies along the orthorhombic $\boldsymbol{a}$ axis, with the same apparently incommensurate magnitude $q = 0.57(1)\times 2\pi/a = 0.61(1)\text{Å}^{-1}$ in both structures. Except for the angle of the non-coplanar tilt, the magnetic orders observed in β- and γ-Li_2IrO_3 are equivalent to each other, though occuring in different lattice settings.

In this work we analyze the origin of this phenomenon by theoretically studying the three Li_2IrO_3 systems at the level of lattice magnetic Hamiltonians. We show that a microscopically-derivable set of nearest-neighbor interactions, consisting of Kitaev, Heisenberg and Ising exchanges, is sufficient for capturing the observed spiral magnetic order. This Hamiltonian is

$$H = \sum_{\langle ij \rangle} \left[K \; S_i^{\gamma_{ij}} S_j^{\gamma_{ij}} + J \; \vec{S}_i \cdot \vec{S}_j + I_c \; S_i^{r_{ij}} S_j^{r_{ij}} \right] \tag{8.1}$$

where K is the Kitaev coupling, and I is a distinct Ising coupling of the spin components parallel to the bond orientation, i.e. $S^{r_{ij}} \equiv \vec{S} \cdot \hat{r}_{ij}$ where $\hat{r}_{ij} = (\vec{i} - \vec{j})/|i-j|$ is the unit vector from site i to site j. In this model the Ising term I_c is chosen to be active only on those symmetry-distinguished bonds which are parallel to the $\boldsymbol{c}$ axis,

where it becomes $I_c S_i^c S_j^c$. For the Kitaev coupling of spin component γ_{ij}, the bond-dependent axis $\gamma_{ij} \in (x, y, z)$ is the Ir-O unit vector from iridium site i to one of the oxygens in its coordinating octahedron, uniquely chosen so that γ_{ij} is perpendicular to r_{ij} or, equivalently, perpendicular to the bond's $\mathrm{Ir}_i\mathrm{O}_2\mathrm{Ir}_j$ square. Here $\hat{z}{=}\hat{b}$ and $\hat{x}, \hat{y}{=}(\hat{a}{\pm}\hat{c})/\sqrt{2}$. As is clear from this representation, the three different exchanges K, J, I are all symmetry-allowed and can be microscopically generated[1] already in the limit of cubic O_6 octahedra.

The phase diagram of Eq. 8.1, shown in Fig. 8.2A, exhibits a remarkable feature. The experimentally-observed spiral order in the β and γ lattices is stabilized in our theoretical model as the ground state on all three lattices, for certain parameters such as $(K, J, I_c) = (-12, 0.6, -4.5)$ meV. Moreover the surrounding phase diagrams, computed by setting Eq. 8.1 on each of the three α, β, γ-$\mathrm{Li_2IrO_3}$ lattices, are all quite similar. In Fig. 8.2 the phase diagrams on α, β, γ lattices are shown for the same parameter range, permitting this visual comparison. This feature suggests that the experimental observations, of the striking similarity between the β- and γ-$\mathrm{Li_2IrO_3}$ spiral orders, may be captured within this effective $S{=}1/2$ Hamiltonian with nearest-neighbor exchanges.

To understand the striking similarity between the Fig. 8.2 phase diagrams found in our numerical computations on the different lattices, we introduce a conceptual toy model consisting of a 1D zigzag chain. This minimal conceptual model may be motivated as follows. Observe that the symmetries of the $\mathrm{Li_2IrO_3}$ polytypes single out the set of Ir-Ir bonds which lie parallel to the crystallographic $\boldsymbol{c}$ axis. These c-bonds, with $r_{ij}{=}c$, all carry Kitaev couplings of $\gamma_{ij}{=}z{=}b$. The remaining "d-bonds" (as well as their $\gamma_{ij}{=}x, y$) all lie diagonal to the a, b, c axes. This symmetry-enforced distinction gives the microscopic motivation for setting $I_d{=}0$ in Eq. 8.1. Now consider decomposing the Hamiltonian Eq. 8.1 into its interactions on c-bonds and on d-bonds, $H = H_c + H_d$. The d-bonds Hamiltonian H_d is then a sum of decoupled 1D zigzag chains at various positions and orientations, $H_d = \sum H_{\mathrm{1D}}$, turning all three lattices into sums over identical H_{1D} building blocks.

8.1.2 Zigzag chain minimal model.

The zigzag chain toy model is a conceptual mechanism for connecting the full numerical computations. Its solution is transparent, clarifying how essentially the same form of spiral order arises from Eq. 8.1 on the distinct 3D lattices. We complement its analytical insight by numerically computing the phase diagrams as we mathematically interpolate between the 3D lattices: even as we smoothly turn off the inter-chain bonds, reducing the 3D lattices to the 1D chain, the spiral phase remains stable.

[1]Microscopic exchange pathways for edge-sharing octahedra have been discussed in Refs. [135, 108, 129, 106, 172, 179, 107, 169, 116, 186].

Since we define $H_{\rm 1D}$ by dropping the inter-chain c-bonds, we here mitigate the loss of the I_c exchange by introducing a second-neighbor Heisenberg J_2 interaction. This J_2 can be discarded when the full 3D lattice is restored. The zigzag-chain geometry is defined in Fig. 8.3; let r_1, r_2 point from an A-sublattice site to its neighboring B sites, and choose the 1D Bravais lattice with vector $a_1 = r_2 - r_1$ so that the A-sites lie at integer positions $r = na_1$. The single-chain Hamiltonian is

$$\begin{aligned} H_{\rm 1D} = \sum_{r=na_1} \Big[& K \ \left(S^x_{A,r}\ S^x_{B,r+r_1} + S^y_{A,r}\ S^y_{B,r+r_2}\right) \\ & + J \ \left(\vec{S}_{A,r}\cdot\vec{S}_{B,r+r_1} + \vec{S}_{A,r}\cdot\vec{S}_{B,r+r_2}\right) \\ & + J_2 \left(\vec{S}_{A,r}\cdot\vec{S}_{A,r+a_1} + \vec{S}_{B,r-r_2}\cdot\vec{S}_{B,r+r_1}\right)\Big] \end{aligned} \tag{8.2}$$

In solving the 1D minimal model, one can focus on the x, y (or equivalently a, c) coplanar mode of the spiral. (Restoring the inter-chain z-type Kitaev couplings will produce the non-coplanar tilt.) This is justified perturbatively near an exactly solvable point, as follows. First consider Eq. 8.2 at J_2=0, K=$-2J$, K<0, where a site-dependent spin rotation[135, 106, 142] exposes it as a pure ferromagnet in a rotated basis. Its exact quantum ground state is a *Stripy* collinear antiferromagnet (AFM) of the original spins. In particular, taking now slightly larger $|K|$, the ground state is Stripy-XY: it has spins collinear along S^x/S^y which are aligned on x/y-type bonds and anti-aligned along y/x-type bonds. Focusing on large FM K<0 with small AF J>0 satisfying K+2J<0, we expect states in the zigzag chain to be x, y-coplanar.

We therefore conceptually consider an ansatz for the x, y spin components, on the sublattices $s \in \{A, B\}$,

$$\left(S^x_{s,r}, S^y_{s,r}\right) = \big(\mathrm{Re}, \mathrm{Im}\big)\left[\exp\{-i\left(q_s\, r + \phi_s\right)\}\right] \tag{8.3}$$

parametrized by the sublattice spiral wavevectors q_A=$\pm q_B$ and the sublattice phases ϕ_A, ϕ_B.

Consider the case of counter-rotation, q_B=$-\,q_A$=θ/a_1 with θ>0 (a_1 is defined in Fig. 8.2). The energy per unit cell is given by

$$E_-(\theta) = K \sin\left(\theta/2\right) \sin(\phi_A{+}\phi_B) + 2J_2 \cos(\theta) \tag{8.4}$$

Minimizing the energy with respect to the sublattice phases (for K<0) immediately fixes their sum to be $\phi_A{+}\phi_B = \pi/2$. Now consider the minimization with respect to the spiral rotation angle θ. There are three cases. (1) For small $|J_2|$, Eq. 8.4 is minimized at $\theta = \pi$, producing the Stripy-XY AFM state, with energy $E_{\rm stripy} = K{-}2J_2$. (2) For larger ferromagnetic $J_2 < 0$, a global minimum develops at an incommensurate wavevector fixed by $\sin\left(\theta/2\right) {=} K/(8J_2)$, for $|J_2| > |K|/8$. This incommensurate counter-rotating spiral phase has energy $E_{\rm spiral} = 2J_2{+}K^2/(16J_2)$. (3) At larger $|J_2|$ it

gives way to the q=0 ferromagnet solution (ϕ_A=ϕ_B) with energy $E_{FM} = K+2J+2J_2$. The computed phase diagram and associated wavevector q are shown in Fig. 8.3.

It is also evident that a mostly-Heisenberg model cannot produce a counter-rotating spiral. This is true even if it is supplemented by e.g. Dzyaloshinskii-Moriya couplings. To see this, examine the generic spin correlations of the ansatz state Eq. 8.3. Between neighboring sites i=(A, r) and j=$(B, r+v)$, they are

$$\left\langle S_i^x S_j^x \pm S_i^y S_j^y \right\rangle = \delta(q_B \mp q_A) \cos\left(q_B v + \phi_B \mp \phi_A\right) \tag{8.5}$$

The upper sign gives the usual Heisenberg correlations, while the lower sign corresponds to the spin-anisotropic correlations of the Kitaev exchange. The delta-function factor ensures that the Heisenberg/Kitaev correlations vanish in the counter/co-rotating spiral, respectively.

8.1.3 Non-coplanar spiral from coupled chains.

Each of the three α, β, γ-Li_2IrO_3 lattices is reached from the decoupled-chains limit, by introducing a particular pattern of inter-chain couplings between chains of various positions and orientations. We find that these inter-chain couplings both help to stabilize the coplanar spiral found in the 1D model, and also introduce an alternating pattern of non-coplanar tilts in the rotation planes of successive zigzag chains, as follows. By taking Eq. 8.3 with appropriate phases and introducing the $\langle S^b \rangle$ component, we describe the full spiral by

$$\vec{S}_{s,r} = \cos(q_s r_a)\langle S^c \rangle \hat{c} - \sin(q_s r_a) \left(\langle S^a \rangle \hat{a} \pm \langle S^b \rangle \hat{b} \right) \tag{8.6}$$

with q_B=$-q_A$=q>0 denoting counter-rotation between upper (s=B) and lower (A) sites on each zigzag chain. The $\pm$ sign alternates between successive zigzag chains, tilting S^a towards $\pm S^b$, with magnitudes satisfying $\langle S^a \rangle^2$+$\langle S^b \rangle^2$=$\langle S^c \rangle^2$ required by the constraint of fixed length spin on each site. This tilting is stabilized energetically by the strong $K_c S_i^b S_j^b$ inter-chain coupling, and its alternating pattern is set by J_c>0. The resulting non-coplanar spiral is composed of a coplanar spiral in each zigzag chain, whose plane of rotation alternates in orientation between adjacent zigzag chains. Fig. 8.3 shows the resulting spiral as viewed in the b-axis projection common to the lattices, for parameters with $q = 0.57\times 2\pi/a$.

8.1.4 Applicability of the 1D model.

We demonstrate the applicability of the 1D model to the physical lattices, by studying the smooth evolution of each lattice to its decoupled-chains limit. In particular, we introduce an inter-chain coupling coefficient λ_c, and map the semiclassical phase diagram of $H_\lambda = \lambda_c H_c + H_d$. Here the Hamiltonian Eq. 8.1 is supplemented

by the J_2 exchange between second-neighbors of the Ir lattice, on the two intra-chain bonds (as in Eq. 8.2) as well as on the four remaining bonds (where it is suppressed by the inter-chain coupling coefficient λ_c). Such a study is shown in Fig. 8.2B, showing the phase diagram as a function of λ_c and J_2 for K_d=0.8K_c, J_c=2J_d=$|I_c|$, I_c=K_c/3. We find that the spiral phase remains stable from the 1D limit λ_c=0 through the isotropic physical lattice λ_c=1, on each of the lattices.

8.1.5 Necessity of strong Kitaev interactions.

We consider a KJI_c−J_2 Hamiltonian, such as the model we previously reported[99] for the spiral order in γ-Li_2IrO_3, and attempt to tune $J_2 \to 0$ while preserving the experimentally-observed spiral phase. Such a study is presented in Fig. 8.2B, showing the phase diagram in $J/|K|$ and J_2/K, here for $I_c/K = 0.375$. We find that to discard the second neighbor interactions, the ratio $|K|/J$ must simultaneously be taken to be quite large $\sim$ 20. One representative such set of nearest-neighbor couplings is $(K, J, I_c) = (-12, 0.6, -4.5)$ meV. Here the overall scale is set so that the mean field ordering temperature T_N=40K matches the experimental T_N. Putting aside the Ising term, this ratio $J/|K| = 0.05$ lies well within the 2D Kitaev quantum spin liquid phase on the honeycomb lattice[106, 107, 131], though it may lie outside the 3D quantum spin liquid phases on the 3D lattices[141].

8.1.6 Semiclassical solutions.

The semiclassical approximation which we employ can capture incommensurate spiral orders as well as other magnetic phases. We represent spins by unconstrained vectors, yielding a quadratic Hamiltonian which is appropriate for capturing fluctuating states with small ordered moments. The lowest energy mode of this quadratic Hamiltonian is associated with the ordering instability of the spin model, and is straightforwardly found by Fourier transform. This is expected to be the leading ordering instability out of a high temperature paramagnetic phase assuming a continuous transition. Potentially quantum fluctuations could play a similar role. Our phase diagrams outline the evolution of this leading instability. We perform numerical minimization by defining a $\pi/8$-spaced grid in the Brillouin zone (which here ranges e.g. from $-2\pi/a$ to $2\pi/a$) and then using the constrained minimization algorithm of Broyden-Fletcher-Goldfarb-Shanno[101, 103], independently starting at each grid point.

The algorithmically-generated phase diagrams in Fig. 8.2 host the Li_2IrO_3 spiral phase as well as various competing orders. These include stripy antiferromagnets, where spins of the given component are aligned only along that Kitaev bond type; incommensurate orders with q-vectors along $\boldsymbol{b}$ or $\boldsymbol{c}$, which retain stripy-like correlations within the unit cell; and ferromagnets with S^c or S^z alignment.

8.1.7 Coplanar and tilt modes.

The experimentally observed spiral phase in the β and γ lattices, expressed in Eq. 8.6 and plotted in Fig. 8.3, was identified numerically in two steps. Observe that the non-coplanar S^b tilt pattern is distinguished from the S^a, S^c coplanar spiral order by a mirror eigenvalue, associated with a $\boldsymbol{c}$-axis reflection. The coplanar spiral is mirror-even while the tilt mode is mirror-odd. Indeed we find that they appear as distinct modes in the Fourier transform of Hamiltonians in the spiral phase. The global ground state is numerically found to be the coplanar spiral mode, which furthermore is found to exhibit $\langle S^a \rangle < \langle S^c \rangle$. Nonlinear effects above our quadratic approximation, which would tend to force the length of spin to be similar across sites, are likely to mix this solution with an additional mode. We adopt the following heuristic approach to include effects of nonlinearity which become more important with growing magnitude of the order parameter. We examine the lowest energy excited mode available for this mixing, and find throughout that it consists of the experimentally-observed $\langle S^b \rangle$ tilt pattern. While the instability analysis provides us a phase diagram that includes an incommensurate spiral, a more controlled calculation of nonlinear effects is required to decide whether the observed magnetic order appears or some other state is favored in this regime of parameters for the quantum S=1/2 Hamiltonian.

This analysis fixes the pattern of non-coplanar tilts. Their rough magnitude (though not their overall sign) can be estimated by constructing a fully-classical configuration from the two mixing modes. For the values (K, J, I_c)=$(-12, 0.6, -4.5)$ meV, the resulting tilt angle is 63°, similar to the angles observed experimentally, 42° and 55°; it can be tuned through these values by varying the relative ratios of the exchange parameters. However we expect fluctuations to be relevant for these systems. Indeed, in the experimentally-determined magnetic structures[99, 97] of β- and γ-Li_2IrO_3, the extracted ordered magnetic moment is not constant in magnitude between sites, but it is smaller by 10-20% when it is aligned in the ab plane compared to when it is pointing along the c-axis. This variation is likely due to a combination of g-factor anisotropies and quantum fluctuations of these S=1/2 moments.

8.1.8 Zigzag-chain mechanism in α-Li_2IrO_3.

α-Li_2IrO_3 [182] has a layered structure of stacked 2D iridium honeycombs separated by layers of Li ions. For comparison with the other lattices we construct an orthorhombic parent unit cell of the same size as for the β and γ structures (for details see [90]) where the honeycombs are in the ($\boldsymbol{a}$+$\boldsymbol{b}$,$\boldsymbol{c}$) plane (Fig. 8.1). The Hamiltonian Eq. 8.1 predicts an incommensurate spiral order in the honeycomb layers with the same pattern of counter-rotation between adjacent sites and non-coplanarity between vertical (c-axis) bonds as in the β and γ lattices. Remarkably, the energetics is such that for the same values of the exchange parameters (K, J, I), the calculated relative angles of spins on nearest-neighbor sites is the same on all three lattices.

In particular, energetic analysis of the (K, J, I) model Hamiltonian on the α-Li_2IrO_3 lattice, with parameters chosen to reproduce the experimentally-observed order on β- and γ-Li_2IrO_3, predicts a magnetic structure where the relative spin orientations between adjacent sites are the same as in the β and γ polytypes. This implies that the projection of the α-Li_2IrO_3 ordering wavevector onto the honeycomb layers is $q_{1D} = q\cos\theta$, where $q = 0.57 * 2\pi/a$ is the propagation vector magnitude in the β and γ lattices, and $\theta = \cos^{-1}(a/\sqrt{a^2+b^2})$ is the angle between the $\boldsymbol{a}$-axis and the α-Li_2IrO_3 honeycomb layers. Here the subscript 1D emphasizes that for a given honeycomb plane, the spiral wavevector lies along a zigzag chain, as in the 1D model of decoupled chains (Eq. 8.2 and Fig. 8.3).

The resulting value for this projection, $q_{1D} \sim 0.35\text{Å}^{-1}$, serves as an estimated lower bound for the magnitude of the 3D ordering wavevector $\boldsymbol{q}_{3D}$ that would occur in the real material. Weak inter-layer couplings can give $\boldsymbol{q}_{3D}$ a finite component normal to the honeycomb layers, suggesting a possible range for the magnitude $|\boldsymbol{q}_{3D}|$. Future experiments on α-Li_2IrO_3 single crystal samples could test these predictions for $\boldsymbol{q}_{3D}$, as well as the predictions for non-coplanarity and counter-rotation, which are highly non-trivial features for the magnetic order on a honeycomb lattice. In particular the non-coplanarity would break the C-centering of the honeycomb lattice, leading to a doubling of the primitive unit cell; this is a rather unusual feature for spiral order, and distinct from other theoretical models[189, 178] for α-Li_2IrO_3.

8.1.9 Conclusion.

The experimental observations in β- and γ-Li_2IrO_3 are intriguing: the two compounds undergo a magnetic ordering transition, at similar temperatures, into an unusual spiral magnetic order, with spiral wavevectors which are the same up to the experimental accuracy. This spiral wavevector appears to be incommensurate, with no clear mechanism for strong lattice pinning. In this work we have found a nearest-neighbor magnetic Hamiltonian which reproduces the complete symmetry of the spiral magnetic order on the two lattices including the pattern of counterrotation and noncoplanarity. The origin of this cross-lattice similarity is clarified by a 1D zigzag chain minimal model. This transparent model is sufficiently minimal to be a common building-block for the lattices, yet sufficiently complex to stabilize the counter-rotating spiral order. Its applicability is verified by smoothly extending it towards the physical lattices, and its predictions for α-Li_2IrO_3 are testable. The apparent commonality across the Li_2IrO_3 family suggests that to capture certain aspects of the magnetism, it may be sufficient to describe the different compounds via the same low-energy effective Hamiltonian. Why this may happen remains to be understood.

Note added. During publication of this manuscript, a preprint[144] has appeared which discusses magnetism on the β, γ-Li_2IrO_3 lattices. One of the magnetic spiral phases identified there correctly captures the magnetic structure observed[97] in β-

Li_2IrO_3. However, that phase, as well as the other spiral phases found in that work, differ in detail (symmetry of the ordering pattern) [2] from the spiral phase discussed here and observed experimentally[99] for γ-Li_2IrO_3.

8.2 Technical detail

8.2.1 Parent orthorhombic setting for α, β, γ-Li_2IrO_3

In this section, we define simple idealizations of the Ir lattices in the crystals, by taking oxygen octahedra to have ideal cubic symmetry. This provides a pedagogically clearer description of the 3D lattices. For the layered α-Li_2IrO_3 monoclinic structure, our definition of parent orthorhombic axes is a key step in our prediction of its magnetic order, as discussed in the text.

We use a coordinate system based on the parent orthorhombic axes shown in Fig. 1. These vectors, which are the conventional crystallographic axes for β, γ-Li_2IrO_3, are related to the Ir-O x, y, z axes by

$$\boldsymbol{a} = (2, 2, 0), \quad \boldsymbol{b} = (0, 0, 4), \quad \boldsymbol{c} = (6, -6, 0). \tag{8.7}$$

In the equation above we have written the a, b, c vectors in terms of the Cartesian (cubic orthonormal) x, y, z coordinate system. The $\hat{x}, \hat{y}, \hat{z}$ lattice vectors in this coordinate system are defined as the vectors from an iridium atom to its neighboring oxygen atoms in the idealized cubic limit, with the unit of length being the Ir-O distance. Nearest neighbor bonds in the resulting Ir lattice have length $\sqrt{2}$, and second neighbors are at distance $\sqrt{6}$.

For each lattice, we express its Bravais lattice vectors, as well as each of its sites of its unit cell, in terms of the a, b, c axes. A given vector or site, written as (n_a, n_b, n_c), is converted to the Cartesian coordinate system by $(n_x, n_y, n_z) = n_a\boldsymbol{a} + n_b\boldsymbol{b} + n_c\boldsymbol{c}$. The conventional unit cell in the orthorhombic setting, which contains 16 sites, is found by combining the primitive unit cell with the Bravais lattice vectors.

β-Li_2IrO_3 hyperhoneycomb lattice (n=0 harmonic honeycomb), space group $Fddd$ (#70):

[2] The a-axis spiral orders discussed in Ref. [144] ("SP_{a^+}" and "SP_{a^-}") exhibit features of non-coplanarity and counter-rotation, but have a different symmetry compared to the spiral phase found experimentally in γ-Li_2IrO_3. The pattern of non-coplanarity of the spiral planes predicted for γ-Li_2IrO_3 is such that it alternates between successive *pairs* of zigzag chains along c; whereas experimentally it is found that it alternates between consecutive zigzag chains[99], as illustrated in Fig. 3 (bottom right). Interestingly, the order in β-Li_2IrO_3 is correctly captured by one of the spiral orders found in that work with sign-flipped Γ-interactions, specifically $\bar{SP}_{a^-}$. In contrast, the experimentally-determined structures for both β and γ-polytypes are captured naturally by the KJI minimal model proposed in Eq. 1.

Primitive unit cell (4 sites):

$$\left(0,0,0\right);\ \left(0,0,\frac{1}{6}\right);\ \left(\frac{1}{4},\frac{-1}{4},\frac{1}{4}\right);\ \left(\frac{1}{4},\frac{-1}{4},\frac{5}{12}\right) \tag{8.8}$$

Bravais lattice vectors (face centered orthorhombic):

$$\left(\frac{1}{2},\frac{1}{2},0\right);\ \left(\frac{1}{2},-\frac{1}{2},0\right);\ \left(\frac{1}{2},0,\frac{1}{2}\right). \tag{8.9}$$

γ-Li_2IrO_3 stripyhoneycomb lattice (n=1 harmonic honeycomb), space group $Cccm$ (#66):

Primitive unit cell (8 sites):

$$\begin{gathered}\left(0,0,0\right);\ \left(0,0,\frac{1}{6}\right);\ \left(\frac{1}{4},\frac{-1}{4},\frac{1}{4}\right);\ \left(\frac{1}{4},\frac{-1}{4},\frac{5}{12}\right);\\ \left(0,0,\frac{1}{2}\right);\ \left(0,0,\frac{2}{3}\right);\ \left(\frac{1}{4},\frac{1}{4},\frac{3}{4}\right);\ \left(\frac{1}{4},\frac{1}{4},\frac{11}{12}\right)\end{gathered} \tag{8.10}$$

Bravais lattice vectors (base centered orthorhombic):

$$\left(\frac{1}{2},\frac{1}{2},0\right);\ \left(\frac{1}{2},-\frac{1}{2},0\right);\ \left(0,0,1\right). \tag{8.11}$$

α-Li_2IrO_3 layered honeycomb lattice (n=∞ harmonic honeycomb), space group $C2/m$ (#12):

To discuss the layered honeycomb α-Li_2IrO_3 polytype within the context of its 3D cousins, we must first set up a single global coordinate system. The two 3D lattices are captured, up to minute distortions, by the same parent simple-orthorhombic coordinate system of a, b, c axes.

The α polytype however has monoclinic symmetry and is conventionally described by a set of monoclinic axes, which we denote $\boldsymbol{a_m}, \boldsymbol{b_m}, \boldsymbol{c_m}$. The parent orthorhombic $\boldsymbol{a}, \boldsymbol{b}, \boldsymbol{c}$ axes defined above are distinct from the conventional monoclinic axes used to describe this $C2/m$ crystal. Here we define an orthorhombic coordinate system from a higher-symmetry idealization of these monoclinic axes, by taking $\boldsymbol{a_o} = \boldsymbol{a_m} + \boldsymbol{c_m},\ \boldsymbol{b_o} = \boldsymbol{a_m} - \boldsymbol{c_m},\ \boldsymbol{c_o} = \boldsymbol{2b_m}$. The a_o, b_o, c_o notation here signifies that, up to the distortions of oxygen octahedra, the resulting a, b, c axes are identical to the orthorhombic axes of the β and γ polytypes. This higher-symmetry idealization consists of the approximation that $|a_m| = |c_m|$, which is wrong in the physical lattice[182] only by about 1%. The transformation between the conventional monoclinic axes and the universal orthorhombic axes is also described by the coordinate notation as

$$\boldsymbol{a_m} = \left(\frac{1}{2},\frac{1}{2},0\right);\ \boldsymbol{b_m} = \left(0,0,\frac{1}{2}\right);\ \boldsymbol{c_m} = \left(\frac{1}{2},-\frac{1}{2},0\right). \tag{8.12}$$

The a, b, c coordinate system preserves the key features used to discuss the other lattices, namely that bonds lying along the c axis carry Kitaev coupling $b = z$, while remaining bonds are diagonal to the a, b, c axes and form the d-bonds zigzag chains. Equivalently, we choose a right handed orthorhombic coordinate system, with the c axis as the unique axis along which one third of Ir-Ir bonds are aligned, and the b axis as the unique axis along which one third of Ir-O bonds are aligned.

Primitive unit cell (2 sites, denoted A and B):

$$\left(0,0,0\right);\ \left(\frac{1}{4},-\frac{1}{4},\frac{1}{12}\right) \tag{8.13}$$

Bravais lattice vectors, here denoted as a_1, a_2, a_3:

$$a_1 = \left(\frac{1}{2},-\frac{1}{2},0\right);\ a_2 = \left(-\frac{1}{4},\frac{1}{4},\frac{1}{4}\right);\ a_3 = \left(\frac{1}{2},\frac{1}{2},0\right) \tag{8.14}$$

where the first two vectors span the 2D honeycomb plane. These vectors are all of the same length ($\sqrt{6}$ in units of Ir-O distance), and span the six second neighbors within a honeycomb plane, plus one of the two additional pairs of sites on adjacent planes which are at the same distance, given by vectors $\pm a_3 = \pm(\hat{x} + \hat{y} + 2\hat{z})$ (the remaining pair belongs to the opposite sublattice).

Within a honeycomb plane, the nearest neighbor vectors from A to B are r_1, r_2, r_3, with $r_3 = -r_1 - r_2$ and

$$r_1 = \left(-\frac{1}{4},\frac{1}{4},\frac{1}{12}\right);\ r_2 = \left(\frac{1}{4},-\frac{1}{4},\frac{1}{12}\right). \tag{8.15}$$

The Bravais vectors above are related by $a_1 = r_2 - r_1$, $a_2 = r_1 - r_3$. For reference we also note these Ir-Ir vectors in the Ir-O coordinate system, $r_1 = -\hat{y} + \hat{z}$, $r_2 = \hat{x} - \hat{z}$, $r_3 = -\hat{x} + \hat{y}$. This immediately implies that the Kitaev labels for (r_1, r_2, r_3) bonds are (x, y, z) respectively.

Zigzag chain as basic structural unit:

The 1D zigzag chain is composed of sites A and B,

$$\left(0,0,0\right);\ \left(\frac{1}{4},-\frac{1}{4},\frac{1}{12}\right), \tag{8.16}$$

together with a single (1D) Bravais lattice vector,

$$a_1 = \left(\frac{1}{2},-\frac{1}{2},0\right). \tag{8.17}$$

The reflection $b \to -b$ takes this zigzag chain to its symmetry-equivalent partner, in which the minus sign in the two equations above is replaced by a plus sign.

In this notation it is evident that the zigzag chains forms the basic structural unit in all three Li_2IrO_3 polytypes. In each lattice, sites are naturally partitioned into pairs which match this zigzag chain unit cell, and each lattice contains the chain's Bravais lattice vector. The magnetic Hamiltonian on each lattice is constructed as the sum of zigzag chain Hamiltonians plus inter-chain interaction terms.

8.2.2 Ising interactions

The Ising term defined in Eq. 1 is distinct from any combination of Kitaev and Heisenberg exchanges. (The geometry is visualized in Fig. 8.5.) It can be related to the "off-diagonal" symmetric interactions which have recently appeared in the literature[186, 212, 133] under the symbols Γ or D. For instance, if on a z-bond one writes the term $+\Gamma(S_i^x S_j^y + S_i^y S_j^x)$, then the triplet KJI reproduces $JK\Gamma$ by setting $(K, J, I) = (K-\Gamma, J+\Gamma, -2\Gamma)$. The bond-Ising interaction may be preferred as its definition, unlike Γ, is independent of coordinate system.

In Eq. 1 we have included the Ising coupling only on c-bonds, for the following reasons. First consider the coplanar spiral mode. Since $r_{ij} \perp \gamma_{ij}$ and on d-bonds $\gamma_{ij} = (\hat{x}, \hat{y})$, the d-bond r_{ij} take values $((\hat{y}, \hat{x}) \pm \hat{z})/\sqrt{2}$, projecting I_d into a Heisenberg-Kitaev term when $\langle S^z \rangle = 0$. In contrast I_c couples spin component $\hat{c} = (\hat{x} - \hat{y})/\sqrt{2}$ and helps stabilize the spiral (Supplementary Fig. 8.4). Second, we observe that the experimentally-observed pattern of non-coplanar tilts is not favored by the d-bonds Ising exchange, whose r_{ij} orientations favor a different symmetry breaking pattern. The correct S^b tilts are instead stabilized by the K_c Kitaev term.

8.2.3 Details of relation between Ising and Γ terms

We show more explicitly how the off-diagonal symmetric interaction term, sometimes called the "Γ" exchange, can be made equivalent to the Ising term introduced above by appropriately modifying the strength of the Kitaev and Heisenberg couplings. This can be seen by writing the spin interaction matrix $J^{a,b}$ for the interaction $S^a J^{a,b} S^b$ (summation implied) of neighboring spins. Let us again write it in the KJI and $JK\Gamma$ notations for the interaction on a c-bond, in the x, y, z basis,

$$\begin{pmatrix} \frac{1}{2}I_c + J & -\frac{1}{2}I_c & 0 \\ -\frac{1}{2}I_c & \frac{1}{2}I_c + J & 0 \\ 0 & 0 & K+J \end{pmatrix} \longleftrightarrow \begin{pmatrix} J & \Gamma_c & 0 \\ \Gamma_c & J & 0 \\ 0 & 0 & K+J \end{pmatrix} \tag{8.18}$$

where we have kept the c subscript on I_c and Γ_c to denote that these are the parameters for the c-type bond. The set of interaction matrices spanned by K, J, I is equivalent to that spanned by $J, K, \pm\Gamma$. In particular, our K, J, I_c model, with Ising interactions on c-bonds, is related to a K, J, Γ_c model with off-diagonal Γ_c couplings on c bonds.

The bond-Ising interaction may be preferred for two reasons. First, its geometric definition, coupling the spin component along the Ir-Ir bond, is independent of coordinate system and thus free of sign ambiguities. In contrast, distinguishing $+\Gamma$ from $-\Gamma$ is coordinate-dependent. This is most evident for the x and y bonds on the 3D lattices, where in the Γ notation the interaction appears with a positive sign on half of the x-bonds and a negative sign on the remaining x-bonds. In contrast, the Ising term directly sets the coupled spin component to the direction of the displacement vector between the two sites, and is invariant to the vector's sign. Second, the

Ising coupling, of spin components along the bond, transparently indicates that this exchange is symmetry-permitted even for ideal O_6 octahedra.

8.2.4 Details of the 1D zigzag-chain solution

Here we present the full solution of the zigzag-chain model within the ansatz shown in the text. The quickest route to deriving the energy function Eq. 8.4 is to plug in the spin-spin correlations into the Hamiltonian Eq. 8.2. The nearest-neighbor correlations are given in Eq. 8.5; the second neighbor correlations are $\langle S{\cdot}S\rangle{=}\cos(qa_1)$. These two equations are sufficient for solving the model.

Alternatively, plugging in the ansatz Eq. 8.3 into the Hamiltonian Eq. 8.2 gives the following energy function,

$$\begin{aligned} E_{1\mathrm{D}} = \sum_{r=na_1} \Big[& J_2 \left(2\cos(\theta)\right) \\ & + K \Big(\cos\left(\theta/2\right)\cos(f_-(r)) \\ & \qquad + \sin\left(\theta/2\right)\sin(f_+(r)) \Big) \\ & + J \ \left(2\cos\left(\theta/2\right)\cos(f_-(r))\right) \Big] \\ f_\pm(r) = & \left[(\phi_A \pm \phi_B) + r(q_A \pm q_B)\right] \end{aligned} \tag{8.19}$$

with $\theta = a_1 q_B$. Performing the average over 1D Bravais lattice sites $r = na_1$, we observe four possibilities. If $q_A = q_B \neq 0, \pi/a_1$, then the term with f_+ vanishes, while f_- are replaced by $(\phi_A - \phi_B)$. This co-rotating spiral is set by the interplay of primarily Heisenberg first and second neighbor exchanges, requires the typical geometrical frustration here encoded by J and J_2 of the same sign, and is the typical spiral one expects from frustrated Heisenberg models. If $q_A = -q_B \neq 0, \pi/a_1$, then the terms with f_- vanish, while f_+ are replaced by $(\phi_A{+}\phi_B)$. This is the counter-rotating spiral. The final possibilities are $\theta = \pm\pi$, leading to the stripy antiferromagnet, or $\theta = 0$, leading to the ferromagnet (in both cases $f_\pm$ are replaced by $(\phi_A \pm \phi_B)$), discussed above.

When studying the counter-rotating spiral, it is important to keep in mind the behavior of the phases under lattice translations. Due to the counter-rotation, here the *average* phase is the physical quantity; the arbitrary "overall phase" of the spiral, freely modified (for incommensurate q) by shifting r, is then the *difference* of phases $\phi_A{-}\phi_B$. We may choose the phases $\phi_A{=}\phi_B{=}\pi/4$ to satisfy $\phi_A{+}\phi_B{=}\pi/2$, keeping in mind that shifting the overall phase does not permit these phases to simultaneously be set to zero.

The stabilization of the spiral by Kitaev interactions can also be observed via Eq. 8.5 by fixing $\phi_A{+}\phi_B = \pi/2$. While the Heisenberg correlator vanishes, the spin

component matching the Kitaev bond type exhibits nonzero correlations, $\langle S^x_r S^x_{r+r_1}\rangle_x = (1/2)\sin(\theta/2)$.

8.2.5 Details of the semiclassical solution

Here we give technical details for the semiclassical solution. First note that the 16-site unit cell of the orthorhombic axes contains 4 sites along the spiral propagation direction a; in contrast, the zigzag-chain 1D Bravais vector a_1 spans two sites. Hence a wavevector in units of π/a_1 is roughly analogous to one in units of $2\pi/a$.

For all three lattices, we use an 8-site unit cell with a base-centered orthorhombic Bravais lattice. In this choice of unit cell, the Brillouin zone is rotated (by 45 degrees) and doubled in area from the BZ associated with the conventional orthorhombic coordinate system; e.g. it extends from $-2\pi/a$ to $+2\pi/a$ along the a-axis.

Let us write the explicit process of solution for the wavevector within the Fourier transform (FT). For concreteness we focus on the minimal parameters $(K, J, I_c) = (-12, 0.6, -4.5)$ meV, on the β (hyperhoneycomb) lattice. This Hamiltonian is minimized at $\vec{q} = 0.57 \times 2\pi/|a| \times \hat{a}$. The FT ground state at this wavevector, energy -14.8 meV, has ordered spin moment $\vec{S} \propto \hat{c} \pm i0.48\hat{a}$, where the $\pm$ sign alternates between successive sites in the unit cells (shown above) when they are listed in order of their c coordinate. The second excited state at this wavevector, energy -12.1 meV is capable of mixing with this ground state, and exhibits a wavefunction $\pm\hat{b}$ where this distinct $\pm$ symbol is chosen to give the same sign on two sites connected by a c-bond, and opposite sign on two sites connected by a d-bond; in other words, it alternates in pairs when sites are listed by their c coordinate. Observe that these definitions of sign structure are consistent with the definition of the wavefunction given in the text, Eq. 8.6.

The mixing mode energy can be tuned towards the ground state, for example in the nearby set of parameters with bond-strength anisotropy in the Kitaev term, $(K_c, K_d, J, I_c) = (-13.2, -11, 0.6, -4.5)$ (in meV), the ground state coplanar mode has energy -13.8 meV, and the tilt mode is its first excited state, at energy -13.5 meV higher. This combined noncoplanar state is found on all three lattices. As discussed in the text, it agrees with the spiral order observed experimentally on both the β and the γ polytypes.

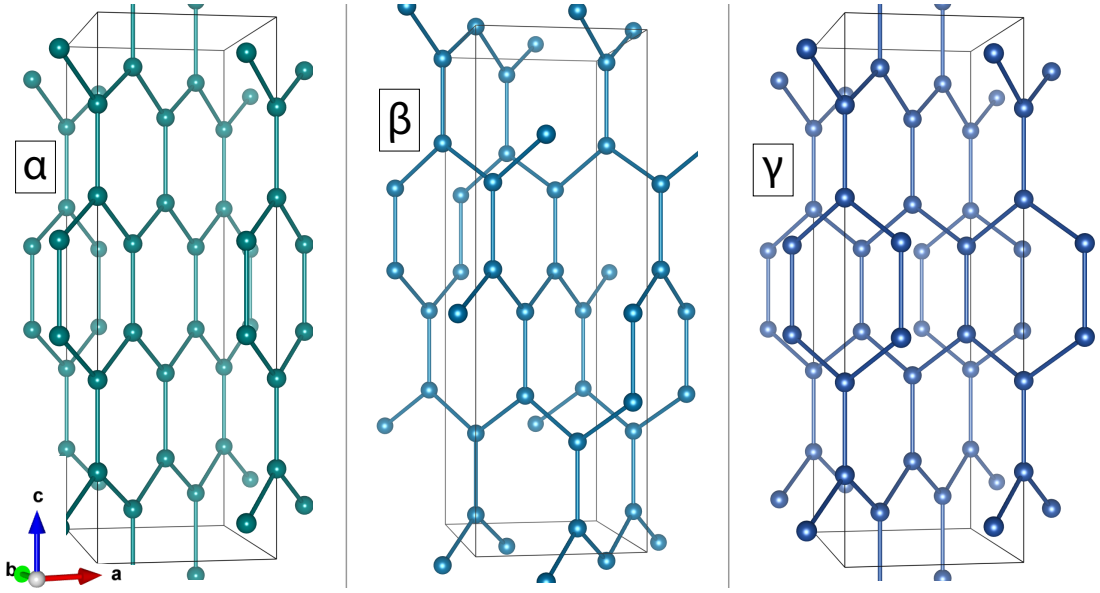

Figure 8.1: **L**attices of Ir in α, β, γ-Li_2IrO_3, with parent orthorhombic a, b, c axes. Experiments on the 3D lattices, β- and γ-Li_2IrO_3, found strikingly similar spiral orders.

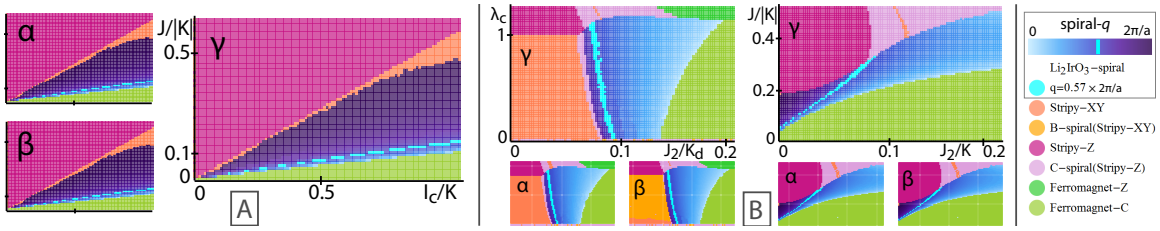

Figure 8.2: **P**hase diagrams on α, β, γ-Li_2IrO_3. In the vicinity of the spiral phase (shaded blue) which contains the experimentally observed magnetic order, the semi-classical phase diagrams appear remarkably similar across the α, β, γ-Li_2IrO_3 lattices. (A) The nearest-neighbor KJI_c model (J_2=0) is sufficient for capturing the observed spiral, and exhibits this cross-lattice similarity. (B) (Left) the spiral from the 1D zigzag chain model persists to the full lattices; (right) taking $J_2 \to 0$ requires large $|K|/J$; see parameters below. For the 2D α-polytype, shading indicates the equivalent spiral $\boldsymbol{q}$ along $\boldsymbol{a}$ as described in the text.

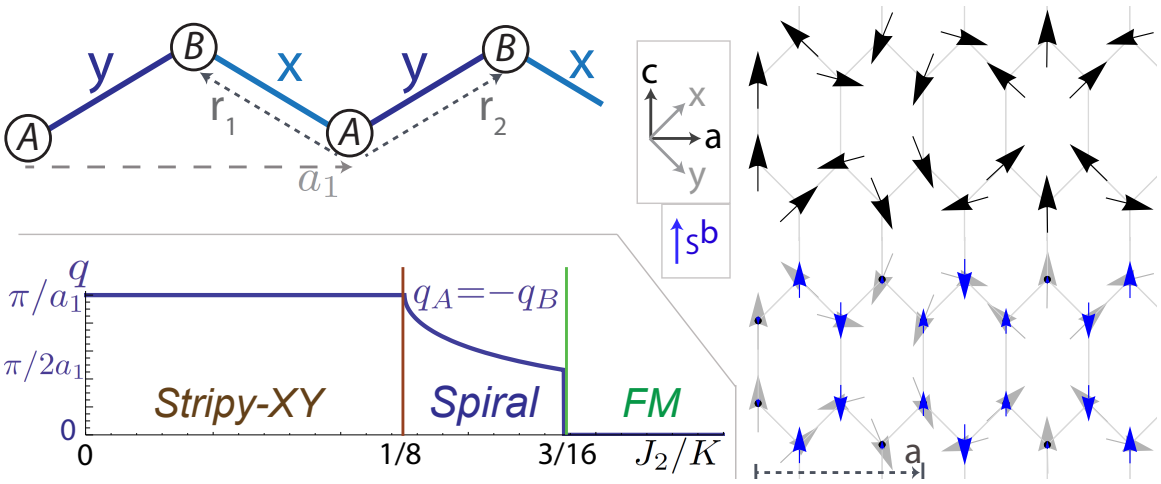

Figure 8.3: **Z**igzag chain and spiral. As evident in this 1D minimal model for the Li_2IrO_3 lattices (top left), the counter-rotating coplanar spiral order can be stabilized by Kitaev interactions (bottom left; here with $K<0$, $J=|K|/3$). For each lattice, restoring the inter-chain couplings preserves the counter-rotating S^a, S^c spiral (top right), while also introducing non-coplanar S^b components (overlayed in blue, bottom right). Together they form the experimentally observed order.

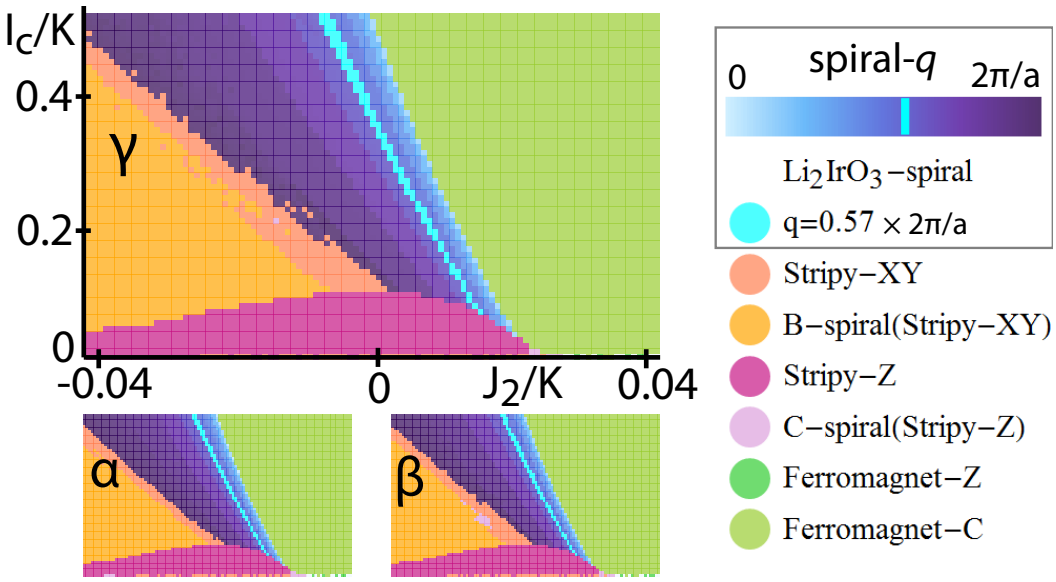

Figure 8.4: Here we observe that for $J = |K|/20$, finite $I_c < 0$ is required regardless of the sign or magnitude of J_2.

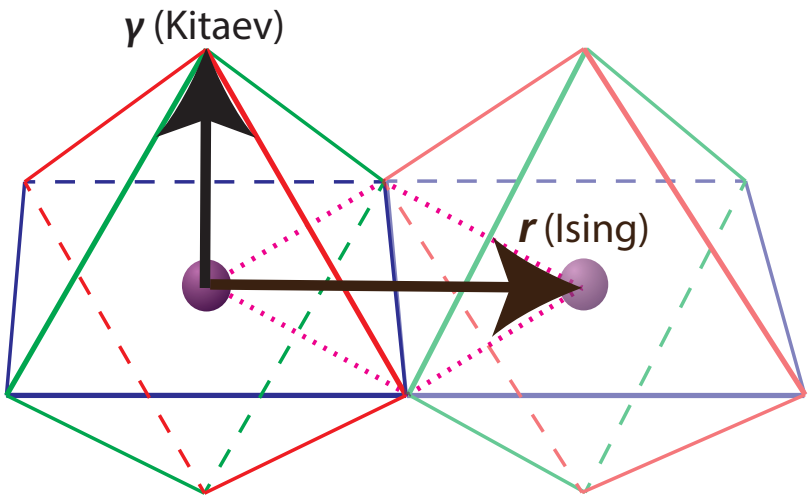

Figure 8.5: **V**isualization of geometry of Kitaev and Ising exchanges. The two neighboring Ir sites (purple spheres), with surrounding oxygens (vertices of octahedra), are shown. The oxygen octahedra of neighboring Ir sites are edge-sharing in these structures. The axes for the anisotropic interaction terms are then determined as follows (see the discussion following Eq. 1 of the main text for details). The Ising interaction axis $\vec{r}$ is the vector connecting the two Ir sites. The Kitaev interaction axis γ is perpendicular to the plane which contains r and the shared octahedra edge. For both interaction terms, the coupling axis for the quadratic spin interaction is defined as an axis with no orientation; here it is shown as an arrow (with an arbitrary direction of the arrow head) for ease of visualization.

Chapter 9

Conclusion

As of current writing, much potential remains for the study of Li_2IrO_3 and related compounds. With the analysis above and further evidence for the relevance of Kitaev exchange in the model magnetic Hamiltonian, this material can contribute to a shift in our understanding of the landscape of possible magnetic exchanges which can can be reasonably expected to arise in spin-orbit coupled systems. Indeed spin orbit coupling is a key ingredient for many topological phases, band-insulating as well as metallic, which are currently being explored. Its effects in interacting systems, and possibilities for both short-ranged-entangled phases as well as phases with long range entanglement, such as the Kitaev spin liquid discussed above, remain at the forefront of current research.

Multiple research avenues could be fruitfully explored. It would be most useful to find theoretical techniques to probe entanglement; though by their very nature, these will likely require a detailed understanding of the physics of the specific system, and may not form a general solution. The concrete features of the three-dimensional spin liquids described above, such as the surrounding phase diagram as well as their finite temperature transition, form the starting point for identifying fractionalization in this context. For future experimental searches, an additional question concerns the quantitative extent of the stability of long range entangled phases (in non-chiral settings such as spin liquids), to the presence of disorder or finite competing interactions. Finally, the conducting states which emerge from fractionalization, which served as some of the original motivations for studying spin liquid, remain in parts mysterious. Though it is difficult to know how reliable, quantitatively or even qualitatively, these predictions may be, as in the analysis above, we expect unconventional conducting or superconducting behavior upon doping a spin liquid,

Experimentally, the possibility of charge doping presents one possible route to realizing exotic physics. Even starting from a magnetic Hamiltonin within an ordered state but close to the transition into a spin liquid, upon charge doping one could uncover the correlated physics associated with the nearby fractionalized phase. Here the experimental handle on entanglement would be again quite indirect, but nonetheless

present its own interesting physics. Controlling such an experimental identification, of underlying fractionalization in a doped system, remains a challenge but should be amenable to proposals in a particular concrete context, as in the transition from spin-triplet to spin-singlet superconductivity expected from the analysis above of a doped antiferromagnetic Kitaev model.

The introduction of mobile charges by chemical doping or using various means of gating presents its own complications, such as disorder, which not captured by the multi-band multi-interacting Hubbard models employed as the microscopic starting point for this study, and would benefit from complementary studies. Good theoretical control of this problem might not be achieved, however; but this should not bottleneck the field. Charge doping may harbor one of the most exciting possibilities for new physics. For this possibility, as for much of the research presented within this present manuscript, collaborations with various physicists including material scientists, crystal growers and device chemists, are likely to lead the way.

Bibliography

[1] I. Kimchi, S. A. Parameswaran, A. M. Turner, F. Wang, A. Vishwanath. Proceedings of the National Academy of Sciences 110 (41): 16378-16383 (2013).

[2] S. A. Parameswaran, I. Kimchi, A. M. Turner, D. M. Stamper-Kurn, A. Vishwanath. Phys. Rev. Lett. 110, 125301 (2013).

[3] S. Yan, D. A. Huse, and S. R. White, Science 332, 6034 (2011).

[4] A. F. Albuquerque, D. Schwandt, B. Hetanyi, S. Capponi, M. Mambrini, and A.M. Lauchli, Phys. Rev. B 84, 024406 (2011).

[5] J. B. Fouet, P. Sindzingre, and C. Lhuillier, Eur. Phys. J. B 20, 241 (2001).

[6] J. Reuther, D. A. Abanin, and R. Thomale, Phys. Rev. B 84, 014417 (2011).

[7] D. J. J. Farnell, R. F. Bishop, P. H. Y. Li, J. Richter, and C. E. Campbell, Phys. Rev. B 84, 012403 (2011).

[8] J. Oitmaa and R. R. P. Singh, Phys. Rev. B 84, 094424 (2011).

[9] Z. Y. Meng, T. C. Lang, S. Wessel, F. F. Assaad and A. Muramatsu, Nature (London) 464, 847-851 (2010).

[10] B. K. Clark, D. A. Abanin, and S. L. Sondhi, Phys. Rev. Lett. 107, 087204 (2011).

[11] H.Y. Yang and K.P. Schmidt, Europhys. Lett. 94, 17004 (2011).

[12] A. Yu. Kitaev, Ann. Phys. 321, 2 (2006).

[13] G. Jackeli and G. Khaliullin, Phys. Rev. Lett. 102, 017205 (2009).

[14] J. Chaloupka, G. Jackeli, and G. Khaliullin, Phys. Rev. Lett. 105, 027204 (2010).

[15] Y. Singh and P. Gegenwart, Phys. Rev. B, 82, 064412 (2010).

[16] Y. Singh, S. Manni, and P. Gegenwart, arXiv:1106.0429.

[17] X. Liu, T. Berlijn, W.-G. Yin, W. Ku, A. Tsvelik, Young-June Kim, H. Gretarsson, Yogesh Singh, P. Gegenwart, and J. P. Hill, Phys. Rev. B 83, 220403(R) (2011).

[18] H.-C. Jiang, Z.-C. Gu, X.-L. Qi, and S. Trebst, Phys. Rev. B, 83, 245104 (2011).

[19] J. Reuther, R. Thomale, and S. Trebst, Phys. Rev. B 84, 100406(R) (2011).

[20] F. Trousselet, G. Khaliullin, and P. Horsch, Phys. Rev. B 84, 054409 (2011).

[21] H. Jin, H. Kim, H. Jeong, C. H. Kim, and J. Yu, arXiv:0907.0743.

[22] S. Bhattacharjee, S. S. Lee, and Y. B. Kim, arXiv:1108.1806.

[23] For a related result see B. J. Yang and Y. B. Kim, Phys. Rev. B 82, 085111 (2010).

[24] An alternative scenario is explored in A. Shitade, H. Katsura, J. Kunes, X.-L. Qi, S.-C. Zhang, and N. Nagaosa, Phys. Rev. Lett. 102, 256403 (2009).

[25] P. W. Anderson, Phys. Rev. 79, 705 (1950).

[26] ALPS collaboration [http://alps.comp-phys.org/]: B. Bauer et al., J. Stat. Mech. P05001 (2011), and A.F. Albuquerque et al., J. of Magn. and Magn. Materials 310, 1187 (2007).

[27] Yi-Zhuang You, Itamar Kimchi, and Ashvin Vishwanath, arXiv:1109.4155.

[28] J. Orenstein and A. J. Millis, Science 288, 468 (2000). Y. Tokura and N. Nagaosa, Science 288, 462 (2000).

[29] L. Balents, Nature (London) 464, 199 (2010).

[30] A. Yu. Kitaev, Ann. Phys. 321, 2 (2006).

[31] Y. Singh and P. Gegenwart, Phys. Rev. B, 82, 064412 (2010).

[32] Y. Singh, S. Manni, and P. Gegenwart, arXiv:1106.0429v1.

[33] B. J. Kim et al., Phys. Rev. Lett. 101, 076402 (2008); B. J. Kim et al., Science 323, 1329 (2009).

[34] G. Jackeli and G. Khaliullin, Phys. Rev. Lett. 102,017205 (2009).

[35] J. Chaloupka, G. Jackeli, and G. Khaliullin, Phys. Rev. Lett. 105, 027204 (2010) .

[36] H.-C. Jiang, Z.-C. Gu, X.-L. Qi, and S. Trebst, Phys. Rev. B, 83, 245104 (2011).

[37] X. Liu et al., Phys. Rev. B 83, 220403(R) (2011).

[38] J. Reuther, R. Thomale, and S. Trebst, arXiv:1105.2005v1.

[39] I. Kimchi and Y. Z. You, Phys. Rev. B 84, 180407(R) (2011).

[40] Subhro Bhattacharjee, Sung-Sik Lee, Yong Baek Kim, arXiv:1108.1806.

[41] H. Jin et al., arXiv:0907.0743.

[42] A. Shitade, H. Katsura, J. Kunes, X.-L. Qi, S.-C. Zhang, and N. Nagaosa, Phys. Rev. Lett. 102, 256403 (2009).

[43] Di Xiao, Wenguang Zhu, Ying Ran, Naoto Nagaosa, Satoshi Okamoto, arXiv:1106.4296

[44] P. W. Anderson, Science, 235, 1196 (1987).

[45] X.-G. Wen, and P. A. Lee, Phys. Rev. Lett. 76, 503 (1996);

[46] N. Read and D. Green, Phys. Rev. B 61, 10267 (2000).

[47] X.-G. Wen, Phys. Rev. B, 65, 165113 (2002).

[48] T. Hyart, A. R. Wright, G. Khaliullin, B. Rosenow, Phys. Rev. B 85, 140510(R) (2012).

[49] J.-W. Mei, Phys. Rev. Lett. 108, 227207 (2012).

[50] M. Hermele, Phys. Rev. B, 76, 035125 (2007).

[51] F. J. Burnell and C. Nayak, arXiv:1104.5485.

[52] X.-G. Wen, Quantum Field Theory of Many-Body Systems, Ch. 9, Oxford (2008).

[53] G. Baskaran, S. Mandal, and R. Shankar, Phys. Rev. Lett. 98, 247201 (2007).

[54] X.-G. Wen, Phys. Rev. B 65, 165113 (2002).

[55] Y.-M. Lu and Y. Ran, Phys. Rev. B, 84, 024420 (2011).

[56] See Supplementary material.

[57] P. A. Lee, N. Nagaosa, and X.-G. Wen, Rev. Mod. Phys. 78, 17-85 (2006).

[58] M. M. Salomaa and G. E. Volovik, Rev. Mod. Phys. 59, 533 (1987).

[59] J. M. Kosterlitz and D. J. Thouless, J. Phys. C 6, 1181 (1973).

[60] L. Ioffe and A. Larkin, Phys. Rev. B 39, 8988 (1989).

[61] F. D. M. Haldane, Phys. Rev. Lett. 61, 2015 (1988).

[62] S. Kivelson Phys. Rev. B 39, 259-264 (1989). N. Read and B. Chakraborty, Phys. Rev. B 40, 7133-7140 (1989).

[63] F. Trousselet, G. Khaliullin, and P. Horsch, arXiv:1104.4707v1.

[64] A. J. Willans, J. T. Chalker, and R. Moessner, Phys. Rev. Lett. 104, 237203 (2010).

[65] F. Wang and T. Senthil, Phys. Rev. Lett. 106, 136402 (2011).

[66] G. Cao, J. Bolivar, S. McCall,J. E. Crow and R. P. Guertin, Phys. Rev. B 57, R11039R11042 (1998).

[67] A. J. Leggett, Rev. Mod. Phys. 47, 331-414 (1975).

[68] A. Kitaev, Ann. Phys. (N.Y.) **321**, 2 (2006).

[69] J. Chaloupka, G. Jackeli and G. Khaliullin, Phys. Rev. Lett.**105**, 027204 (2010).

[70] B. J. Kim, H. Ohsumi, T. Komesu, S. Sakai, T. Morita, H. Takagi, T. Arima, Science **323**, 1329 (2009).

[71] Y. Singh, P. Gegenwart, Phys. Rev. B**82**, 064412 (2010).

[72] X. Liu, T. Berlijn, W.-G. Yin, W. Ku, A. M. Tsvelik, Young-June Kim, H. Gretarsson, Yogesh Singh, P. Gegenwart, and J. P. Hill, Phys. Rev. B**83**, 220403(R) (2011).

[73] S. K. Choi, R. Coldea, A. N. Kolmogorov, T. Lancaster, I. I. Mazin, S. J. Blundell, P. G. Radaelli, Yogesh Singh, P. Gegenwart, K. R. Choi, S.-W. Cheong, P. J. Baker, C. Stock, and J. Taylor, Phys. Rev. Lett.**108**, 127204 (2012).

[74] F. Ye, S. Chi, H. Cao, B. C. Chakoumakos, J. A. Fernandez-Baca, R. Custelcean, T. F. Qi, O. B. Korneta, and G. Cao, Phys. Rev. B**85**, 180403(R) (2012).

[75] H. Gretarsson, J. P. Clancy, Y. Singh, P. Gegenwart, J. P. Hill, J. Kim, M. H. Upton, A. H. Said, D. Casa, T. Gog, and Y.-J. Kim, Phys. Rev. B**87**, 220407(R) (2013).

[76] M. J. O'Malley, H. Verweij and P.M. Woodward, J. Solid State Chem. **181**, 1803 (2008).

[77] Y. Singh, S. Manni, J. Reuther, T. Berlijn, R. Thomale, W. Ku, S. Trebst, and P. Gegenwart, Phys. Rev. Lett.**108**, 127203 (2012).

[78] S. Mandal and N. Surendran, Phys. Rev. B**79**, 024426 (2009).

[79] Eric Kin-Ho Lee, R. Schaffer, S. Bhattacharjee, and Y. B. Kim, Phys. Rev. B **89**, 045117 (2014).

[80] I. Kimchi, J. G. Analytis, A. Vishwanath, arXiv:1309.1171 (2013).

[81] T. Takayama, A. Kato, R. Dinnebier, J. Nuss, H. Takagi, arXiv.org/1403.3296 (2014).

[82] K. A. Modic, T. E. Smidt, I. Kimchi, N. P. Breznay, A. Biffin, S. Choi, R. D. Johnson, R. Coldea, P. Watkins-Curry, G. T. McCandless, J. Y. Chan, F. Gandara, Z. Islam, A. Vishwanath, A. Shekhter, R. D. McDonald, and J. G. Analytis, Nature Comm **5**, 4203 (2014).

[83] J. P. Hill, D. F. McMorrow, Acta Cryst A **52**, 236, (1996).

[84] G. Jackeli and G. Khaliullin, Phys. Rev. Lett.**102**, 017205 (2009).

[85] Supplemental material

[86] S. Boseggia, R. Springell, H. C. Walker, H. M. Rønnow, Ch. Rüegg, H. Okabe, M. Isobe, R. S. Perry, S. P. Collins, and D. F. McMorrow, Phys. Rev. Lett. **110**, 117207 (2013).

[87] http://forge.ill.eu/svn/magnetix

[88] *BasiReps* software part of the *FullProf* suite, J. Rodriguez-Carvajal, Physica B **192**, 55 (1993).

[89] J. G. Rau, Eric Kin-Ho Lee, H. Y. Kee, Phys. Rev. Lett. **112**, 077204 (2014).

[90] *See the Supplemental Material of this manuscript for details*, Supplemental Material.

[91] A. F. Albuquerque, D. Schwandt, B. Hetényi, S. Capponi, M. Mambrini, and A. M. Läuchli. Phase diagram of a frustrated quantum antiferromagnet on the honeycomb lattice: Magnetic order versus valence-bond crystal formation. *Phys. Rev. B*, 84:024406, Jul 2011.

[92] P. W. Anderson. Generalizations of the weiss molecular field theory of antiferromagnetism. *Phys. Rev.*, 79:705–710, Aug 1950.

[93] P. W. Anderson. Limits on the energy of the antiferromagnetic ground state. *Phys. Rev.*, 83:1260–1260, Sep 1951.

[94] E. J. Bergholtz, A. M. Läuchli, and R. Moessner. Symmetry breaking on the three-dimensional hyperkagome lattice of $na_4ir_3o_8$. *Phys. Rev. Lett.*, 105:237202, Dec 2010.

[95] H. Gretarsson, J. P. Clancy, X. Liu, J. P. Hill, Emil Bozin, Yogesh Singh, S. Manni, P. Gegenwart, Jungho Kim, A. H. Said, D. Casa, T. Gog, M. H. Upton, Heung-Sik Kim, J. Yu, Vamshi M. Katukuri, L. Hozoi, Jeroen van den Brink, and Young-June Kim. Crystal-Field Splitting and Correlation Effect on the Electronic Structure of A2IrO3. *Phys. Rev. Lett.*, 110:076402, Feb 2013.

[96] S. Bhattacharjee, S.-S. Lee, and Y. B. Kim. Spin-orbital locking, emergent pseudo-spin and magnetic order in honeycomb lattice iridates. *New Journal of Physics*, 14(7):073015, July 2012.

[97] A. Biffin, R. D. Johnson, S. Choi, F. Freund, S. Manni, A. Bombardi, P. Manuel, P. Gegenwart, and R. Coldea. Unconventional magnetic order on the hyperhoneycomb Kitaev lattice in β-Li2IrO3: full solution via magnetic resonant x-ray diffraction. *ArXiv e-prints*, August 2014.

[98] A. Biffin, R. D. Johnson, I. Kimchi, R. Morris, A. Bombardi, J. G. Analytis, A. Vishwanath, and R. Coldea. Non-coplanar and counter-rotating incommensurate magnetic order stabilized by Kitaev interactions in γ-Li2IrO3. *ArXiv e-prints*, July 2014.

[99] A. Biffin, R. D. Johnson, I. Kimchi, R. Morris, A. Bombardi, J. G. Analytis, A. Vishwanath, and R. Coldea. Non-coplanar and counter-rotating incommensurate magnetic order stabilized by Kitaev interactions in γ-Li2IrO3. *ArXiv e-prints*, July 2014.

[100] W. F. Brinkman and T. M. Rice. Single-particle excitations in magnetic insulators. *Phys. Rev. B*, 2:1324–1338, Sep 1970.

[101] C. G. Broyden. The convergence of a class of double-rank minimization algorithms 1. general considerations. *IMA Journal of Applied Mathematics*, 6(1):76–90, 1970.

[102] F. J. Burnell and Chetan Nayak. Su(2) slave fermion solution of the kitaev honeycomb lattice model. *Phys. Rev. B*, 84:125125, Sep 2011.

[103] R. H. Byrd, P. Lu, and J. Nocedal. A limited memory algorithm for bound constrained optimization. *SIAM Journal on Scientific and Statistical Computing,*, 16,5:1190–1208, 1995.

[104] G. Cao, T. F. Qi, L. Li, J. Terzic, V. S. Cao, S. J. Yuan, M. Tovar, G. Murthy, and R. K. Kaul. Evolution of magnetism in the single-crystal honeycomb iridates (Na1-xLix)2IrO3. *Phys. Rev. B*, 88(22):220414, December 2013.

[105] G. Cao, Y. Xin, C. S. Alexander, J. E. Crow, P. Schlottmann, M. K. Crawford, R. L. Harlow, and W. Marshall. Anomalous magnetic and transport behavior in the magnetic insulator $sr_3ir_2o_7$. *Phys. Rev. B*, 66:214412, Dec 2002.

[106] Jiri Chaloupka, George Jackeli, and Giniyat Khaliullin. Kitaev-heisenberg model on a honeycomb lattice: Possible exotic phases in iridium oxides A_2iro_3. *Phys. Rev. Lett.*, 105:027204, Jul 2010.

[107] Jiri Chaloupka, George Jackeli, and Giniyat Khaliullin. Zigzag magnetic order in the iridium oxide Na2IrO3 *Phys. Rev. Lett.*, 110:097204, Feb 2013.

[108] Gang Chen and Leon Balents. Spin-orbit effects in $na_4ir_3o_8$: A hyper-kagome lattice antiferromagnet. *Phys. Rev. B*, 78:094403, Sep 2008.

[109] Mou-Shan Chen, Lars Onsager, Jill Bonner, and John Nagle. Hopping of ions in ice. *The Journal of Chemical Physics*, 60(2):405–419, 1974.

[110] S. K. Choi, R. Coldea, A. N. Kolmogorov, T. Lancaster, I. I. Mazin, S. J. Blundell, P. G. Radaelli, Yogesh Singh, P. Gegenwart, K. R. Choi, S.-W. Cheong, P. J. Baker, C. Stock, and J. Taylor. Spin waves and revised crystal structure of honeycomb iridate na_2iro_3. *Phys. Rev. Lett.*, 108:127204, Mar 2012.

[111] Radu Coldea. *presentation at the MPI-Dresden workshop on Spin Orbit Entanglement*, July 2013.

[112] R. Comin, G. Levy, B. Ludbrook, Z.-H. Zhu, C. N. Veenstra, J. A. Rosen, Yogesh Singh, P. Gegenwart, D. Stricker, J. N. Hancock, D. van der Marel, I. S. Elfimov, and A. Damascelli. na_2iro_3 as a novel relativistic mott insulator with a 340-mev gap. *Phys. Rev. Lett.*, 109:266406, Dec 2012.

[113] S. Depenbrock and F. Pollmann. Phase diagram of the isotropic spin-(3)/(2) model on the z=3 Bethe lattice. *Phys. Rev. B*, 88(3):035138, July 2013.

[114] Stefan Depenbrock, Ian P. McCulloch, and Ulrich Schollwöck. Nature of the spin-liquid ground state of the $s = 1/2$ heisenberg model on the kagome lattice. *Phys. Rev. Lett.*, 109:067201, Aug 2012.

[115] Lukasz Fidkowski. Entanglement spectrum of topological insulators and superconductors. *Phys. Rev. Lett.*, 104:130502, Apr 2010.

[116] Kateryna Foyevtsova, Harald O. Jeschke, I. I. Mazin, D. I. Khomskii, and Roser Valenti analysis of the tight-binding parameters and magnetic interactions in Na2IrO3 *Phys. Rev. B*, 88:035107, Jul 2013.

[117] H. Gretarsson, J. P. Clancy, X. Liu, J. P. Hill, E. Bozin, Y. Singh, S. Manni, P. Gegenwart, J. Kim, A. H. Said, D. Casa, T. Gog, M. H. Upton, H.-S. Kim, J. Yu, V. M. Katukuri, L. Hozoi, J. van den Brink, and Y.-J. Kim. Crystal-Field Splitting and Correlation Effect on the Electronic Structure of A_2IrO_3. *Physical Review Letters*, 110(7):076402, February 2013.

[118] H. Gretarsson, J. P. Clancy, Yogesh Singh, P. Gegenwart, J. P. Hill, Jungho Kim, M. H. Upton, A. H. Said, D. Casa, T. Gog, and Young-June Kim. Magnetic excitation spectrum of na_2iro_3 probed with resonant inelastic x-ray scattering. *Phys. Rev. B*, 87:220407, Jun 2013.

[119] T. Grover, A. M. Turner, and A. Vishwanath. Entanglement entropy of gapped phases and topological order in three dimensions. *Phys. Rev. B*, 84(19):195120, November 2011.

[120] M. Z. Hasan and C. L. Kane. *Colloquium* : Topological insulators. *Rev. Mod. Phys.*, 82:3045–3067, Nov 2010.

[121] M. Zahid Hasan and Joel E. Moore. Three-Dimensional Topological Insulators. In *Annual Review of Condensed Matter Physics*, volume 2, pages 55–78. 2011.

[122] Christopher L. Henley. The coulomb phase in frustrated systems. *Annual Review of Condensed Matter Physics*, 1(1):179–210, 2010.

[123] Christopher L. Henley. *private communication*, March 2013.

[124] M. Hermanns and S. Trebst. Quantum spin liquid with a Majorana Fermi surface on the three-dimensional hyperoctagon lattice. *ArXiv e-prints*, January 2014.

[125] Michael Hermele, Matthew P. A. Fisher, and Leon Balents. Pyrochlore photons: The $u(1)$ spin liquid in a $s = \frac{1}{2}$ three-dimensional frustrated magnet. *Phys. Rev. B*, 69:064404, Feb 2004.

[126] David A. Huse, Werner Krauth, R. Moessner, and S. L. Sondhi. Coulomb and liquid dimer models in three dimensions. *Phys. Rev. Lett.*, 91:167004, Oct 2003.

[127] T. Hyart, A. R. Wright, G. Khaliullin, and B. Rosenow. Competition between d-wave and topological p-wave superconducting phases in the doped Kitaev-Heisenberg model. *Phys. Rev. B*, 85(14):140510, April 2012.

[128] Ashvin Vishwanath Itamar Kimchi. *(unpublished).*

[129] G. Jackeli and G. Khaliullin. Mott insulators in the strong spin-orbit coupling limit: From heisenberg to a quantum compass and kitaev models. *Phys. Rev. Lett.*, 102:017205, Jan 2009.

[130] H.-C. Jiang, Z. Wang, and L. Balents. Identifying topological order by entanglement entropy. *Nature Physics*, 8:902–905, December 2012.

[131] Hong-Chen Jiang, Zheng-Cheng Gu, Xiao-Liang Qi, and Simon Trebst. Possible proximity of the mott insulating iridate na$_2$iro$_3$ to a topological phase: Phase diagram of the heisenberg-kitaev model in a magnetic field. *Phys. Rev. B*, 83:245104, Jun 2011.

[132] T. A. Kaplan and N. Menyuk. Spin ordering in three-dimensional crystals with strong competing exchange interactions. *Philosophical Magazine*, 87(25):3711–3785, 2007.

[133] V. M. Katukuri, S. Nishimoto, V. Yushankhai, A. Stoyanova, H. Kandpal, S. Choi, R. Coldea, I. Rousochatzakis, L. Hozoi, and J. van den Brink. Kitaev interactions between j = 1/2 moments in honeycomb Na_2IrO_3 are large and ferromagnetic: insights from ab initio quantum chemistry calculations. *New Journal of Physics*, 16(1):013056, January 2014.

[134] G. Khaliullin. Order from disorder: Quantum spin gap in magnon spectra of latio$_3$. *Phys. Rev. B*, 64:212405, Nov 2001.

[135] Giniyat Khaliullin. Orbital Order and Fluctuations in Mott Insulators. *Progress of Theoretical Physics Supplement*, 160(160):155–202, 2005.

[136] Giniyat Khaliullin and Satoshi Okamoto. Quantum behavior of orbitals in ferromagnetic titanates: Novel orderings and excitations. *Phys. Rev. Lett.*, 89:167201, Sep 2002.

[137] Giniyat Khaliullin and Satoshi Okamoto. Theory of orbital state and spin interactions in ferromagnetic titanates. *Phys. Rev. B*, 68:205109, Nov 2003.

[138] B. J. Kim, Hosub Jin, S. J. Moon, J.-Y. Kim, B.-G. Park, C. S. Leem, Jaejun Yu, T. W. Noh, C. Kim, S.-J. Oh, J.-H. Park, V. Durairaj, G. Cao, and E. Rotenberg. Novel $J_{\text{eff}} = 1/2$ mott state induced by relativistic spin-orbit coupling in sr$_2$iro$_4$. *Phys. Rev. Lett.*, 101:076402, Aug 2008.

[139] B. J. Kim, H. Ohsumi, T. Komesu, S. Sakai, T. Morita, H. Takagi, and T. Arima. Phase-sensitive observation of a spin-orbital mott state in sr2iro4. *Science*, 323(5919):1329–1332, 2009.

[140] Beom Hyun Kim, G. Khaliullin, and B. I. Min. Electronic excitations in the edge-shared relativistic mott insulator Na2IrO3. *Phys. Rev. B*, 89:081109, Feb 2014.

[141] Itamar Kimchi, James G. Analytis, and Ashvin Vishwanath. Three-dimensional quantum spin liquids in models of harmonic-honeycomb iridates and phase diagram in an infinite-d approximation. *Phys. Rev. B*, 90:205126, Nov 2014.

[142] Itamar Kimchi and Ashvin Vishwanath. Kitaev-heisenberg models for iridates on the triangular, hyperkagome, kagome, fcc, and pyrochlore lattices. *Phys. Rev. B*, 89:014414, Jan 2014.

[143] Itamar Kimchi and Yi-Zhuang You. Kitaev-heisenberg-J_2-J_3 model for the iridates $A_2\mathrm{iro}_3$. *Phys. Rev. B*, 84:180407, Nov 2011.

[144] E. Kin-Ho Lee and Y. B. Kim. Theory of Magnetic Phase Diagrams in Hyper-honeycomb and Harmonic-honeycomb Iridates. *ArXiv e-prints*, July 2014.

[145] E. Kin-Ho Lee, R. Schaffer, S. Bhattacharjee, and Y. B. Kim. Heisenberg-Kitaev model on hyper-honeycomb lattice. *ArXiv e-prints*, August 2013.

[146] A Kitaev. Anyons in an exactly solved model and beyond. *Annals of Physics*, 321(1):2–111, January 2006.

[147] Akihisa Koga and Norio Kawakami. Frustrated heisenberg antiferromagnet on the pyrochlore lattice. *Phys. Rev. B*, 63:144432, Mar 2001.

[148] John B. Kogut. An introduction to lattice gauge theory and spin systems. *Rev. Mod. Phys.*, 51:659–713, Oct 1979.

[149] Hiromichi Kuriyama, Jobu Matsuno, Seiji Niitaka, Masaya Uchida, Daisuke Hashizume, Aiko Nakao, Kunihisa Sugimoto, Hiroyuki Ohsumi, Masaki Takata, and Hidenori Takagi. Epitaxially stabilized iridium spinel oxide without cations in the tetrahedral site. *Applied Physics Letters*, 96(18):182103, 2010.

[150] G. Lang, J. Bobroff, H. Alloul, G. Collin, and N. Blanchard. Spin correlations and cobalt charge states: Phase diagram of sodium cobaltates. *Phys. Rev. B*, 78:155116, Oct 2008.

[151] Michael J. Lawler, Hae-Young Kee, Yong Baek Kim, and Ashvin Vishwanath. Topological spin liquid on the hyperkagome lattice of $\mathrm{na}_4\mathrm{ir}_3\mathrm{o}_8$. *Phys. Rev. Lett.*, 100:227201, Jun 2008.

[152] Michael J. Lawler, Arun Paramekanti, Yong Baek Kim, and Leon Balents. Gapless spin liquids on the three-dimensional hyperkagome lattice of $\mathrm{na}_4\mathrm{ir}_3\mathrm{o}_8$. *Phys. Rev. Lett.*, 101:197202, Nov 2008.

[153] Michael J. Lawler, Arun Paramekanti, Yong Baek Kim, and Leon Balents. Gapless spin liquids on the three-dimensional hyperkagome lattice of $na_4ir_3o_8$. *Phys. Rev. Lett.*, 101:197202, Nov 2008.

[154] S. Lee, E. Kin-Ho Lee, A. Paramekanti, and Y. B. Kim. Order-by-disorder and magnetic field response in Heisenberg-Kitaev model on a hyperhoneycomb lattice. *ArXiv e-prints*, September 2013.

[155] P. W. Leung and Veit Elser. Numerical studies of a 36-site *kagome* antiferromagnet. *Phys. Rev. B*, 47:5459–5462, Mar 1993.

[156] Michael A. Levin and Xiao-Gang Wen. String-net condensation: a physical mechanism for topological phases. *Phys. Rev. B*, 71:045110, Jan 2005.

[157] Wei Li, Jan von Delft, and Tao Xiang. Efficient simulation of infinite tree tensor network states on the bethe lattice. *Phys. Rev. B*, 86:195137, Nov 2012.

[158] Elliott H. Lieb. Two theorems on the hubbard model. *Phys. Rev. Lett.*, 62:1201–1204, Mar 1989.

[159] Elliott H. Lieb. Flux phase of the half-filled band. *Phys. Rev. Lett.*, 73:2158–2161, Oct 1994.

[160] T. Liu, S.-J. Ran, W. Li, X. Yan, Y. Zhao, and G. Su. Featureless quantum spin liquid, 1/3-magnetization plateau state and exotic thermodynamic properties of spin-1/2 Heisenberg antiferromagnet on Husimi lattice. *ArXiv e-prints*, August 2013.

[161] X. Liu, T. Berlijn, W.-G. Yin, W. Ku, A. Tsvelik, Young-June Kim, H. Gretarsson, Yogesh Singh, P. Gegenwart, and J. P. Hill. Long-range magnetic ordering in na_2iro_3. *Phys. Rev. B*, 83:220403, Jun 2011.

[162] Yuan-Ming Lu, Ying Ran, and Patrick A. Lee. $\mathbb{z}_2$ spin liquids in the $s = \frac{1}{2}$ heisenberg model on the kagome lattice: A projective symmetry-group study of schwinger fermion mean-field states. *Phys. Rev. B*, 83:224413, Jun 2011.

[163] J. M. Luttinger. A note on the ground state in antiferromagnetics. *Phys. Rev.*, 81:1015–1018, Mar 1951.

[164] J. M. Luttinger and L. Tisza. Theory of dipole interaction in crystals. *Phys. Rev.*, 70:954–964, Dec 1946.

[165] Y. Machida, S. Nakatsuji, Y. Maeno, T. Tayama, T. Sakakibara, and S. Onoda. Unconventional anomalous hall effect enhanced by a noncoplanar spin texture in the frustrated kondo lattice $pr_2ir_2o_7$. *Phys. Rev. Lett.*, 98:057203, Jan 2007.

[166] Saptarshi Mandal and Naveen Surendran. Exactly solvable Kitaev model in three dimensions. *Physical Review B*, 79(2):1–8, January 2009.

[167] S. Manni, S. Choi, I. I. Mazin, R. Coldea, M. Altmeyer, H. O. Jeschke, R. Valentí, and P. Gegenwart. Effect of isoelectronic doping on the honeycomb-lattice iridate A_2IrO_3. *Phys. Rev. B*, 89(24):245113, June 2014.

[168] S. Manni, Y. Tokiwa, and P. Gegenwart. Effect of nonmagnetic dilution in the honeycomb-lattice iridates Na_2IrO_3 and Li_2IrO_3. *Phys. Rev. B*, 89(24):241102, June 2014.

[169] I. I. Mazin, Harald O. Jeschke, Kateryna Foyevtsova, Roser Valentí, and D. I. Khomskii. na_2iro_3 as a molecular orbital crystal. *Phys. Rev. Lett.*, 109:197201, Nov 2012.

[170] I. I. Mazin, S. Manni, K. Foyevtsova, H. O. Jeschke, P. Gegenwart, and R. Valentí. Origin of the insulating state in honeycomb iridates and rhodates. *Phys. Rev. B*, 88(3):035115, July 2013.

[171] Igor Mazin. *Private Communication*, 2014.

[172] T. Micklitz and M. R. Norman. Spin hamiltonian of hyper-kagome $na_4ir_3o_8$. *Phys. Rev. B*, 81:174417, May 2010.

[173] K. A. Modic, Tess E. Smidt, Itamar Kimchi, Nicholas P. Breznay, Alun Biffin, Sungkyun Choi, Roger D. Johnson, Radu Coldea, Pilanda Watkins-Curry, Gregory T. McCandless, Julia Y. Chan, Felipe Gandara, Z. Islam, Ashvin Vishwanath, Arkady Shekhter, Ross D. McDonald, and James G. Analytis. Realization of a three-dimensional spinanisotropic harmonic honeycomb iridate. *Nat Commun*, 5:–, June 2014.

[174] S. J. Moon, H. Jin, K. W. Kim, W. S. Choi, Y. S. Lee, J. Yu, G. Cao, A. Sumi, H. Funakubo, C. Bernhard, and T. W. Noh. Dimensionality-controlled insulator-metal transition and correlated metallic state in $5d$ transition metal oxides. *Phys. Rev. Lett.*, 101:226402, Nov 2008.

[175] Daniel Nagaj, Edward Farhi, Jeffrey Goldstone, Peter Shor, and Igor Sylvester. Quantum transverse-field ising model on an infinite tree from matrix product states. *Phys. Rev. B*, 77:214431, Jun 2008.

[176] Á. Nagy. Simulating quantum systems on the Bethe lattice by translationally invariant infinite-tree tensor network. *Annals of Physics*, 327:542–552, February 2012.

[177] J. Nasu, T. Kaji, K. Matsuura, M. Udagawa, and Y. Motome. Finite-Temperature Phase Transition to a Quantum Spin Liquid in a Three-Dimensional Kitaev Model on a Hyperhoneycomb Lattice. *ArXiv e-prints*, September 2013.

[178] S. Nishimoto, V. M. Katukuri, V. Yushankhai, H. Stoll, U. K. Roessler, L. Hozoi, I. Rousochatzakis, and J. van den Brink. Strongly frustrated triangular spin lattice emerging from triplet dimer formation in honeycomb Li2IrO3. March 2014.

[179] M. R. Norman and T. Micklitz. Electronic structure of hyper-kagome $na_4ir_3o_8$. *Phys. Rev. B*, 81:024428, Jan 2010.

[180] Satoshi Okamoto. Global phase diagram of a doped kitaev-heisenberg model. *Phys. Rev. B*, 87:064508, Feb 2013.

[181] Yoshihiko Okamoto, Minoru Nohara, Hiroko Aruga-Katori, and Hidenori Takagi. Spin-liquid state in the $s = 1/2$ hyperkagome antiferromagnet $na_4ir_3o_8$. *Phys. Rev. Lett.*, 99:137207, Sep 2007.

[182] Matthew J. O'Malley, Henk Verweij, and Patrick M. Woodward. Structure and properties of ordered li2iro3 and li2pto3. *Journal of Solid State Chemistry*, 181(8):1803 – 1809, 2008.

[183] Ingo Peschel. Calculation of reduced density matrices from correlation functions. *Journal of Physics A: Mathematical and General*, 36(14):L205, 2003.

[184] Dmytro Pesin and Leon Balents. Mott physics and band topology in materials with strong spin–orbit interaction. *Nature Physics*, 6(5):376–381, March 2010.

[185] Xiao-Liang Qi and Shou-Cheng Zhang. Topological insulators and superconductors. *Rev. Mod. Phys.*, 83:1057–1110, Oct 2011.

[186] Jeffrey G. Rau, Eric Kin-Ho Lee, and Hae-Young Kee. Generic spin model for the honeycomb iridates beyond the kitaev limit. *Phys. Rev. Lett.*, 112:077204, Feb 2014.

[187] Johannes Reuther, Dmitry A. Abanin, and Ronny Thomale. Magnetic order and paramagnetic phases in the quantum J_1-J_2-J_3 honeycomb model. *Phys. Rev. B*, 84:014417, Jul 2011.

[188] Johannes Reuther, Ronny Thomale, and Stephan Rachel. Magnetic ordering phenomena of interacting quantum spin hall models. *Phys. Rev. B*, 86:155127, Oct 2012.

[189] Johannes Reuther, Ronny Thomale, and Stephan Rachel. Spiral order in the honeycomb iridate li$_2$iro$_3$. *Phys. Rev. B*, 90:100405, Sep 2014.

[190] Johannes Reuther, Ronny Thomale, and Simon Trebst. Finite-temperature phase diagram of the heisenberg-kitaev model. *Phys. Rev. B*, 84:100406, Sep 2011.

[191] I. Rousochatzakis, U. K. Rössler, J. van den Brink, and M. Daghofer. Z_2-vortex lattice in the ground state of the triangular Kitaev-Heisenberg model. *ArXiv e-prints*, September 2012.

[192] I. Rousochatzakis, U. K. Rössler, J. van den Brink, and M. Daghofer. Z_2-vortex lattice in the ground state of the triangular Kitaev-Heisenberg model. September 2012.

[193] Subir Sachdev. Kagome and triangular-lattice heisenberg antiferromagnets: Ordering from quantum fluctuations and quantum-disordered ground states with unconfined bosonic spinons. *Phys. Rev. B*, 45:12377–12396, Jun 1992.

[194] Lucile Savary and Leon Balents. Coulombic quantum liquids in spin-1/2 pyrochlores. *Phys. Rev. Lett.*, 108:037202, Jan 2012.

[195] Atsuo Shitade, Hosho Katsura, Jan Kuneš, Xiao-Liang Qi, Shou-Cheng Zhang, and Naoto Nagaosa. Quantum spin hall effect in a transition metal oxide na$_2$iro$_3$. *Phys. Rev. Lett.*, 102:256403, Jun 2009.

[196] P. Sindzingre, G. Misguich, C. Lhuillier, B. Bernu, L. Pierre, Ch. Waldtmann, and H.-U. Everts. Magnetothermodynamics of the spin- $\frac{1}{2}$ kagomé antiferromagnet. *Phys. Rev. Lett.*, 84:2953–2956, Mar 2000.

[197] Yogesh Singh and P. Gegenwart. Antiferromagnetic mott insulating state in single crystals of the honeycomb lattice material na$_2$iro$_3$. *Phys. Rev. B*, 82:064412, Aug 2010.

[198] Yogesh Singh, S. Manni, J. Reuther, T. Berlijn, R. Thomale, W. Ku, S. Trebst, and P. Gegenwart. Relevance of the heisenberg-kitaev model for the honeycomb lattice iridates A_2iro$_3$. *Phys. Rev. Lett.*, 108:127203, Mar 2012.

[199] T. Takayama, A. Kato, R. Dinnebier, J. Nuss, and H. Takagi. Hyper-honeycomb iridate β-Li2IrO3 as a platform for Kitaev magnetism. *ArXiv e-prints*, March 2014.

[200] Tiamhock Tay and Olexei I. Motrunich. Variational study of J_1-J_2 heisenberg model on kagome lattice using projected schwinger-boson wave functions. *Phys. Rev. B*, 84:020404, Jul 2011.

[201] O. Tchernyshyov, R. Moessner, and S. L. Sondhi. Flux expulsion and greedy bosons: Frustrated magnets at large n. *EPL (Europhysics Letters)*, 73(2):278, 2006.

[202] F. Trousselet, M. Berciu, A. M. Oleś, and P. Horsch. Hidden Quasiparticles and Incoherent Photoemission Spectra in Na_2IrO_3. *Physical Review Letters*, 111(3):037205, July 2013.

[203] F. Trousselet, P. Horsch, A. M. Oles, and W.-L. You. From Hidden Quasiparticles to non-Fermi Liquid in the Kitaev-Heisenberg Model. *ArXiv e-prints*, August 2013.

[204] Ari M. Turner, Yi Zhang, and Ashvin Vishwanath. Entanglement and inversion symmetry in topological insulators. *Phys. Rev. B*, 82:241102, Dec 2010.

[205] G. Vidal. Classical simulation of infinite-size quantum lattice systems in one spatial dimension. *Phys. Rev. Lett.*, 98:070201, Feb 2007.

[206] Xiangang Wan, Ari M. Turner, Ashvin Vishwanath, and Sergey Y. Savrasov. Topological semimetal and fermi-arc surface states in the electronic structure of pyrochlore iridates. *Phys. Rev. B*, 83:205101, May 2011.

[207] Xiangang Wan, Ashvin Vishwanath, and Sergey Y. Savrasov. Computational design of axion insulators based on $5d$ spinel compounds. *Phys. Rev. Lett.*, 108:146601, Apr 2012.

[208] Chong Wang and T. Senthil. Boson topological insulators: A window into highly entangled quantum phases. *Phys. Rev. B*, 87:235122, Jun 2013.

[209] Fa Wang and Ashvin Vishwanath. Spin-liquid states on the triangular and kagomé lattices: A projective-symmetry-group analysis of schwinger boson states. *Phys. Rev. B*, 74:174423, Nov 2006.

[210] Xiao-Gang Wen. Quantum orders and symmetric spin liquids. *Phys. Rev. B*, 65:165113, Apr 2002.

[211] Xiao-Gang Wen. *Quantum Field Theory of Many-Body Systems*. Oxford University Press, 2004.

[212] Y. Yamaji, Y. Nomura, M. Kurita, R. Arita, and M. Imada. Honeycomb Lattice Iridates Na2IrO3 under Strong Spin-Orbit Interaction and Electron Correlation Studied by Ab Initio Scheme. *ArXiv e-prints*, February 2014.

[213] Simeng Yan, David A. Huse, and Steven R. White. Spin-liquid ground state of the s = 1/2 kagome heisenberg antiferromagnet. *Science*, 332(6034):1173–1176, 2011.

[214] Daiki Yanagishima and Yoshiteru Maeno. Metal-nonmetal changeover in pyrochlore iridates. *Journal of the Physical Society of Japan*, 70(10):2880–2883, 2001.

[215] Hong Yao and Steven A. Kivelson. Exact chiral spin liquid with non-abelian anyons. *Phys. Rev. Lett.*, 99:247203, Dec 2007.

[216] Hong Yao and Xiao-Liang Qi. Entanglement entropy and entanglement spectrum of the kitaev model. *Phys. Rev. Lett.*, 105:080501, Aug 2010.

[217] Feng Ye, Songxue Chi, Huibo Cao, Bryan C. Chakoumakos, Jaime A. Fernandez-Baca, Radu Custelcean, T. F. Qi, O. B. Korneta, and G. Cao. Direct evidence of a zigzag spin-chain structure in the honeycomb lattice: A neutron and x-ray diffraction investigation of single-crystal na_2iro_3. *Phys. Rev. B*, 85:180403, May 2012.

[218] Yi-Zhuang You, Itamar Kimchi, and Ashvin Vishwanath. Doping a spin-orbit mott insulator: Topological superconductivity from the kitaev-heisenberg model and possible application to $(na_2/li_2)iro_3$. *Phys. Rev. B*, 86:085145, Aug 2012.

[219] Y. Zhang, T. Grover, A. Turner, M. Oshikawa, and A. Vishwanath. Quasiparticle statistics and braiding from ground-state entanglement. *Phys. Rev. B*, 85(23):235151, June 2012.

[220] Yi Zhou, Patrick A. Lee, Tai-Kai Ng, and Fu-Chun Zhang. $Na_4Ir_3O_8$ as a 3d spin liquid with fermionic spinons. *Phys. Rev. Lett.*, 101:197201, Nov 2008.